

## REPORT DOCUMENTATION PAGE

Form Approved  
OMB No. 0704-0188

The public reporting burden for this collection of information is estimated to average 1 hour per response, including the time for reviewing instructions, searching existing data sources, gathering and maintaining the data needed, and completing and reviewing the collection of information. Send comments regarding this burden estimate or any other aspect of this collection of information, including suggestions for reducing the burden, to Department of Defense, Washington Headquarters Services, Directorate for Information Operations and Reports (0704-0188), 1215 Jefferson Davis Highway, Suite 1204, Arlington, VA 22202-4302. Respondents should be aware that notwithstanding any other provision of law, no person shall be subject to any penalty for failing to comply with a collection of information if it does not display a currently valid OMB control number.

PLEASE DO NOT RETURN YOUR FORM TO THE ABOVE ADDRESS.

1. REPORT DATE (DD-MM-YYYY) 16-12-2011			2. REPORT TYPE Final Technical Report		3. DATES COVERED (From - To) April 2009 - September 2011	
4. TITLE AND SUBTITLE Final Technical Report Hawaii Energy and Environmental Technologies (HEET) Initiative					5a. CONTRACT NUMBER	
					5b. GRANT NUMBER N00014-09-1-0709	
					5c. PROGRAM ELEMENT NUMBER	
6. AUTHOR(S) Rocheleau, Richard E; Bethune, Keith; Virji, Maheboob; Antal, Michael J, Jr; Cooney, Michael J; Liaw, Bor Yann; Turn, Scott Q; Piavis, William; Nurunnabi, Md; Yu, Jian; Yosa, Brandon; Hihara, Lloyd; Masutani, Stephen M; Busquet, Severine; Cutshaw, Larry; Reshetenko, Tatyana; Zhai, Yunfeng					5d. PROJECT NUMBER 09PR06845-00	
					5e. TASK NUMBER	
					5f. WORK UNIT NUMBER	
7. PERFORMING ORGANIZATION NAME(S) AND ADDRESS(ES) University of Hawaii 2530 Dole Street, Sakamaki D200 Honolulu, HI 96822					8. PERFORMING ORGANIZATION REPORT NUMBER	
9. SPONSORING/MONITORING AGENCY NAME(S) AND ADDRESS(ES) Office of Naval Research Regional Office Seattle-N63374 1107 NE 45th Street, Suite 350 Seattle WA 98105-4631					10. SPONSOR/MONITOR'S ACRONYM(S) ONR	
					11. SPONSOR/MONITOR'S REPORT NUMBER(S)	
12. DISTRIBUTION/AVAILABILITY STATEMENT Approved for public release; distribution is unlimited.						
13. SUPPLEMENTARY NOTES						
14. ABSTRACT This report covers efforts by the Hawaii Natural Energy Institute (HNEI) of the University of Hawaii under the ONR-funded HEET Initiative that addresses critical technology needs for exploration/utilization of seabed methane hydrates, development/testing of advanced fuel cells and fuel cell systems, an expanded effort on fuel processing and purification, and a new task addressing testing and evaluation of alternate energy sources, with initial activities in testing of heat exchangers for ocean thermal energy conversion (OTEC), grid storage, and photovoltaics. In addition to work involving fuel cell testing, HNEI also participated in fuel cell development activities, including efforts in support of biocarbon fuel cells and the development of enzymatic bio-fuel cells.						
15. SUBJECT TERMS Fuel Cells, Fuel Cell Testing, MEA Assembly, Hardware-in-Loop Testing, Synthetic Fuel Production, Fuels Purity, Methane Hydrates, Biocarbons, Bio-Fuel Cells, OTEC, Heat Exchangers, Grid Storage, Photovoltaics						
16. SECURITY CLASSIFICATION OF:			17. LIMITATION OF ABSTRACT	18. NUMBER OF PAGES	19a. NAME OF RESPONSIBLE PERSON	
a. REPORT	b. ABSTRACT	c. THIS PAGE			Yaa-Yin Fong, Director of Research Services	
U	U	U	UU	199	19b. TELEPHONE NUMBER (Include area code) (808) 956-9081	

# **FINAL TECHNICAL REPORT**

## **Hawaii Energy and Environmental Technologies (HEET) Initiative**

**Office of Naval Research**

**Grant Award Number N00014-09-1-0709**

**For the period April 1, 2009 to September 30, 2011**

**Hawaii Natural Energy Institute**



**School of Ocean and Earth Science and Technology  
University of Hawaii at Mānoa**

**December 2011**

20111223011



## Table of Contents

<u>Section No.</u>	<u>Section Title</u>	<u>Page</u>
A.	Executive Summary	vii
B.	Introduction	xiii
I.	Fuel Cell Systems	1
1.1	Fuel Cell Testing and Evaluation	1
1.1.1	Test Stands and Infrastructure Upgrade	1
1.1.2	Component, Cell and Stack Testing	2
1.1.2.1	Air Contaminant Studies: Component Degradation during SO <sub>2</sub> Contamination and Performance Recovery	2
1.1.2.2	Air Contaminant Studies: Mechanistic Modeling of SO <sub>2</sub> Adsorption on Pt/C	5
1.1.2.3	Manufacturing Defect Performance Implications: Gas Diffusion Layer Defect Influence on Air Permeability of PEM Cathodes	10
1.1.3	Fuel Cell Hardware-in-Loop and System Simulation	19
1.1.3.1	Scope of Work and Approach	19
1.1.3.2	Ion Tiger UAV Power Pack Characterization: Evaluation of Protonex's On-Board Fuel Cell Performance Recovery Method under Mission Load Profiles using the HiL Test System	19
1.1.3.3	Ion Tiger UAV Power Pack Characterization: HiL Evaluation Utilizing 12 Volt Battery Pack to Provide Power during Fuel Cell Regeneration Events	27
1.1.3.4	Ion Tiger UAV Power Pack Characterization: Hybridization Study of the UAV System	31
1.1.4	Alternate Cell Evaluation	39
1.1.5	Papers and Presentation Resulting from These Efforts	39
1.2	Fuel Cell Development	41
1.2.1	Biocarbons for Fuel Cells	41
1.2.1.1	Technical Accomplishments	41
1.2.1.2	References Cited	42
1.2.2	Bioactive Fuel Cells	43
1.2.2.1	Scope of Work and Approach	43
1.2.2.2	Technical Accomplishments	44
1.2.2.3	References	57
1.2.2.4	Papers and Presentations Resulting from Efforts	59





2.6.3	References	135
2.6.4	Publications and Presentations	135
2.7	Biofuel Corrosion Research	137
2.7.1	Scope of Work and Approach	137
2.7.2	Technical Accomplishments	137
2.7.2.1	Literature Review	138
2.7.2.1.1	Case Studies	138
2.7.2.2	Laboratory Setup for MIC	139
2.7.2.3	Preliminary Biofuels Corrosion Experiment in Potable Water-Biofuel Mixtures	139
2,7,2,3,1	Methodology	139
2,7,2,3,2	Results	141
2,7,2,3,3	Discussion	150
2,7,2,3,4	Conclusions	150
2.7.2.4	Characterization of Bacteria Found	150
2.7.2.5	Work in Progress	152
2.7.3	References	156
2.8	Waste Management Using the Flash Carbonization™ Process	157
2.8.1	Scope of Work and Approach	157
2.7.2	Technical Accomplishments	158
3.	Methane Hydrates	161
3.1	Objectives	161
3.2	Scope of Work and Approach	162
3.3	Technical Accomplishments	163
Hydrate Energy		163
Environmental Impacts of Methane Release from Seafloor Hydrates		173
Hydrate Engineering Applications		182
International Collaborative Research and Development		187
3.4	Publications Resulting from Efforts	188
3.5	References	188

4. Alternative Energy Systems	193
4.1 OTEC Heat Exchangers	193
4.2 Storage Analysis	194
4.3 Photovoltaic (PV) Assessment	197

**Final Technical Report for the  
Hawaii Energy and Environmental Technologies (HEET) Initiative  
Grant Award Number N00014-09-1-0709  
(April 1, 2009 to September 30, 2011)**

**A. Executive Summary**

This report summarizes work conducted under Grant Award Number N00014-09-1-0709, the Hawaii Energy and Environmental Technologies (HEET) Initiative, funded by the Office of Naval Research (ONR) to the Hawaii Natural Energy Institute (HNEI) of the University of Hawaii. The effort under this award continued a focus on critical technology needs associated with the development and testing of advanced fuel cells and fuel cell systems, an expanded effort on fuel processing and purification, and the exploration and utilization of seabed methane hydrates. This award also began new efforts relating to the interest of ONR in the use of Hawai'i as a Model for Distributed Energy Systems for the Pacific Region. These efforts include new tasks addressing testing and evaluation of alternative energy systems, with initial activities in testing of heat exchangers for Ocean Thermal Energy Conversion (OTEC), grid storage, and photovoltaic systems. This represents the sixth award of the initiative.

Major accomplishments under the first grant award, Number N00014-01-1-0928, included the planning, design and construction of the Hawaii Fuel Cell Test Facility (HFCTF), which opened in May 2003. In partnership with industry, HNEI established test protocols and initiated a variety of long-term durability studies. The methane hydrates activities under the first agreement initiated studies to characterize hydrate thermochemistry and kinetics, hydrate microbiology and development of international collaborations.

Under the second award (N00014-04-1-0682), HNEI expanded its test capabilities with the addition of three fuel cell test stands at the HFCTF, including two for fuels purity studies. Tests to characterize the effects of contaminants in the hydrogen fuel were initiated. The third stand was designed for high speed dynamic testing for use in Hardware-in-Loop (HiL) work. Modeling and simulation of a fuel cell energy/power system for use in an unmanned underwater vehicle (UUV) was also completed and reported. Novel fuel cell component research was conducted to explore the use of biocarbons in fuel cell bipolar plates and development of enzymatic bio-fuel cells. A small effort in alternative fuel research focused on fuel processing and gas conditioning for hydrogen production. HNEI's activities in the area of methane hydrates included studies of hydrate destabilization phenomena, with shakedown testing of HNEI's destabilization facility and design and fabrication of a novel fiberoptic probe to identify sample aspects within the calorimeter sample cell using Raman spectroscopy. HNEI sponsored and manned the organizing committee of the 4<sup>th</sup> International Workshop on Methane Hydrates that took place in Victoria, British Columbia, Canada on 9-11 May 2005.

Under the third award (N00014-06-1-0086), the capacity of the HFCTF was again expanded, by increasing the number of test stands and modifying the existing test stands for increased performance. The dynamic HiL test stand was modified to enhance response and to improve operating flexibility, safety, and test stand reliability. Simulation tools for evaluation and screening of fuel cell systems for UUV propulsion systems were developed. HNEI continued research on fuel processing and gas conditioning for hydrogen production, focused on sulfur



removal from fuel gas using activated-carbon-based sorbents, and reformation of seafloor methane for use in underwater fuel cells. Work continued in the development of novel fuel cells, specifically in the areas of biocarbons for fuel cell use and development of enzymatic bio-fuel cells. HNEI's activities in the area of methane hydrates included an expanded effort in hydrate destabilization with development of a novel instrument that combined spectroscopy and calorimetry to study reagent-induced decomposition of the hydrates. As part of our goal to promote international collaboration, HNEI personnel participated in a multi-national research cruise off New Zealand in June and July 2006.

In the course of the fourth award (N00014-06-1-1055), more test stands were added to the HFCTF and several existing stands were modified to allow testing of small stacks. Several test stands were used to support Ion Tiger, an ONR-funded unmanned aerial vehicle (UAV) project. Research focused primarily on understanding the performance impact of contaminants present in the anode and cathode feed streams. The HiL test stand was also upgraded, allowing testing of fuel cell stacks up to 1 kW. Simulation tools were modified for evaluation of fuel cell systems for propulsion of a UAV. A plasma reforming effort was initiated with the design, construction, and testing of two different plasma arc reactor designs. The reverse-vortex reactor performed better than the planar plasma, gliding arc design. In support of the DARPA-sponsored Direct Carbon Fuel Cell research project at SRI International (SRI), HNEI prepared biocarbons from various biomass feedstocks to aid in optimizing performance of SRI's carbon fuel cells. Development of enzymatic bio-fuel cells continued, focused on enzyme immobilization utilizing macroporous chitosan polymer composites. The methane hydrates activities included significant progress in understanding hydrate destabilization using thermodynamic inhibitors. The impact of seafloor methane from hydrates on the marine environment was explored via both experiments and modeling. HNEI again supported and helped organize the 6<sup>th</sup> International Workshop on Methane Hydrate R&D that was held in Bergen, Norway in May 2008. The workshop was attended by scientists, engineers, and other stakeholders from 12 countries and a meeting report is available from the Naval Research Laboratory (NRL).

Under the fifth award (N00014-07-1-1094), several upgrades to test stands and infrastructure were implemented. Research included work on SO<sub>2</sub> contamination mechanisms and recovery, testing of Protonex hydrogen/air stacks under pure oxygen in support of the Naval Undersea Warfare Center (NUWC) at Newport, RI, development of a new segmented-cell flow-field design, and continued testing and analysis in support of Ion Tiger. Efforts to characterize a non-thermal plasma reactor for methane reforming were continued. Parametric tests were conducted and system performance was characterized using various metric features. HNEI continued providing biocarbons to SRI in support of its DARPA-sponsored work with direct carbon fuel cells. HNEI also completed a study of carbonization of sewage sludge from a treatment plant on O'ahu. Cost estimations of HNEI's commercial-scale Flash Carbonization<sup>TM</sup> reactor were completed, revealing the high cost of providing compressed air for operation of a pressurized catalytic afterburner (CAB) needed to meet emissions regulations. The focus of the enzymatic bio-fuel work continued to be enzyme immobilization utilizing macroporous chitosan polymer composites that support both mediator-based and direct-electron-transfer mechanisms. The methane hydrates activities included laboratory and analytical investigations of hydrate destabilization by chemical reagents, comparison of obtained data with models developed to predict the fate of methane released from the seafloor into the water column, experimental and modeling efforts examining the impact of methane from hydrates on the marine environment,

exploratory laboratory studies of H<sub>2</sub> storage, and the promotion of international R&D partnerships via support and help in organizing the 6<sup>th</sup> International Workshop on Methane Hydrate R&D held in Bergen, Norway in May 2008 and the 7<sup>th</sup> workshop held in Wellington, New Zealand in May 2010.

In the course of this award (N00014-09-1-0709), work was continued under the Fuel Cell Testing and Evaluation tasks. Test stand and infrastructure upgrades focused on increasing the maximum station power test capability to 5 kW to support Navy UUV interests.

Component and stack testing encompassed air contamination studies and investigations concerning the impact of manufacturing defects on fuel cell performance. The air contamination work covered component degradation during SO<sub>2</sub> contamination and performance recovery, and mechanistic modeling of SO<sub>2</sub> adsorption on catalysts consisting of carbon-supported platinum nanoparticles. HNEI's segmented cell system which includes cell hardware and a data acquisition system was used to characterize the impact of defects in the MEA. Defect location was found to be an important element, with defects located at an outlet resulting in more significant impact on performance.

Fuel cell Hardware-in-Loop (HiL) activities concentrated on Ion Tiger power pack characterization. Mission load profiles were used to evaluate the Protonex on-board fuel cell performance recovery method and to evaluate use of the 12-volt battery pack to provide power during fuel cell regeneration events. Performance comparisons were obtained for two types of lithium ion batteries. UAV system simulations were developed in a Matlab/Simulink environment for different system configurations (non-hybrid, traditional full hybrid, and novel partial hybrid) to study the impact of adding battery packs (weight) and controller hardware (weight and power losses) on the flight duration of the UAVs for a given propulsion and ancillary load profile.

HNEI produced and characterized biocarbons from corncob, oak wood and sweet gum wood in support of biocarbon fuel cells. The two woody materials were supplied by the Dow-Corning Corporation that employs charcoal as a reductant to manufacture silicon from quartz. The research resulted in two publications and a third that is in preparation. Development of enzymatic bio-fuel cells also continued, focused on enzyme immobilization utilizing macroporous chitosan polymer composites. In addition, development of unique *in situ* characterization techniques to investigate immobilization phenomena and processes was initiated. These activities have helped to secure additional funding from the Air Force Office of Scientific Research for a Multi-disciplinary University Research Initiative project and from the National Geospatial-Intelligence Agency for a postdoctoral fellow research project.

The work under the Technology for Synthetic Fuels Production task included a biofuel characterization planning. This subtask sought to identify biofuel components in support of Navy operations in tropical island settings. Pathways for bioenergy systems were explored, fit-for-purpose screening standards for F-76 and JP-5 fuels were summarized, and special equipment requirements for fuel quality research program needs were presented.

The second subtask involved plasma arc processing of fuels to produce hydrogen-rich fuels for fuel cell applications. Specific accomplishments were achieved in characterization of the performance of the reformer on methane over a range of conditions, additional design and



selection of fuel system components required for delivery of fuel to the reactor, and initial work on a numerical model of the plasma reactor system.

Thermocatalytic conversion of syngas into liquid fuels constituted the third subtask. A Fischer-Tropsch reactor system was designed for production of high-quality clean fuels from biomass-derived synthesis gas. The system consists of three major subsystems: a pre-reactor subsystem to meter reactants to the reactors, the reactor subsystem comprising the synthesis reactor and catalyst preparation reactor, and the post-reactor subsystem to condition the reactor outlet stream and analyze products.

Extraction of bio-oils and protein from biomass was explored using a novel solvent-based approach in the fourth subtask. The co-solvent system consisted of a hydrophilic ionic liquid and polar covalent molecule. Through direct transesterification, microalgal biomass yielded fatty acid methyl esters, and efforts continued in optimizing this process. Other efforts characterized how protein was partitioned in the co-solvent system.

Biochemical conversion of syngas into liquid fuels constituted the fifth subtask. Accomplishments included research results on mechanisms, kinetics, key enzymes, and the role of individual gases in the conversion process. Specific progress is presented in the production of liquid fuels from polyesters by methanolysis and thermal degradation.

The sixth subtask addressed biocontamination of alternative fuels. Accomplishments included enumeration of microbiological contaminants, description of a specific contaminated sample, isolation and characterization of microorganisms, measurement of degradation kinetics, and contaminant mediation and detection.

Biofuel corrosion research made up the seventh subtask. Work accomplished included a literature review with examination of case studies, establishment of a laboratory for study of microbiologically influenced corrosion, and results of preliminary laboratory experiments.

The final subtask focused on waste management using the HNEI patented Flash-Carbonization™ process for the production of biocarbons (charcoal). Efforts concentrated on modifications to the existing HNEI demonstration-scale Flash-Carbonization™ reactor and tests conducted with a laboratory-scale reactor. Many of these tests used Hawaii Kai sewage sludge as the feedstock. The Hawaii Kai sewage sludge has peculiar properties, perhaps due to additives employed by the Hawaii Kai treatment facility. Work focused on this feedstock and its carbonization behavior is continuing.

The task for Methane Hydrates activities comprised four subtasks: Hydrate Energy, Environmental Impacts of Methane Release from Seafloor Hydrates, Hydrate Engineering Applications, and International Collaborative R&D.

Our previous experimental and modeling activities focused on simple gas-water-hydrate systems. Natural hydrate deposits, however, occur in permafrost and seafloor sediments. Experiments were therefore initiated to investigate hydrate formation and destabilization in porous media. Quantities of two “standard” sands employed by the Japanese and U.S. national programs on methane hydrate R&D were obtained and employed in exploratory studies using the Raman calorimeter. The experiments validated the performance of that instrument when employed with sand-water-methane samples and provided preliminary data suggesting a significant impact of sand properties and “memory effects” on hydrate formation and dissociation.



The kinetic behavior of methane hydrate as it dissociates in the presence of thermodynamic inhibitors has been investigated experimentally in previous phases of the HEET initiative. Based on those results, we have proposed a mechanism where an inhibitor disrupts the dynamic equilibrium between hydrate formation and decomposition at the surface by binding up released water molecules and preventing them from re-crystallizing. During the present reporting period, we initiated additional experiments to test our hypothesis. The reagent of interest was glycerol ( $C_3H_8O_3$ ), a triol having three hydroxyl groups. Glycerol appears to be an attractive alternative to alcohols or ethylene glycol, since it is inexpensive and relatively benign from a toxicity/environmental health perspective.

Microbial processes in the sediment and the water column are believed to play a major role in determining methane levels throughout the marine environment. The underlying metabolic pathways and the factors that affect these processes are not well understood and have been a focus area of the HNEI methane hydrate task. During the present phase of the HEET initiative, we participated in an oceanographic research cruise in the Beaufort Sea off the North Slope of Alaska, during which sediment samples were collected from shallow and cold water environments in methane-rich areas. Six of these samples were selected for long-term enrichment incubations and for DNA extraction. PCR amplification of the extracts indicate a diverse community of microorganisms associated with methane cycling including Type I methanotrophic bacteria, sulfate reducing microbes, and methanogens. Attempts to employ micro-calorimetry to observe quantifiable rates of microbial oxidation and reduction of methane in the most promising samples to date have not been successful.

As part of our goal to explore the use of gas hydrates for various engineering applications, we continued our investigation of hydrate  $H_2$  storage. Although the extremely high pressures and low temperatures required to synthesize and maintain pure  $H_2$  hydrate make it impractical as a medium to store and transport fuel, certain hydrate promoters such as tetrahydrofuran (THF) appear to show potential to stabilize the  $H_2$  hydrate at less severe conditions. We were able successfully to synthesize both THF +  $H_2$  and tetra-n-butylammonium bromide (TBAB) +  $H_2$  hydrates using the Raman calorimeter and currently are pursuing development of both of these inhibitors.

Finally, for methane hydrates, as part of our goal to foster international collaborative R&D on methane hydrates, HNEI supported and helped to organize the 7<sup>th</sup> International Workshop on Methane Hydrate R&D that was held in Wellington, New Zealand in May 2012. A report on that workshop can be downloaded from the GNS Science website. During the present reporting period, planning also commenced for the 8<sup>th</sup> workshop that will be held in Sapporo, Japan at the end of May 2012. The Hokkaido branch of the National Institute of Advanced Industrial Science and Technology Science (AIST), an agency of the Government of Japan, is taking the lead for this workshop and HNEI will once again serve on the organizing committee and provide sponsorship.

Under the Alternate Energy Systems section, activities were completed for OTEC heat exchangers, storage analysis, and photovoltaic (PV) assessment. For the OTEC efforts, a heat exchanger performance testing facility was constructed, functional testing of an evaporator and condenser was completed, and a series of 6- to 18-month corrosion samples were removed from corrosion testing. The storage analysis work included scoping studies to determine battery size and operating characteristics, and siting studies to identify potential locations for battery system deployments. PV assessment activities encompassed the execution of a project plan including

planning, design, implementing, and managing tasks to fully instrument an existing grid-connected PV Inverter system on the Big Island of Hawai‘i.

## **B. Introduction**

The Hawaii Energy and Environmental Technologies (HEET) Initiative, funded to the Hawaii Natural Energy Institute (HNEI) of the University of Hawaii through the Office of Naval Research (ONR), was initiated in the summer of 2001 under Grant Award Number N00014-01-1-0928 to address critical technology needs associated with the exploration and utilization of seabed methane hydrates and the development and testing of advanced fuel cells and fuel cell systems.

These efforts and a smaller effort in fuels purification were continued under two subsequent agreements (Award No. N00014-04-1-0682: June 15, 2005 to June 30, 2006; and Award No. N00014-06-1-0086: October 17, 2005 to September 30, 2007). Under these programs, the focal point of our activity was testing and development of PEM fuel cell technology for commercial and military applications, and research to characterize the chemical and physical properties of methane hydrates. Research in these areas was described in these reports.

Under the fourth HEET program (Award No. N00014-06-1-1055), for the period September 14, 2006 to December 31, 2008, work was continued in the areas of fuel cell systems and methane hydrate. In addition, efforts were begun concerning fuel processing and gas conditioning for hydrogen production.

Our fifth HEET program (Award No. N00014-07-1-1094), was for the period September 27, 2007 to March 31, 2010. Under this award, efforts in the areas of fuel cell systems and methane hydrates continued, with increased emphasis on fuel processing and purification studies.

The sixth and current HEET program (Award No. N00014-09-1-0709) was for the period April 1, 2009 to September 30, 2011. Work under this award has included continuation of the fuel cell and methane hydrates efforts, and an increased effort under the label: technology for synthetic fuels production. HNEI also initiated a new effort in testing and evaluation of alternate energy technologies of interest for Asia-Pacific development. Initial efforts have focused on heat exchangers for OTEC, battery storage, and photovoltaics. The remaining portions of this report focus on each of the major areas covered within the current HEET initiative. Section 1 is on fuel cell systems, Section 2 reports results for synthetic fuels, Section 3 covers methane hydrates, and Section 4 presents the studies on alternative energy systems, including OTEC heat exchangers, energy storage analysis, and photovoltaic system assessment.

This page is intentionally blank.



# **1. Fuel Cell Systems**

This task area is organized into two subtasks: 1) fuel cell testing and evaluation, and 2) fuel cell development. Under this grant, HNEI has performed testing and evaluation of Polymer Electrolyte Membrane (PEM) fuel cells and stacks, and identification/evaluation of alternate cell technologies; and investigations of novel fuel cell components. Details for the activities conducted under each of these subtasks are given below.

## **1.1 Fuel Cell Testing and Evaluation**

Efforts in this subtask area focused on issues associated with fuel cell and stack performance and durability, particularly in regard to operation in harsh environments and specific fuel and oxidant systems required for autonomous aerial vehicles (UAV) and undersea (UUV) applications. During the past year, only minor improvements were made to the test stand and facility infrastructure. The only upgrade effort of significance undertaken was to evaluate various options to increase the maximum station power test point to 5kW to support Navy UUV interests. As part of the continuing efforts to understand the impact of contaminants, a series long term SO<sub>2</sub> contamination experiments were conducted to increase understanding of the effect of poisoning and recovery processes on durability. Additional studies in a nitrogen environment simulating SO<sub>2</sub> adsorption under process conditions were also conducted to further understand the SO<sub>2</sub> contamination mechanisms and aid in the development of a mechanistic model of the SO<sub>2</sub> poisoning process. Expanding upon contamination studies, additional experiments were added to look at the effects of the manufacturing defects on hydrogen polymer electrolyte fuel cells (PEMFCs) performance. This work was performed to support the DOE manufacturing initiative for PEMFC production. The work was focused on investigation of effects of a GDL defect on the localized air permeability. This work utilized the segmented cell system developed previously. For the final effort in this section of the project during the grant period, HNEI's state-of-the-art HiL system was used in support of Naval Research Laboratory (NRL) efforts to further characterize Protonex's fuel cell stack with the focus on improving the stack's performance and durability for use in Ion Tiger unmanned aerial vehicle (UAV).

### **1.1.1 Test Stands and Infrastructure Upgrade**

During the past year, only minor improvements were made to the test stand and facility infrastructure. The effort of significance undertaken was to evaluate various options to increase the maximum station power test point to 5 kW to support Navy UUV interests. The 5 kW power level was selected as this is the maximum operating level for the current facility infrastructure, particularly the electrolyzer and zero-grade air generation system. The final option selected was to perform a full mechanical overhaul of an existing UTC station, while maintaining the original electrical and process instrumentation hardware. The primary selection points were the cost of a new station, ~150-250k, and delivery estimates of > 18 weeks. Parts acquisition and build time for the in-house option were estimated to take ~10 weeks, with an approximate hardware cost of ~ 60k. In addition, by performing the overhaul in-house, HNEI maintains greater control and flexibility for future upgrades, especially utilizing HNEI software as well. The projected first test program is short stack testing as part of an upcoming ONR program utilizing a GM automotive fuel cell system as an UUV power source. The test station build began in the final

month of this project. Following a year of operation, additional upgrades will be made to support contaminant studies in recirculation systems.

## 1.1.2 Component Cell and Stack Testing

### 1.1.2.1 Air Contaminant Studies: Component Degradation during SO<sub>2</sub> Contamination and Performance Recovery

In the present award period a series long term SO<sub>2</sub> contamination experiments were conducted to increase understanding of the effect on durability. The long term tests include two (repeat) 300 hrs baseline testing without SO<sub>2</sub> exposure, two (repeat) 300 hrs (20 hrs pre-poisoning + 200 hrs poisoning + 80 hrs self-recovery) continuous contamination testing with 2 ppm SO<sub>2</sub>, and a 4 cycles poisoning-recovery (one cycle: 20 hrs pre-poisoning + 20 hrs poisoning + 40 hrs self-recovery + potential scanning recovery) test.

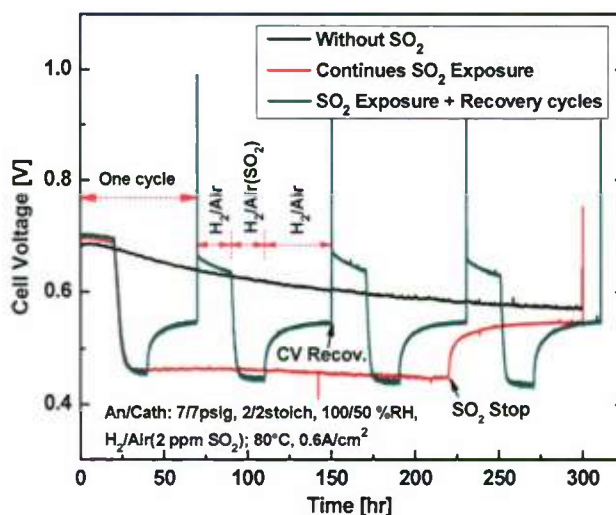


Figure 1.1.1 Cell voltage response during baseline test without SO<sub>2</sub> exposure, 2 ppm continuous SO<sub>2</sub> exposure and SO<sub>2</sub> exposure + recovery cycles

Figure 1.1.1 shows the cells performance response during the long term tests. The figure shows that the cell voltage continuously degraded about 16% over the 300 hours constant current operating without SO<sub>2</sub> contamination. For the continuous SO<sub>2</sub> exposure test and the SO<sub>2</sub> exposure + recovery test, the cell voltage shows a similar rapid degradation with the starting of the SO<sub>2</sub> injection, and reached a similar steady state at about 0.45 V. Even the performance self-recovery is also identical and the final cell voltage degradation for both tests was about 21% of their initial performance. These results indicate that the cell performance degradation and self-recovery are independent of exposure time when the contamination reached an equilibrium state. From the cycling test result, it is apparent that the cell performance can be further recovered by CV scanning (0.08V-1.2V vs. RHE, 15 scans). Each individual cycle had showed similar behaviors until the MEA failed after 4 completed cycles. Occasionally, the cycling test lasted similar total time with the baseline and long-term SO<sub>2</sub> contamination tests. These results suggest that the recovery cycling directly resulted in the MEA failure.

**Table 1.1.1 Summary of the characterization results for the MEAs after long-term tests**

Testing	H <sub>2</sub> Xover	Ca ECA	Membrane Thickness
W/O SO <sub>2</sub>	↑ 23 %	↓ 12 %	↓ 38 %
W/ SO <sub>2</sub>	↑ 63 %	↓ 11 %	↓ 56 %
W/ SO <sub>2</sub> + Recovery	↑ 260 %	↓ 29 %	↓ 62 %

The results of the electrochemical analysis before and after the long-term tests and individual cycle were not shown here, but the summary results are shown in Table 1.1.1. As for the cycling test, the hydrogen crossover increased gradually with cycling. And it become more severe up to about 260% at the end of the 4<sup>th</sup> cycle, and showed the first signs of MEA failure. The MEA failed/broke during the air polarization measurement for end life diagnostic. These results suggest that the membrane degradation was accelerated by the SO<sub>2</sub> exposure, especially with the recovery cycling. The cathode electrochemical active area (ECA) results indicate that the SO<sub>2</sub> contamination effect on the electrode is recoverable, but the potential scanning (CV) recovery method caused a severe non-recoverable performance loss in the cathode.

To visually investigate the SO<sub>2</sub> contamination and the CV recovery method effect on the membrane degradation, SEM was applied to analyze the cross-sections of the fresh and tested MEAs at gas inlet, middle and outlet sections. Figure 1.1.2 shows cross sections SEM images of the middle in the MEAs after tests. The decreases in the membranes are also shown in Table 1.1.1. This result indicate that the more severe membrane degradation occurred during the contamination tests, and the CV recovery method might not affect the membrane thickness too much but the MEA failure might caused by the mechanical damage from the shut-down and start-up operation during the CV recovery.

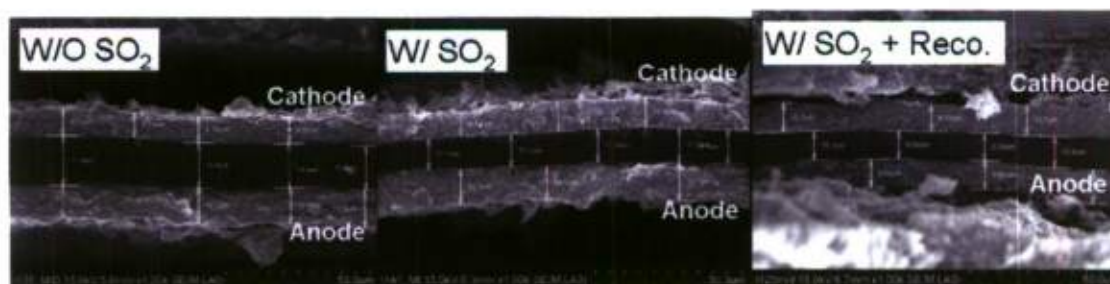


**Figure 1.1.2 Cross-section SEM images in middle of the MEAs after long-term tests**



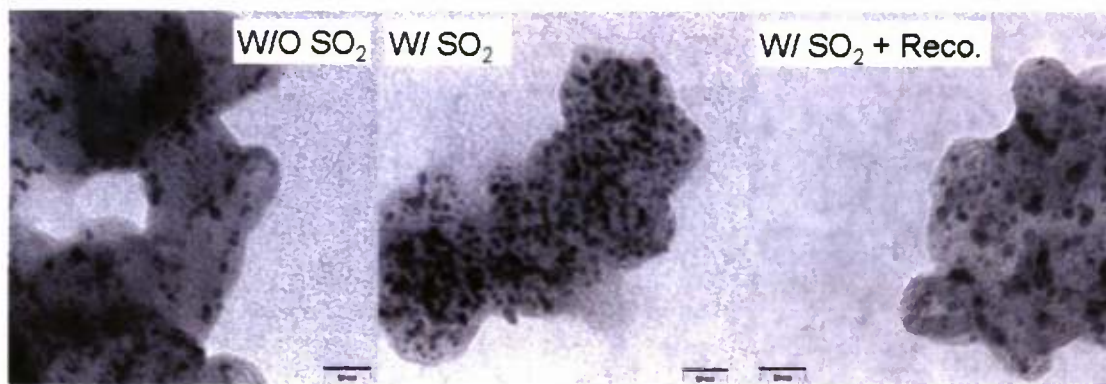


**Figure 1.1.3 TEM images of Pt/C in cathode of the MEAs after long-term tests**

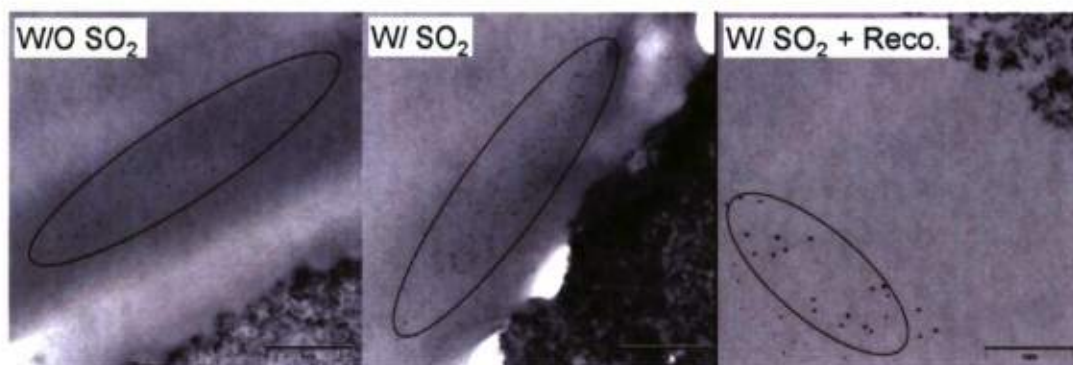


**Figure 1.1.4 TEM images of Pt in the membrane nearby cathode catalyst layer of the MEAs after long-term tests**

To determine the  $\text{SO}_2$  contamination and the CV recovery method effect on the electrode, TEM was applied to analyze the cross-sections and catalyst Pt/C in cathode of the fresh and tested MEAs at gas inlet, middle and outlet sections. The images in Figure 1.1.3 show that the platinum particle sizes after the Baseline test are similar with those of the continuous  $\text{SO}_2$  contamination test, but bigger platinum particles were obtained after the cycling test. The cross-section TEM images of the cathode side in MEAs are shown in Figure 1.1.4. They show clear platinum immigration in the membranes. The MEA after continuous  $\text{SO}_2$  contamination test shows similar size of deposited platinum particles with the baseline test. But the platinum distribution zone is closer to the cathode catalyst layer. The cycled MEA shows bigger particles size and farther platinum distribution zone from the cathode catalyst layer. These results showed no impact of  $\text{SO}_2$  contamination on the platinum dissolution-immigration but the clear evidence for the cathode potential effect.

In summary, the  $\text{SO}_2$  contamination had insignificant impact on the platinum agglomeration or dissolution-immigration, but the CV recovery method accelerated the platinum agglomeration or dissolution-immigration. The acceleration had been reported by other researcher with CV experiments but without  $\text{SO}_2$  contamination. These results were supported the similar ECA loss

for the cathode of the Baseline test and the continuous SO<sub>2</sub> contamination test, but more for recovery cycling test.

### 1.1.2.2 Air Contaminant Studies: Mechanistic Modeling of SO<sub>2</sub> Adsorption on Pt/C (catalyst consisting of carbon-supported platinum nanoparticles)

In the present award period additional simulating SO<sub>2</sub> adsorption and *in-situ* SO<sub>2</sub> adsorption experiments were also conducted to further understand the SO<sub>2</sub> contamination mechanisms. The simulating SO<sub>2</sub> adsorption experiments were performed by exposing the MEA cathode to 10 ppm SO<sub>2</sub> in N<sub>2</sub> at certain potential and typical operating conditions of a PEMFC for certain time, then immediately applying potential scanning within different potential ranges to study the adsorption potential effect on the chemical states of sulfur adsorbate by analyzing the electrochemical reduction and oxidation potential and charge. As for the *in-situ* SO<sub>2</sub> adsorption experiments, a PEMFC under typical operating conditions with 2 ppm SO<sub>2</sub> in air was interrupted at different steady states (poisoning or recovery) by applying potential scanning with the cathode chamber sealed. We then attempted to detect the chemical states of sulfur adsorbate during the SO<sub>2</sub> contamination in the cathode of the fuel cell under real operating conditions.

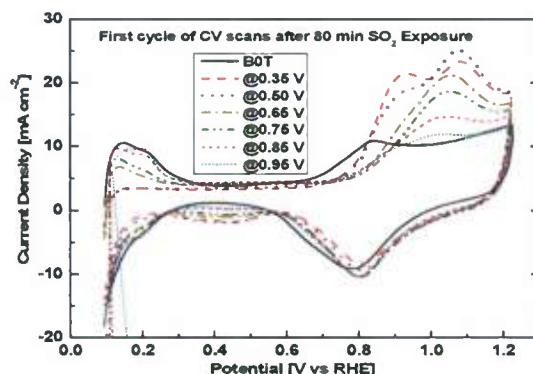
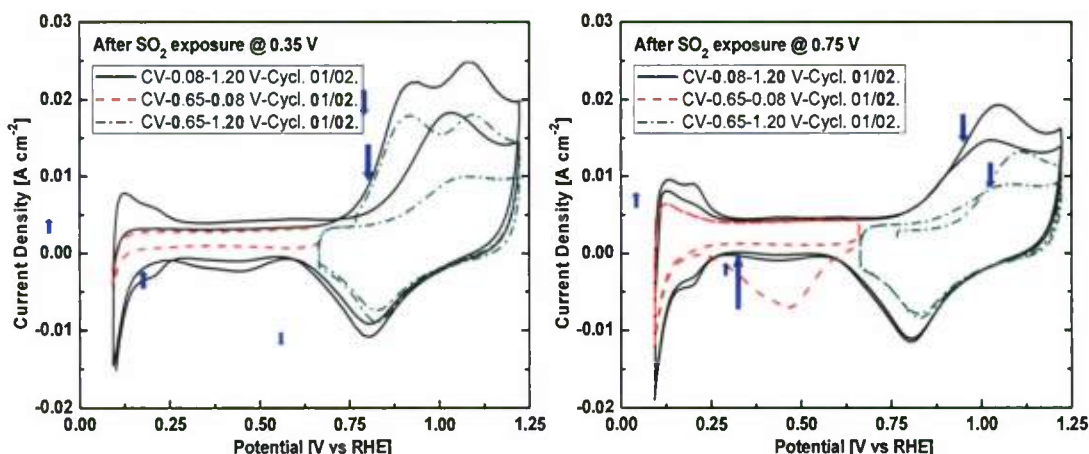


Figure 1.1.5 The CV scan profiles of the first cycle after an 80 min SO<sub>2</sub> exposure at different potentials

Figure 1.1.5 shows the CV scan profile of the first cycles just after 80 min of SO<sub>2</sub> adsorption at different adsorption potentials during the simulating test. When the adsorption potential is lower than 0.65 V, both the Pt(edge) and Pt(111) sites of the Pt crystal structure were completely covered and there are two S-ads. oxidation peaks and one reduction peak observed. Also the S-ads reduction peaks have a similar current magnitude. When the adsorption potential is between 0.65 and 0.95 V, only Pt(111) sites of the Pt crystal structure are covered and Pt(edge) sites are still available. There is only one S-ads oxidation peak and one reduction peak observed. The oxidation current peak observed at lower adsorption potentials, which had an onset at ~0.65 V and peak at ~0.95 V, did not appear. Also, the S-ads oxidation and reduction current peak magnitudes now decrease with increasing adsorption potential. When the adsorption potential was equal to 0.95 V, there were no obvious S-ads oxidation or reduction peaks within the potential range of 0.08~1.2 V, and the H<sub>ads</sub> oxidation current is close to the BOT level. This may indicate that when the adsorption potential is equal to 0.95 V or higher, SO<sub>2</sub> is fully oxidized into sulfate/bisulfate (SO<sub>4</sub><sup>2-</sup>/HSO<sub>4</sub><sup>2-</sup>) on Pt(edges) and Pt(111).

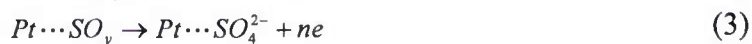


**Figure 1.1.6** CVs for the first two cycles after 80 min exposure to 10 ppm SO<sub>2</sub> at (left) 0.35 V and (right) 0.75 V vs. RHE. Arrows show changes between first and second cycle

In order to analyze the chemical state of the adsorbates, the CV scans with different potential ranges was applied after the saturated adsorption at different potentials. Figure 1.1.6 (left) shows CVs after SO<sub>2</sub> adsorption at 80 °C and 0.35 V vs. RHE. No peak was detected for the low potential range scan (0.65 to 0.08 V vs. RHE). This result indicates a complete coverage of Pt sites and sulfur valence in the S-ads is 0 when the SO<sub>2</sub> adsorption on Pt in the MEA occurs at 0.35 V in N<sub>2</sub>. The first CV cycle for the high potential range scan (0.65 to 1.2 V vs. RHE) led to two peaks at 0.92 and 1.09 V vs. RHE, indicative of sulfur adsorbate oxidation.



The charge transfer number,  $n$  in reaction (1) can be calculated to be approximately 8.6. The sulfur coordination number  $x$  in S-ads is about 1.4. Considering the Pt(111) sites on the Pt crystal cluster surface in the MEA is about 63%, which can be confirmed by the S-ads coverage value of about 63% after saturated SO<sub>2</sub> adsorption at 0.75 V, it can be concluded that the Pt(edges)-S<sub>2</sub> and Pt(111)-S might be formed during SO<sub>2</sub> ads. @ 0.35 V; and then, they were oxidized at 0.92 and 1.09 V, respectively, during the high potential range CV scans. Figure 1.1.6 (right) shows CVs after SO<sub>2</sub> adsorption at 80 °C and 0.75 V vs. RHE. A significant peak was detected at 0.45 V vs. RHE during the first cycle of the low potential range scan. Interestingly, only one oxidation peak appeared at 1.11 V vs. RHE during the first high potential range CV cycle. These results indicated that after the SO<sub>2</sub> adsorption on Pt at 0.75 V, the S-ads can be reduced to zero-valent sulfur at about 0.47 V, and also be oxidized to 6-valent sulfur, SO<sub>4</sub><sup>2-</sup>/HSO<sub>4</sub><sup>2-</sup> at about 1.11 V. The reduced S-ads during the low potential scan can be oxidized to SO<sub>4</sub><sup>2-</sup>/HSO<sub>4</sub><sup>2-</sup> at about 1.07 V.



The charge transfer number,  $n$  in reaction (2), (3) and (4) can be calculated out, yielding about 3.9, 2.2 and 6.2, respectively. This means that the coordination number  $x$  and  $y$  in the S-ads is approximately 1 and 2, respectively. This result suggested that the S-ads is Pt(111)-SO<sub>2</sub> when



the SO<sub>2</sub> adsorption on Pt in MEA occurs at 0.75 V in N<sub>2</sub>. The Pt(111)-SO<sub>2</sub> can be reduced to Pt(111)-S at about 0.47 V and oxidized to SO<sub>4</sub><sup>2-</sup>/HSO<sub>4</sub><sup>2-</sup> at about 1.11 V. The reduced Pt(111)-S can be oxidized to SO<sub>4</sub><sup>2-</sup>/HSO<sub>4</sub><sup>2-</sup> at about 1.07 V.

As reported in the literature, S-ads on Pt surfaces can be completely removed by CV scanning only after several scan cycles. Figure 1.1.7 (left) and (right) show the profiles of CV cycles (*i* = 1, 2, 3, and 10 cycles) after SO<sub>2</sub> saturated adsorption at 0.35 and 0.75 V vs. RHE, respectively. For adsorption at 0.35 V, after the first cycle, the Pt(edge) sites were released, and the subsequent cycles show only one S-ads oxidation at about 1.03 V, and two reduction current peaks at about 0.36 V and 0.44 V. The S-ads oxidation peak onset starts at ~0.72 V and the onset of reduction start at ~0.58 V. With increasing scan cycles, the S-ads oxidation and reduction current peaks decrease, and the H<sub>ads</sub> oxidation current on Pt(111) increases. For adsorption at 0.75 V, all the cycles show similar behavior to cycles 2, 3, and 10 for the adsorption at 0.35 V. These results confirm previous conclusions that the peak at ~0.93 V relates to the oxidation of S-ads on Pt(edge) sites and the reduction peak at 0.44 V can be attributed to the reduction of reaction products from oxidation of the S-ads on Pt(111) during the previous forward scan, and/or the adsorbate itself. These results also suggest that the SO<sub>2</sub> adsorbed on Pt(edge) sites can be easily removed but adsorbates on Pt(111) sites are difficult to remove. This may account for the different adsorption structures of the S-ads on different Pt crystal faces.

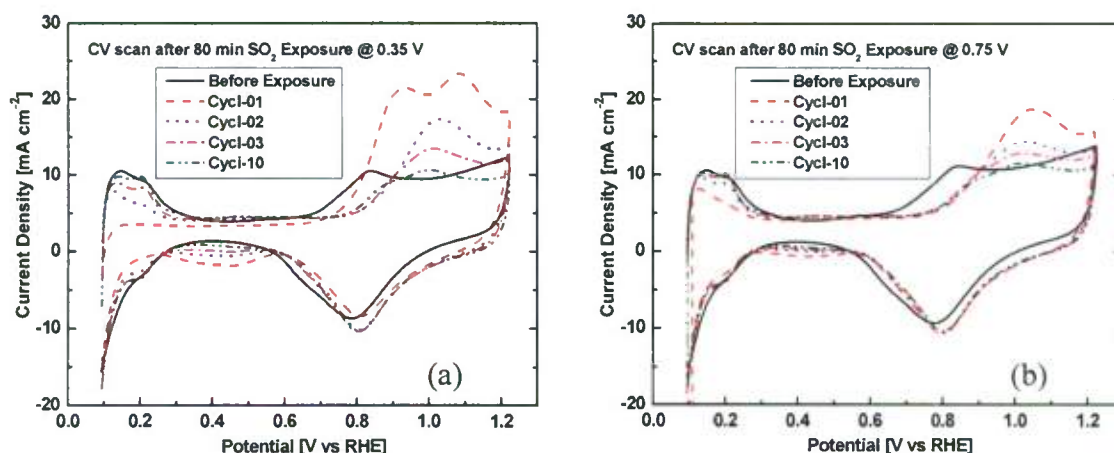
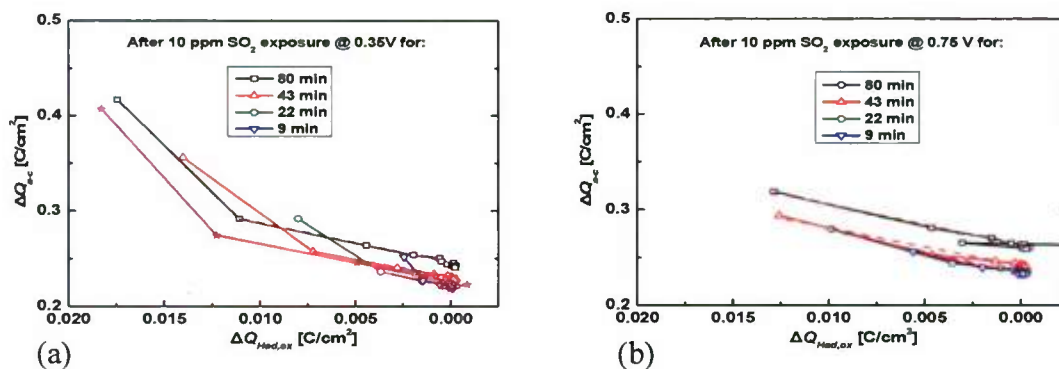


Figure 1.1.7 The profiles of CV cycles after SO<sub>2</sub> saturated adsorption on Pt electrode at 0.35 V vs. RHE (left), and 0.75 V vs. RHE (right)

CV scan data from adsorption potentials at 0.35V and 0.75V was also used to estimate the chemical state of S-ads during CV scanning by linear fitting on the relation between anodic/cathodic charge difference and ECA increase of each cycle, as shown in equation [1].

$$\Delta Q_{a-c}^i = (n/\eta - 1)\Delta Q_{H_{ads},ox}^i + Q_{H_2,ox} + Q_{C,ox} + Q_{Pt,dis} - Q_{H_2,ev} \quad [1]$$

where *i* the cycle number of the CV scan and  $\eta$  is the removal efficiency of CV one cycle. The charge number, *n*, can be calculated from the slope of equation [1].



**Figure 1.1.8** The charge difference between anodic and cathodic scans, vs. the increase in Hads oxidation charge,  $\Delta Q_{sc}$  vs.  $\Delta Q_{Had,ox}$  during CV scans after  $\text{SO}_2$  saturated adsorption on Pt electrode at 0.35 V vs. RHE, (left) and 0.75 V vs. RHE, (right)

Thus for the data shown in Figure 1.1.8 (left) and (right), the charge numbers are estimated at 3.4 for adsorption at 0.35V and 1.9-3.5 for adsorption at 0.75 V with different times, respectively. This indicates that  $\text{Pt(111)}_2=\text{SO}$  and  $\text{Pt(111)-S}$  may be formed due to the reduction of S-ads at about 0.44 V and 0.36 V during the cathodic scanning after the first anodic scanning, and then is oxidized at ~1.03 V.

In summary, as illustrated in the following schematic of Figure 1.1.9, the adsorption potential affects depend not only on the valance of S in the adsorbate, but also on the adsorption structure:

- Adsorption potential lower than 0.65 V vs. RHE, the chemical state of adsorbate is independent of Pt surface coverage. Pt-edges and Pt(111) were fully covered, Pt-edges- $\text{S}_2$  and Pt(111)-S might be adsorption products.
- Adsorption between 0.95 and 0.65 V, only Pt(111) were fully covered, Pt(111)- $\text{SO}_2$  might be produced and Pt-edges left available.
- Adsorption potential equal to or higher than 0.95 V vs. RHE,  $\text{SO}_2$  was directly oxidized to  $\text{SO}_4^{2-}/\text{HSO}_4^{2-}$ , no obvious S-adsorbate redox reaction during CV scanning.
- The saturation coverage of sulfur adsorbates on Pt surface decrease with increase of the adsorption potential.

In addition, S-adsorbate also varies with cycling of CV scans from 0.08-1.2 V:

- $\text{S}_2$  on Pt-edges could be oxidized and removed completely during the first scan.
- Pt(111)-S and Pt(111)- $\text{SO}_2$  were oxidized during the first forward scanning and then reduced partially to  $\text{Pt(111)}_2=\text{SO}$  and Pt(111)-S during the following scans, results in one SO cover two Pt sites.
- Pt(111)- $\text{SO}_2$  were reduced Pt(111)-S during the first backward scanning and then oxidized during following scans.

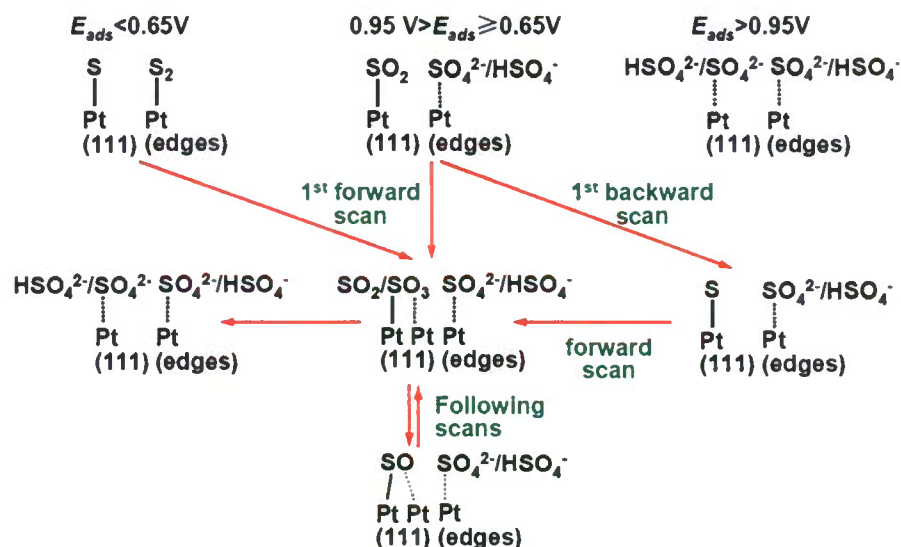


Figure 1.1.9 The schematic of the reactions during CV scans after  $\text{SO}_2$  saturated adsorption on Pt electrode at different potential under typical PEMFC operating conditions

As for in-situ  $\text{SO}_2$  adsorption experiments, only two successful experiments were obtained due to the instrument's limit in our lab. Figure 1.1.10 shows the CV curves during the scanning at the poisoning steady state and self-recovery steady state. During the first scanning within low potential range, the poisoning steady state has only one reduction peak at about 0.25 V and all platinum sites were completed covered, but the self-recovery steady state has two reduction peaks at about 0.42 V and 0.32 V and only Pt(111) was completed covered. The following scanning within high potential range, the poisoning steady state has two oxidation peaks at about 0.86 V and 0.106 V but the self-recovery steady state has only one oxidation peak at about 1.05 V. These results suggest the S-ads at the poisoning steady state may be Pt(edges)- $\text{SO}_2$  and Pt(111)-S; and during the self-recovery, the Pt(edges)- $\text{SO}_2$  desorbed or was oxidized and Pt(edges) site was released, the Pt(111)-S was oxidized to Pt(111)-SO or/and Pt(111)- $\text{SO}_2$ . However, this contamination mechanism needs to be confirmed in further experiments.

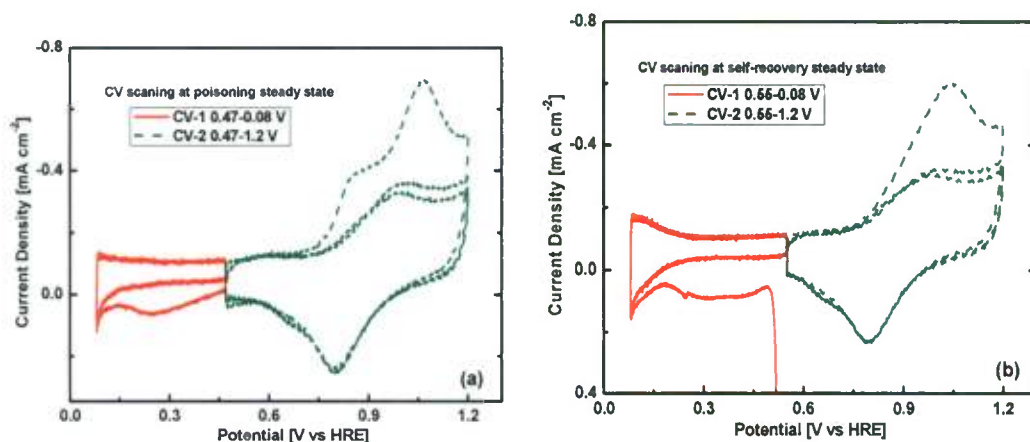


Figure 1.1.10 The CV curves during the scanning at (left) poisoning steady state and (right) self-recovery steady state



### 1.1.2.3 Manufacturing Defect Performance Implications: Gas Diffusion Layer Defect Influence on Air Permeability of PEM Cathodes

During this year we continued to study effects of the manufacturing defects on hydrogen polymer electrolyte fuel cells (PEMFCs) performance. This work was performed to support the DOE manufacturing initiative for PEMFC production. In this part such gas diffusion layer's (GDL) characteristic as air permeability was chosen as variable parameter and the work was focused on investigation of effects of the such GDL defect as well as the impact of the defect location (inlet or outlet part of membrane electrode assembly (MEA)) on a fuel cell performance by using a segmented cell system.

All experiments were conducted using HNEI's segmented cell system. This diagnostic tool enables collection of spatial information during a standard fuel cell experiment. The segmented cell is operated as a single cell fuel cell using a Fuel Cell Technologies test station. Current and power limitations of the station were 240 A and 1.2 kW, respectively. The segmented cell system includes cell hardware and a data acquisition system composed of a custom built current transducer system and a National Instrument PXI data acquisition instrument. A custom LabView program controls the National Instrument PXI. For current sensing, a closed loop Hall sensor device from Honeywell, Model CSNN191, was employed. Segment currents of up to  $2 \text{ A cm}^{-2}$  are measured in the high current mode. The maximum current density is lowered to  $400 \text{ mA cm}^{-2}$  in the low current mode, which is typically used for spatially distributed electrochemical diagnostics (CV, LSV).

The segmented cell hardware was based on a HNEI  $100 \text{ cm}^2$  cell design. The hardware contains a segmented flow field which consists of ten cell segments forming a continuous path with ten serpentine channels. Each segment has an area of  $7.6 \text{ cm}^2$  and has its own distinct current collector and GDL. The cell hardware segmentation can be applied to either the anode or the cathode.

A  $100 \text{ cm}^2$  Ion Power catalyst coated membrane (CCM) with a single anode GDL and 10 cathode GDLs of reduced size to cover each segment were used. The electrodes were made of Pt/C catalyst coated on a Nafion 212 ( $50 \text{ }\mu\text{m}$ ) with a loading of  $0.4/0.4 \text{ mg}_{\text{Pt}} \text{ cm}^{-2}$  on the anode and cathode respectively. A standard 25 BC GDL (SGL) was used at the anode and GDS3215 (Ballard) the cathode. GDS1120 GDL (Ballard) was used as defect GDL. Also tests were done at opposite configuration when GDS1120 was used as standard cathode GDL, and GDS3215 – defect GDL. Teflon gaskets of 203 and  $185 \text{ }\mu\text{m}$  thickness were respectively used for the anode and cathode.

The cell operating temperature was  $60^\circ\text{C}$ . The anode/cathode standard operating parameters were:  $\text{H}_2/\text{air}$ , 2/2 stoichiometry,  $48.3/48.3 \text{ kPa}_g$  back pressure, and 100/50 % relative humidity. Experiments were also performed also with  $\text{H}_2/\text{O}_2$  configurations. For this test the same flow rates as during  $\text{H}_2/\text{air}$  operation were used to maintain the cell water management. Consequently, the stoichiometry for the  $\text{O}_2$  the stoichiometry increased to 9.5. These gas configurations were used to determine segments' overpotentials. The activation overpotential  $\eta_{act}$  was obtained by subtracting the ohmic loss corrected  $\text{H}_2/\text{O}_2$  polarization curve from the theoretical open circuit voltage of 1.23 V. The ohmic overpotential  $\eta_{Ohm}$  was obtained by multiplying the high frequency resistance (HFR) with the respective current density. Subtraction of the  $\text{H}_2/\text{air}$  data from the  $\text{H}_2/\text{O}_2$  data yielded the mass transport overpotential  $\eta_{MT}$ .



The cell and segments spatially distributed voltage was measured under galvanostatic control. These experiments were combined with EIS measurements to determine the cell and segments resistance as well as impedance spectra for all ten segments at each current. The selected EIS frequency range was 0.1 to 10 kHz and the amplitude of the sinusoidal current signal perturbation was 2 A which resulted in a cell voltage response of 10 mV or less. The high frequency resistance was determined from the intercept of the EIS with the real impedance axis at high frequencies (Nyquist plot).

CV experiments were conducted to measure the electrochemically active surface area (ECA) using a Parstat 2273 potentiostat/galvanostat from EG&G Instruments Corp. CVs were performed at a cell temperature of 35°C with a scan rate of 20 mV s<sup>-1</sup>, while 100 % relative humidity hydrogen and nitrogen were supplied to the reference/counter and working electrodes, respectively, at a flow rate of 750 ml min<sup>-1</sup>. For each measurement, three cycles were recorded over a potential range of -0.015 to 1.1 V vs. hydrogen reference electrode (HRE). The hydrogen desorption peak area of the third cycle was used to determine the ECA. Hydrogen crossover experiments were performed at the same temperature and flow conditions as the ECA measurements using a single potential sweep from 0.1 to 0.4 V vs. HRE at a scan rate of 0.1 mV s<sup>-1</sup>.

The GDL defects were created by exchanging the standard cathode GDL (GDS3215) material at segment 4 and segment 9 with a substitute GDL (GDS1120). The GDLs parameters are presented in Table 1.1.2. The GDLs have microporous layer and same thickness of 210 µm. Also they were treated by PTFE, have close values of resistance and area weight. GDS3215 has higher air permeability through and in plane than GDS1120. For the opposite GDL configuration test the standard GDL (GDS1120) at the segment 4 was exchanged by GDS 3215. The defect simulated the different air permeability expected from manufacturing variations. Prior to the defect insertion, the segmented cell was assembled using an “intact” GDL and a set of diagnostics was performed (CV, LSV, polarization curves, and EIS using H<sub>2</sub>/air and H<sub>2</sub>/O<sub>2</sub> gas configurations). The cell was subsequently disassembled, the defect inserted, the cell reconditioned and an identical set of diagnostics completed. A comparison between both set of diagnostics gave insights into the defect effects as well as an assessment of the feasibility to detect and localize GDL defects.

**Table 1.1.2 Main parameters of several Ballard GDLs**

GDL	Thickness, µm @ 0.7 N cm <sup>-2</sup>	Area weight, g m <sup>-2</sup>	PTFE	MPL	Air permeability, s/100 cm <sup>3</sup>		Resistance, mΩ cm <sup>2</sup>
					Through plane	In plane	
GDS1120	210	79	yes	yes	210	108	14.5
GDS3215	210	85	yes	yes	80	83	14.0

A slight decrease in ECA (up to 7 %) was found for both anode and cathode electrodes after the defect introduction at segment 4 and subsequently at segment 9. The ECA drop is attributed to catalyst degradation during hardware disassembly, catalyst exposure to air, and degradation resulting from cell operation. Hydrogen crossover distributions showed the absence of pinhole formation.

Defect – low air permeable GDL, location at segment 4: The impact of the GDL defect characterized by low air permeability on the performance distribution is shown in Figure 1.1.11, where segment voltage distribution is presented as a function of segment location at different fixed current densities. Results indicate that detection is facilitated at higher current densities ( $\geq 1.0 \text{ A cm}^{-2}$ ). The segment 4 voltage drop after the defect insertion was 0.039 V at  $1.0 \text{ A cm}^{-2}$ , 0.09 V at  $1.1 \text{ A cm}^{-2}$ , and 0.160 V at  $1.2 \text{ A cm}^{-2}$ . The defect presence affected the segments performance downstream at high current density operation: segments 5-10 showed an increase of the performance.

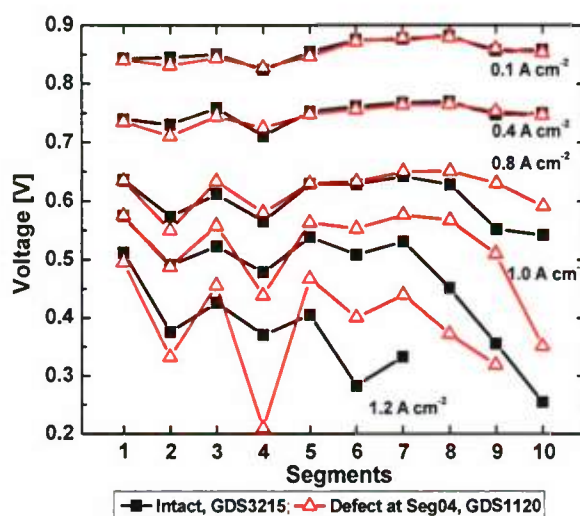


**Figure 1.1.11 Voltage distributions before and after the defect introduction at segment 4 (GDS1120 as defect GDL). Anode/cathode:  $\text{H}_2/\text{air}$ , 2/2 stoichiometry, 100/50 % relative humidity, 48.3/48.3 kPa<sub>g</sub>, 60°C.**

Overpotential data indicated that the main contributors to the segment 4 performance change were mass transfer losses (Figure 1.1.12). The overpotential increase was 0.022, 0.083 and 0.132 V at 1.0, 1.1 and  $1.2 \text{ A cm}^{-2}$  respectively, which accounts to 90 % of the losses.

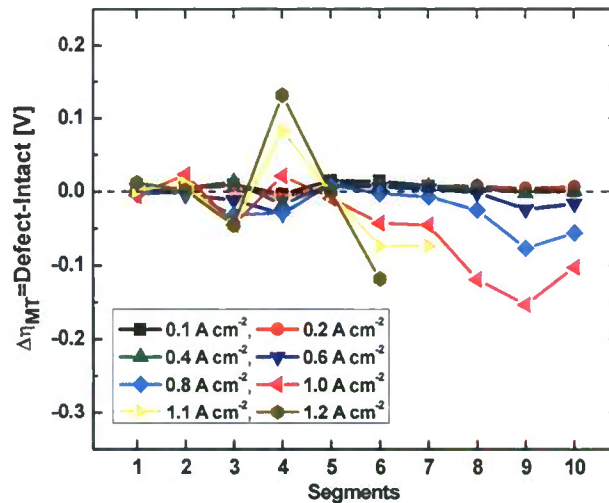


Figure 1.1.12. Difference in mass transfer overpotential distributions between MEAs with and without a GDL defect at segment 4 (GDS1120 as defect GDL). Anode/cathode: 2/2 stoichiometry, 100/50 % relative humidity, 48.3/48.3 kPa<sub>g</sub>, 60°C.

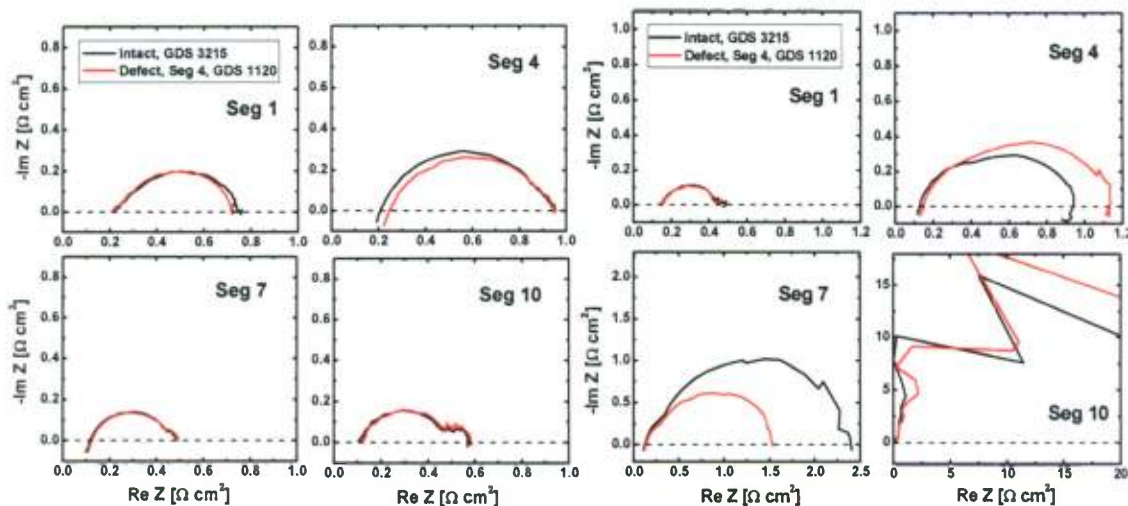


Figure 1.1.13 EIS spectra for segments 1, 4, 7, 10 recorded at total cell current density  $i = 0.1$  (left) and  $1.0 \text{ A cm}^{-2}$  (right) (GDS1120 as defect GDL). Anode/cathode:  $\text{H}_2/\text{air}$ , 2/2 stoichiometry, 100/50% RH, 60°C, 48.3/48.3 kPa<sub>g</sub>.

Figure 1.1.13 shows EIS data collected at a total cell current density of  $0.1$  and  $1.0 \text{ A cm}^{-2}$  for segments 1, 4, 7, 10 before and after defect introduction at the segment 4. The results of these four segments were representative for the trends observed in the entire cell. At a low current density of  $0.1 \text{ A cm}^{-2}$ , the presence of a local change in air permeability content is not noticeable except a slight increase of HFR from  $0.209$  to  $0.247 \text{ Ohm cm}^{-2}$  (Figure 1.1.13, left). Such an increase of HFR might be connected to assembling/disassembling of the cell and/or different



adhesive properties of the GDL. At low current densities, the EIS curve is described by a high frequency anode charge transfer resistance loop (it is often negligible), a high frequency cathode arc attributed to a charge transfer resistance and a double layer capacitance. At higher current densities, an additional low frequency arc is usually observed reflecting cathode mass transfer limitations. At  $0.1 \text{ A cm}^{-2}$ , the variation of air permeability does not affect the cathode charge transfer resistance. However, at  $1.0 \text{ A cm}^{-2}$  the presence of the defect resulted in an increase of the low frequency loop (Figure 1.1.13, right) representing diffusion limitations within the cathode GDL and the catalyst layer due to poor mass transport. At the same time the downstream segments demonstrated a decrease of the diffusion loop and an increase of their performance.

A decrease of the local air permeability of GDL results in growing of the local mass transfer losses and diffusion limitations since the transport of reagents and removal of water from the catalyst later become difficult at high current density operation. This creates conditions for flooding at the defect area and local decrease of the performance. As water removal from the defected segment is an obstacle, so less water is emitted to downstream. This causes more dry conditions for the segments after the defect one and downstream segments have an improved performance.

Defect – low air permeable GDL, location at segment 9: Figure 1.1.14 presents voltage distributions as a function of segment position before and after the GDL defect introduction at segment 9. A main impact of the defect on the performance was found at high current density operation. A decrease of the local air permeability results in a local performance drop of 0.034 and 0.239 V at  $0.8$  and  $0.9 \text{ A cm}^{-2}$ , respectively. At the same time, the performance of the segments 6-8 increases as well as downstream segment 10, as was observed in the previous section.

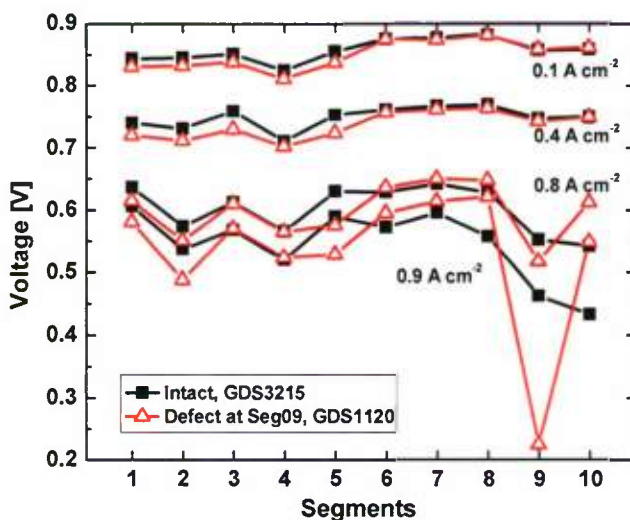


**Figure 1.1.14 Voltage distributions before and after the defect introduction at segment 9 (GDS1120 as defect GDL). Anode/cathode:  $\text{H}_2/\text{air}$ , 2/2 stoichiometry, 100/50% relative humidity, 48.3/48.3 kPa<sub>g</sub>, 60 °C.**

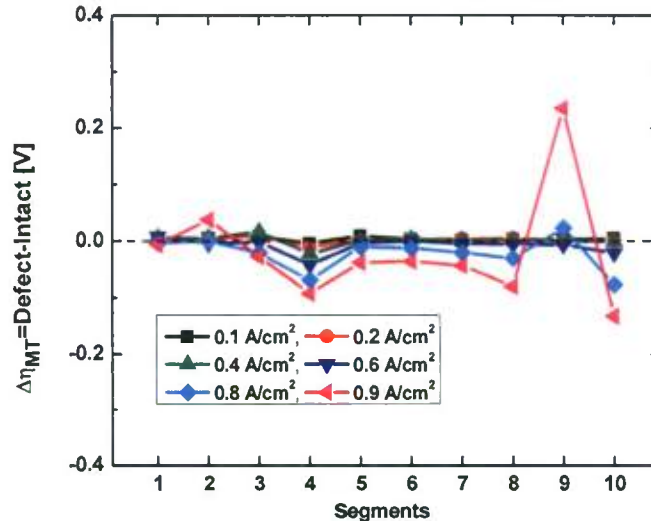


**Figure 1.1.15** Difference in mass transfer overpotential distributions between MEAs with and without a GDL defect at segment 9 (GDS1120 as defect GDL). Anode/cathode: 2/2 stoichiometry, 100/50% relative humidity, 48.3/48.3 kPa<sub>g</sub>, 60 °C.

The observed local performance drop after at the defected segment is accounted mainly by mass transfer losses as might be seen from Figure 1.1.15. The growth of this overpotential is 0.025 and 0.234 V at 0.8 and 0.9 A cm<sup>-2</sup> respectively; and it corresponds to 95 % of the performance decrease.

Figure 1.1.16 presents EIS spectra for segments 1, 4, 9, and 10 recorded at 0.1 and 1.0 A cm<sup>-2</sup> total current density before and after the defect introduction at the segment 9. At low current density (Figure 1.1.16, left) the air permeability defect did not significantly impact the impedance of the segments. However at high current density EIS shows changes in the segment 9 behavior (Figure 1.1.16, right). There is an increase of low frequency loop, representing diffusion limitations. So a decrease of the air permeability results to the performance loss.

A comparison of the defect impact depending on its location (segment 4 vs. segment 9) shows that the defect at a cell outlet (segment 9) becomes more pronounced and results in critical performance drop at lower current than the defect located at a cell inlet (segment 4). Also the defect detection is possible at 1.1-1.2 A cm<sup>-2</sup> for the inlet location, whereas for the outlet location at 0.8-0.9 A cm<sup>-2</sup>.

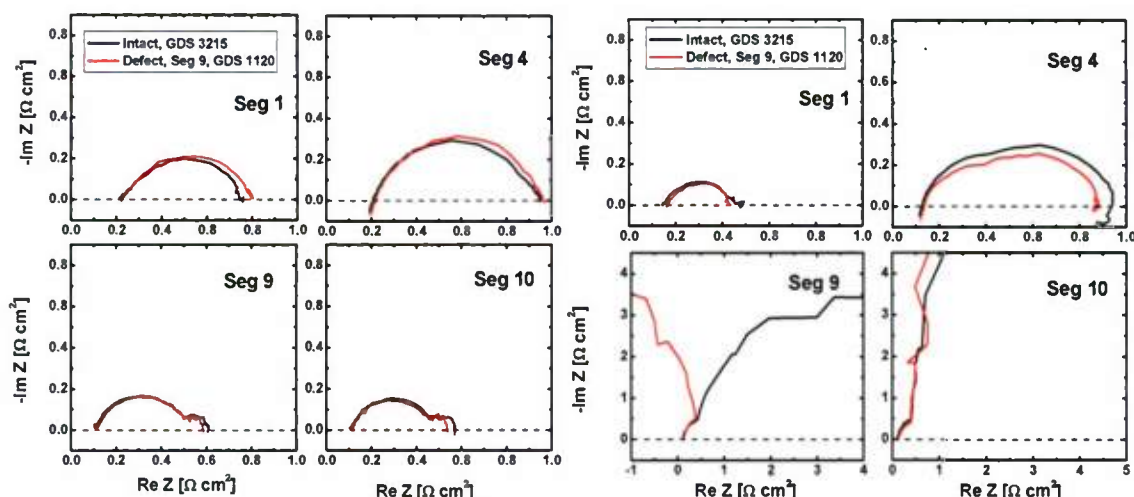


**Figure 1.1.16** EIS spectra for segments 1, 4, 9, 10 recorded at total cell current density  $i = 0.1$  (left) and  $1.0 \text{ A cm}^{-2}$  (right) (GDS1120 as defect GDL). Anode/cathode:  $\text{H}_2/\text{air}$ , 2/2 stoichiometry, 100/50% RH,  $60^\circ\text{C}$ , 48.3/48.3 kPa<sub>g</sub>.

*Defect – high air permeable GDL, location at segment 4:* The impact of the GDL defect characterized by high air permeability on the performance distribution is presented at Figure 1.1.17. It should be noted that the initial performance of the cell with GDS1120 as a standard cathode GDL was lower than with GDS3215, so voltage distributions are presented at fixed current densities of 0.1, 0.2, and  $0.4 \text{ A cm}^{-2}$ . It was observed that the defect GDL makes a positive impact on a local performance. An increase of the segment 4 performance is 0.033 and 0.205 V at 0.2 and  $0.4 \text{ A cm}^{-2}$  respectively. There is a slight variation of the downstream segments' performance.

Analysis of the overpotential losses revealed that the main contributors to the segment 4 performance change were mass transfer losses (Figure 1.1.18). An increase of air permeability at the segment 4 leads to a decrease of the mass transfer overpotential. The overpotential drop was 0.028 and 0.200 V at 0.2 and  $0.4 \text{ A cm}^{-2}$  respectively, which corresponds to 90 % of the losses.

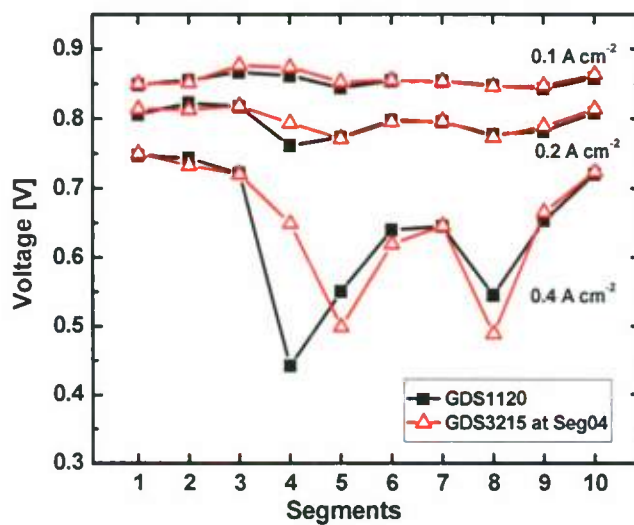


Figure 1.1.17 Voltage distributions before and after the defect introduction at segment 4 (GDS3215 as defect GDL). Anode/cathode: H<sub>2</sub>/air, 2/2 stoichiometry, 100/50% relative humidity, 48.3/48.3 kPa<sub>g</sub>, 60 °C.

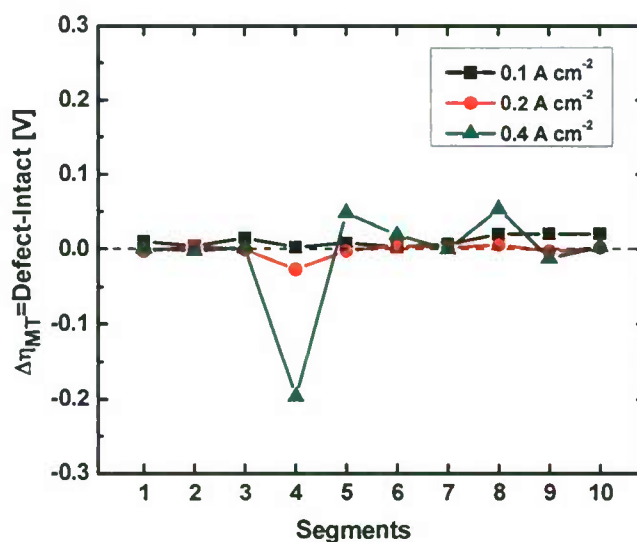
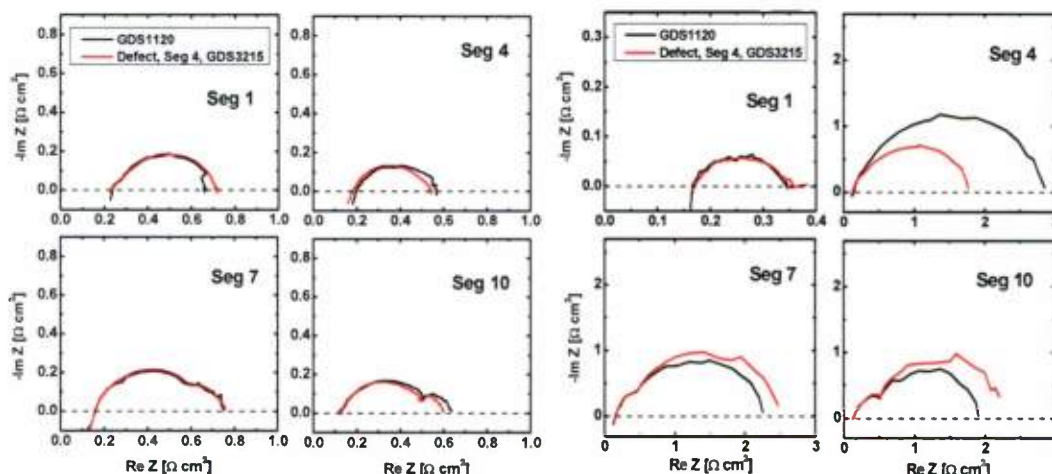


Figure 1.1.18 Difference in mass transfer overpotential distributions between MEAs with and without a GDL defect at segment 4 (GDS3215 as defect GDL). Anode/cathode: 2/2 stoichiometry, 100/50% relative humidity, 48.3/48.3 kPa<sub>g</sub>, 60 °C.

The obtained performance data are supported by EIS results. Figure 1.1.19 presents EIS spectra for segments 1, 4, 7, and 10 recorded at 0.1 and 0.4 A cm<sup>-2</sup> total current density before and after the defect introduction at the segment 4. At low current density operation there are no any changes in EIS responses after the defect introduction (Figure 1.1.19, left). However at 0.4 A



$\text{cm}^{-2}$  the segment 4 shows a decrease of the low frequency arc after the changing of the GDL, indicating on an improvement of local mass transfer properties due to an increase of the air permeability of the defected GDL (Figure 1.1.19, right).



**Figure 1.1.19** EIS spectra for segments 1, 4, 7, 10 recorded at total cell current density  $i = 0.1$  (left) and  $0.4 \text{ A cm}^{-2}$  (right) (GDS3215 as defect GDL). Anode/cathode:  $\text{H}_2/\text{air}$ , 2/2 stoichiometry, 100/50% RH,  $60^\circ\text{C}$ , 48.3/48.3 kPa<sub>g</sub>.

In review, the effect of a localized cathode GDL air permeability variation on the PEMFC performance was studied using segmented cell approach. An artificial GDL defect was created by exchanging a standard cathode GDL at the segment 4 location with a substitute GDL with different air permeability. Main changes in local performances were observed at high current density operation. An increase of the local air permeability caused a growth of the local performance, while a decrease of this parameter resulted in a drop of the segment performance. Polarization and EIS data analysis revealed that such performance changes are attributed to changes of mass transfer overpotentials: an increase of the air permeability leads to a decrease of the mass transfer losses and opposite. Air permeability is directly connected to mass transfer properties of the GDL and higher air permeability provides more efficient transport of reagents to a catalyst layer and removal of reaction product – water.

A comparison effects of defect locations at a cell showed that the defect located at outlet made more significant impact on the local performance. The outlet defect was more pronounced and detected at lower current density than the inlet defect. The outlet part of the cell experiences noticeable mass transfer losses due to a decrease of the oxygen partial pressure and an increase of the water in a gas stream. Any slight local changes in diffusion properties of the GDL at these conditions are significant for the local performance, however the total cell performance might not be greatly affected by the defect. It should be noted that the local GDL defects can be successfully detected by a combination of spatial VI and EIS.

### 1.1.3 Fuel Cell Hardware-in-Loop and System Simulation

#### 1.1.3.1 Scope of Work and Approach

During the grant period HNEI's state-of-the-art HiL system was used primarily in support of Naval Research Laboratory (NRL) efforts to further characterize a fuel cell stack with the focus on improving the stack's performance and durability for use in Ion Tiger unmanned aerial vehicle (UAV). Work under this activity involved the following:

- Using the HiL test system and UAV system simulation developed earlier under the Ion Tiger UAV project, HNEI further characterized the performance of the a 500 W Protonex fuel cell stack and other balance of plant (BoP) components of the UAV system under different operating strategies and dynamic propulsion load profile. HiL was configured to incorporate hardware and control software of different operating components of the actual UAV system, such as anode purge system, air blower, external humidifier and durability shorting process (oxide cleaning method). This was done in order to test and analyze fuel cell stack and some balance of plant (BoP) components under different operating conditions and strategies.
- Analyzing the effect of hybridization of the load following (non-hybrid) UAV system and design of a novel partial hybrid UAV system to minimize losses due to hybridization and to have the flexibility of switching operation of the system from hybrid to non-hybrid mode. Two fuel cell–battery hybrid (full and partial) simulations were developed in the Matlab/Simulink environment with different system configurations in order to study the impact of adding battery packs (weight) and controller (weight & power losses) on the flight duration of the UAVs for a given propulsion and ancillary load profile.

#### 1.1.3.2 Ion Tiger UAV Power Pack Characterization: Evaluation of Protonex's On-Board Fuel Cell Performance Recovery Method under Mission Load Profiles using the HiL Test System

The objective of this study was to characterize the effect of the shorting intervals and the impact of avoiding a shorting process at different power levels on the Ion Tiger stack under dynamic UAV mission profiles. The shorting process utilizes a MOSFET shorting device that short circuits the stack for 120 msec at every 200 sec. intervals. During the short circuit period oxide layers on the cathode catalyst surface (Pt-OH/Pt=O) are reduced. This oxide cleaning process improves the overall cell voltage that increases the thermal efficiency of the stack. The HiL testing was performed using Load Following (LF) UAV system simulation with a 20 minute mission profile.

For the 'shorting interval' investigation, the following shorting intervals were used:

**Shorting Intervals:** = 10, 25, 50, 100, 200, and 600 sec.  
= 360, 144, 72, 36, 18, and 6 shorting events per hour.

For the 'avoiding shorting process at different power levels' investigation, all the tests were performed using a shorting interval of 200 sec and shorting was avoided when the stack power was greater than shorting power level cutoff.

**Shorting Power Level Cutoffs:** Stack power >350, 400, 450, 500 and 550 W.

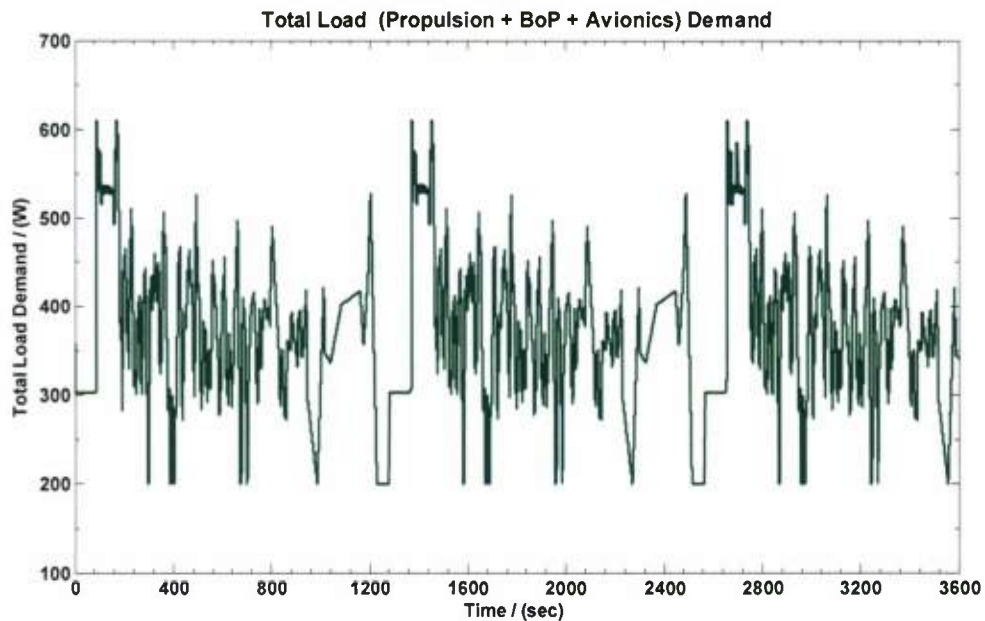


**Figure 1.1.20 One hour load profile used for the shorting investigation**

A one hour (3×20 minute) load profile (Figure 1.1.20) was used for testing the stack for each of these shorting investigations. Prior to initiating any one-hour HiL shorting interval test, the stack was held at the same starting condition while the baseline experiments were performed at the beginning (BoT) and at the end (EoT) of each shorting investigation in order to maintain repeatability throughout the test matrix. Table 1.1.3 shows the overall test matrix or sequence for the shorting interval investigation. A similar test matrix was also used for avoiding shorting process at different power levels. A one-hour HiL baseline test without any shorting was also performed in order to compare with the data from the HiL shorting interval experiments.

**Table 1.1.3 Experimental sequence for shorting interval investigation**

Test ID	Experiment Description
1	Pre-Test Conditioning
2	Baseline Evaluation (BoT)
3	Hold at 800 mA/cm <sup>2</sup> for Data Saving & HiL Test Setup 10 sec Shorting Interval Evaluation
4	Hold at 800 mA/cm <sup>2</sup> for Data Saving & HiL Test Setup 25 sec Shorting Interval Evaluation
5	Hold at 800 mA/cm <sup>2</sup> for Data Saving & HiL Test Setup 50 sec Shorting Interval Evaluation
6	Hold at 800 mA/cm <sup>2</sup> for Data Saving & HiL Test Setup 100 sec Shorting Interval Evaluation
7	Hold at 800 mA/cm <sup>2</sup> for Data Saving & HiL Test Setup 200 sec Shorting Interval Evaluation
8	Hold at 800 mA/cm <sup>2</sup> for Data Saving & HiL Test Setup 600 sec Shorting Interval Evaluation
9	Baseline Evaluation (EoT)
10	Pre-Test Conditioning
11	Shut Down

The stack operating condition and UAV simulation setup for these investigations were as follows:

**Operating Conditions:**

Cathode Oxidant:	Air Blower
Cathode Stoichiometry:	~ 2.5
Relative Humidity:	External Humidifier
Anode Purging:	Straight purging, dry gas inlet
Anode Purge Duration (sec):	1 sec
Anode Purge Interval (sec):	7 secs
Anode Stoichiometry assumption	1.02 or 98 % H <sub>2</sub> utilization in the simulation
Coolant inlet Temperature:	55 °C
Coolant Flow Rate:	1-1.5 l/m

**UAV Simulation Setup:**

Propulsion Load Profile Name

20 minute Ion Tiger Mission Profile

Ancillary Load Profiles (Peak Demand)

V Load	= 45 + 0.4 = 45.04 W (Servo, H <sub>2</sub> -Valve)
12V Load	= 4 + 8 + 18 = 30 W (Autopilot, Payload & Radiator Fan)
17 V BoP Load	= Function of stack current



### DC-DC Converter

5V	Converter Efficiency = 90 %
12 V	Converter Efficiency = 93 %
17V	Converter Efficiency = 93 %

### Battery Pack

Type (A123 HP Lithium Ion)	= 26650
No. of Cells	= 4
Capacity	= 2.3 Ah /cell
Nominal Voltage	= 3.3 volts / cell
Total Mass	= 0.28 kg
Initial SoC	= 100 %
Min. SoC Limits	= 10 %

During the test matrix experiments, the time series data for stack voltage and current and individual cell voltages were recorded. A sample rate of 10 msec was used to calculate hydrogen consumption of the stack using the stack current and anode stoichiometry of 1.02 (98% H<sub>2</sub> Utilization). The stack's electrical efficiency was also calculated by integrating the stack power and dividing by total H<sub>2</sub> energy consumed over the one hour UAV mission profile (3 × 20 minutes). The hydrogen consumption and stack efficiency results for each test were compared with baseline data (without a shorting process, i.e., no oxide cleaning) to see the effect of the shorting interval and avoiding the shorting process at a different power levels on the stack performance and durability improvement. Projected increase or decrease in mission duration over one hour test results due to the shorting process were also extrapolated over the 24-hour period.

The test matrix results from the shorting interval investigation are presented in Table 1.1.4 and on Figures 1.1.21 and 1.1.22. These results show the comparisons of test results of the shorting interval investigation tests with both the baseline test, at the beginning of the test (BoT) and end of the test (EoT) respectively. From these results, it can be concluded that the high frequency of oxide cleaning, i.e., at low interval (<100 sec) leads to greater improvement in stack efficiency and lower hydrogen consumption that in turn project over a 24-hour mission period, an increment of >100 minutes of extra duration at shorting interval > 10 sec. Test matrix results also show that performance of the stack had deteriorated by the end of the shorting interval investigation, i.e., > 8 hours of testing and therefore the baseline test at the end of the investigation (EoT) had lower stack electrical efficiency of 44% as compared to the BoT efficiency of 45%. Overall, the durability of the stack would improve significantly with the shorting oxide cleaning process as the stack ages or stack load-hour increases.

Table 1.1.4 Results of the shorting interval investigation tests compared with baseline tests

Shorting Interval (sec)	H <sub>2</sub> Consumed (kg)	$\eta_{\text{Stk\_Ele}}$ (%)	Compare with BoT		Compare with EoT	
			% Diff in H <sub>2</sub> Consumed (%)	Projected 24 hrs Duration (mins)	% Diff in H <sub>2</sub> Consumed (%)	Projected 24 hrs Duration (mins)
Baseline (BoT)	0.0208	45.09	-	-	1.32	18.77
10	0.01971	47.63	5.41	82.39	6.64	102.50
25	0.01982	47.42	4.88	73.84	6.12	93.83
50	0.02001	46.93	3.94	59.12	5.20	78.91
100	0.02081	45.13	0.14	1.94	1.44	20.98
200	0.02086	45.01	-0.13	-1.81	1.18	17.18
600	0.02090	44.95	-0.32	-4.61	0.99	14.34
Baseline (EoT)	0.0211	44.48	-1.32	-18.77	-	-

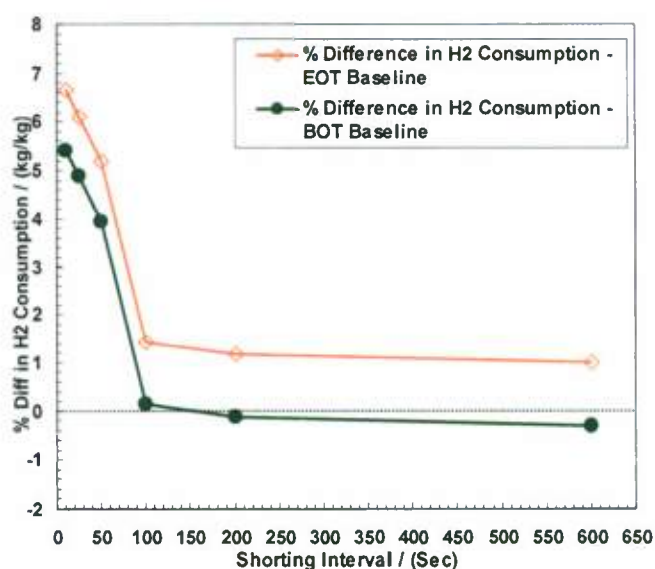
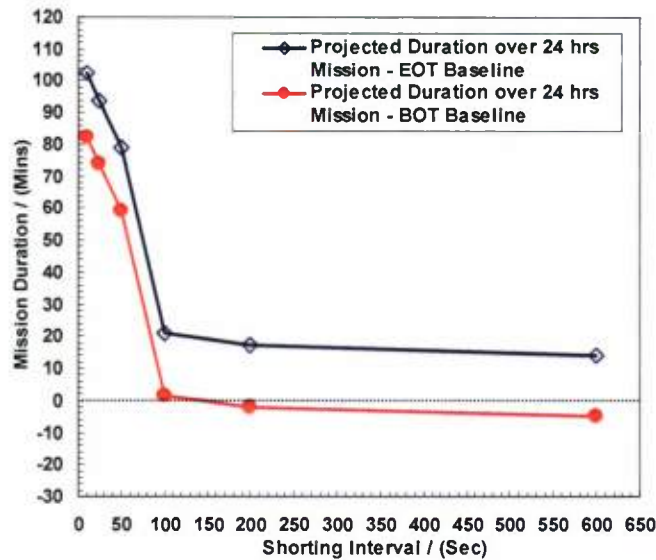


Figure 1.1.21 Percent difference in H<sub>2</sub> consumption at different shorting intervals compared with baseline tests



**Figure 1.1.22 Projected duration over the 24 hrs mission at different shorting intervals compared with baseline tests**

The test results from the power cutoff shorting investigation with constant shorting interval of 200 sec are presented in Figures 1.1.23 and 1.1.24. This investigation was carried out with shorting interval of 200 sec, to correspond to the interval used on the actual Ion Tiger UAV System. As the number of the shorting processes increased from 4 to 18 as the power cut-off level increased from 350 to 550 W, the stack became more efficient and less hydrogen was consumed. As a result, the 24-hour projected duration also increased as the power cut-off level increased. Table 1.1.5 shows the % loss in mission duration by limiting the number of shorting process at different power cut-off levels. The calculation assumes 0% loss at 550 W where the maximum shorting processes (18) occurred and gained 38.19 minutes in mission duration. Figure 1.1.25 shows typical measurement results of stack voltage with (every 10 sec) and without the shorting process over the one hour load profile. The figure also shows the improvement in stack voltage due to shorting oxide cleaning process.

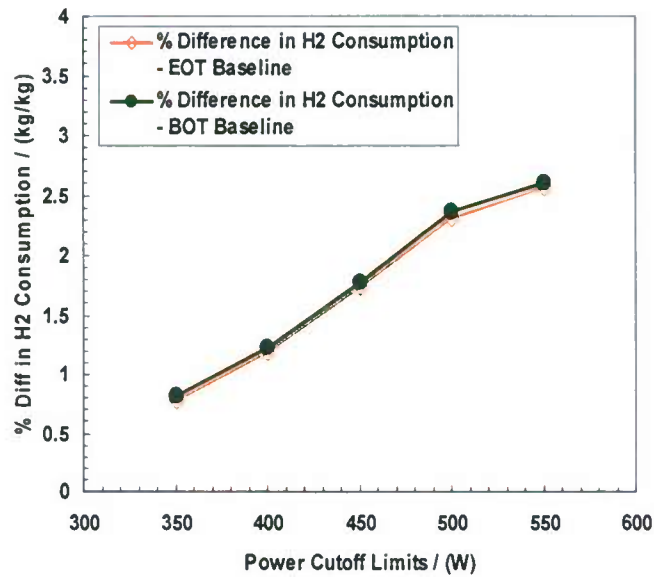


Figure 1.1.23 Percent difference in H<sub>2</sub> consumption at different power cutoff levels compared with baseline tests

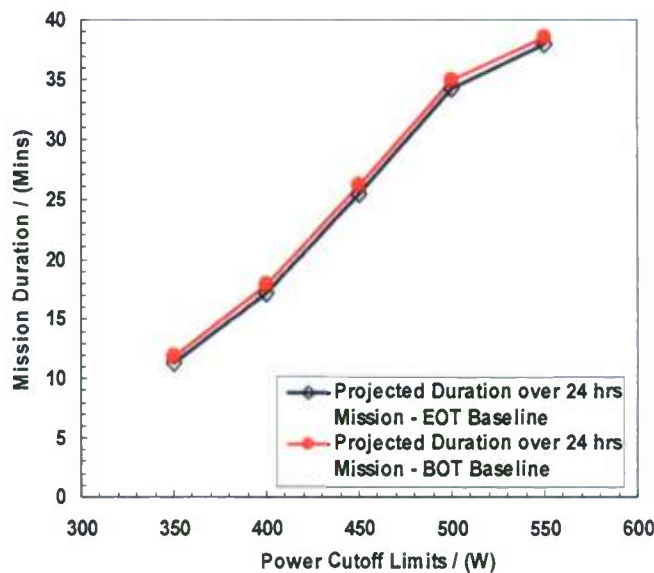
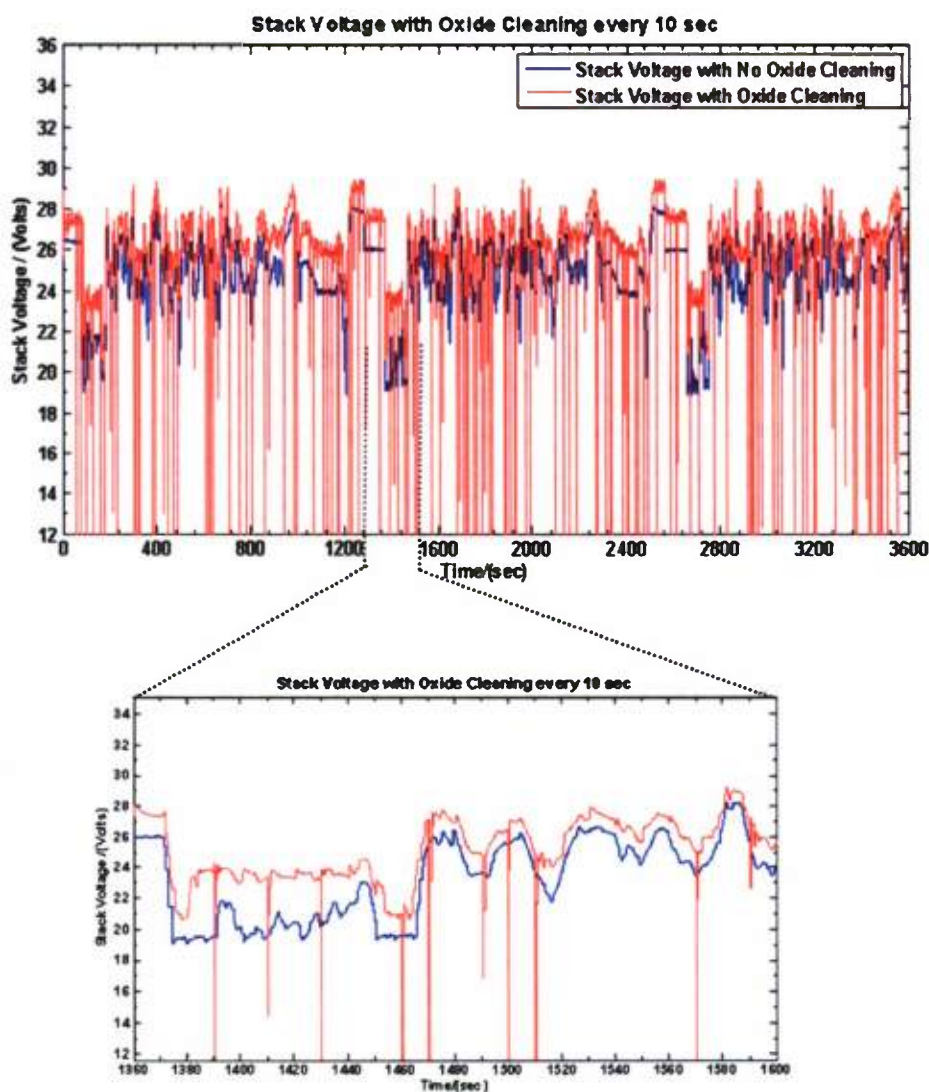


Figure 1.1.24 Percent difference in H<sub>2</sub> consumption at different power cutoff levels compared with baseline tests



**Table 1.1.5 Loss in duration due to limiting number of shorting process at different cut-off power levels at shorting interval of 200 sec**

Power Cut-Off Limit (W)	No of shorting process (#)	Average BoT & EoT gain in 24 hrs duration (mins)	Loss due to limiting No. of shorting at different power level (%)
350	4	11.57	69.71%
400	8	17.55	54.06%
450	12	25.68	32.76%
500	15	34.45	9.79%
550	18	38.19	0.00%



**Figure 1.1.25 Stack Voltage measurement without and with shorting oxide cleaning process every 10 sec**

### 1.1.3.3 Ion Tiger UAV Power Pack Characterization: HiL Evaluation Utilizing 12 Volt Battery Pack to Provide Power during Fuel Cell Regeneration Events

The objectives of this simulation study was to propose an additional electrical system to the existing Ion Tiger UAV Load Following (LF) system in order to use a 12 volt battery pack to supply all ancillary and propulsion power during the shorting duration. Two different types of Lithium Ion cells (Type 26650 and Type 18700) were used for this study. The performance of the battery pack and system overall were investigated under the following conditions:

- Two different mission profiles (2 of 3 ×20 minute profiles);
- Shorting interval (10 and 200 seconds);
- Initial State of Charge (SoC) of the battery packs (50% and 100%).

An additional electrical circuit was proposed to the existing Ion Tiger UAV system to enable the 12 volt battery pack to supply power during the shorting process. Figure 1.1.26 shows the schematic of proposed IT UAV electrical system with the additional circuit shown with red dotted lines.

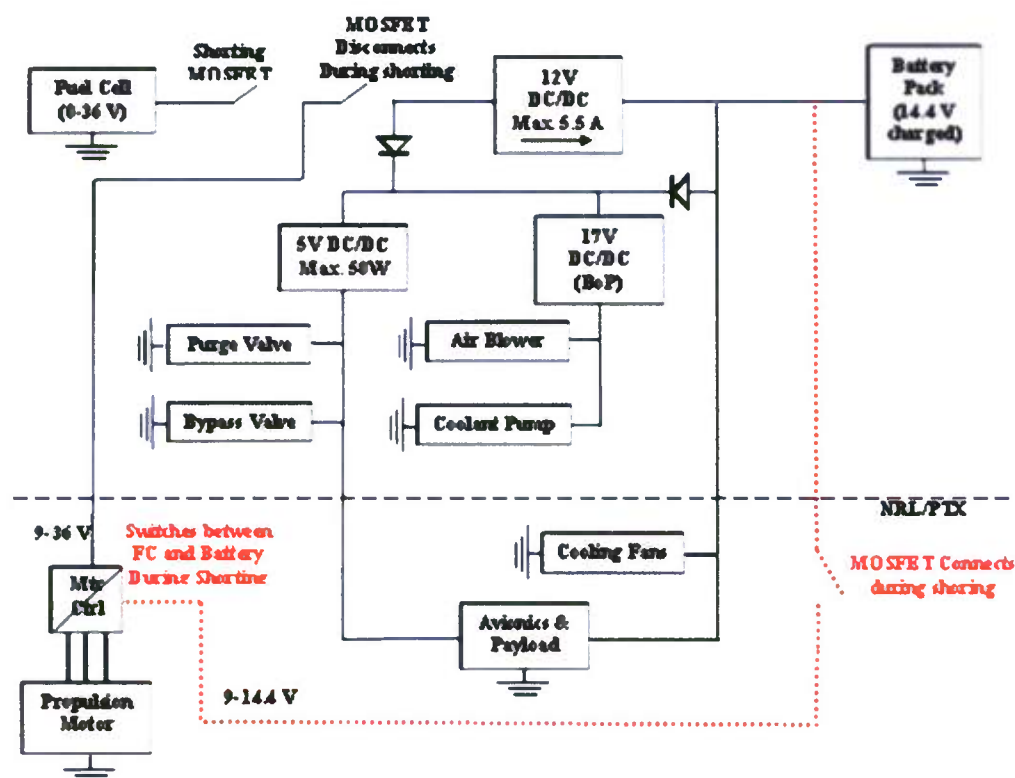


Figure 1.1.26 Schematic of the proposed IT UAV Electrical System for using 12 V battery pack during the shorting process

During the shorting process the MOSFET switch connects the battery pack to the propulsion system of the UAV to supply all propulsion and ancillary power of the system. The following assumptions were assumed for this simulation study during the shorting duration:

The battery pack connects to the motor controller during the shorting process. The motor controller (AC/DC inverter) voltage range (9-36V) is capable of regulating the battery power to the propulsion motor;

- All MOSFET switches work fast and simultaneously;
- The 12 DC-DC converters stop when the stack is disconnected;
- The battery supplies all the avionics, BoP and propulsion loads;
- The battery voltage would vary from 8-14.4 volts (2-3.6 V/cell);
- The battery will be charged with the existing 12 V DC-DC converter with maximum current limit of 5.5 Amps.

**SIMULATION TEST MATRIX:** The LF IT UAV simulation was setup to run a test matrix to study the performance of the 12 volt battery packs at different UAV flight scenarios. The simulation used two 20 minute UAV mission profiles to study the effect on the performance of the UAV power system and battery packs; Actual and Modified profiles. The modified 20 minute profile includes a sudden 500 W propulsion power demand for 400 sec. Figure 1.1.27 shows the actual and the modified 20 minute profiles used in this study.

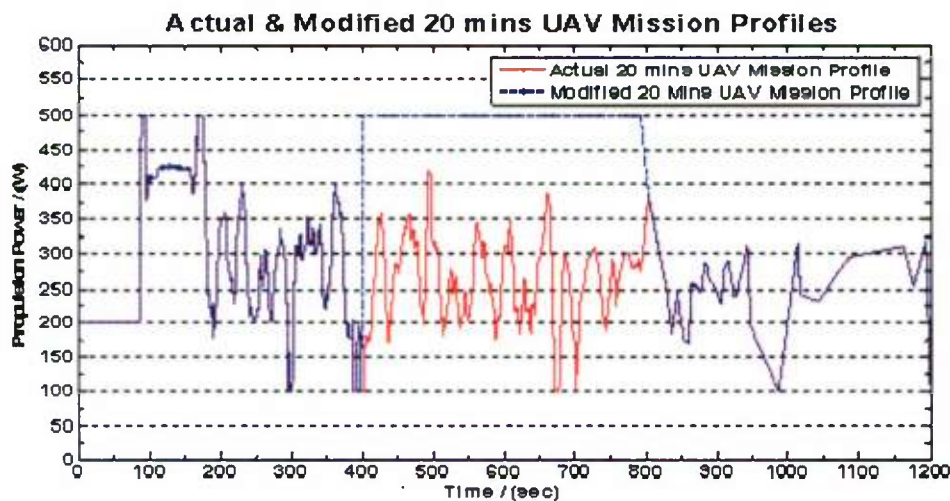


**Figure 1.1.27 Actual and Modified 20 minutes Mission Profiles**

For the simulation test matrixes run, the Load Following (LF) UAV simulation, had the following setup:

**PEMFC System:**

- VI Curve data used in the simulation: IT Stack 242845, measured on HiL with stack running with Air Blower, External Humidifier and Oxide Cleaning
- Cathode Oxidant and Stoichiometry: Air Blower and ~ 2.5
- Cathode Relative Humidity: ~ 75% (Assuming with Ext. Humidifier)
- Coolant inlet Temperature: 55 °C
- Hydrogen in Tank: 0.5 kg
- Anode Stoichiometry: 1.02 or 98% utilization (Dry)



#### Ancillary Load Profiles (Peak Demand):

- 5V Load =  $45 + 0.4 = 45.04$  W (Servo + H2 Valve)
- 12V Load =  $4 + 8 + 18 = 30$  W (Autopilot, Payload & Radiator Fan)
- 17 V BoP Load = Function of stack current

#### DC-DC Converter:

- 5V Converter Efficiency = 90%
- 12 V Converter Efficiency = 93%
- 17V Converter Efficiency = 93%

#### Battery Packs Battery Pack:

##### Type: 26650

##### Type 18700

- |                   |                      |                       |
|-------------------|----------------------|-----------------------|
| • No. of Cells    | = 4                  | = 4                   |
| • Capacity        | = 2.3 Ah/cell        | = 0.7 Ah/cell         |
| • Nominal Voltage | = 3.3 volts/cell     | = 3.3 volts/cell      |
| • Total Mass      | = 0.28 kg (70g/cell) | = 0.152 kg (38g/cell) |

RESULTS AND CONCLUSIONS: Table 1.1.6 and 1.1.7 show the results of shorting study for battery type 26650 and 18700 under both the mission profiles, respectively. The table shows the battery SoC at the end of one hour and 24 hour tests, the maximum battery current and corresponding minimum voltage attained during the hour long test and minimum SoC reached during the 24 hour test. Figure 1.1.28 shows the typical one hour simulation results for battery type 26650 under a modified mission profile with shorting duration of 200 sec and initial SoC of the battery of 50%. Results showed that both lithium Ion battery types (26650 and 18700) performed well under the actual mission profile and at both shorting intervals (10 sec & 200 sec) with the battery initial SoC of 100% and 50%. However, during the shorting duration the battery voltage drop to the minimum voltage of 8V (2V/cell) at maximum power of ~ 600 W for the 26650 battery type compared to the 18700 battery type, which drop to 11-12 volts. Both battery packs were charged back to 100% SoC at end of 24 hour mission under the actual mission profile. Under the modified mission profile (Figure 1.1.27), both battery packs were fully discharged by the end of 24 hour mission profile when the shorting duration was 10 sec. For shorting duration of 200 sec, the higher amp-hour battery pack (26650) retained more charge (80-100%) than the battery type 18700 (30-100%) under the modified profile.

The study's conclusion for both battery types is that if a 12V battery pack were to supply power during shorting process, then a shorting interval of  $\geq 200$  sec would be advised in case there is sudden increase of maximum power demand during the shorting period. Further recommendation to NRL Ion Tiger team would be to limit battery power by limiting the maximum current from the battery to between 40-50 amps during shorting period. This could be achieved by programming the algorithm which demands the power for the propulsion motor to demand some ideal power during the shorting duration and back to normal power demand when the fuel cell is connected. Possibly the motor controller (AC-DC inverter) may automatically limit the current drawn from the battery pack, due to lower range of battery voltage (8-14.4V) compared to fuel cell stack voltage (18-36 V).



**Table 1.1.6 Simulation results for Battery Type 26650 under actual and modified Profiles**

Simulation Setup for Battery Type 26650		Results from the LF IT UAV System Simulation with Actual 3x20 Mins Mission Profile				
Shorting Interval (sec)	Initial SoC (%)	1-Hr-Test Final SoC (%)	24-Hr Final SoC (%)	Max Battery Current (Amps)	Min Battery Voltage (Volts)	Min SoC During the Test (%)
10	100	100	100	76	8.00	99.46
10	50	100	100	76	8.00	50.00
200	100	100	100	76	9.77	99.50
200	50	100	100	55	8.00	50.00
Simulation Setup for Battery Type 26650		Results from the LF IT UAV System Simulation with Modified 3x20 Mins Mission Profile				
Shorting Interval (sec)	Initial SoC (%)	1-Hr-Test Final SoC (%)	24-Hr Final SoC (%)	Max Battery Current (Amps)	Min Battery Voltage (Volts)	Min SoC During the Test (%)
10	100	82.80	10	76	8	76
10	50	40.59	10	76	8	28
200	100	93.20	93-100%	76	8	76
200	50	68.45	80-100%	76	8	41

**Table 1.1.7 Simulation results for Battery Type 18700 under actual and modified Profiles**

Simulation Setup for Battery Type 18700		Results from the LF IT UAV System Simulation with Actual 3x20 Mins Mission Profile				
Shorting Interval (sec)	Initial SoC (%)	1-Hr-Test Final SoC (%)	24-Hr Final SoC (%)	Max Battery Current (Amps)	Min Battery Voltage (Volts)	Min SoC During the Test (%)
10	100	100	100	50.00	12.20	98.33
10	50	100	100	55.35	11.00	50
200	100	100	100	35.20	12.80	98.55
200	50	100	100	38.70	11.65	50
Simulation Setup for Battery Type 18700		Results from the LF IT UAV System Simulation with Modified 3x20 Mins Mission Profile				
Shorting Interval (sec)	Initial SoC (%)	1-Hr-Test Final SoC (%)	24-Hr Final SoC (%)	Max Battery Current (Amps)	Min Battery Voltage (Volts)	Min SoC During the Test (%)
10	100	10	10	65	9.33	10
10	50	10	10	64.50	9.45	10
200	100	75.49	30-100%	55	10.86	27.20
200	50	75.49	30-100%	55	10.60	20.20

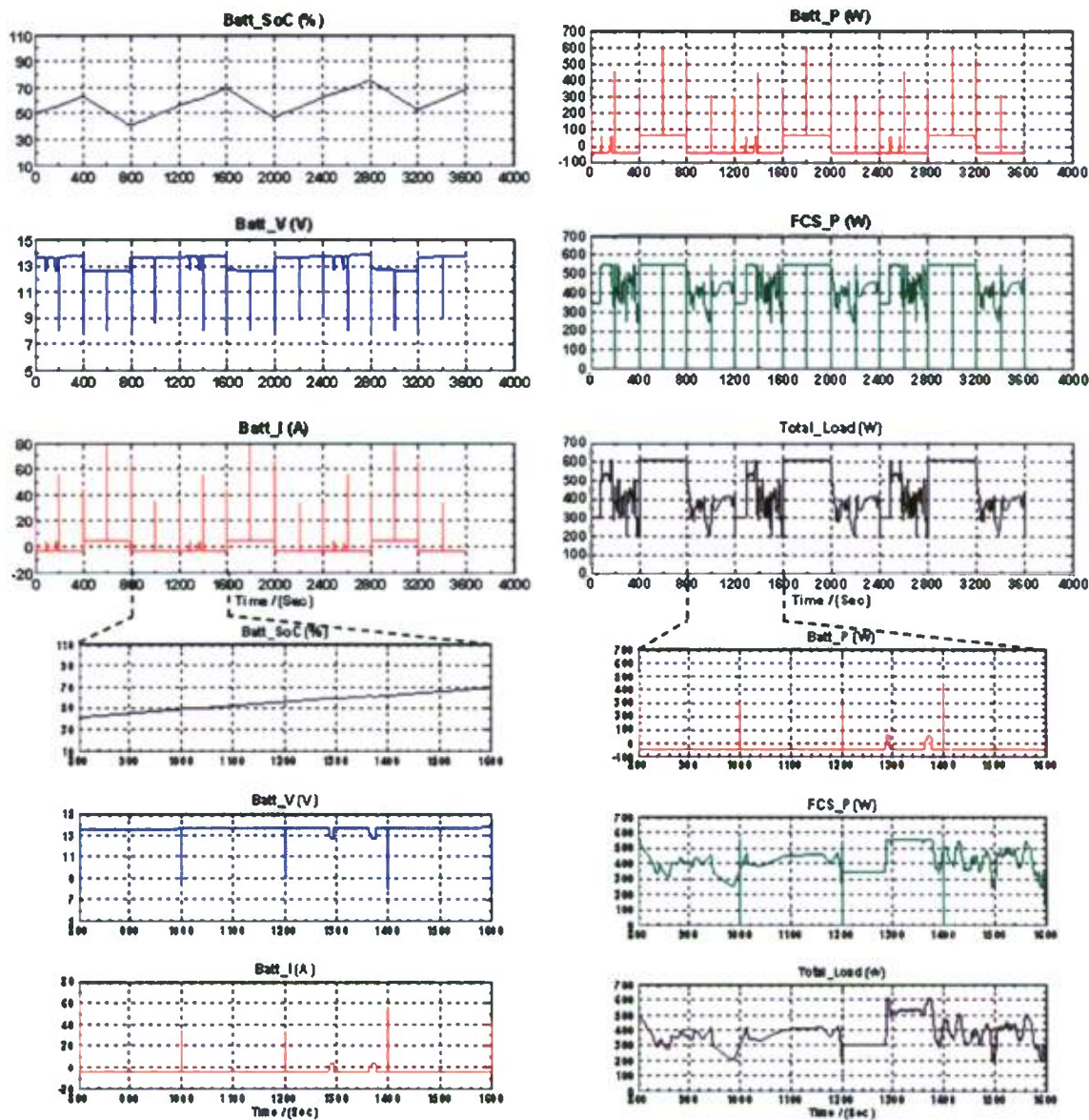


Figure 1.1.28 Typical one hour simulation results for battery type 26650 under a modified mission profile (Shorting duration = 200 sec and initial SoC of the battery = 50%)

#### 1.1.3.4 Ion Tiger UAV Power Pack Characterization: Hybridization Study of the UAV System

The objective was to study the effects of hybridization of the load following (non-hybrid) UAV system and propose a novel partial hybrid UAV system which would minimize the losses due to hybridization and has the flexibility of switching operation of the UAV system from hybrid to non-hybrid mode. Three UAV system simulations were developed in a Matlab/Simulink environment with different system configurations (non-hybrid, traditional full hybrid and novel partial hybrid) to study the impact of adding battery packs (weight) and controller hardware



(weight & power losses) on the flight duration of the UAVs for a given propulsion and ancillary load profile. The system simulations were used for a system design as well as a 24+ hour endurance analysis. In addition, the HiL test system was used to characterize the performance of each system under a 20 minute load profile with an actual PEMFC stack and some balance of plant (BoP) components to estimate the energy balance over this period.

Figure 1.1.29 shows the system configuration of each of these systems and highlight the main pros and cons of each system. The non-hybrid system is a load following system (LF) where all the propulsion and ancillary power comes from the fuel cell stack while in the full hybrid (FH) system, all the power is supplied via the hybrid battery with fuel cell stack acting as a battery charger. In the partial hybrid (PH) system, the propulsion and ancillary power is shared by the fuel cell stack and hybrid battery pack according to the operational/control strategies of the controller.

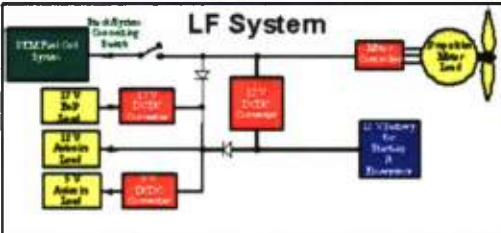
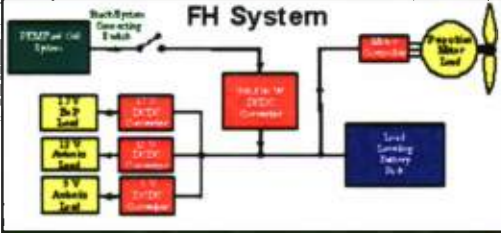
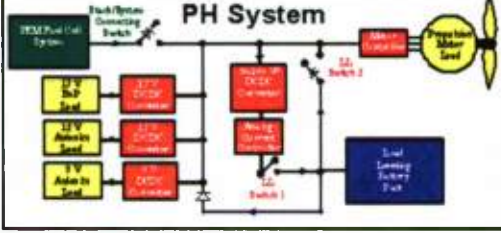
UAV System Types	Pros	Cons
 <p><b>LF System</b></p>	<ul style="list-style-type: none"> <li>• Smaller battery pack</li> <li>• Smaller DC-DC converter for battery charging</li> <li>• No weight penalty</li> </ul>	<ul style="list-style-type: none"> <li>• Only stack provides all power to the system</li> <li>• Stack always operates in dynamic mode</li> <li>• Lower durability and lifetime of stack</li> </ul>
 <p><b>FH System</b></p>	<ul style="list-style-type: none"> <li>• Battery takes all dynamics</li> <li>• Stack operates at constant or controlled dynamics</li> <li>• Down sizing of stack</li> <li>• Improve durability and lifetime of the stack</li> </ul>	<ul style="list-style-type: none"> <li>• Large dc-dc converter</li> <li>• High power losses</li> <li>• Weight penalty</li> <li>• Battery discharges quickly at continues peak power</li> <li>• Stack can't provide power to the system directly</li> </ul>
 <p><b>PH System</b></p>	<ul style="list-style-type: none"> <li>• Flexible mode of operations</li> <li>• Stack &amp; battery supply power</li> <li>• Smaller dc-dc converter</li> <li>• Stack operates at high efficiency</li> <li>• Improves durability and lifetime of the stack</li> </ul>	<ul style="list-style-type: none"> <li>• Weight penalty</li> <li>• Complex system</li> <li>• Extra hardware for control</li> </ul>

Figure 1.1.29 System configurations of the non-hybrid, full and partial hybrids UAV Systems

The PH system was designed to minimize the large power losses through the DC-DC converter which the FH occurs by using a smaller DC-DC converter and have the flexibility of switching modes of operation from Parallel (power shared by stack and battery) to Load Leveling (stack power limited) to Load Following (stack provides all system power including battery charging power). This flexibility of switching mode of operation is great advantage to have in the event the battery is fully discharged due to a long period of high power demand (e.g., at high flight turbulence). If this is the case, then the UAV could change to Load Following mode where all power would comes from the stack. In the FH system, once the batteries are fully discharged,

the flight mission would have to be terminated even if there is still fuel in the hydrogen tank on board the UAV.

The size of the DC-DC converter was optimized to be large enough to maintain the battery state of charge (SoC) between 60-50% and small enough to minimize both power losses and weight penalty. The battery pack size was selected to meet the voltage range of the propulsion motor controller and to have an optimal parallel to the Load Leveling operational voltage ratio. Figure 1.1.30 shows the performance curves of the fuel cell and battery discharge curves for different battery sizes over lapped to find the optimal voltage range for parallel mode of operation. A battery pack with 9 cells has low LL/Parallel ratio and the operation is dominated by battery pack while the 7 cell battery pack has large LL/Parallel ratio. An 8 cell battery pack size was the optimal choice that gave a good LL/parallel ratio over large range of stack power.

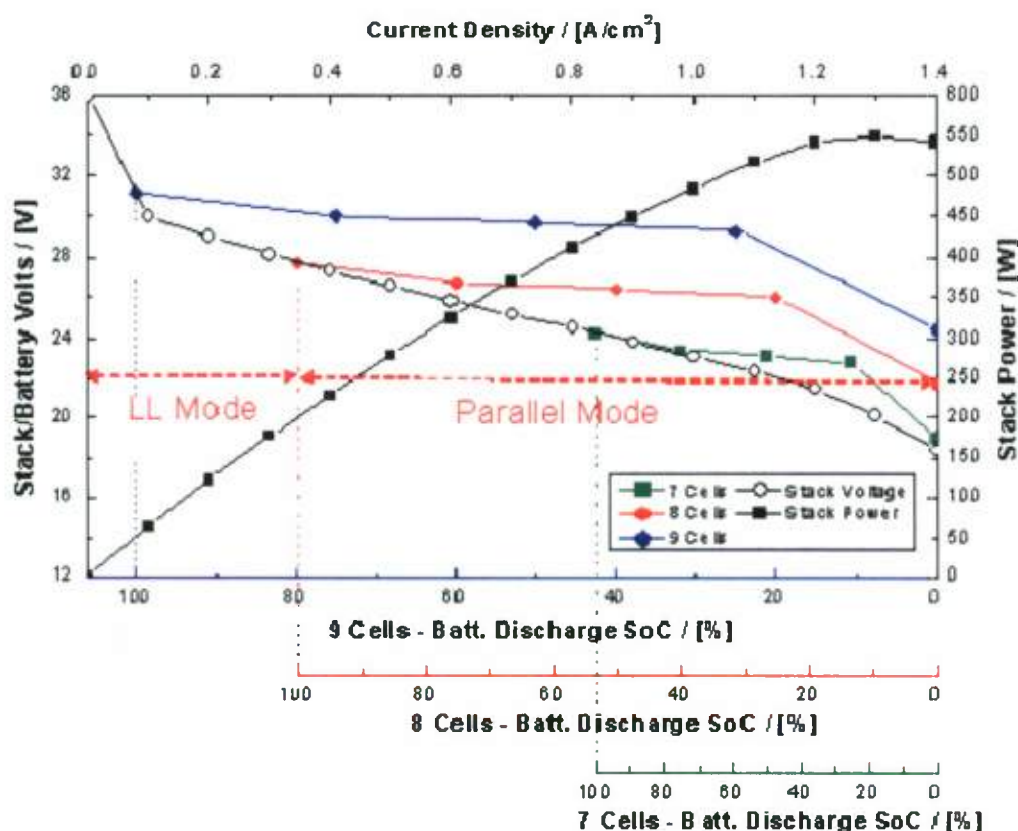
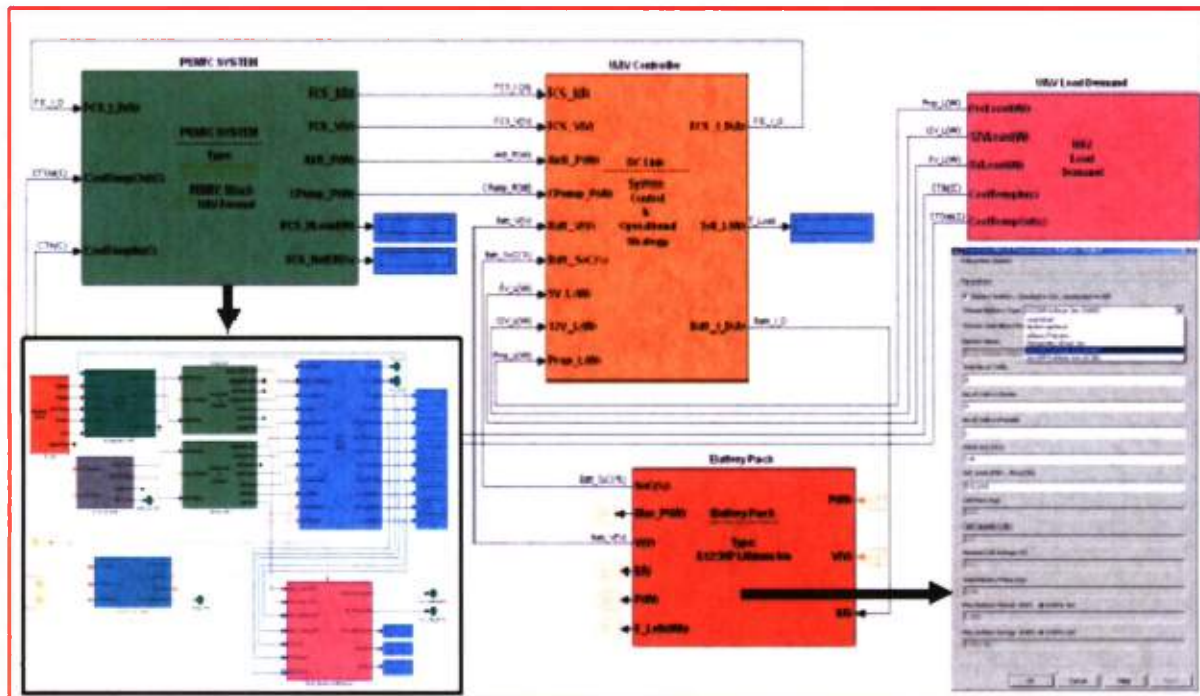


Figure 1.1.30 Fuel cell and Battery performance curves for sizing-up of hybrid battery pack

The UAV simulation tool shown in Figure 1.1.31 was used to analysis the duration of the three UAVs systems under a repeated 20 minute load profile with 0.5 kg of hydrogen on board and a fully charged battery pack. The flight duration was determined by repeating the 20 minute profile (Figure 1.1.27) until the all the hydrogen fuel was consumed and the battery pack was discharged to 10% of SoC.





**Figure 1.1.31 UAV Simulation Tool in Matlab/Simulink Environment**

The following simulation setup was used for this UAV endurance analysis. Table 1.1.8 shows the increase in system weight and propulsion power due to hybrid battery and DC-DC converter. These increase in weight and power losses were programmed into the simulation and accounted for in the endurance simulation study. The analyses were done at three different ancillary loads with the lithium Ion battery pack and 500 W PEMFC stack.

*Propulsion Load Profile & System Weight Penalty:*

- 20 mins Load Profile - Repeated to calculate the final duration of the system
- Repeated Until - 0.5 k of H<sub>2</sub> is consumed and SoC% Battery ≤ 10%
- Total weight penalty - Increase in propulsion power

*System Ancillary Loads:*

- Zero Avionics + BoP
- Nominal Avionics (cruise) + BoP
- Maximum Avionics (peak) + BoP

*PEMFC System*

- Nom. Power: 500 W
- Peak Power: 550 W
- Anode and Cathode Stoich.: 1.02 and ~ 2.5

*Battery Pack: Lithium Ion*

- Capacity: 2.3 Ah
- Nom. Voltage: 3.3 volts
- Initial SoC: 100%

**Table 1.1.8 Weight and Propulsion Power Penalty for each of the UAV Systems**

<b>UAV SYSTEM TYPES</b>	<b>FL</b>	<b>Full</b>	<b>PH</b>
<b>No of Cells of Lithium Ion</b>	4	8	8
<b>Increase in Battery Wt (g) (70g/cell)</b>	0.0	280	280
<b>Increase in Electronics Wt (g) DC-DC Converter/MOSFET/Diodes</b>	0.0	100	112
<b>Net Increase in System Weight (g)</b>	0.0	380	392
<b>Net Increase in Propulsion Power (W)</b>	0.0	7.54	7.78

Figure 1.1.32 shows the results from the endurance analysis of the three UAV system simulations at different ancillary loads (zero, nominal and peak). The results show a 10% difference in flight duration with the FH UAV system when compared to the LF UAV system at same nominal avionics load. This loss in duration is reduced to 2% by design of a novel partial hybrid UAV system mainly due to lower DC-DC power losses (from 50W to 7.5W). Although the LF UAV system (the baseline system) has no losses due to weight and power losses, it will have long term durability losses due to constant dynamic demand on the fuel cell stack compared to the PH hybrid system where stack load demand dynamics are much smoother and the peak power is much lower. This effect was observed in the HiL results where the actual stack, which was used for the analysis, had done approximately 75% of the design load hours and the stack performance had degraded over time.

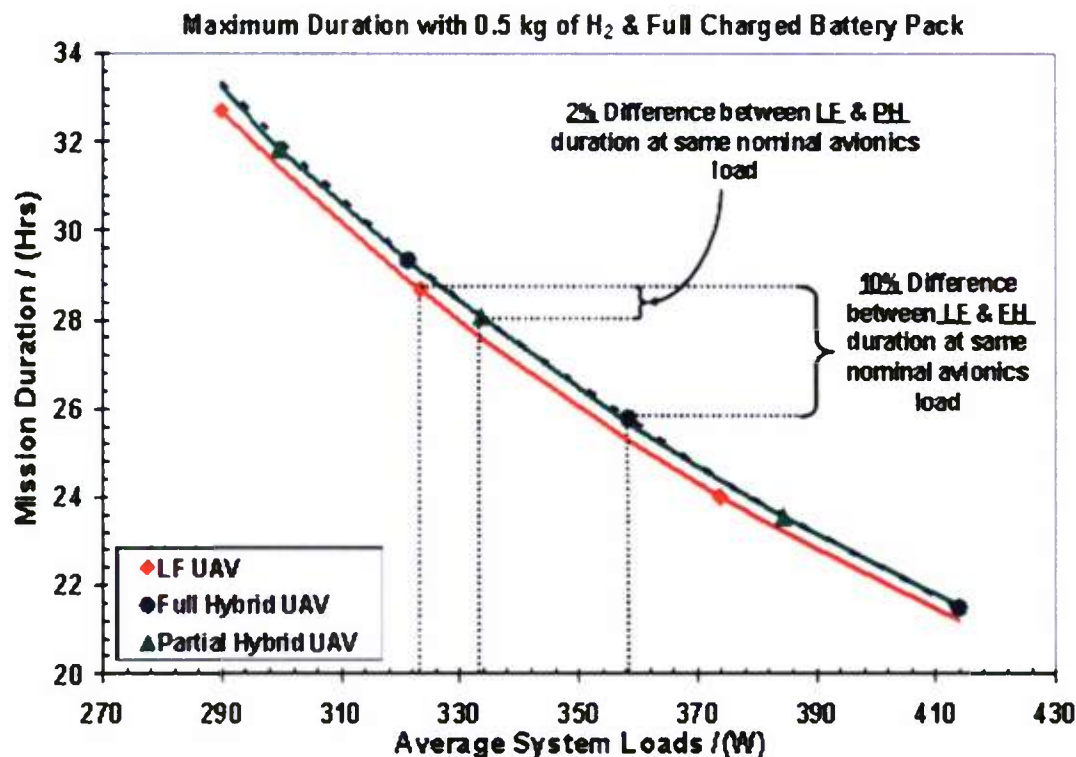


Figure 1.1.32 Results of the endurance analysis for three UAV systems with 0.5 kg of H<sub>2</sub> and a fully charged Lithium Ion battery pack

20 MINUTES HARDWARE-IN-THE-LOOP (HiL) ANALYSIS: The HiL analysis involved characterizing the performances of three UAV systems with actual fuel cell stack and other balance of plant hardware under a 20-minute load profile (Figure 1.1.27). Figure 1.1.33 shows the operational concept of the HiL test system. The three UAVs systems (LF, FH, PH) simulation were converted into real time simulation and were then used to run the HiL test with actual fuel cell stack operating on dry hydrogen with an anode purge system and air from the air blower and external humidifier. The air blower was designed to run at a cathode stoichiometry of ~2.5 and the external humidifier at 75% relative humidity.

Results of the HiL test for the three systems are summarized in Figure 1.1.34. The figure shows the screen shot of the real time results for the total system load (yellow) and the corresponding stack power (blue) for the three UAV systems. For the LF UAV system, the stack operates in a highly dynamic mode and since the performance of the stack had degraded over time (completed  $\geq 75\%$  load hours), the stack power could not meet the total system demand. Hence, with this degraded stack the projected duration would have been reduced by two hours, i.e., ~ 8% of the designed 24 hours duration. In both the FH and PH systems, the power from the degraded stack was sufficient with the battery supplementing the difference in power demand. Although the hybrid system has the apparent penalty of extra weight and power losses that will lead to lower flight duration, the long term payback of the hybrid system would be to improve the durability and lifetime of the stack.



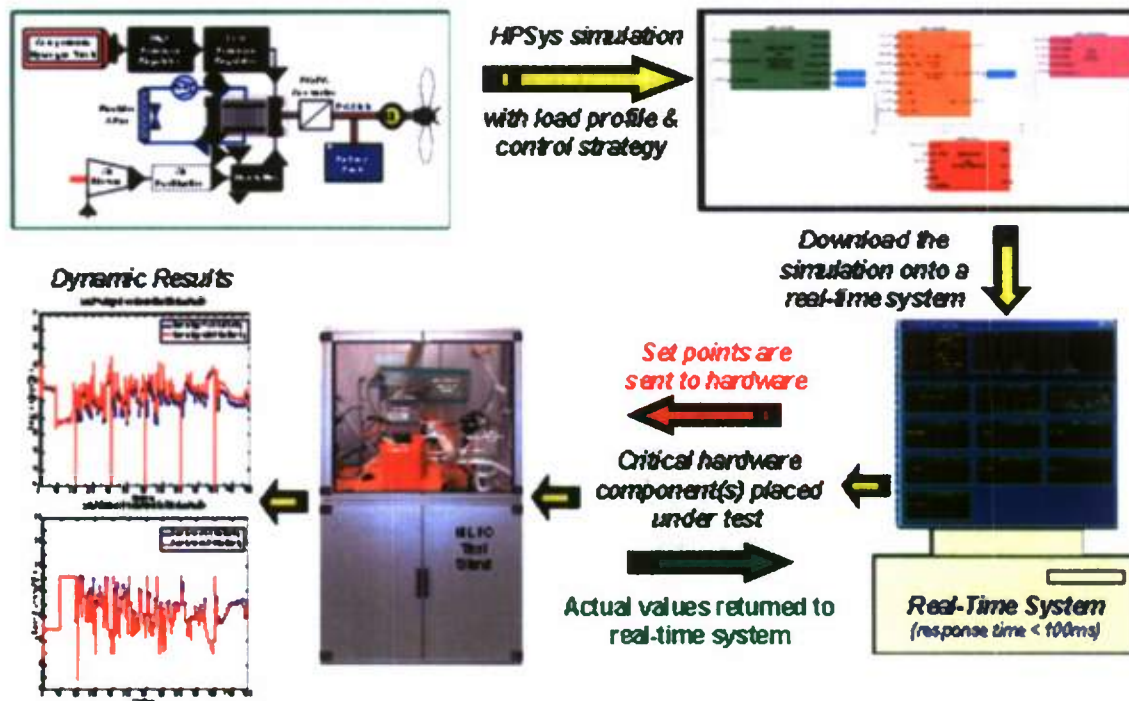


Figure 1.1.33 Operating concept of the HiL Testing System

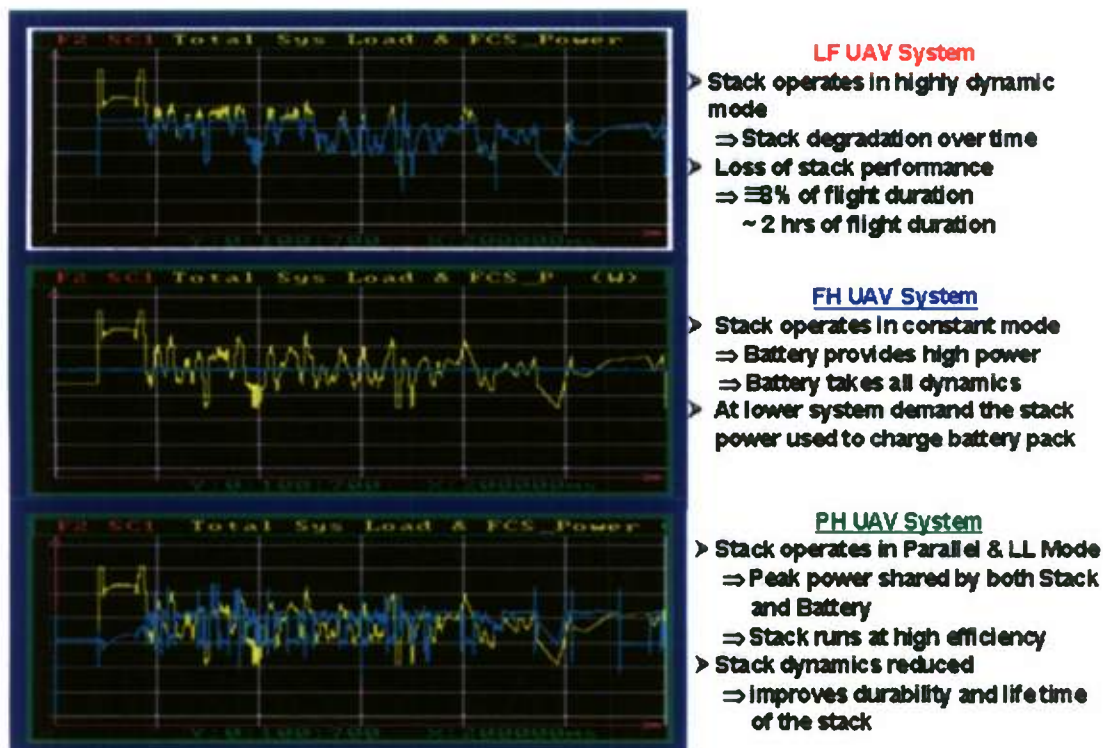


Figure 1.1.34 Results of the HiL Tests for the three UAV System Under 20 mins Mission Profile



An estimated energy balance was also calculated using the measured HiL test data for each system over the 20-minute load profile. Figure 1.1.35 shows the schematic of UAV system with all the energy sources and losses that were considered in the energy balance. The energy balance was carried out using the following assumptions:

- Stack energy balance was based on 98% H<sub>2</sub> utilization, 2.5 Air Stoichiometry and 75% Relative Humidity of Cathode
- Surface radiation and convection losses were estimated assuming the fuel cell as a black body

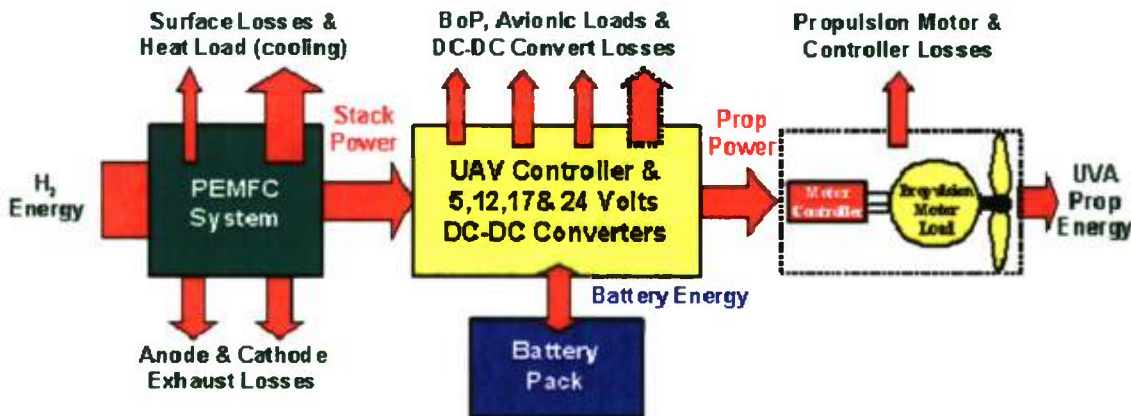


Figure 1.1.35: Schematic of energy balance over the UAV System

Table 1.1.9 shows the results of the energy balance for the three systems over the 20 minute load profile based on a lower heating value (LHV) of hydrogen, the peak ancillary load, and the assumptions stated above. The results of the energy balance show the PH UAV system consumed the least amount of H<sub>2</sub>, resulting in lower heat load losses from the system. The FH UAV system had the largest heat load losses, since the stack was operating at constant power even when the demand was lower than the stack power. The LF UAV system required 2% more H<sub>2</sub> energy to complete the mission profile. Overall, the novel PH UAV system has much lower losses than FH UAV system and a much lower dynamic operation of the stack than the LF UAV system, leading to longer stack lifetime and more durable UAV system.

Table 1.1.9 Energy balance result for the three UAV systems under a 20-minute load profile

Based on Peak Ancillary Loads & LHV of H <sub>2</sub>	LF UAV System				FH UAV System				PH UAV System			
	Energy In	%	Energy Out	%	Energy In	%	Energy Out	%	Energy In	%	Energy Out	%
	Wh	%	Wh	%	Wh	%	Wh	%	Wh	%	Wh	%
<b>PEMFC System</b>												
Anode Inlet H <sub>2</sub>	251	93%			264	91%			242	90%		
Electrical Power			126	47%			135	46%			124	46%
Cathode Air Inlet	19	7%			22	8%			21	8%		
Anode Exhaust			5	2%			5	2%			5	2%
Cathode Exhaust			31	11%			28	10%			27	10%
Heat Load			109	40%			118	41%			108	40%
<b>Battery Pack</b>												
Battery Energy	[100% SoC]		0.3	0.1%	4	1%	[99% SoC]		6	2%	[99% SoC]	
<b>System Loads</b>												
5 V DCDC Load (Avionics & Sensor)			17	6%			17	6%			17	6%
12 V DCDC Load (Auto Pilot, Payload & Radiator Fan)			16	6%			11	4%			11	4%
17 V DCDC Load (Air Blower & Cooling Pump)			8	3%			8	3%			8	3%
24 V DCDC Load (Hybrid Battery Pack Charger)			0	0%			12	4%			1	0.3%
<b>Propulsion Power</b>			90	33%			92	32%			92	34%
<b>Total</b>	270	100%	274	102%	290	100%	290	100%	268	100%	268	100%

#### 1.1.4 Alternate Cell Evaluation

HNEI continued to evaluate alternative (non-PEM) fuel cell technologies to identify candidate technologies for testing for Department of Defense applications. We initiated discussions regarding testing of advanced alkaline technology, but no testing was initiated.

#### 1.1.5 Papers and Presentations Resulting from These Efforts

##### Publications

- Y. Zhai, S. Dorn, K. Bethune and R. Rocheleau, "The Impact of SO<sub>2</sub> Contamination on the Degradation of MEA Components in PEMFCs," in preparation, will be submitted to J. Electrochem. Soc..
- Y. Zhai, G. Bender, S. Dorn, K. Bethune and R. Rocheleau, "Influence of Operating Conditions on Sulfur Dioxide Contamination in PEMFCs Part II: Cell Voltage, Cathode Relative Humidify and Cathode Air Flow Rate," in preparation, will be submitted to J. Power Sources.
- Y. Zhai, G. Bender, S. Dorn, K. Bethune and R. Rocheleau, "Influence of Operating Conditions on Sulfur Dioxide Contamination in PEMFCs Part I: Cell Temperature," manuscript finished, will be submitted to J. Power Sources.
- Y. Zhai, K. Bethune, J. St-Pierre and R. Rocheleau, "Effect of Potential on SO<sub>2</sub> Adsorption onto Pt/C Catalyst for PEMFCs," manuscript finished, will be submitted to J. Electrochem. Soc..

- Y. Zhai, K. Bethune, S. Dorn, G. Bender and R. Rocheleau, "Electrochemical Impedance Spectroscopy Analysis on SO<sub>2</sub> Contamination in PEMFCs," manuscript finished, will be submitted to J. Electrochem. Soc..

#### **Conference Proceedings/Papers**

- M. Virji, K. Bethune, R. Rocheleau, "Effect of Hybridization on the Performance of Fuel Cell Energy/Power Systems for Unmanned Aerial Vehicle (UAV)," ASME 2010 Congress, IMECE2010-3884.
- Y. Zhai, K. Bethune, J. St-Pierre and R. Rocheleau, "Effect of Potential on SO<sub>2</sub> Adsorption onto Pt/C Catalyst for PEMFCs," *ECS Trans.* - Montreal, Canada, 35(xxx) Page: xxx, 2011. This issue is scheduled to be published in September, 2011.
- Y. Zhai, K. Bethune, S. Dorn, G. Bender and R. Rocheleau, "Electrochemical Impedance Spectroscopy Analysis on SO<sub>2</sub> Contamination in PEMFCs," *ECS Trans.* - Vancouver, Canada, 28(23) Page: 313, 2010.
- S. Dorn, Y. Zhai, R. Rocheleau, "The Impact of SO<sub>2</sub> on the Degradation of MEA Components in PEMFCs," *ECS Trans.* - Vancouver, Canada, 28(23) Page: 183, 2010.

#### **Conference Presentations**

- Y. Zhai, K. Bethune, J. St-Pierre and R. Rocheleau, "Effect of Potential on SO<sub>2</sub> Adsorption onto Pt/C Catalyst for PEMFCs," 219th ECS Meeting, Oral, May 1, 2011, Montreal, QC, Canada.
- S. Dorn, Y. Zhai, R. Rocheleau, "The Impact of SO<sub>2</sub> on the Degradation of MEA Components in PEMFCs," 217th ECS Meeting, Oral, April 28, 2010, Vancouver, Canada.
- Y. Zhai, K. Bethune, S. Dorn, G. Bender and R. Rocheleau, "EIS Analysis on SO<sub>2</sub> Contamination in PEMFCs," 217th ECS Meeting, Poster, April 27, 2010, Vancouver, Canada.



## 1.2 Fuel Cell Development

The effort to develop novel fuel cell components included two major activities: biocarbons for fuel cells, and bioactive fuel cells. Each of these topics is addressed in the following paragraphs.

### 1.2.1 Biocarbons for Fuel Cells

#### 1.2.1.1 Technical Accomplishments

Under this subtask, biocarbons were produced using the HNEI Flash Carbonization™ reactor, with various feedstocks, including corn cobs, oak wood and sweet gum wood. The results of the corn cob work are described in a recent publication.<sup>1</sup> The following is the abstract of this publication:

*Elevated pressure secures the highest fixed-carbon yields of charcoal from corncob. Operating at a pressure of 0.8 MPa a Flash-Carbonization reactor realizes fixed-carbon yields that range from 70 to 85% of the theoretical thermochemical equilibrium value from Waimanalo corncob. The fixed-carbon yield is reduced to a range from 68 to 75% of the theoretical value when whole Waimanalo corncobs are carbonized under nitrogen at atmospheric pressure in an electrically heated muffle furnace. The lowest fixed-carbon yields are obtained by the standard proximate analysis procedure for biomass feedstocks: this yield falls in a range from 49 to 54% of the theoretical value.*

*A round-robin study of corncob charcoal and fixed-carbon yields involving three different thermogravimetric analyzers (TGAs) revealed the impact of vapor-phase reactions on the formation of charcoal. Deep crucibles that limit the egress of volatiles from the pyrolyzing solid greatly enhance charcoal and fixed-carbon yields. Likewise, capped crucibles with pinholes increase the charcoal and fixed-carbon yields compared with values obtained from open crucibles. Large corncob particles offer much higher yields than small particles. These findings show that secondary reactions involving vapor-phase species (or nascent vapor-phase species) are at least as influential as primary reactions in the formation of charcoal.*

*Our results offer considerable guidance to industry for its development of efficient biomass carbonization technologies. Size reduction handling of biomass (e.g., tub grinders and chippers), which can be a necessity in the field, significantly reduces the fixed-carbon yield of charcoal. Fluidized bed and transport reactors, which require small particles and minimize the interaction of pyrolytic volatiles with solid charcoal, cannot realize high yields of charcoal from biomass. When a high yield of corncob charcoal is desired, whole corncobs should be carbonized at elevated pressure. Under these circumstances, carbonization is both efficient and quick.*

The oak wood and sweet gum wood were supplied to us by the Dow-Corning Corporation. Dow-Corning is interested in the use of charcoals produced from these woods as reductants in the manufacture of pure silicon from quartz. We have completed our study of these woods and their charcoals, and are now preparing a paper on this topic for publication. We expect to submit the paper to *Energy & Fuel* before the end of the year.

We supplied biocarbons for testing to Ben Thien of Scientific & Research Associated, Inc. (SARA). For many years SARA has had Department of Defense support for its development of a direct carbon fuel cell.



This subtask also enabled us to complete and publish a study of the thermodynamic properties of water at high pressures and temperatures.<sup>2</sup> These properties are relevant to the development of aqueous-alkaline-carbonate direct carbon fuel cells.

HNEI's development of an aqueous-alkaline-carbonate direct carbon fuel cell with primary support from the National Science Foundation is ongoing and will be completed next year. This subtask has been supportive of the NSF activity. Results will be reported next year.

References cited

#### 1.2.1.2 References Cited

1. Wang, L.; Trninic, M.; Skreiberg, O.; Gronli, M.; Considine, R.; Antal, M. J., Is Elevated Pressure Required to Achieve a High Fixed-Carbon Yield of Charcoal from Biomass? 1. Round Robin Results for Three Different Corncob Materials. *Energy Fuels* **2011**, 25, 3251-3265.
2. Manya, J. J.; Antal, M. J.; Kinoshita, C. K.; Masutani, S. M., Specific Heat Capacity of Pure Water at 4.0 MPa between 298.15 and 465.65 K. *Ind. Eng. Chem. Res.* **2011**, 50, 6470-6484.

### 1.2.2 Bioactive Fuel Cells

Bioactive fuel cells or enzymatic bio-fuel cells (EBFCs) are fuel cells that use enzymatic biocatalysts to convert chemical energy directly to electricity as power sources. They are promising alternatives to complement conventional fuel cell technologies that rely on transitional metal oxides or noble metals as catalysts for conversion of chemical energy, typically stored in hydrogen or other biofuels, to useful electrical energy. An EBFC exhibits some promising technical merits as follows:

- Selectivity – Enzyme catalysts are fuel specific and capable of handling complex fuels in the liquid phase, which can simplify fuel logistics and cell design;
- Abundance in fuels and catalysts supply – Unlike conventional Pt-based catalysts, enzymatic catalysts can be produced via biological or chemical methods, thus promising a potentially low-cost mass production and unlimited supply; similarly, the biofuels, as diverse as we can be in choosing proper biocatalysts to convert the chemical energy, can be produced from photosynthesis or alternative refinement pathways, thus considered renewable and green as abundant supplies;
- Wider range of operation – Due to their selectivity, enzymes are generally more adaptive to extreme conditions and tolerant to contaminants;
- Reformulation – If the gene coding for the enzyme is obtained, a suite of directed evolution techniques exists to create mutants that are more effective in catalysis; and
- Self-assembly – Unique in biological systems, to simplify fabrication processes for micro-devices *in situ*.

The continuation of support has enabled us to execute fundamental studies that have (i) elucidated charge transfer limitations in enzyme-catalytic electrodes, (ii) developed preferred immobilization matrices for enhancing enzyme activity and stability, (iii) designed and fabricated standardized test cells for performance testing, and (iv) developed some unique *in situ* characterization techniques to understand the immobilization process of mediators on carbon or metal electrode. We have transferred this knowledge into improved engineering designs of practical *bio-fuel cells* including, more recently, microbial fuel cells. To this end, the following long-term objectives have been achieved under this program:

- Established an array of quantitative *in situ* characterization techniques, test cells, and modeling capabilities to determine limitations to bioelectrocatalysis [1-7],
- Developed a test bed modular cell that has allowed us to test cell performance of enzyme-based bioelectrocatalysis operation [8, 9];
- Developed macroporous flow-through immobilization matrices permitting improved catalyst performance (activity and lifetime) [10-13]
- Developed working enzyme fuel cells [14, 15]

#### 1.2.2.1 Scope of Work and Approach

Over the course of this project, three major tasks in the EBFC work have been focused on:

- 1) Developing platform fabrication technology to control the resulting multidirectional pore structure of three-dimensional electrodes, and immobilization techniques;

- 2) Developing qualitative and quantitative fluorescence as a characterization technique for enzyme fuel cells; and
- 3) Developing *in situ* interface characterization techniques utilizing imaging ellipsometry with quartz crystal microbalance and electrochemical techniques to facilitate fabrication and testing of bio-fuel cells and to understand the interfacial charge transfer mechanism for future optimization of the charge transfer efficiency.

For this specific funding period, we were funded to pursue the following:

- 1) Continue to develop in-situ characterization techniques using fluorescence to explore protein aggregation in the immobilized state, as a means to characterize chitosan based immobilization of multiple enzymes that can more fully oxidize complex energy fuels, and
- 2) Continue to apply *in situ* characterization techniques based on spectroscopic imaging ellipsometry with microgravimetric and electrochemical techniques to study the enzyme-electrode interaction on the electrode surface and the associated dynamic behavior, aiming to understanding the charge transfer process with more direct measurements and correlation.

#### 1.2.2.2 Technical Accomplishments

*Summary of work from previous project periods.* In past reports, we have presented several prototype cells constructed to deliver gas (e.g., hydrogen) fuels. A final working hydrogenase enzymatic bio-fuel cell was constructed and tested (Figure 1.2.1). The design considerations and test applications were described in Final Technical Report, ONR Grant N00014-01-1-0928, June 2005. Complete details on this work have been published [1]. From this work we determined, and reported previously, that the use of gaseous fuels is limited by the solubility of the gaseous fuel in the aqueous buffer that is required to maintain enzyme activity.

In past reports we have also commented on the development of a suite of characterization techniques, including potentiostatic DC polarization, dynamic potentiometry, and electrochemical impedance spectroscopy (EIS) combined with spectrophotometric detection of enzyme activity, in order to characterize electrode performance, and to differentiate between the relative contributions towards charge transfer efficiency. Among the results of our efforts, in particular, we believe we were one of the first groups to report charge transfer efficiency for bound enzyme [1] and to report a mass transport modeling effort that can be combined with DC-polarization data to yield information valuable for future electrode development [2]. A detailed description of the technique application, data and results can be found in the literature. A summary can also be found in Final Technical Report, ONR Grant N00014-07-1-1094, August 2010 (Section 3.3.2).

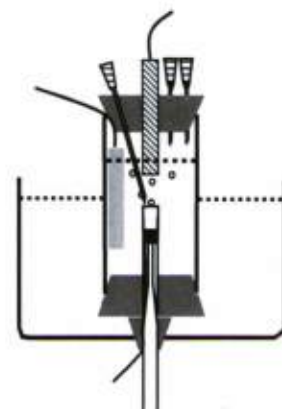


**Figure 1.2.1**  
Hydrogenase enzyme  
fuel cell

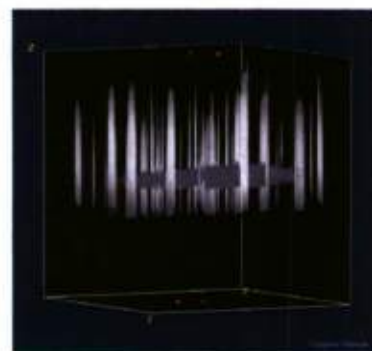


**Figure 1.2.2 3D**  
distribution of tagged  
enzyme within polymer



To characterize the distribution of enzymes within the polymer films used to immobilize the enzymes, we have applied the technique of fluorescence. Electrode fabrication methodologies using the immobilization process with polymer films inherently assume that the immobilized enzymes are homogeneously distributed. Our work, which has tagged ethanol-oxidizing enzymes with various fluorescent probes, has used laser-scanning confocal microscopy to image the spatial distribution of the enzyme within the film. Our results, which have been published [3] (see Figure 1.2.2), have clearly demonstrated that this is not necessarily the case, and that the tagged enzymes may not be homogeneously distributed within polymer films. To investigate how the charge-charge interaction between the enzyme and the polymer affect the immobilization process, we have also studied the steady-state and dynamic polarization of fluorescent probes when placed in solution with charged polymers. This work has shown that the enzymes are retained in the micelles of the hydrophobically-modified polymer as it dries, but are not entrapped within those polymers while mixed in free solution [4].

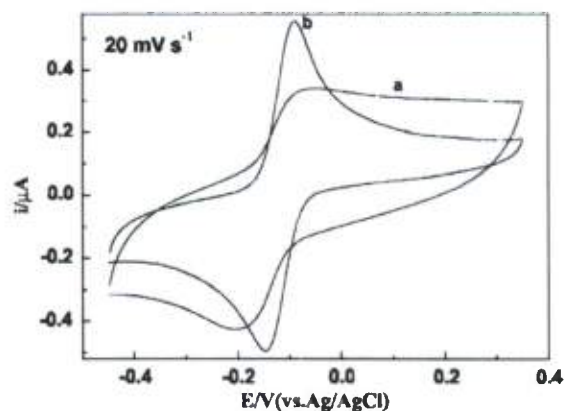


**Figure 1.2.3** Cyclic voltammograms of (a) PQQ-bound CHIT-modified GCE and (b) PQQ-bound CHIT-CNT-modified GCE in 0.1 M PBS and scanned at 20 mV/s

The premise of conducting *in situ* investigation is to characterize and understand charge transfer process and its limitations in a bio-fuel cell operation, which is strongly and critically dependent on the interfacial property of the electrode surface, and where the charge transfer occurs and high efficiency matters. The interfacial properties need to be characterized *in situ* in the environment where the electrocatalytic reaction occurs. To study such property and behavior of the interface, we have developed a unique capability which employs an advanced spectroscopic imaging ellipsometry with complementary tools, such as microgravimetric and electrochemical techniques to assist us understand the nature of such charge transfer process on the electrode surface.

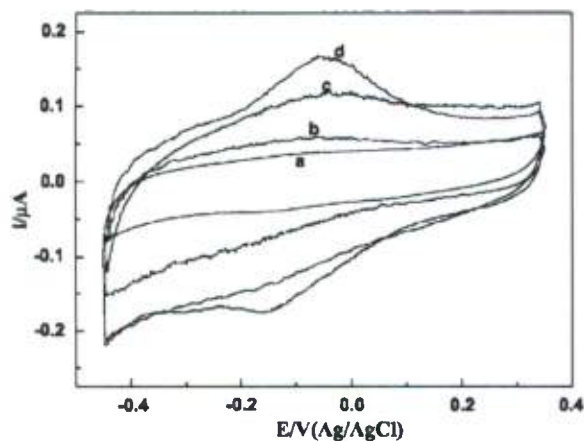


**Figure 1.2.4** Cyclic voltammograms of (a) GCE, (b) CHIT-modified GCE, (c) CHIT-CNT-modified GCE, and (d) PQQ-GDH-bound CHIT-CNT-modified GCE in 0.1 M PBS at 20 mV/s

Mediator films immobilized on electrode surface have been suggested to be an effective method to promote charge transfer. Such mediator immobilization has been pursued in our laboratory. Two major pathways are considered. One is chemical route and another electrochemical.

In the chemical pathway, we have initiated an enzyme immobilization effort to consider the feasibility of developing a common platform for apo-enzyme reconstitution. This approach is of particular interest with prosthetic group that contains pyrroloquinoline quinine (PQQ) and PQQ-dependent glucose dehydrogenase (PQQ-GDH), which is attractive for



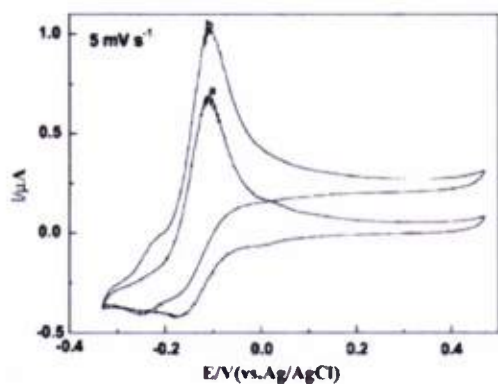


**Figure 1.2.5** Cyclic voltammograms of PQQ-GDH-bound CHIT-CNT-modified GCE in 0.1 M PBS and 40  $\mu$ M of PMS at 5 mV/s in the (a) absence and (b) presence of 10 mM glucose

glucose oxidation. For instance, PQQ and PQQ-GDH have been chemically bound to CHIT-CNT films in the presence of EDC (1-ethyl-3-[3-dimethylaminopropyl] carbodiimide hydro-chloride), respectively, on glassy carbon electrodes (GCEs). The immobilized PQQ-GDH on CHIT-CNT matrix displays a quasi-reversible electron transfer with a formal potential  $E^{\circ'} = -0.110$  V, which is found to be independent of the scan rate. The bioactivity of the immobilized PQQ-GDH was retained.

Interestingly, the enzyme-free bound PQQ exhibits a more facile electron transfer with GCE than immobilized PQQ-GDH, suggesting that PQQ-bound CHIT-CNT films hold promise as a platform for reconstitution of PQQ-dependent apo-enzymes, and greater potential for applications in biosensors and bio-fuel cells. Evidence of electron transfer between bound

PQQ-GDH and the GCE has been observed when the PQQ-GDH has been coupled with EDC to a CNT-CHIT film. The experimental results suggest that the presence of CNT in the CHIT film promotes the electron transfer of bound PQQ-GDH to the GCE.

A quasi-reversible electrochemical reaction, as revealed by a pair of well-defined redox peaks, is observed by cyclic voltammetry, with PQQ-bound CHIT-CNT-modified GCE (Figure 1.2.3). Additional experimental results suggest that the activity of PQQ-GDH was retained in PQQ-GDH-bound CHIT-CNT/GCE (Figure 1.2.4), which permits its use as a biocatalyst for a mediated bio-fuel cell or amperometric biosensor for glucose detection (Figure 1.2.5). It should be noted that PQQ bound to CHIT-CNT film also exhibited an effective charge transfer with GCE, suggesting that it can be used as a promising platform for reconstitution of various PQQ-dependent apo-enzymes. This work has been published in *Electrochem. Solid State Letters* [10].

The electrochemical approach of mediator immobilization is demonstrated in the work for NADH-dependent alcohol-based biofuel cell applications. Methylene green (MG) and its polymer forms (poly-MG) have been reported as effective mediators for alcohol partial oxidation. It is also known that poly-MG can be immobilized on GCE using cyclic voltammetric deposition. In order to understand its functionality, it is important to characterize the electrochemical deposition process, the modified electrode surface, the stability and property of such electrochemically immobilized poly-MG films.

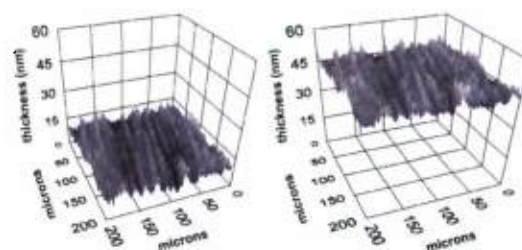


**Figure 1.2.6** Time-resolved ellipsometric observations of poly-methylene green films and their thickness during electrochemical deposition on Pt electrode

Figure 1.2.6 shows that we can evaluate poly-MG film thickness during electrochemical deposition on a Pt electrode using time-resolved imaging ellipsometry. The time-resolved imaging ellipsometry is an *in situ* observation and a unique capability in our laboratory. We can perform real time monitoring of film growth and the film's physico-chemical property on an electrode surface. In this work, we use the imaging ellipsometry and cyclic voltammetric deposition technique to track the thickness of the deposited film with cycle number. This valuable technique may allow us collect new information of the fundamental reaction kinetics and mechanisms underlying the electrochemical deposition of conductive poly-MG films onto electrode surfaces (see Figure 1.2.6). The time resolved observation provides nanometer resolution with film thickness and the imaging results in real time monitoring of the surface morphology and roughness. The work has been published in Ref. [5].

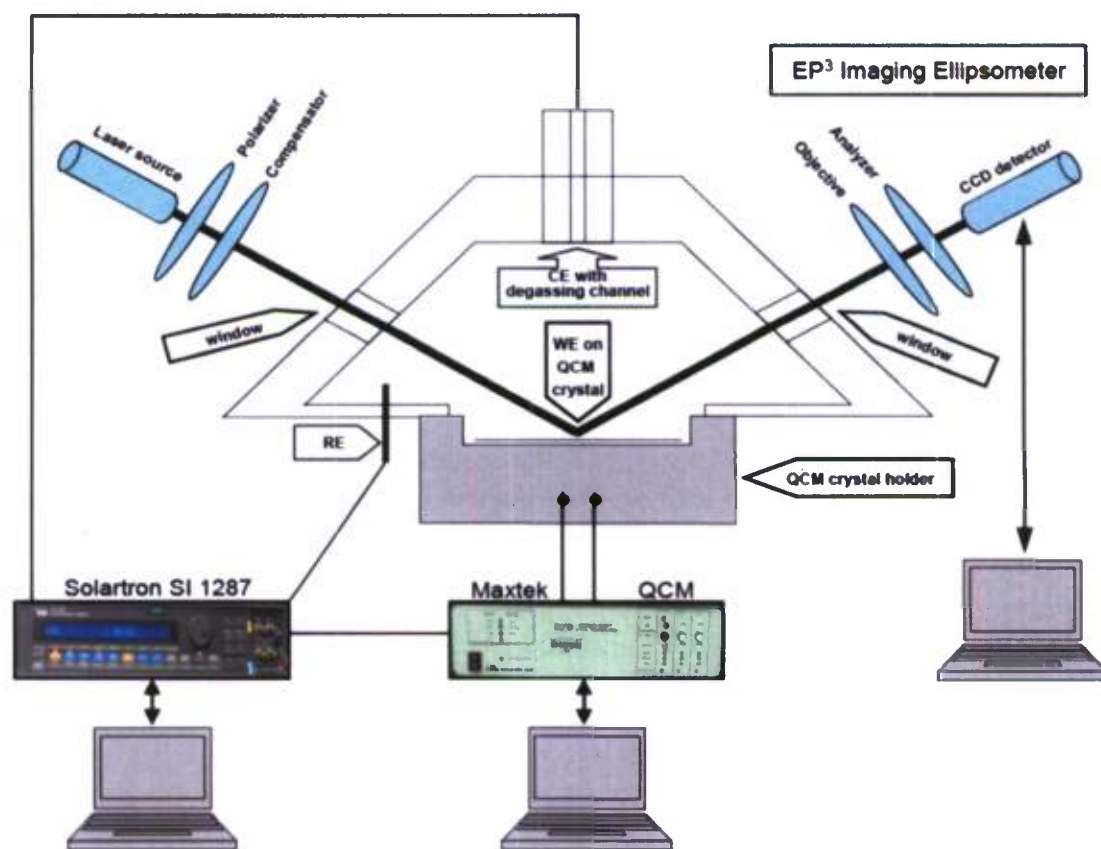


**Figure 1.2.7 A unique combination of spectroscopic imaging ellipsometry (EP<sup>3</sup>) with quartz crystal microbalance (QCM) and electrochemical techniques to perform *in situ* characterization of surface of electrodes**

To understand the kinetics of the deposition process, we further combine the imaging ellipsometry with quartz crystal microbalance (QCM) and cyclic voltammetric techniques to characterize the film deposition (Figure 1.2.7). We are able to control the film deposition with accurate thickness and morphology, at the same time correlate the mass, charge, and the film properties (ellipsometric angles, which can be used to estimate film thickness and identify film



chemical composition changes) in the deposition process (Figure 1.2.8). It helps us understand the stepwise underlying mechanism in the deposition and provide unprecedented details in the film formation process involving redox reactions. We intend to use this technique to study the redox kinetics involved in other mediator oxidation.

During this period, these outcomes were also used to leverage two extramurally funded projects. The first one was a grant from the Intelligence Community Postdoctoral Fellow Research Program to support development of bio-fuel cells for micro-power source applications (B.Y. Liaw, PI). The second was an sub-award from the AFOSR Multi-disciplinary University Research Initiative (MURI) program (M.J. Cooney, PI), awarded to the lead institution, the University of New Mexico (P. Atanassov, PI). Both awards have lent national recognition of this EBFC program.

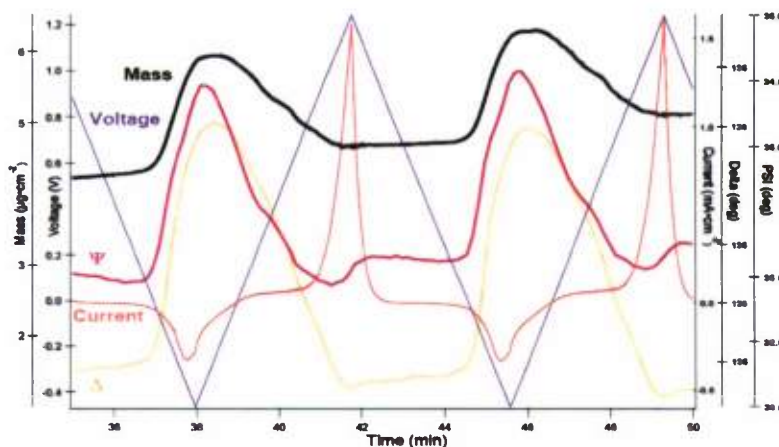


**Figure 1.2.8 Combined imaging ellipsometry with quartz crystal microbalance and electrochemical techniques correlate mass, voltage, current, and optical properties (ellipsometric angles) of the film deposited on the Pt electrode surface**

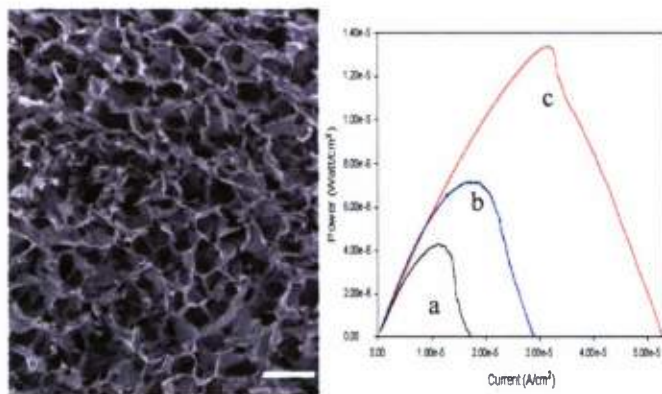


**Figure 1.2.9 SEM image of chitosan scaffold (Left) and power curves from chitosan film (a) and scaffolds (b, c)**

significantly increased for mediator-based systems (Figure 1.2.9). This work has been published in the Journal of Materials Chemistry [11]. We have also fabricated three-dimensional chitosan/CNT scaffolds that provide a basis for enzymes that are capable of direct electron transport. The chitosan essentially acts as a binder of the carbon nanotubes and one is left with scaffold structures similar to that presented in Figure 1.2.9, but with carbon nanotubes lining the surface. These scaffolds are highly conductive and represent a new methodology to create

In collaboration with these partner programs, we have explored chitosan and chitosan-composite scaffolds as a material for the fabrication of macroporous electrodes that can support both mediator-based and direct electron transfer. Work accomplished has included the development of protocols for the fabrication of hydrophobically-modified chitosan scaffolds immobilizing NADH-dependent glucose oxidase, and chitosan/CNT composites for attachment of PQQ-enzymes. With respect to the fabrication of hydrophobically-modified chitosan scaffolds, we have demonstrated proof-of-principle data that shows that the power density can be

multidirectional and multidimensional 3D structures of electrochemically-active carbon nanotube surfaces [12].

We have also developed a liquid-phase prototype Bio-fuel Test Cell (Figure 1.2.10). This prototype, which we term the modular stack cell, was designed as a characterization tool. For example, we sent duplicate models of the modular stack cell to three cooperating laboratories in the U.S. that also specialize in enzyme fuel cell development. Each laboratory (Dr. Shelley Minter at St. Louis University, Dr. Plamen Atanasov at the University of New Mexico, and Dr. Scott Barton at Michigan State University) was given the same protocol to execute (i.e., to develop a poly[methylene green] electrode film that oxidizes NADH), and the electrochemical data from all laboratories were consolidated and statistically analyzed for reproducibility. The results demonstrated that the modular stack cell provides a framework for comparative analysis of systems. The results have been published in the Journal of Electroanalysis [8, 17]. With this confidence, we have fabricated a full ethanol-based bio-fuel cell based on this design (Figure 1.2.11). Although we have achieved full operation (see power curves in Figure 1.2.11) with an air-breathing cathode, this work was not published.



**Figure 1.2.10 The modular stack cell**

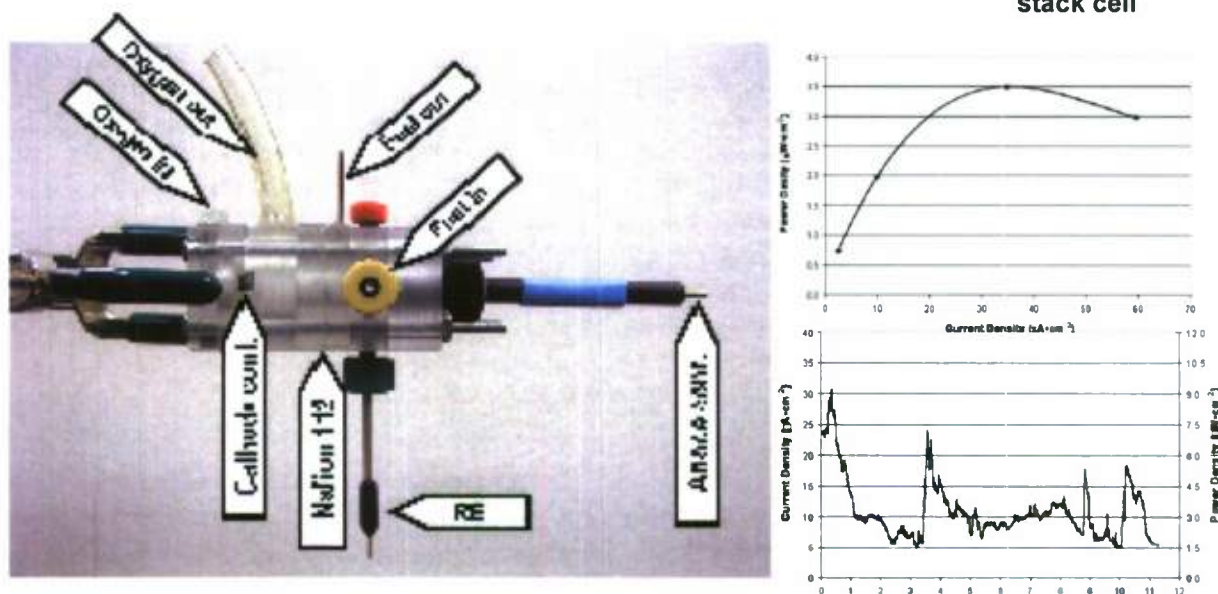


**Figure 1.2.11 Operational biofuel cell, based on modular stack cell design**

Of special interest for an enzymatic power generation from ethanol as biofuel are NAD-dependent dehydrogenases, like alcohol dehydrogenase (ADH) or malate dehydrogenase (MDH), which lie within the Krebs cycle. This fundamental metabolic pathway involves eight enzymes for energy production through aerobic respiration. In order to exploit the entire cycle on a bioanode, and within the context of increased power generation, a polymer system that can immobilize and stabilize all eight enzymes in a three-dimensional matrix is needed. In support



of developing macroporous chitosan and chitosan-derivate scaffolds as advanced materials for fabrication of biofuel cell electrodes, as specified in 1), we have immobilized MDH within modified chitosan-polymer scaffolds placed upon a poly(methylene green) modified glassy carbon electrode. The current and power density for this MDH bioanode have been tested in half cell mode (Figure 1.2.12) and tested in a full biofuel cell. The half cell mode results represented a significant advance in the development of flow-through electrodes and confirmed the application of an enzyme immobilized in a modified chitosan polymer [14]. We have also used fluorescence to track the spatial distribution of enzyme immobilized in the hydrophobically-modified polymer (Figure 1.2.13) [5]. This work, which has been published, clearly demonstrated that the distribution of a fluorescently-tagged enzyme (the pink in Figure 1.2.13) distributes quite differently in various forms of the hydrophobically-modified chitosan polymer (i.e., native, butyl-modified, and ALA-modified).

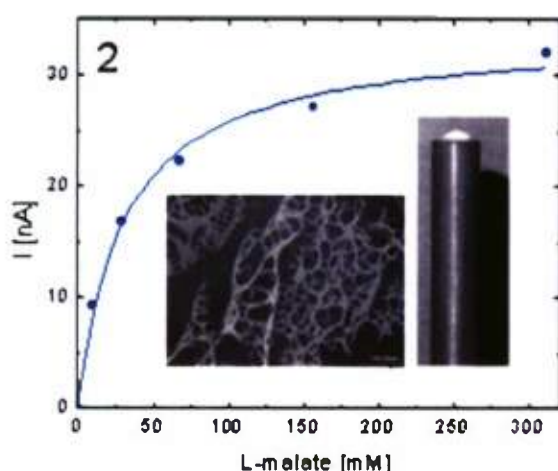


**Figure 1.2.12 Electrical results for MDH bioanode**

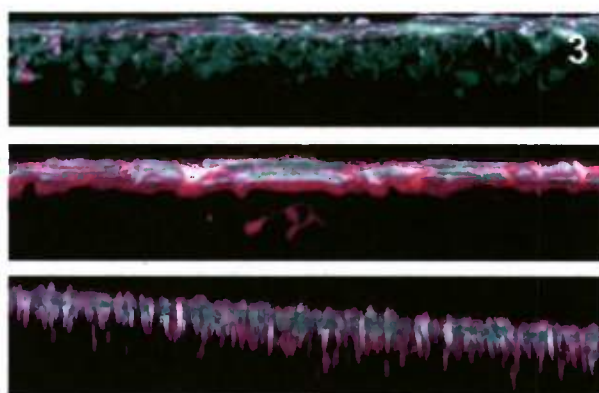


**Figure 1.2.13 Enzyme spatial distribution**

Additional work has been executed wherein polarity sensitive fluorescent probes have been attached to enzyme and immobilized within native and modified chitosan polymer [6]. This work has been designed to quantitatively characterize the chemical microenvironment immediately surrounding the enzyme when in the immobilized state. Specifically, polar sensitive probes were used to correlate the relative hydrophobicity of the chemical microenvironment. The results are shown in Figure 1.2.14 wherein acrylodan labeled cMDH was suspended in the presence of aqueous native and modified chitosan (A), immobilized in native and modified chitosan scaffolds (B), immobilized in native and modified chitosan dehydrated scaffolds (B), and immobilized in native and modified chitosan rehydrated scaffolds (C). Figure 1.2.14 compares emission profiles of acrylodan-tagged enzymes in aqueous solution against those immobilized within the polymers. In Figure 1.2.14(A), the emission peaks of acrylodan-cMDH suspended in aqueous solutions of native and modified chitosan polymer did not vary relative to each other, suggesting that the various polymers (as 0.5 (w/w)% solutions) provided identical chemical microenvironments (in terms of polarity – i.e., neither were relatively more or less hydrophobic). This assumes that the chemical environment surrounding

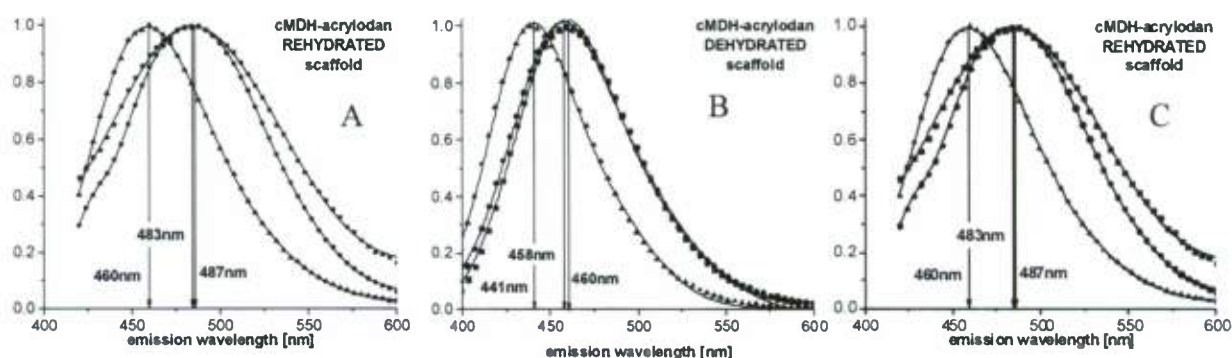


**Figure 1.2.14** In all three (A, B and C) the polymers are represented by the following (■ – CHIT ● – ALA-CHIT ▲ – C4-CHIT). All samples were excited with  $\lambda_{\text{ex}} = 360 \text{ nm}$

the tagged enzyme is dominated by water and not the chitosan polymer. In contrast, when the tagged enzymes were immobilized within the same polymers, the emission maxima not only occurred at lower wavelengths, but they also varied significantly across the three polymers (Figure 1.2.14(B)). This result suggests that when in the immobilized state the various modified polymers provided altered chemical microenvironments, thus corroborating two separate theories: (1) that modified chitosan polymers can provide altered chemical microenvironment, and (2) that the altered chemical microenvironments are most pronounced after the polymer has been precipitated (e.g., through freezing or drying processes) into its final structure. The latter result supports our previous suggestion that the enzymes are not interacting with or being affected by the amphiphilic regions of the polymer, until the freezing or precipitating process. The overall blue shift observed in the dried polymer can be partially attributed to their dehydration during the freeze-drying process. The removal of water molecules surrounding the immobilized enzyme will obviously lead to a reduction in polarity. By contrast, re-hydration should reintroduce water molecules into the chemical environment and thereby increase the relative polarity. To verify this, the scaffold films were rehydrated in identical buffer solution. Although the rehydrated films showed a trend for relatively more polar chemical microenvironments, the same trends in blue shift was observed across all forms of the polymer (Figure 1.2.14(C)). This confirms that the chitosan polymer does impact the chemical microenvironment of the enzyme when in the immobilized state.

For the purposes of correlation, malate dehydrogenase was immobilized within the three target polymers: native chitosan, butyl-modified and alpha linoleic acid a poly(methylene green) coated glassy carbon electrode. The electrocatalytic activity of each polymer was then measured in half cell mode using amperometry. The amperometric current of NADH oxidation on poly(methylene green) was measured at an applied potential of +300 mV. The catalytic oxidation of NADH occurs in the chosen potential range (selected to be higher than the half-wave potential to maximize electrocatalytic reaction). Electrochemical currents, measured at the same potentials, can be used as apparent catalytic activity.

The results, normalized to 1.0, are shown in Figure 1.2.15. Normalizing the activity to the highest output, the butyl-modified chitosan gave a 10-fold increase in current density and the ALA-modified a 4-fold increase when compared against the unmodified native chitosan. This suggests that the activity of the immobilized enzyme follows the measurement of the chemical microenvironment in terms of polarity.

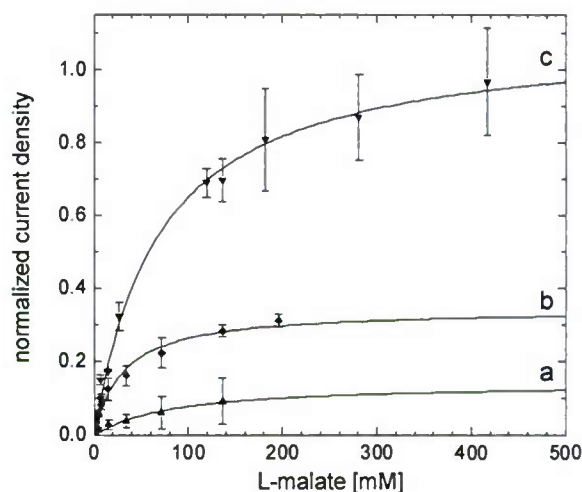


**Figure 1.2.15 Electrochemical activity as normalized current density of immobilized MDH in different chitosan polymers. (c): C4-Chitosan film; (b): Chitosan film; (a): ALA-Chitosan film**

In most recent work we were able to use fluorescent tags to individual enzymes to verify the presence of enzyme aggregation in the immobilized state [6]. Specifically, we combined three techniques; (1) light scattering, (2) Förster Resonance Energy Transfer (FRET), and (3) traditional native PAGE gels to measure the aggregation of a single enzyme in solution and immobilized within three-dimensional chitosan scaffolds (Figure 1.2.16). The analysis has been applied to a range of chitosan polymers (of varying amphiphilicity) previously used to correlate enzyme activity to the relative polarity of the chemical microenvironment [18]. Based on the FRET analysis, the average distance between proteins in aqueous solutions (chitosan:  $r = 51.3 \pm 0.9 \text{ nm}$ ; C4-chitosan:  $r = 53.3 \pm 0.2 \text{ nm}$ ) correlate to the aggregation state of a monomer/dimer mix. When the protein is immobilized within a chitosan scaffold, a decrease in the average separation ( $r = 45.9 \pm 0.1 \text{ nm}$ ) suggests an increase in the aggregation due to immobilization. Further, the hydrophobic modification of the polymer results in a further decrease in protein separation ( $r = 41.8 \pm 0.3 \text{ nm}$ ). This indicates that the immobilization process is inducing aggregation and may be a method for producing enzyme complexes that mimic metabolic pathways.



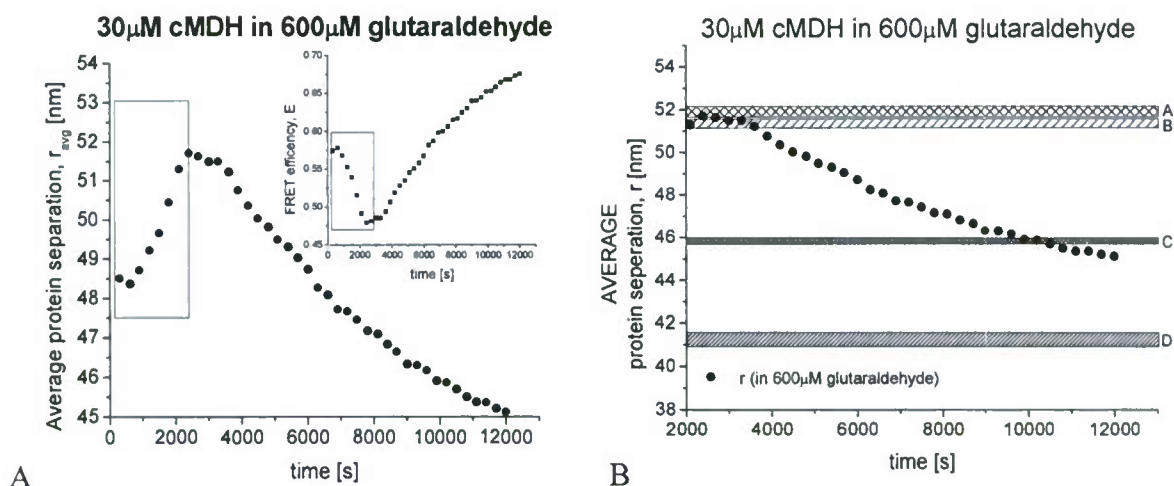


**Figure 1.2.16** (A) Calculated radial separation from the emission scans in pt A (calculations detailed in text) [inset] = FRET efficiency calculated from scans in pt A. (note: the data highlighted in the boxes represents the initial dispersal of the protein within the buffer); (B) Calculated radial separation as a function of time over the span of 3.5 hrs in 5 min increments (not all data shown) for a solution of 50% *Alexa*<sup>®</sup>555 tagged cMDH (30 M) and 50% *Alexa*<sup>®</sup>647 tagged cMDH (30 M) in a 600 M glutaraldehyde, 50 mM TRIS buffer (pH7.4) solution. The solid bars represent the average radial separation in A – aqueous chitosan, B – aqueous C4 – chitosan, C – freeze dried chitosan scaffolds, and D – freeze dried C4 – chitosan scaffolds.

The poly(methylene green) mediator has been considered one of the best mediators for a  $\text{NAD}^+$ -dependent biocatalytic process and thus of great interest to the enzymatic bio-fuel cell operation. However, the interfacial property of this mediator polymer film on biocatalytic electrodes is not well understood to date. We have used electrochemical microgravimetric imaging ellipsometry (EmIE) to study the interfacial property of this mediator compound on Pt or glassy carbon electrode surfaces. The EmIE technique allows us to correlate changes of mass, charge, and ellipsometric angle measurements in a synchronized manner to derive information on chemical and electrochemical behavior of this polymer mediator film (Figure 1.2.7). This technique can be applied to both steady state and transient dynamic regimes.

As a result of such studies, we have produced some interesting results based on the EmIE approach in the study of poly(methylene green) mediator [7, 19]. Highlights are as follows:

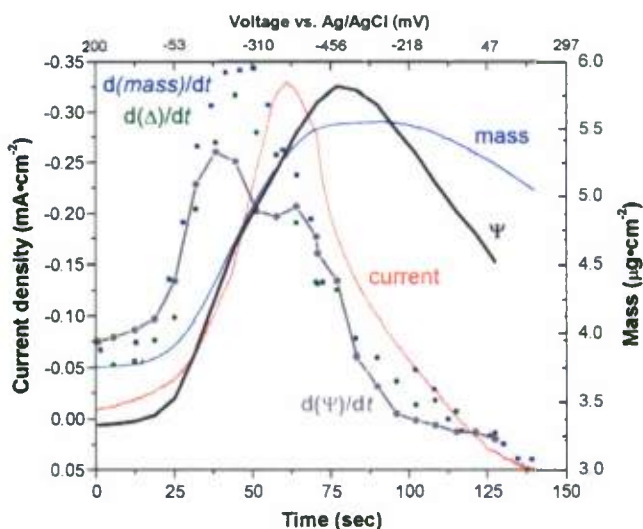


**Figure 1.2.17** Current and mass variations



Figure 1.2.17 shows that the transient change of mass and current do not coincide in the synchronized measurements. However, the ellipsometric measurements show that the ellipsometric angle  $\Delta$  is in sync with transient mass changes at all times, indicating that the mass change is actually detectable and the corresponding change in such a surface film thickness is also measurable by the ellipsometric method. The electrochemical redox reaction, on the other hand, occurs at a different time scale and the corresponding current change is also in sync with the ellipsometric angle change in  $\Psi$ , which has a split peak: one corresponds to the mass (thus film thickness) change and the other to the chemical change in the redox process. It is therefore interesting to observe this transient behavior of the film development, where the mass change is related to adsorption, while the redox reaction does not have a direct correlation with mass measured [19].

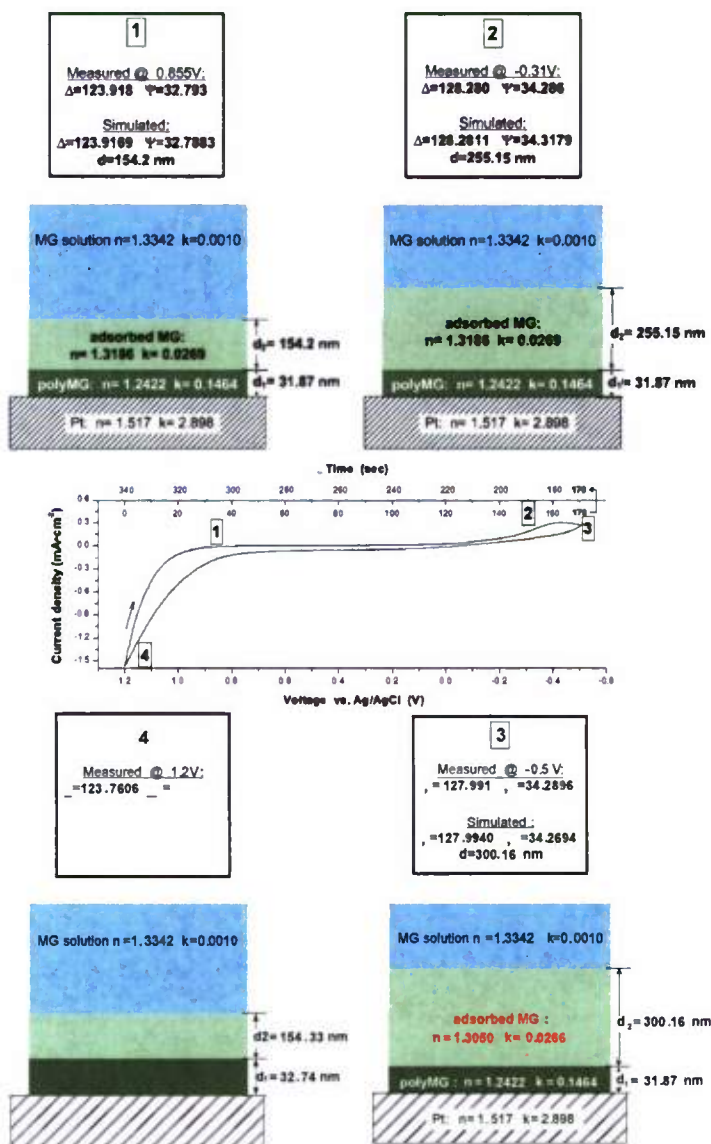


Figure 1.2.18 Simulation of film thickness changes with deposition conditions

We also showed that with proper estimates of the parameters in the optical model, we can simulate the film thickness changes with deposition conditions (Figure 1.2.18). This is a powerful tool to allow real-time *in situ* observation with quantitative characterization [20].

In the effort to continue to develop PQQ-dependent enzymatic systems for bio-anode application<sup>1</sup>; we found the reconstitution of the PQQ-dependent enzymes such as glucose dehydrogenase (GDH) on glassy carbon electrodes with chitosan-carbon nanotube matrix have not been effective in making electronic conduction to promote the enzymatic electrocatalytic kinetics [13]. The turnover rate for the reconstituted GDH electrodes has been low. We are searching for other mediators that can provide better relay units for charge transfer.

In the effort to develop *in situ* interfacial characterization techniques to assess the practicality of using self-assembled monolayers (SAMs) for enzyme immobilization, we have found that the surface conditions of the glassy carbon or gold electrode are very sensitive to contamination and thus the SAM formation is not reproducible and difficult to control (Svoboda and Liaw, unpublished results). In short, both the mediator-cofactor reconstitution and SAM-based immobilization approaches have produced limited success in improving enzymatic electrocatalysis processes. We consider these techniques to possess limited potential for significant improvement of bio-fuel cell performance at the present time.

*Summary of additional work accomplished during this period.* Work towards the development and characterization of chitosan co-block polymers that immobilize multiple enzymes that can more fully oxidize complex energy fuels begins with the development of a technique to lay down and characterize micron thin films. This work is in its initial stages and now under the direction of a graduate student. To date, a thin-film fabrication technique has been developed. Specifically, the thin-film scaffolds were prepared using a modified technique based on the procedure outlined elsewhere [5]. The system application is shown in Figure 1.2.19.

---

<sup>1</sup> These enzymes can be bound to either chitosan-CNT or conductive polymers, such as polypyrrole, as novel immobilization approaches that can realize direct electron transfer.

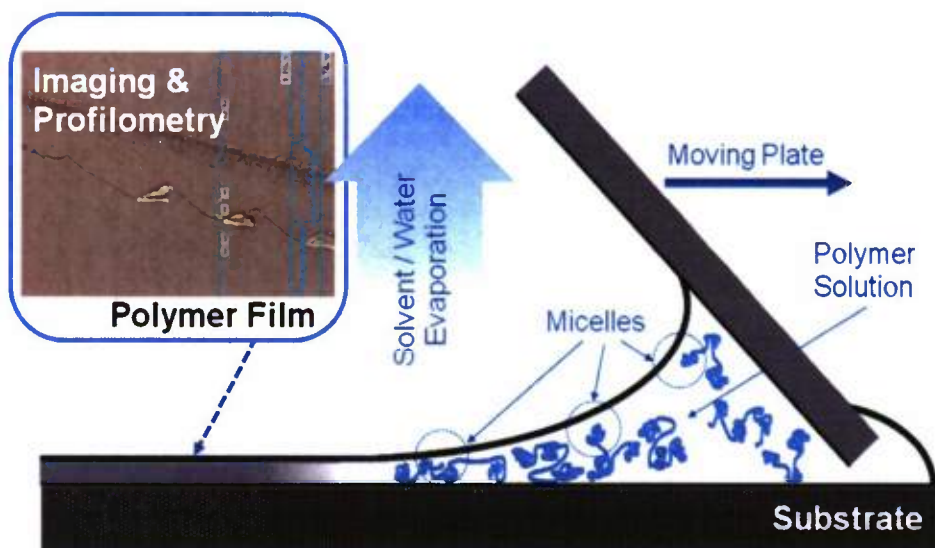


**Figure 1.2.19** Schematic of film deposition with inlayed microscope image from thickness measurement of air-dried film (top left). Deacetylated or butyl-modified chitosan solutions were pipetted on the obtuse side of the intersection of the two glass slides held at an angle of  $30 \pm 1^\circ$ . A meniscus forms under the leading slide as it pushes against the solution droplet and across the lower glass substrate at a constant velocity, leaving a thin layer of solution behind. Films formed as the solution was air-dried.

This work characterizes the method of spread coating to form polymeric films with controlled thickness. The thickness of spread-coated films made from both deacetylated and butyl-modified chitosan was correlated to deposition rate and solution micellar structure, and demonstrated how differences in the underlying micellar structure can, to a certain degree, impact the final film thickness. At intermediate deposition rates, the thickness of chitosan films was predictable and well controlled. Furthermore, it was shown that hydrophobic modification of the chitosan extended the range of deposition rates (from 5-16 cm/hr to 6-30 cm/hr) that allowed for which a linear relationship between film thickness and deposition rate were found. Hydrophobic modification also extended the range of thickness achieved from 0.06-0.10  $\mu\text{m}$  to 0.04-0.14  $\mu\text{m}$ . These features are accredited to the domination of intramolecular forces at lower concentrations of hydrophobically modified chitosan solutions as opposed to equal concentration of the deacetylated chitosan solutions, as supported by the viscosity and fluorescence experiments. Although both deacetylated and butyl-modified chitosan solutions were found to have inter- and intramolecular interactions and hydrophobic domains able to incorporate a fluorophore, deacetylated chitosan is much more interconnected via intermolecular interactions at higher concentrations. This work has been submitted to *Langmuir* and is currently under review.

In the effort of continuing to apply *in situ* characterization techniques based on spectroscopic imaging ellipsometry with microgravimetric and electrochemical techniques to study the enzyme-electrode interaction on the electrode surface and the associated dynamic behavior, aiming to understanding the charge transfer process with direct measurements and correlations, We have improved the capability for such characterization. We have upgraded our imaging ellipsometry to a spectroscopic model with a high intensity Xenon arc lamp as white light source,



which can provide a wavelength range from 360 nm to 1,000 nm with a monochromator that consists of 46 interference filters to provide  $\pm 6$  nm of bandwidth resolution. The spectroscopic model will provide us additional control on the wavelength control for the incident light besides incident angle for more information gathering on the surface and film properties. We are currently using this capability to study the poly(methylene green) mediator properties (Chiu and Liaw). We anticipate receiving more quantitative results on the film characterization.

In addition to these efforts outlined above, through the IC Postdoctoral Fellow Research Program, we have investigated other alternative approaches to harnessing chemical energy in bio-fuels for fuel cell operation [21]. One such investigation has led us to achieve a sustainable current generation with ammonia oxidation, with assistance from conductive polymers such as polypyrrole [21]. Figure 1.2.20 shows the current production as a function of ammonia concentration in the presence of polypyrrole and hydrogen peroxide at different concentrations in the solution. Without ammonia, the current production was not obvious, even with the presence of peroxide. Therefore, it is a clear indication that the current was produced by the oxidation of ammonia, which was promoted by peroxide in the interaction with polypyrrole.

In a separate study of glucose oxidation, we also discovered a unique pathway to promote charge transfer of partial oxidation of glucose to produce current with the help of mediators such as methyl viologen [15]. In this study, high current density and power density were observed with glucose oxidation in alkaline solutions with the presence of a mediator.

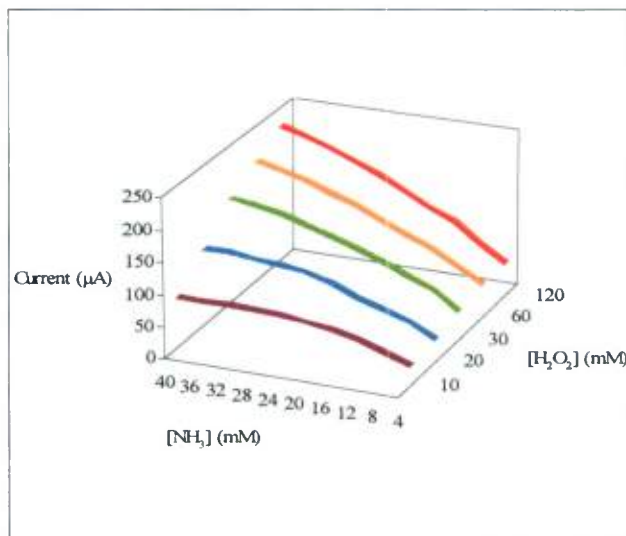


**Figure 1.2.20** The current produced from different concentrations of ammonia based on different concentrations of  $\text{H}_2\text{O}_2$

### 1.2.2.3 References

1. Johnston, W., M.J. Cooney, B.Y. Liaw, R. Sapra, and M.W.W. Adams, Design and characterization of redox enzyme electrodes: new perspectives on established techniques with application to an extremophilic hydrogenase. *Enzyme and Microbial Technology*, 36, 540 - 549 (2005).
2. Johnston, W., N. Maynard, B. Liaw, and M.J. Cooney, *In situ* measurement of activity and mass transfer effects in enzyme immobilized electrodes. *Enzyme and Microbial Technology*, 39, 131 - 140 (2006).
3. Konash, S., M.J. Cooney, B.Y. Liaw, and D. Jameson, Characterization of Polymer-Enzyme Interactions using Fluorescence. *Journal of Materials Chemistry*, DOI: 10.1039/b611686h. (2006).

4. Martin, G., M.J. Cooney, S.D. Minter, J.A. Ross, and D.A. Jameson, Fluorescence characterization of polymer chemical microenvironments in hydrophobically modified chitosan. *Carbohydrate Polymers*, 77, 695 - 702 (2009).
5. Martin, G., S.D. Minter, and M.J. Cooney, Spatial distribution of malate dehydrogenase in chitosan scaffolds. *Applied Materials & Interfaces*, 1(2), 367-372 (2009).
6. Martin, G.L., S.D. Minter, and M.J. Cooney, Fluorescence characterization of chemical microenvironments in immobilization matrices: Polarity. *Applied Materials and Interfaces*, Submitted (2010).
7. Svoboda, V., M.J. Cooney, C. Rippolz, and B.Y. Liaw, In-Situ Characterization of Electrochemically Polymerized Methylene Green Films on Platinum and Glassy Carbon Electrodes. *Journal of the Electrochemical Society*, 154(3), D113 - D116 (2006).
8. Svoboda, V., M.J. Cooney, B.Y. Liaw, S.D. Minter, E. Piles, D. Lehnert, S.C. Barton, R. Rincon, and P. Atanassov, Standardized characterization of electrocatalytic electrodes. *Electroanalysis*, In Press. (2008).
9. Svoboda, V., M.J. Cooney, C. Rippolz, and B.Y. Liaw, *In situ* Characterization of an Enzyme Catalyzed Bio-Fuel Cell. In Preparation (2007).
10. Cooney, M.J., J. Peterman, C. Lau, and S.D. Minter, Fabrication and Characterization of hydrophobically modified Chitosan Scaffolds. *Carbohydrate Polymers*, 75(3), 428-435 (2008).
11. Cooney, M.J., M. Windmeisser, B.Y. Liaw, C. Lau, T. Klotzbach, and S.D. Minter, Design of chitosan gel pore structure: Towards enzyme catalyzed flow-through electrodes. *Journal of Materials Chemistry*, 18, 667 - 674 (2007).
12. Lau, C., M.J. Cooney, and P. Atanassov, Conductive macroporous composite chitosan-carbon nanotube scaffolds. *Langmuir*, 24, 7004 - 7010 (2008).
13. Sun, D., D. Scott, M.J. Cooney, and B.Y. Liaw, A promising reconstitution platform of PQQ-glucose dehydrogenase in chitosan - carbon nanotube matrices. *Electrochemical Solid State Letters*, 11(6), B101-B104 (2007).
14. Lau, C., S.D. Minter, and M.J. Cooney, Development of a chitosan scaffold electrode. *Electroanalysis*, In Press (2009).
15. Scott, D. and B.Y. Liaw, Harnessing electric power from monosaccharides — A carbohydrate-air alkaline fuel cell mediated by redox dyes. *Energy and Environmental Science*, 2, 965-969 (2009).
16. Cooney, M.J. and B.Y. Liaw, *In Situ Characterization Techniques for Design and Evaluation of Micro and Nano Enzyme-Catalyzed Power Sources*, in *Nano-Scale Sciences & Technology in Biomolecular Catalysis*, P.S. Wang and J.B. Kim, Editors. 2007, American Chemical Society.
17. Svoboda, V., M.J. Cooney, B.Y. Liaw, S. Minter, E. Piles, D. Lehnert, B.S. C., R. Rincon, and P. Atanassov, Towards standardized characterizations of enzyme bioelectrocatalysis *Journal of Electroanalysis*, To be submitted (2007).
18. Martin, G., S. Minter, and M.J. Cooney, Fluorescence characterization of immobilization induced enzyme aggregation. *Chemical Communications (Cambridge, United Kingdom)*, In Press (2011).

19. Svoboda, V. and B.Y. Liaw, In-situ transient study of polymer nano-film growth via simultaneous correlation of charge, mass, and ellipsometric measurements. *Pure and Applied Chemistry*, 80 2439-2449 (2009).
20. Liaw, B.Y., *In situ characterizations of porous media for applications in biofuel cells: Issues and challenges*, in *Porous Media: Applications in Biological Systems and Biotechnology*, Z. Vafai, Editor. 2010, CRC Press, Taylor and Francis Co: Boca Raton, FL.
21. Scott, D., M.J. Cooney, and B.Y. Liaw, Sustainable current generation from the ammonia-polypyrrole interaction. *Journal of Materials Chemistry*, 27, 3216-3222 (2009).

#### 1.2.2.4 Papers and Presentations Resulting from Efforts (since 2005)

##### Papers

- 2010 Lau, C., Minteer, S. D., and M. J., Cooney<sup>✉</sup>. *Development of a chitosan scaffold electrode*. *Electroanalysis*. 22(7-8):793-798.
- 2010 Martin, G. L., Minteer, S. D., and M. J. Cooney<sup>✉</sup>. *Fluorescence characterization of chemical microenvironments in immobilization matrices: Polarity*. *The Analyst*. 135 (5):1131-1137.
- 2010 Cooney<sup>✉</sup>, M. J. *Kinetic Measurements for Enzyme Immobilization*. In (S. Minteer, Editor) *Enzyme Stabilization: Methods and Protocols*. Humana Press. 679:Chapter 17.
- 2009 Scott D. and B.Y. Liaw<sup>✉</sup>. *Harnessing electric power from monosaccharides — A carbohydrate-air alkaline fuel cell mediated by redox dyes*. *Energy Environ. Sci.* 2:965–969.
- 2009 Martin, G. L., Ross, J. A., Minteer, S. D., Jameson<sup>✉</sup>, D. M., and M. J. Cooney<sup>✉</sup>. *Fluorescence characterization of polymer chemical microenvironments*. *Carbohydrate Polymers*. doi:10.1016/j.carbpol.2009.02.021.
- 2009 Martin, G., Minteer, S. D., and M. J. Cooney<sup>✉</sup>. *Spatial distribution of malate dehydrogenase in chitosan scaffolds*. *Applied Materials & Interfaces*. 1(2):367–372
- 2009 Cooney<sup>✉</sup>, M. J., Petermann, J., Lau, C., and S. D. Minteer<sup>✉</sup>. *Fabrication and Characterization of Hydrophobically Modified Chitosan Scaffolds*. *Carbohydrate Polymers*, 75(3):428-435.
- 2009 V. Svoboda and B.Y. Liaw<sup>✉</sup>, “In-situ transient study of polymer nano-film growth via simultaneous correlation of charge, mass, and ellipsometric measurements” *Pure Applied Chem.*, 80 (2008) 2439–2449
- 2008 Cooney, M. J., Lau, C., Martin, G., Svoboda, V., and S. D. Minteer<sup>✉</sup>, *Biofuel Cells*. *Energy and Environmental Science*. *Energy & Environmental Science*, 1:320 - 337.
- 2008 Lau, C., Cooney<sup>✉</sup>, M. J., and P. Atanassov. *Conductive macroporous composite chitosan-carbon nanotube scaffolds*. *Langmuir*. 24, 7004-7010.
- 2008 Scott, D., Cooney, M. J., Liaw<sup>✉</sup>, B. Y. *Sustainable current generation from the ammonia-polypyrrole interaction*. *Journal of Materials Chemistry*. (27),3216-3222.



- 2008 Sun, D., Cooney, M. J., and B. Y. Liaw<sup>✉</sup>. *PQQ-glucose dehydrogenase immobilized in chitosan / carbon nanotubes composite films*. *Electrochemical Solid State Letters*. 11(6) B101-B104.
- 2008 Svoboda, V., Cooney<sup>✉</sup>, M. J., Liaw, B. Y., Minteer, S., Piles, E., , Lehnert, D. Barton, S. C., Dmitri Ivnitiski, D., and P. Atanassov. *Standardization of a common platform for bioelectrocatalysis characterizations*. *Electroanalysis*, 20(10):1099 – 1109.
- 2008 Cooney<sup>✉</sup>, M. J., Windmesier, M, Lau, C., Liaw, B. Y., Klotzbach, T. and S. Minteer<sup>✉</sup>. *Design of Chitosan Gel Pore Structure: Towards Enzyme Catalyzed Flow-Through Electrodes*. *Journal of Materials Chemistry*. 18, 667 – 674.
- 2008 Cooney<sup>✉</sup>, M.J., and B. Y. Liaw<sup>✉</sup>. *In situ characterization techniques for design and evaluation of micro and nano enzyme-catalyzed power sources*. In ( P.S Wang and J. B. Kim Editors) *Biomolecular Catalysis: Nanoscale Science and Technology*. ACS Symposium Series 986, Oxford University Press.
- 2007 Atanassov, P., Apblett, C., Banta, S., Brozik, S., Barton, S. C., Cooney, M. J., Liaw, B. Y., Mukerjee, S. and S. Minteer. *Enzymatic Biofuel Cells*. *The Electrochemical Society Interface*.
- 2007 Svoboda, V., Rippolz, C., Cooney<sup>✉</sup>, M. J., and Bor Yann Liaw<sup>✉</sup> *Characterization of electrochemically polymerized methylene green films on platinum and vitreous carbon supports*. *The Journal of Electrochemical Society*. 154(3): D113 – D116.
- 2006 Konash, A., Cooney<sup>✉</sup>, M. J., Liaw<sup>✉</sup>, B. Y., Bor Yann Liaw, and D. M. Jameson. *Characterization of enzyme-polymer interactions using fluorescence*. *Journal of Materials Chemistry*, (42), 4107-4109.
- 2006 Johnston, W. J, Cooney<sup>✉</sup>, M. J., and B. Y. Liaw<sup>✉</sup>. *In situ measurement of effective diffusion coefficients in enzyme immobilized electrodes*. *Enzyme and Microbial Technology*. 39:131 – 140.
- 2005 Johnston, W. J., Liaw, B. Y., Sapra, R., Adams, M. W. W., and M. J. Cooney<sup>✉</sup>. *Design and characterization of redox enzyme electrodes: new perspectives on established techniques with application to an extremeophilic hydrogenase*. *Journal of Enzyme and Microbial Technology*. 36(4): 540 – 549.

## Presentations

- 2010 Higgins, S., Minteer, S. D., and M. J. Cooney. *Characterization of flow-through microbial fuel cells*. 240<sup>th</sup> American Chemical Society, August 22-26, Boston, MA.
- 2010 Cooney, M. J. *Modification and Characterization of Chemical Microenvironments for Enzyme Immobilization*. 240<sup>th</sup> American Chemical Society, August 22-26, Boston, MA.
- 2010 S. Higgins, M. Cooney, S. Minteer, P. Atanassov, C. Lau, A. Cheung, O. Bretschger and K. Nealson. *Characterization of Flow-Through Microbial Fuel Cells*. 217th ECS Meeting in Vancouver, BC, Canada.
- 2010 G. Martin, S. Minteer and M. Cooney. *Fluorescence Characterization of Enzyme Aggregation in the Immobilized State*. 217th ECS Meeting in Vancouver, BC, Canada.
- 2010 G. Martin, C. Lau, S. Minteer and M. Cooney. *Fluorescence Characterization of Immobilized Enzymes*. 217th ECS Meeting in Vancouver, BC, Canada.

- 2009 Martin, G. L., Minter, S. D., and M. J. Cooney. *Fluorescence characterization of chemical microenvironments in hydrophobically modified chitosan*. 238<sup>th</sup> ACS National Meeting, Washington, DC, August 16-20.
- 2009 Lau, C., Minter, S. D., and M. J. Cooney. *Three dimensional chitosan scaffolds for increased power generation in biofuel cells*. 215<sup>th</sup> ECS Meeting, May 24-29, San Francisco CA.
- 2008 Lau, C., Minter, S. D., and M. J. Cooney. *Three dimensional chitosan scaffolds for biofuel cell application*. 214<sup>th</sup> ECS Meeting, October 12-17, Honolulu HI.
- 2008 Martin, G. L., Ross, J. A., Jameson, D. M., and M. J. Cooney. Fluorescence characterization of chitosan-fluorophore/enzyme interactions. 7th International Weber Symposium, June 6-12, Kauai, Hawaii.
- 2008 Lau, C., Cooney, M.J., Atannassov, P. *Three dimensional chitosan carbon nanotube composite material for biofuel cell application*. 213<sup>th</sup> ECS meeting, May 18-23, Phoenix Arizona.
- 2008 Cooney, M. J. *Microporous chitosan scaffolds as a material for fabrication of enzyme catalyzed flow through electrodes*. 213<sup>th</sup> ECS meeting, May 18-23, Phoenix Arizona.
- 2008 Svoboda, V., Liaw, B. Y., Cooney, M.J., Minter, S., Atannassov, P. *Structure and Morphology of Electrochemically Grown Poly-Methylene Green Films*. 213<sup>th</sup> ECS meeting, May 18-23, Phoenix Arizona.
- 2007 Minter, S. D., Klotzbach, T, Cooney, M. J., and Liaw, B.Y. *Nanopore Engineering of Chitosan Polymer for Enzyme Immobilization and Stabilization*. November 4 -9, Salt Lake City, Utah.
- 2007 Cooney, M. J., Liaw, B.Y., Lau, C., and S. D. Minter. *Application of Mesopore Engineered Chitosan Polymer for Fabrication of Multi-Dimensional and Multi-Directional Enzyme Catalyzed Electrodes*. November 4 -9, Salt Lake City, Utah.
- 2007 Scott, D. Liaw, B.Y., and Cooney, M.J. Improved Current Sustainability from the Ammonia, PPy Interaction with H<sub>2</sub>O<sub>2</sub> - One Step Closer to a Urine Fuel Cell. The 212th ECS Meeting, October 7-12.
- 2007 Liaw, B.Y., Cooney, M.J., Svoboda, V., Konash, A., Jameson, D.M. *In situ characterization of polymer matrices for bio-electrode applications*. 17th International Symposium on Fine Chemistry and Functional Polymers (FCFP-XVII) & 3rd IUPAC International Symposium on Novel materials and their Synthesis (NMS-III), Shanghai, China, October 18th-20th.
- 2007 Svoboda, V., Liaw, B.Y., and Cooney, M.J. *In-situ transient characterization of electrochemical polymerization of methylene green with analysis of stepwise reaction mechanism*. 211<sup>th</sup> ECS Meeting, Chicago, Illinois. May 6-11<sup>th</sup>.
- 2007 Liaw, B. Y, Svoboda, V., Cooney, M. J., and Minter, S. *Fabrication of an effective biocatalytic electrode with in situ characterization of electrode and its materials*. 211<sup>th</sup> ECS Meeting, Chicago, Illinois. May 6-11<sup>th</sup>.
- 2007 Cooney, M. J., Windmeisser, M., Liaw, B.Y., and Minter, S. *Design of chitosan gel pore structure: towards enzyme catalyzed electrodes*. 211<sup>th</sup> ECS Meeting, Chicago, Illinois. May 6-11<sup>th</sup>.

- 2006 Konash, A., Cooney, M.J., Liaw, B.Y, and Jameson, D. *Enzyme-polymer interaction study using fluorescence probes*. Symposium on Nano-scale Science and Technology in Biomolecular Catalysis. 232<sup>nd</sup> ACS National Meeting, San Francisco CA, Sept 10 – 14.
- 2006 Svoboda, V., Cooney, M.J., Rippolz, C., and Liaw, B.Y. *Development of an Enzymatic Ethanol Bio-Fuel Cell for Micro-Power Generation*. Fuel Cell Seminar, Honolulu HI, November 13 – 17.
- 2006 Cooney, M.J., Svoboda, V., Rippolz, C., and Liaw, B.Y. *Design considerations and characterization of enzymatic ethanol fuel cells*. 209th ECS Meeting, May 7-12, Denver, CO.
- 2006 Svoboda, V., Cooney, M.J., Rippolz, C. and Liaw, B.Y. *Design Consideration and In-situ Characterization of Bio-Anode for Enzymatic Ethanol Fuel Cell Application*. IBA –HBC 2006, Waikoloa, Hawaii, 9-12 January.
- 2006 Cooney, M.J., Svoboda, V., Rippolz, C., and Liaw, B.Y. *Design considerations and characterization of enzymatic ethanol fuel cells*. 209th ECS Meeting, May 7-12, Denver, CO.
- 2005 Liaw, B.Y., Quinlan, F., Cooney, M.J. *Polypyrrole Deposition in Aqueous Solutions: Film Characteristic Dependence on Deposition Conditions*. 208th Meeting of the Electrochemical Society. Los Angeles, California. Oct. 16-21, 2005.
- 2005 Liaw, B.Y., Svoboda, V., Cooney, M.J. *Morphological Study of Conducting Polymer via Electrochemical Deposition Using Imaging Ellipsometry and RQCM Technique*. 208th Meeting of the Electrochemical Society. Los Angeles, California. Oct. 16-21.
- 2005 Cooney, M.J., Johnston, W. and Liaw, B.Y. *Modeling the relative contribution of mass transfer limitation on performance in enzyme fuel cells*. 207th Meeting of the Electrochemical Society, Quebec City, Canada. May 15 - May 20.
- 2005 Quinlan, F., Cooney, M.J. and Liaw, B.Y. *Investigation of polypyrrole morphology with different deposition conditions*. 207th Meeting of the Electrochemical Society, Quebec City, Canada. May 15 - May 20.
- 2005 Liaw, B.Y., Cooney, M.J., Quinlan, F., Svoboda, V. and Maynard, N. *Engineering Effective Bioelectrocatalysis Electrodes for Power Generation*. Second International Conference on Polymer Batteries and Fuel Cells (Fuel Cells). Las Vegas, Nevada from June 12 - June 17.
- 2003 Johnston, W.A., Cooney, M.J., and Liaw, B.Y. *Evaluating adsorption and charge transfer of redox enzymes bound to carbon support*. The 204<sup>th</sup> Meeting of the Electrochemical Society, Inc. July, Orlando, Florida.



## **2. Technology for Synthetic Fuels Production**

This section addresses various features involved with the production of synthetic fuels and certain related biocontamination and biofuels corrosion issues. The following subsections address each of these features.

### **2.1 Biofuel Characterization Planning**

As the Navy moves toward greater use of alternative fuels blended with petroleum F-76 diesel and JP-5 jet fuel, there is imminent need to understand how these blends will compare with conventional petroleum products. Two general areas of comparison are of interest, (1) the combustion characteristics, and (2) the broader area termed “fit-for-purpose.” This latter group includes compatibility with materials commonly found in fuel tanks and piping, compatibility with elastomer seals (o-rings) used in engines and fuel delivery equipment, and susceptibility of the fuel blends to maintain levels of microbial and corrosion activity comparable to, or lower than, petroleum fuels in current use.

#### **2.1.1 Scope of Work and Approach**

Under this subtask HNEI will seek to identify a range of biofuel components that could support Navy operations in tropical island settings, including primary sources of potential supply for identified biofuel components, critical material quality monitoring points along the supply chain, appropriate tests for each of these critical monitoring points, and equipment, personnel, and lab facilities and associated costs that would be required to conduct testing.

#### **2.1.2 Technical Accomplishments**

Figure 2.1.1 shows possible pathways to biofuels in tropical island settings. The list of potential feedstock sources on the right is not complete but serves to demonstrate the variety of available materials. Sugars, starch, oils, and fiber are the four intermediate products that can be most readily converted to produce alternative drop-in replacements for F-76 and JP-5. Sugar, starch, and oil production will require dedicated efforts if they are to support biofuel production, whereas fiber resources may be residue byproducts streams from primarily agricultural activities. Each intermediate product has at least one conversion and upgrading pathway option to produce drop in replacements for F-76 and JP-5.

Not shown on Figure 2.1.1, but an equally important source of fiber, is the biogenic fraction of municipal solid waste (MSW). MSW amounts and availability are related to population, levels of economic activity, and current management practices. Previously installed waste-to-energy facilities can compete with new efforts to utilize this resource for biofuels. Siting landfills in tropical island settings is commonly a difficult political issue. Diverting material from landfills to productive uses such as biofuel production would be, in-general, more acceptable since it creates economic activity and can aid in managing an otherwise negative-revenue material. Siting industrial-scale MSW sorting and conversion facilities in island environments may be a challenge, but their footprint will be smaller compared to that of a landfill and, with proper planning and design, can have limited visual and environmental impact.

The supply chain for biofuel production systems will depend on the particular production pathway selected from Figure 2.1.1 and may typically look as depicted in Figure 2.1.2. In an

island chain such as Hawaii, biomass feedstocks or intermediate products may need to be transported between islands to amass sufficient material to achieve economies of scale. Similarly, final products may require interisland shipment between points of production and points of end use. Although the large number of possible combinations of feedstocks, intermediate products, conversion facility locations, and points of use could make supply chain monitoring onerous, the main, and perhaps only, qualities that need to be monitored up until the point at which the Navy takes delivery of the neat biofuel, relate to the Navy criteria for renewable fuels; e.g., the production inputs and processes used in manufacture.

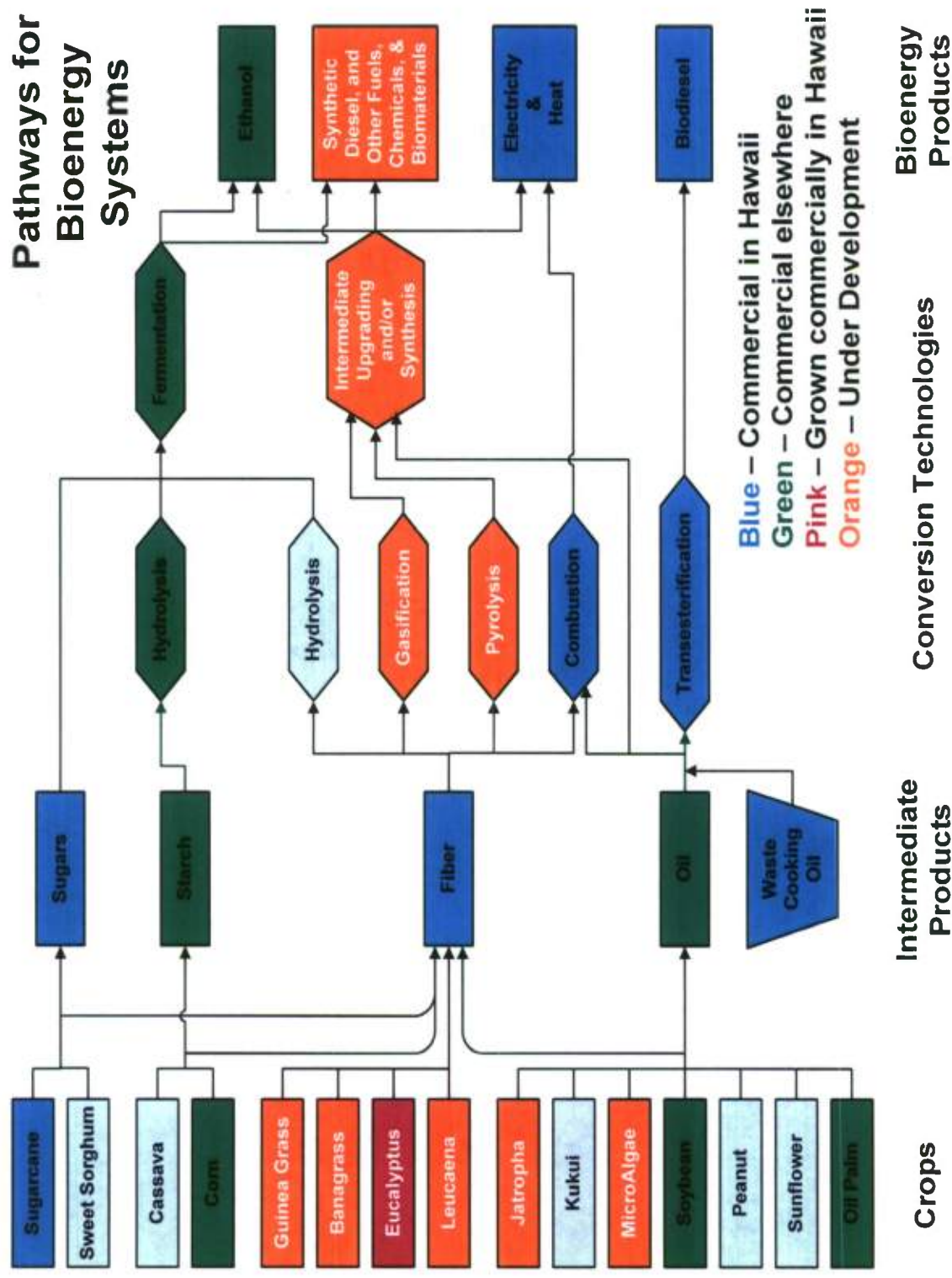


Figure 2.1.1 Bioenergy pathways for Hawaii and tropical island settings



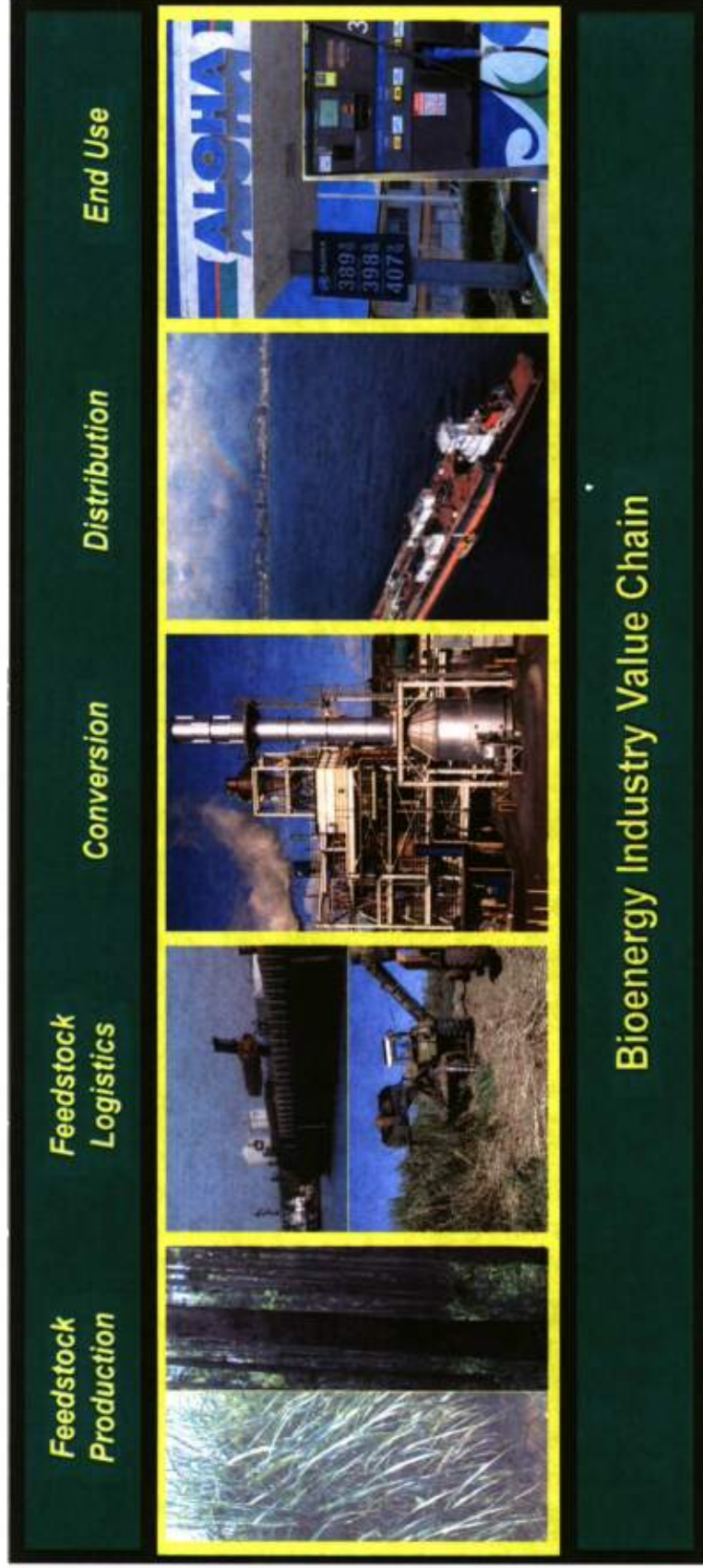


Figure 2.1.1.2 Potential bioenergy industry value chain for tropical island settings

DoD standard practices (Anon., 1999) can be used as guidelines to identify points for monitoring fuel quality and the frequency of occurrence. Fuels stored for more than six months are considered to be in long-term storage. F-76 stored in bulk should be tested every six months and that stored in packages should be tested every 12 months at a minimum. Note that these are minimum frequencies and that neat biofuel and biofuel blended with petroleum products should be monitored more frequently, at a three-month interval, until sufficient data sets have been established to support less frequent testing. In addition to storage guidelines, quality monitoring guidelines are provided for fuels when taking initial possession and extend to storage, pipelines, vessel loading, vessel discharge, transfers within installations or depots, road and rail tank car containers, package fuel products, and collapsible fabric tanks and drums. Each of these monitoring points or conditions is accompanied by a description of when and how the sample is to be taken, the type of sample, and the required testing.

Required testing (Anon., 1999) ranges from complete specification inspection testing (e.g., initial acceptance/possession), to hourly visual inspection during pipeline transfers. More commonly, a reduced set of tests are mandated to monitor principal characteristics most likely to have been affected in the course of storing or moving the product, or for contaminants such as water or particulates. In the case of neat biofuel or biofuel blended with petroleum product, it would appear prudent that more rigorous, complete specification inspection testing be conducted until sufficient data sets are established to guide the selection of reduced testing regimens.

Navy laboratories for fuel testing in Hawaii are located at the Fleet and Industrial Supply Center (FISC) at Pearl Harbor. Although not verified for this report, it is assumed that FISC Pearl Harbor maintains all equipment necessary to conduct fuel quality testing. A typical listing of specification properties for F-76 diesel fuel is presented in Table 2.1.1. Alternative fuels and fuel blends must meet these specifications in order to pass the first level of screening to qualify as drop-in replacements for F-76. The Institute of Petroleum's standard method, *IP 309: Diesel and Domestic Heating Fuels – Determination of Cold Filter Plugging Point*, is also included as a test method for F-76.

**Table 2.1.1 Summary of ASTM methods cited in MIL-DTL-16884L, the detailed specification for naval distillate fuel, F-76 (Anon, 2006). ASTM ID numbers in bold indicate designation as “referee test method” in MIL-DTL-16884L.**

ASTM ID No.	Title
<b>D86</b>	Standard Test Method for Distillation of Petroleum Products at Atmospheric Pressure (DoD adopted)
<b>D93</b>	Standard Test Methods for Flash-Point by Pensky-Martens Closed Cup Tester (DoD adopted)
<b>D97</b>	Standard Test Method for Pour Point of Petroleum Products (DoD adopted)
D129	Standard Test Method for Sulfur in Petroleum Products (General Bomb Method) (DoD adopted)
<b>D130</b>	Standard Test Method for Corrosiveness to Copper from Petroleum Products by Copper Strip Test (DoD adopted)
D189	Standard Test Method for Conradson Carbon Residue of Petroleum Products (DoD adopted)
D287	Standard Test Method for API Gravity of Crude Petroleum and Petroleum Products (Hydrometer Method) (DoD adopted)
<b>D445</b>	Standard Test Method for Kinematic Viscosity of Transparent and Opaque Liquids (and Calculation of Dynamic Viscosity) (DoD adopted)
<b>D482</b>	Standard Test Method for Ash from Petroleum Products (DoD adopted)
<b>D524</b>	Standard Test Method for Ramsbottom Carbon Residue of Petroleum Products (DoD adopted)
<b>D613</b>	Standard Test Method for Cetane Number of Diesel Fuel Oil (DoD adopted)
D664	Standard Test Method for Acid Number of Petroleum Products by Potentiometric Titration (DoD adopted)
D974	Standard Test Method for Acid and Base Number by Color-Indicator Titration (DoD adopted)
D976	Standard Test Methods for Calculated Cetane Index of Distillate Fuels (DoD adopted)
D1141	Standard Practice for the Preparation of Substitute Ocean Water (DoD adopted)
D1266	Standard Test Method for Sulfur in Petroleum Products (Lamp Method) (DoD adopted)
<b>D1298</b>	Standard Test Method for Density, Relative Density (Specific Gravity), or API Gravity of Crude Petroleum and Liquid Petroleum Products by Hydrometer Method (DoD adopted)
<b>D1401</b>	Standard Test Method for Water Separability of Petroleum Oils and Synthetic Fluids (DoD adopted)
<b>D1500</b>	Standard Test Method for ASTM Color of Petroleum Products (ASTM Color Scale) (DoD adopted)
D1552	Standard Test Method for Sulfur in Petroleum Products (High-Temperature Method) (DoD adopted)
D2274	Standard Test Method for Oxidation Stability of Distillate Fuel Oil (Accelerated Method) (DoD adopted)
<b>D2500</b>	Standard Test Method for Cloud Point of Petroleum Products (DoD adopted)
D2622	Standard Test Method for Sulfur in Petroleum Products by Wavelength Dispersive X-Ray Fluorescence Spectrometry (DoD adopted)
D2709	Standard Test Method for Water and Sediment in Middle Distillate Fuels by Centrifuge (DoD adopted)



**Table 2.1.1 (continued) Summary of ASTM methods cited in MIL-DTL-16884L, the detailed specification for naval distillate fuel, F-76 (Anon, 2006). ID numbers in bold indicate designation as “referee test method” in MIL-DTL-16884L.**

D3120	Standard Test Method for Trace Quantities of Sulfur in Light Liquid Petroleum Hydrocarbons by Oxidative Microcoulometry (DoD adopted)
D3605	Standard Test Method for Trace Metals in Gas Turbine Fuels by Atomic Absorption and Flame Emission Spectroscopy
D4052	Standard Test Method for Density and Relative Density of Liquids by Digital Density Meter (DoD adopted)
D4057	Standard Practice for Manual Sampling of Petroleum and Petroleum Products (DoD adopted)
<b>D4176</b>	Standard Test Method for Free Water and Particulate Contamination in Distillate Fuels (Visual Inspection Procedures) (DoD adopted)
D4177	Standard Practice for Automatic Sampling of Petroleum and Petroleum Products (DoD adopted)
<b>D4294</b>	Standard Test Method for Sulfur in Petroleum and Petroleum Products by Energy-Dispersive X-Ray Fluorescence Spectrometry (DoD adopted)
D4530	Standard Test Method for Determination of Carbon Residue (Micro Method) (DoD adopted)
D4539	Standard Test Method for Filterability of Diesel Fuels by Low-Temperature Flow Test (LTFT)
D4808	Standard Test Methods for Hydrogen Content of Light Distillates, Middle Distillates, Gas Oils, and Residua by Low-Resolution Nuclear Magnetic Resonance Spectroscopy (DoD adopted)
D5291	Standard Test Methods for Instrumental Determination of Carbon, Hydrogen, and Nitrogen in Petroleum Products and Lubricants
<b>D5304</b>	Standard Test Method for Assessing Middle Distillate Fuel Storage Stability by Oxygen Overpressure (DoD adopted)
D5452	Standard Test Method for Particulate Contamination in Aviation Fuels by Laboratory Filtration (DoD adopted)
<b>D5453</b>	Standard Test Method for Determination of Total Sulfur in Light Hydrocarbons, Spark Ignition Engine Fuel, Diesel Engine Fuel, and Engine Oil by Ultraviolet Fluorescence
D5771	Standard Test Method for Cloud Point of Petroleum Products (Optical Detection Stepped Cooling Method)
D5772	Standard Test Method for Cloud Point of Petroleum Products (Linear Cooling Rate Method)
D5773	Standard Test Method for Cloud Point of Petroleum Products (Constant Cooling Rate Method)
D5949	Standard Test Method for Pour Point of Petroleum Products (Automatic Pressure Pulsing Method)
D5950	Standard Test Method for Pour Point of Petroleum Products (Automatic Tilt Method)
D5985	Standard Test Method for Pour Point of Petroleum Products (Rotational Method)
D6045	Standard Test Method for Color of Petroleum Products by the Automatic Tristimulus Method
<b>D6217</b>	Standard Test Method for Particulate Contamination in Middle Distillate Fuels by Laboratory Filtration
D6371	Standard Test Method for Cold Filter Plugging Point of Diesel and Heating Fuels

<b>Table 2.1.1 (continued) Summary of ASTM methods cited in MIL-DTL-16884L, the detailed specification for naval distillate fuel, F-76 (Anon, 2006). ID numbers in bold indicate designation as "referee test method" in MIL-DTL-16884L.</b>	
D6450	Standard Test Method for Flash Point by Continuously Closed Cup (CCCFP) Tester
D6920	Standard Test Method for Total Sulfur in Naphthas, Distillates, Reformulated Gasolines, Diesels, Biodiesels, and Motor Fuels by Oxidative Combustion and Electrochemical Detection
D7039	Standard Test Method for Sulfur in Gasoline and Diesel Fuel by Monochromatic Wavelength Dispersive X-Ray Fluorescence Spectrometry
<b>D7111</b>	Standard Test Method for Determination of Trace Elements in Middle Distillate Fuels by Inductively Coupled Plasma Atomic Emission Spectrometry (ICP-AES)
<b>D7171</b>	Standard Test Method for Hydrogen Content of Middle Distillate Petroleum Products by Low-Resolution Pulsed Nuclear Magnetic Resonance Spectroscopy
E29	Standard Practice for Using Significant Digits in Test Data to Determine Conformance with Specifications (DoD adopted)

Additional testing for alternative fuels is required to determine whether the fuels meet fit-for-purpose requirements based on two levels. Level 1 and Level 2 screening standards for alternative F-76 fuels that are not included in Table 2.1.1 are summarized in Tables 2.1.2 and 2.1.3, respectively. In addition, Level 1 and Level 2 screening standards for fuels under consideration for use as alternatives to shipboard aviation fuel, JP-5, are summarized in Tables 2.1.4 and 2.1.5, respectively.

**Table 2.1.2 Summary of Level 1 fit-for-purpose screening standards  
for alternative F-76 fuels (Morris, 2011)**

ASTM ID No.	Title
E659	Standard Test Method for Autoignition Temperature of Liquid Chemicals
D971	Standard Test Method for Interfacial Tension of Oil Against Water by the Ring Method
D1322	Standard Test Method for Smoke Point of Kerosene and Aviation Turbine Fuel
D1331	Standard Test Methods for Surface and Interfacial Tension of Solutions of Surface-Active Agents
D2425	Standard Test Method for Hydrocarbon Types in Middle Distillates by Mass Spectrometry
D2624	Standard Test Methods for Electrical Conductivity of Aviation and Distillate Fuels
D3241	Standard Test Method for Thermal Oxidation Stability of Aviation Turbine Fuels
D3703	Standard Test Method for Hydroperoxide Number of Aviation Turbine Fuels, Gasoline and Diesel Fuels
D4052	Standard Test Method for Density, Relative Density, and API Gravity of Liquids by Digital Density Meter
D4054	Standard Practice for Qualification and Approval of New Aviation Turbine Fuels and Fuel Additives
D4809	Standard Test Method for Heat of Combustion of Liquid Hydrocarbon Fuels by Bomb Calorimeter (Precision Method)
D5001	Standard Test Method for Measurement of Lubricity of Aviation Turbine Fuels by the Ball-on-Cylinder Lubricity Evaluator (BOCLE)
D6379	Standard Test Method for Determination of Aromatic Hydrocarbon Types in Aviation Fuels and Petroleum Distillates—High Performance Liquid Chromatography Method with Refractive Index Detection
D6890	Standard Test Method for Heat of Combustion of Liquid Hydrocarbon Fuels by Bomb Calorimeter (Precision Method)
D7111	Standard Test Method for Determination of Trace Elements in Middle Distillate Fuels by Inductively Coupled Plasma Atomic Emission Spectrometry (ICP-AES)

**Table 2.1.3 Summary of Level 2 fit-for-purpose screening standards  
for alternative F-76 fuels (Morris, 2011)**

ASTM ID No.	Title
D2716	Standard Test Method for Determining Specific Heat Capacity by Sinusoidal Modulated Temperature Differential Scanning Calorimetry
D2717	Standard Test Method for Thermal Conductivity of Liquids
D2766	Standard Test Method for Specific Heat of Liquids and Solids
D6793	Standard Test Method for Determination of Isothermal Secant and Tangent Bulk Modulus



**Table 2.1.4 Summary of Level 1, fit-for-purpose screening standards  
for alternative JP-5 fuels (Morris, 2011)**

ASTM ID No.	Title
D6379	Standard Test Method for Specific Heat of Liquids and Solids
D1319	Standard Test Method for Hydrocarbon Types in Liquid Petroleum Products by Fluorescent Indicator Adsorption
E659	Standard Test Method for Autoignition Temperature of Liquid Chemicals
D4052	Standard Test Method for Density, Relative Density, and API Gravity of Liquids by Digital Density Meter
D6890	Standard Test Method for Determination of Ignition Delay and Derived Cetane Number (DCN) of Diesel Fuel Oils by Combustion in a Constant Volume Chamber
D86	Standard Test Method for Distillation of Petroleum Products at Atmospheric Pressure
D4054	Standard Practice for Qualification and Approval of New Aviation Turbine Fuels and Fuel Additives
D2425	Standard Test Method for Hydrocarbon Types in Middle Distillates by Mass Spectrometry
D3705	Standard Test Method for Misting Properties of Lubricating Fluids
D971	Standard Test Method for Interfacial Tension of Oil Against Water by the Ring Method
D5001	Standard Test Method for Measurement of Lubricity of Aviation Turbine Fuels by the Ball-on-Cylinder Lubricity Evaluator (BOCLE)
D1840	Standard Test Method for Naphthalene Hydrocarbons in Aviation Turbine Fuels by Ultraviolet Spectrophotometry
D4629	Standard Test Method for Trace Nitrogen in Liquid Petroleum Hydrocarbons by Syringe/Inlet Oxidative Combustion and Chemiluminescence Detection
D971	Standard Test Method for Interfacial Tension of Oil Against Water by the Ring Method
D2887	Standard Test Method for Boiling Range Distribution of Petroleum Fractions by Gas Chromatography
D3241	Standard Test Method for Thermal Oxidation Stability of Aviation Turbine Fuels
D6732	Standard Test Method for Determination of Copper in Jet Fuels by Graphite Furnace Atomic Absorption Spectrometry
D7111	Standard Test Method for Determination of Trace Elements in Middle Distillate Fuels by Inductively Coupled Plasma Atomic Emission Spectrometry (ICP-AES)
D445	Standard Test Method for Kinematic Viscosity of Transparent and Opaque Liquids (and Calculation of Dynamic Viscosity)
D4809	Standard Test Method for Heat of Combustion of Liquid Hydrocarbon Fuels by Bomb Calorimeter (Precision Method)

**Table 2.1.5 Summary of Level 2, fit-for-purpose screening standards  
for alternative JP-5 fuels (Morris, 2011)**

ASTM ID No.	Title
D6793	Standard Test Method for Determination of Isothermal Secant and Tangent Bulk Modulus
D924	Standard Test Method for Dissipation Factor (or Power Factor) and Relative Permittivity (Dielectric Constant) of Electrical Insulating Liquids
E681	Standard Test Method for Concentration Limits of Flammability of Chemicals (Vapors and Gases)
D4054	Standard Practice for Qualification and Approval of New Aviation Turbine Fuels and Fuel Additives
D2779	Standard Test Method for Estimation of Solubility of Gases in Petroleum Liquids
D2766	Standard Test Method for Specific Heat of Liquids and Solids
D1331	Standard Test Methods for Surface and Interfacial Tension of Solutions of Surface-Active Agents
D2717	Standard Test Method for Thermal Conductivity of Liquids
D6378	Standard Test Method for Determination of Vapor Pressure (VPX) of Petroleum Products, Hydrocarbons, and Hydrocarbon-Oxygenate Mixtures (Triple Expansion Method)

Preliminary review of the methods in Tables 2.1.1 to 2.1.5 identified equipment needed to conduct fuel quality testing. Standard method and equipment requirements are summarized in Table 2.1.6. Preliminary estimates of total budget needed to purchase the equipment identified in Table 2.1.6 is \$250,000. A reduced set of equipment may be justified if only selected quality parameters are deemed relevant to biofuel research. Preliminary analysis indicates that one post-doctoral fellow and one graduate student would be sufficient to conduct a fuel quality research program.

**Table 2.1.6 Summary of special equipment requirements for fuel quality research program needs**

ASTM ID No.	Required Equipment
D93	Pensky-Martens closed cup flash test apparatus
D130	Copper strip corrosion pressure vessel
D445	Viscometer
D1160	Vacuum distillation apparatus
D1298	Hydrometer
D1401	Water separability test station
D1500	Fuel Color Comparator
D2500	Cloud Point Analyzer
D4294	Energy dispersive X-ray fluorescence analyzer
D5304	Storage stability testing apparatus
D5453	Sulfur by UV-fluorescence analyzer
D6079	High-frequency reciprocating rig apparatus

### **2.1.3 References**

Anon. 1999. Department of Defense Standard Practice: Quality surveillance for fuels, lubricants, and related products. MIL-STD-3004. Department of Defense, Washington DC.

Anon. 2006. Detail Specification, Fuel, Naval Distillate, MIL-DTL-16884L. Department of Defense, Washington DC.

Morris, R. 2011. Naval Research Laboratory. Personal communication.



## 2.2 Plasma Arc Processing

Under FY07 funding our lab began research on the non-thermal plasma reforming of methane. This involved the design and construction of a reverse vortex flow reformer (Figure 2.2.1) and subsequent parametric and factorial testing of system parameters to optimize performance for hydrogen selectivity under FY08 funding. We achieved 83.3% hydrogen selectivity, had a specific energy requirement of  $144 \text{ kJ mol}^{-1}$  of hydrogen produced and operated at 43.5% efficiency. At this point the reformat was comprised of 35.53% hydrogen, 0.23% oxygen, 16.58% carbon monoxide, 1.42% carbon dioxide and 5.69% methane. The results were compiled into a manuscript titled "An experimental investigation of reverse vortex flow plasma reforming of methane." We are responding to peer review critiques in order to resubmit the article for review and publication in the International Journal of Hydrogen Energy.

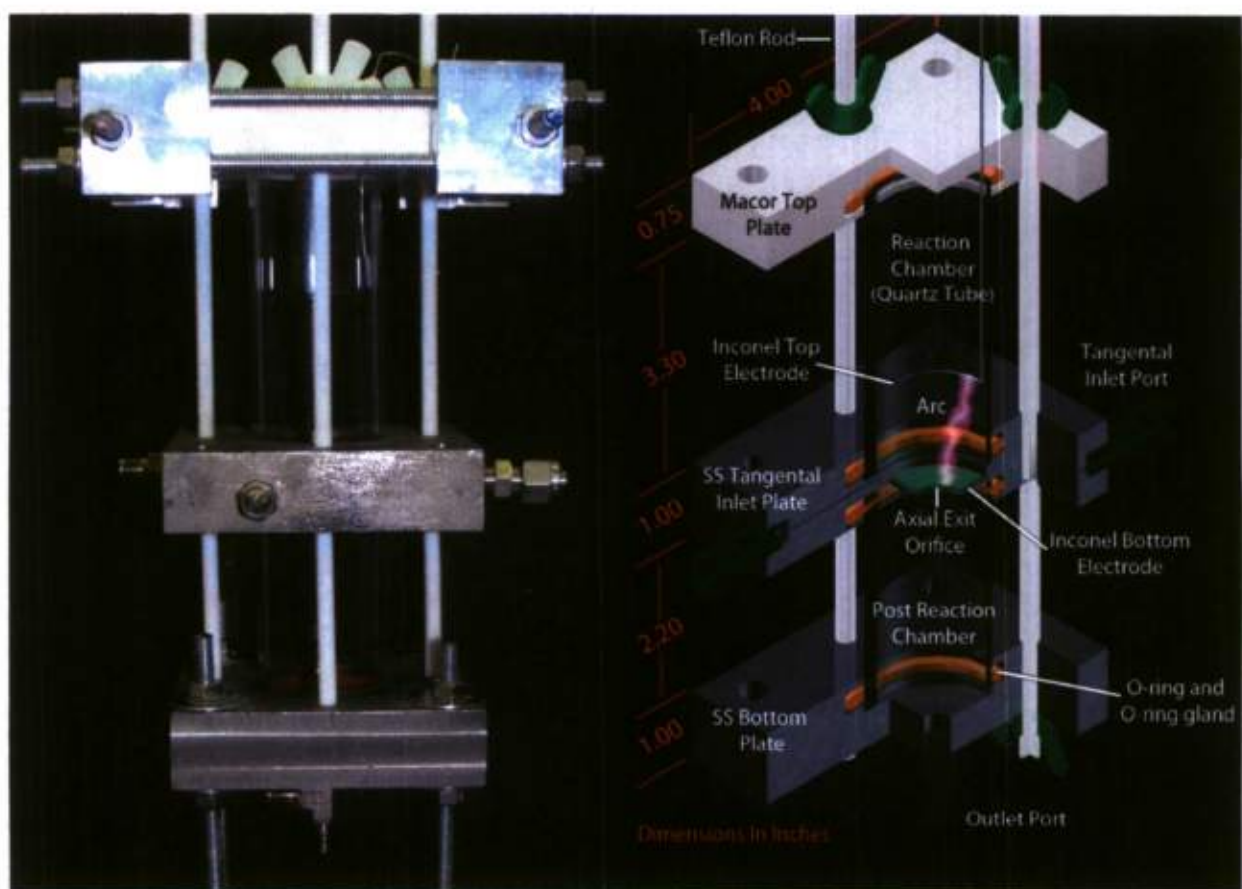


Figure 2.2.1 Reverse vortex flow non-thermal plasma reformer image and diagram

Our current work, based on the non-thermal plasma reforming of methane, focuses on the reforming of liquid hydrocarbons, in particular dodecane ( $\text{C}_{12}\text{H}_{26}$ ), a model diesel compound. The reforming of liquid hydrocarbons within non-thermal plasma presents challenges not encountered while reforming gases. Chief among them is the introduction of the liquid hydrocarbon to the reaction chamber in a suitable form. This dictated the redesign of the

components of the fuel delivery system, reformer and reformat analysis system. This report details results of the FY08 effort.

### 2.2.1 Scope of Work

Objectives of the FY08 effort are described below.

1. To fully characterize the performance of the reformer on methane over a range of experimental conditions. Independent variables for experimental design include plasma voltage, electrode geometry, reactant volumetric flow rate, fuel reactant ratios (fuel, air, O<sub>2</sub>, steam, etc.), reactor temperature as affected by reactor insulation, and use of catalyst. Reformate will be characterized using gas analysis equipment and data will be used to compute reformate performance parameters including the yield of hydrogen relative to the methane fuel input.
2. Conduct additional design and selection of fuel system components required to deliver a suitable fuel flow to the reactor will be conducted. Fuel delivery will be characterized and preliminary testing using liquid fuels will be conducted.
3. Initiate work on a numerical model of the plasma reactor system.

### 2.2.2 Technical Accomplishments

Sections 2.2.2.1, 2.2.2.2, and 2.2.2.3 describe the technical accomplishments corresponding to the three objectives, respectively, identified in section 2.2.2.

#### 2.2.2.1 Methane Reforming

The results of the methane reforming investigation using the plasma arc system are described in the following sections. Relevant nomenclature is provided here.

$\epsilon_0$  = vacuum permittivity (A s<sup>4</sup> m<sup>-3</sup> kg<sup>-1</sup>)

$\theta$  = angle between electrodes (deg)

$\lambda$  = heat conductivity (W m<sup>-1</sup> K<sup>-1</sup>)

$\sigma$  = electrical conductivity (W m<sup>-1</sup> K<sup>-1</sup>)

$\tau$  = characteristic time of arc formation (ms)

$c_k$  = molar fraction of gas component (-)

$d$  = discharge gap (m)

$D_e$  = electron drift coefficient (-)

$e_0$  = elementary charge (C)

$E$  = electric field (V m<sup>-1</sup>)

$E_i$  = transitional electric field from thermal to direct electron impact ionization

$E_\infty$  = effective ionization potential (kJ mol<sup>-1</sup>)

$H$  = Standard enthalpy of formation at 298 °K and 101.3 kPa pressure (kJ mol<sup>-1</sup>)

$I$  = ionization potential (kJ mol<sup>-1</sup>)

$J$  = electrical current (A)

$k$  = Boltzmann's constant (-)

$k_i$  = ionization constant (-)

$\ell$  = length of arc column (m)

LHV = lower heating value (MJ kg<sup>-1</sup>)

$\dot{m}$  = mass flow rate ( $\text{kg sec}^{-1}$ )  
 $n$  = gas concentration ( $\text{cm}^{-3}$ )  
 $n_e$  = electron concentration ( $\text{cm}^{-3}$ )  
 $p$  = pressure (atm)  
 $P$  = power (W)  
 $Q_{\text{eq}}$  = energy dissipated in equilibrium regime (J)  
 $Q_{\text{non-eq}}$  = energy dissipated in non-equilibrium regime (J)  
 $R$  = power supply serial resistance ( $\Omega$ )  
 $R_0$  = power supply internal resistance ( $\Omega$ )  
 $t$  = time (s)  
 $T$  = temperature (K)  
 $T_0$  = gas temperature along axis of arc (K)  
 $v$  = velocity of gliding arc ( $\text{m s}^{-1}$ )  
 $v_{\text{drift}}$  = electron drift velocity ( $\text{m s}^{-1}$ )  
 $V$  = voltage (V)  
 $V_0$  = open circuit voltage (V)  
 $w$  = dissipated power per unit length of arc column ( $\text{W m}^{-1}$ )

#### 2.2.2.1.1 Introduction

Environmental impacts of greenhouse gases, rising fuel prices, and a dependency on foreign sources of fuel have made it necessary to develop alternative sources of energy [1]. The electrochemical oxidation of hydrogen in a fuel cell yields power, heat, and water, which has made it a popular alternative fuel option.

Hydrogen can be produced domestically from sources such as natural gas reforming, coal and biomass gasification, and water electrolysis [1]. Large scale industrial processes utilizing reforming of natural gas and coal are expected to play the largest roles in the world production of hydrogen [1]. The reforming process converts a primary fuel into a desired fuel product, e.g. methane into hydrogen and carbon monoxide. The delivery from these large scale industrial hydrogen production plants will likely involve three different methodologies. Depending on the needs of a given area these may include truck delivery in the form of compressed gas or cryogenic liquid, or pipeline distribution [2]. Hydrogen production via onsite fuel reforming can avoid the need to develop new hydrogen delivery infrastructure. Non-thermal plasma reforming of a primary fuel into hydrogen rich gas is a potential on-site method.

The research presented focuses on performance evaluation of non-thermal, gliding arc plasma stabilized in a reverse vortex flow. It sought to find the effects of varying system parameters on the reformer's ability to reform methane. Parametric tests determined the effects of single system parameters, while a full factorial experiment investigated second order effects, found optimal operating conditions and operational limits for the reverse vortex flow reformer.

Due to its ability to easily transmit energy to other materials and cause reactions in dilute reactant mixtures [4,5] plasma treatment of fuels has been investigated as a potential method for fuel reforming since the early 90's [6]. Plasma reformer performance depends on the type of plasma, additive gases, the plasma power generator, the utilization of catalysts, water vapor injection, and the geometry of the reformer [7]. The earliest research focused on thermal plasmas, in which the temperature of the electrons, ions and neutral particles exist in



thermodynamic equilibrium. Thermal plasma has the ability to reform the gas, but suffers significant draw backs, chief among them, excessive power consumption and the inability to control the chemical processes [8]. Non-thermal plasmas in which the ion and neutral particle temperatures are significantly lower than the electron temperatures allow for good selectivity and control over the chemical processes [9]. They however, suffer their own drawbacks such as extremely limited power consumption, and operational pressure ranges [3]. However, transitional plasma, also non-thermal, existing between purely thermal plasma and a low-power density, non-thermal plasma can transcend the negative aspects of both the thermal and non-thermal plasmas making them well suited to fuel reforming plasma chemistry [9]. They have non-thermal characteristics with electron temperature higher than heavy particle temperature [8,10], operate at atmospheric pressure, maintain control over the reforming process, all while maintaining significantly high power densities required for industrial reforming of gasses [3,11-13].

Gliding arc plasma, a transitional plasma [6], has shown promising results within the realm of fuel reforming. It has very low specific power consumption [6], even when compared to other non-thermal plasma reforming processes as seen in Petitpas' comprehensive literature review [3]. Their endothermic chemical reactions can absorb up to 80% of the electrical energy provided to the arc [8]. Where as many different electrode configurations have been utilized [10,14-17], the electrical discharge of a typical gliding arc forms between two or more diverging electrodes [16]. Typical gliding arc reactors with two in-plane diverging electrodes produce a thin plasma arc propagated along the blades by the gas flow, which permits very high gas throughputs [8,17]. However only 10 to 15% of the gas flow has direct contact with the arc and experiences a very low residence time [18] ( $\sim 10^{-3}$  seconds [8]). The limited quantity of excited species produced by the plasma is insufficient to provide energy required for complete reformation of the feed gas resulting in extremely non-uniform gas treatment [17].

Equation (1) [19] states a general equation for the reforming of methane. When y equals 0 and x is greater than 0 steam reforming takes place [19] following equation (2) [20]. Partial oxidation occurs when x = 0 and y > 0 yet is less than needed for the combustion of methane (equation 3) [20]. This paper primarily investigates the partial oxidation of methane in a fuel rich environment, and thus oxygen considered exists in pure form or air and steam is neglected (equation 4) [20].

$CH_4 + xH_2O + yO_2 + Q \rightarrow aCO_2 + bCO + cH_2O + dH_2$		(1)
$CH_4 + H_2O_{vapor} \rightarrow CO + H_2$	$\Delta H = 205.7 kJ mol^{-1}$	(2)
$CH_4 + 2O_2 \rightarrow CO_2 + 2H_2O_{liquid}$	$\Delta H = -890.8 kJ mol^{-1}$	(3)
$CH_4 + 0.5O_2 \rightarrow CO + 2H_2$	$\Delta H = -36.1 kJ mol^{-1}$	(4)

As opposed to a gliding arc between two diverging electrodes, a reverse vortex flow reformer can propagate the arc in 3 dimensions (Figure 2.2.2). This can overcome the traditional

diverging electrode gliding arc's limitation of non-uniform gas treatment by increasing the residence time within the plasma [17].

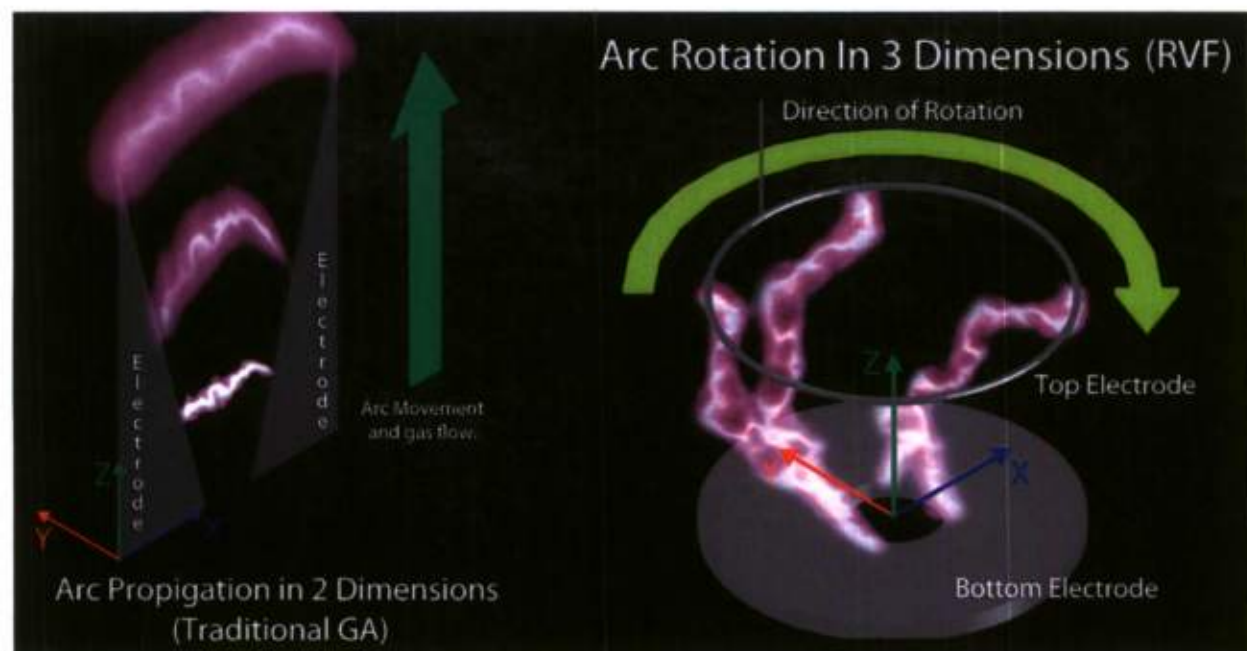


**Figure 2.2.2 Schematic diagrams of two- and three-dimensional plasma arc systems relevant to reforming**

The reverse vortex functions by the tangential injection of gases at the base of a cylindrical volume with an axial exit at the center of the base [5]. The gas enters the reaction chamber at velocities between 10 and 50  $\text{m s}^{-1}$  and slows as it expands downstream [5,10]. Gas flows between 1 and 10  $\text{m s}^{-1}$  have the ability to propagate a gliding arc without immediately extinguishing it [14]. Incoming gases flow along the cylinder walls spiraling towards the top and create a barrier between the hot axial zone and the walls of the reactor [5]. At the top, the gas reverses flow in the axial direction and forms a tighter spiral down the axis of the reactor, exiting through a hole in the center of the base. This creates what can be imagined as a tornado that upon reaching the top of the reaction chamber turns around and exits along its own axis. This increases the thermal efficiency of the reformer 25% over that of a forward vortex flow in which gases are injected tangentially at the top of the reactor and exit axially through the base [17]. Additionally the swirling, reverse-flow vortex flow pattern convectively cools the arc and pushes it further toward a non-thermal regime [10,17].

Kalra et al. reported that the arc initially forms between the cathode and the inner edge of the axial exit (anode), rotating there indefinitely [17]. The arc travels rapidly around the electrodes and thus does not deteriorate the surfaces [10]. If the arc extinguishes and the electrodes are further apart than the initial break down gap, re-ignition can still occur by following a path through the electric field within the gas [17]. At high flow rates, a plasma jet may form, exiting the reformer with the axial flow. The majority of reactions take place within the reformer and the gas composition immediately following the plasma jet does not change significantly as the reformat cools and passes through post reaction chambers and heat exchangers [9].

### 2.2.2.1.2 Material and Methods

Figure 2.2.3 shows a schematic of the laboratory scale plasma reformer test bed. The test bed included three main component groups with different functions. The front end of the system metered reactants and prepared them for input into the reverse vortex reformer. The reformer section included the reverse vortex reformer and power supply, and the back end of the system conditioned and analyzed the reformed gas mixture. A National Instruments SCB-68 data acquisition board (National Instruments, Austin, TX) and LabView software (National Instruments, Austin, TX) running on a laptop computer controlled the system and monitored and recorded data.

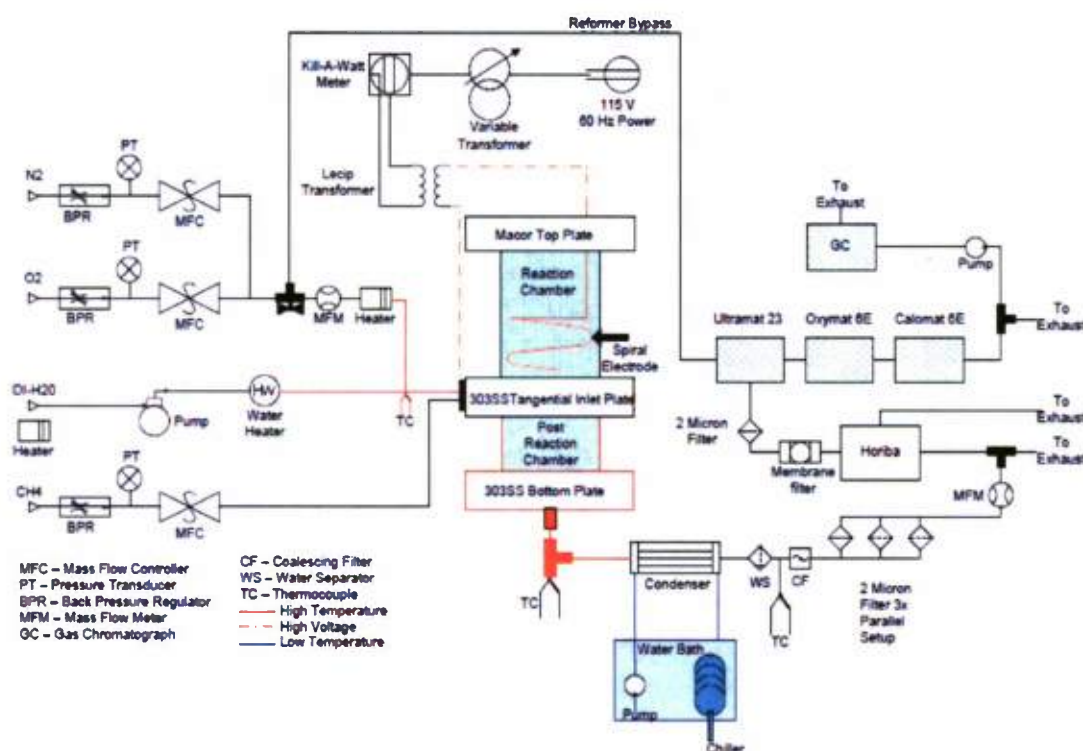


Figure 2.2.3 Schematic of the laboratory scale plasma reformer test bed for methane

#### Front End

The front end of the system served primarily to meter reactants into the reverse vortex reformer. Brooks 5850E mass flow controllers metered bottled oxygen and nitrogen to the reformer. The proportions of the two were set to produce a composition very close to air. The air mixture passed through a fabricated resistance heater and mixed with the steam input stream produced by an Eldex 38M 1/8" piston metering pump pushing de-ionized water through a fabricated water



heater. A hot plate maintained the de-ionized water reservoir at 50 °C in order to minimize water heater fluctuations downstream. A thermocouple at the steam and gas mixing point provided feedback in order to maintain the mixture at 120 °C. This mixture entered the reverse vortex flow reformer via one of two tangential gas inlets. A 50 mm length of polytetrafluoroethylene (PTFE) tube between the 316 stainless steel air/steam delivery components and the 303 stainless steel tangential inlet plate, acting as the lower electrode, provided electrical isolation between the two component groups.

A Brooks 5850EM mass flow controller metered bottled, grade 4, methane to a second tangential gas inlet in the reformer flange via PTFE tubing.

### *Reformer Section*

The reformer (Figure 2.2.4) consisted of a top plate, a reaction chamber, an inlet plate, a post reaction chamber, a bottom plate, and upper and lower electrodes. The ceramic top plate (Macor<sup>®</sup> Corning Inc., Corning, NY) formed the top of the reaction chamber and held the upper electrode in place. The inlet plate fabricated from 303-stainless steel, served several purposes. Two tangential reactant gas inlets created a reverse vortex flow in the reaction chamber. The inlet diameters reduced to 1.066 mm upon entering the reaction chamber. The resulting flow field caused the arc formed between the top ring electrode and the bottom electrode to revolve in the reaction chamber. The 1.07 mm diameter wire top electrode had an outer ring diameter of 38 mm. The inlet plate conducted electricity from the transformer line to the washer electrode with an outer diameter of 38 mm, and an inner orifice diameter ranging from 3.4 to 17.4 mm as seen in Figure 2.2.5. Inconel was chosen as the material for the electrodes due to its ability to withstand high temperatures and oxidation [9,12].

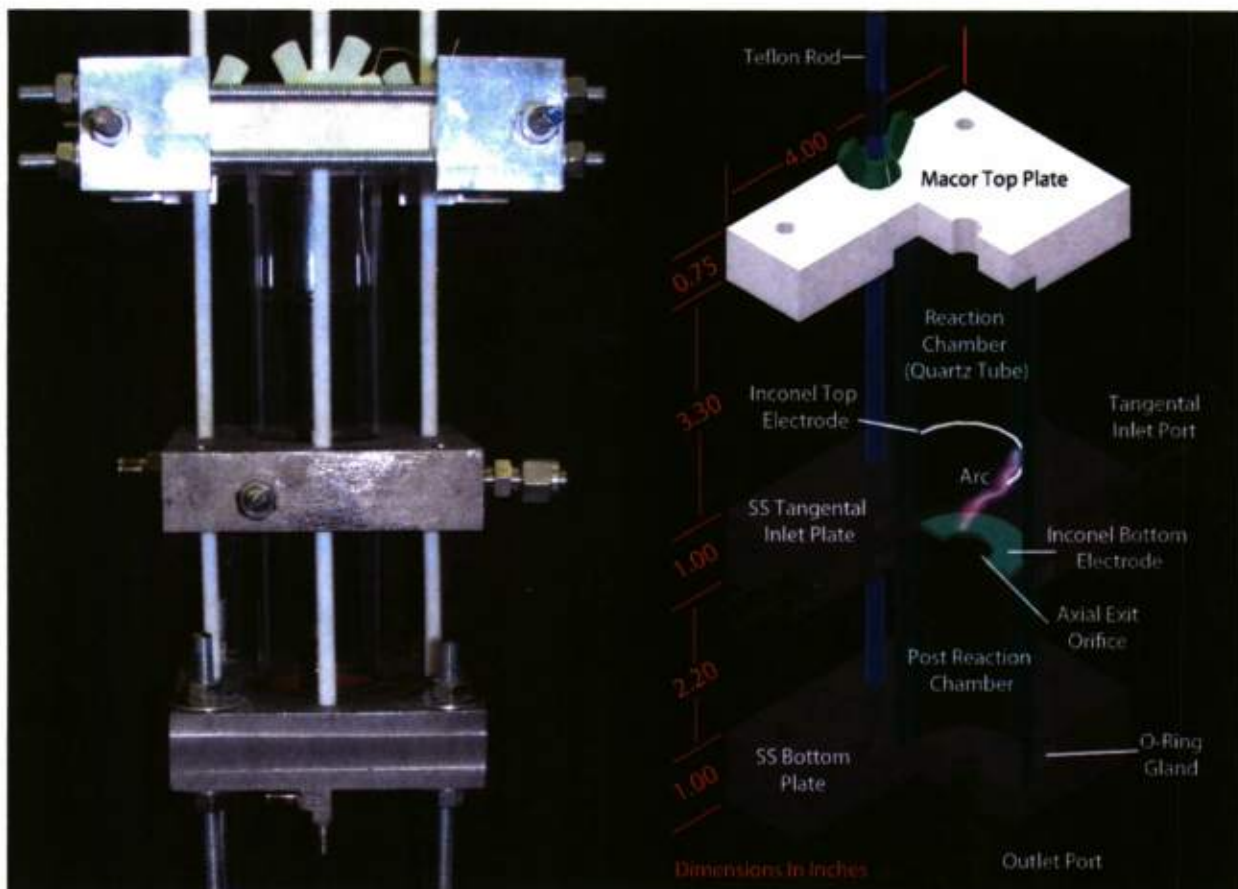


**Figure 2.2.4 Photo and cut away diagram of plasma arc reactor system for methane**

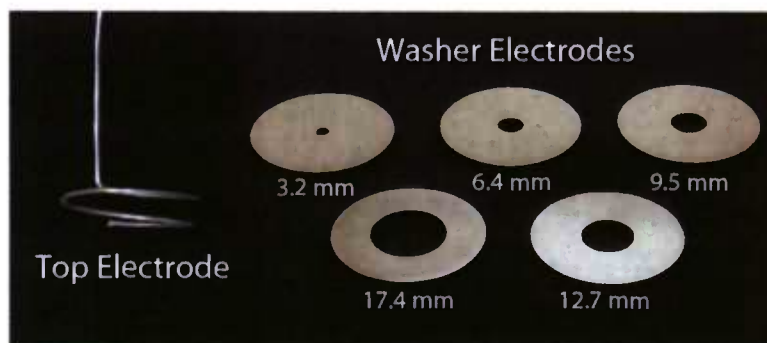


**Figure 2.2.5 Outlet orifices for plasma arc reactor system for methane**

The 303 stainless steel bottom plate served as the connection point for the back end of the system. The quartz tube, post-reaction chamber served as a mixing zone for the treated gases and electrically isolated the inlet plate from the bottom plate and the back end of the system. Thermal insulation was placed around the post reaction chamber. Non-conducting PTFE threaded rods held the entire assembly together and silicone o-rings sealed the interfaces between the plates and the quartz tubes of the reaction and post reaction chambers.

The system's power supply utilized two major components; a variable autotransformer (Staco, model 3PN1410B, ISE Inc., Cleveland), and a neon sign transformer (Lecip Sentry, model 4B15N6-CB, Allanson International, Toronto). The Staco autotransformer could step up or down line voltage of 120 V, 60 Hz to a range of 0 to 140 V which was then supplied to the Lecip Sentry transformer. The Lecip Sentry neon sign transformer stepped up the incoming AC voltage 125 times and had a maximum output of 400 W at 15 kV, however we throttled this to 250 W via the autotransformer. As the arc was a fixed length between the upper and lower electrodes, the power consumed by the arc remained relatively constant over time. This allowed for a meter (Kill A Watt™, Model p4460) plugged directly into the outlet of the Statco autotransformer to measure the power delivered to the Lecip Sentry transformer. Insulated, high-voltage wires carried the charge from the transformer to the middle plate and upper electrode.

### *Back End*

The back end of the system conditioned the product stream to permit determination of flow rate and composition. A water condenser (Fisher, Pyrex Graham 300 mm) with a water jacket cooled by an external immersion chiller (VWR Scientific, Model 1109), and a water separator reduced the reformat temperature from ~250 °C to ~26 °C and removed liquid water. A coalescing filter (Balston, Model 31G ) removed any remaining water before the gas passed through a parallel array of three 2 µm pore size filters (Swagelok SS-4F-2). A calibrated mass flow meter (Omega, Model FMA1820S) determined the volumetric flow of the reformat prior to analysis.

A sampling unit (Horiba, model PS-200) pulled 2.6 lpm of reformat from the gas stream and removed any remaining vapor. The treated flow passed through a membrane filter (United Filtration Systems, model SM105.221) and an additional 2 µm pore size (Swagelok, model SS-4F-2) filter. Sample flow passed through three on-line gas analyzers in series. A non-dispersive, infrared analyzer (Siemens, model Ultramat 23) measured the volume percentage of methane, carbon monoxide, and carbon dioxide, a zircon dioxide based sensor in the second analyzer (Siemens, model Oxymat 6E) measured the oxygen content, and a thermal conductivity based measurement was made in the final analyzer (Siemens, model Calomat 6E) for hydrogen content.

A pump (Air Dimensions 1/6 hp) pulled a 2 lpm stream from the flow exiting the online analyzers and directed it to a gas chromatograph (GC) (Shimadzu, Model 14A, Columbia, MD). The pump started 2 min after the GC sampled and ran for 6.5 min, allowing 1.5 min of the 10 min cycle for the gas pressure in the sample valve to equilibrate with atmospheric pressure.

The GC was equipped with a 1.52 m x 3 mm Carboxen™ 1000 column (SUPELCO, Bellafonte, PA) and a thermal conductivity detector. Tests were run in accordance with American Society for Testing and Materials Standard D1946-90 – Standard Practice for Analysis of Reformed Gas by Gas Chromatography. GC analyses utilized an initial oven temperature of 80 °C as this produced the same results as those conducted with the ASTM recommended 45 °C and allowed for more rapid cycling of the analysis.

### *System Variables*

The following section outlines both the dependent and independent variables within the system.

Reactor temperature – dependent variable



The power input level, reactant gas inputs, and the length of the arc all affected reactor temperature.

#### Volumetric flow rate – dependent variable

The volumetric flow rate in the present work was measured as clean, cool, dry gas flow downstream of the reactor. This flow rate can be used as a basis to compute a wet, volumetric flow rate at reactor temperature. As the gas composition, steam input, and temperature at the inlet changed, the reformat changed in volume, thus changing the volumetric flow rate within the reaction chamber. Effects of volumetric flow rate were explored after the parametric and factorial tests determined optimal system parameters.

#### Reactor chamber – independent variable: to remain fixed

The geometry of the reaction chamber affects the flow characteristics and the residence time within the reactor.

#### Electrode gap distance – independent variable

Increasing the gap distance, the distance between the top electrode and the bottom washer electrode, increases both the non-thermal properties of the arc and the residence time of the gas within the arc [21]. If the gap distance is too small the arc exists in a thermal regime leading to poor performance. If the gap is too large the arc cannot sustain itself in a non-thermal regime.

#### Axial exit size – independent variable

As stated in the literature, the axial exit of the reforming chamber must be significantly smaller than the diameter of the chamber in order to produce the reverse vortex flow [17]. The area of the axial exit from the reformer was varied in size by changing the axial orifice washer electrode. As the axial exit diameter decreases, the reformat exits the chamber at a higher velocity.

#### Oxygen input – independent variable: to remain fixed

The oxygen flow rate was held constant at 0.56 slpm and the oxygen to carbon ratio changed by increasing or decreasing the methane flow rate. Oxygen and nitrogen flows had the same proportion as air.

#### Nitrogen input – independent variable: to remain fixed

The N<sub>2</sub> flow rate was set at a constant flow rate of 2 slpm to maintain a ratio with the O<sub>2</sub> flow rate equal to that of air.

#### Methane input – independent variable

Methane was the fuel in the experiments. Methane input was varied from 0.4 to 1.2 slpm, corresponding to equivalence ratios of 0.23 to 0.7, while holding the oxygen flow rate constant. The equivalence ratio is defined as the oxygen to fuel ratio of the reaction divided by the stoichiometric oxygen to fuel ratio [22] (Equation 5)).

$$\text{Equivalence Ratio} = \frac{\left( \frac{\dot{n}_{O_2}}{\dot{n}_{CH_4}} \right)_{\text{actual}}}{\left( \frac{\dot{n}_{O_2}}{\dot{n}_{CH_4}} \right)_{\text{stoichiometric}}} \quad (5)$$

Where  $\dot{n}$  is the molar flow rate of each species.

Steam input – independent variable

The steam input to the system prevents soot formation and provides for additional hydrogen if reacted. However, the steam absorbs energy for ionization, reducing the energy available for the methane conversion reaction.

Power input – independent variable

The power input directly affected the length of the arc and the number of electrons available for ionization of neutral particles. Power greater than necessary for arc formation was applied to the system to create an initial arc and then reduced to the desired setting for the test conditions.

### *Parametric Tests*

A parametric test was conducted for each independent variable revealing the effects of system geometry and individual parameters on reformer performance. Independent variables and their base case values for parametric tests are shown in Table 2.2.1. They did not show second order effects, nor were they employed to find optimal operating conditions. Rather the parametric tests showed the systems response to changing one variable while holding all other variables constant regardless of interactions between the parameters.

**Table 2.2.1 Independent variables, base case values, and value ranges for parametric tests**

Variable	Base case value	Range of values for parametric test
Reactor Chamber	0.095 L	fixed
Electrode Gap Distance	25 mm	10 mm to maximum achievable arc
Axial Exit Size	17.4 mm	3.2mm, 6.35 mm, 9.5 mm, 12.7 mm
Oxygen Input	0.56 slpm	fixed
Nitrogen Input	2 slpm	fixed
Methane Input	1 slpm	0.4 - 1.24 slpm
Power Input	200 W*	175 – 250 W
Steam Input (as liquid)	1.6 g min <sup>-1</sup>	0.4 – 2.4 g min <sup>-1</sup>

\* The gap distance parametric tests were conducted at two different power levels, 160W and 200W, to identify stable arc conditions.

### *Factorial Design*

Based on the results of the parametric tests, full factorial experiments, utilizing a 2<sup>4</sup> design, explored the effects of four independent variables – methane input, steam input, power input, and gap distance. Each independent variable was assigned a high and low level based around a center point leading to 16 total points per factorial test. Randomization of the test point run order helped alleviate any test-to-test drift error. The four factor, factorial design allowed for determination of optimum values of the four independent variables, estimated the effects of each variable – showing which variables affected the system the most, identified interactions or higher order effects between variables and allowed for the determination of operational system limits. Without performing a factorial test it would not be possible to say with certainty that the various system parameters have no effect on each other.

Table 2.2.2 shows the center point and corresponding step sizes for the first and second factorial designs. The center point for the first factorial design was based on data from the literature and

from results of the parametric tests. Test results from the first factorial design allowed for the calculation of a path of steepest ascent using response surface methodology in the factor space and led to the second factorial test's center point. The second factorial test exposed functional limits of the system as its center point neared an optimal operating condition.

**Table 2.2.2 Center points for first and second factorial designs with corresponding step sizes**

First Factorial Design				Second Factorial Design			
Variables	center point	step size	units	Variables	center point	step size	units
Gap Distance	30	2.5	mm	Gap Distance	36.5	2	mm
Steam Input	0.8	0.2	g / min	Steam Input	0.4	0.2	g / min
Methane Input	0.8	0.1	slpm	Methane Input	1.35	0.1	lpm
Power Input	200	10	W	Power Input	250	10	W

### *Data Acquisition*

Temperature measured at the reformer exit was allowed to reach equilibrium before any measurements of the reformat composition were recorded. Data from the analyzers was recorded for the last 5 minutes of each 10 minute test condition and averaged. This allowed for the system to come to equilibrium after system input parameters were changed. The gas chromatograph sampled at the end of each 10 minute test condition. During the experiments, a stable condition was maintained at each operating point until a minimum of four ten minute gas samples were analyzed via gas chromatography (GC). This provided sufficient data to calculate a mean and standard deviation at each point.

### *Data Reduction*

Calculation of performance indicators from data collected from the experiments conformed to those established by Petipas et al. [3]. Parametric test performance was based on hydrogen yield, selectivity, efficiency, specific energy requirements and methane conversion, while the factorial tests pursued optimal selectivity.

Hydrogen yield is defined by the number of hydrogen atoms in hydrogen gas in the reformat divided by the total amount of hydrogen atoms in the feed gas (equation (6) [3].

$$\text{Hydrogen Yield} = \frac{\text{Hydrogen Atoms in } H_2 \text{ in reformat}}{\text{Hydrogen Atoms in } CH_4 \text{ Feed Gas}} * 100 \quad (\%) \quad (6)$$

Indarto described hydrogen selectivity as the hydrogen yield divided by the methane conversion as shown in equation (7). This provides an index of the system's ability to reform methane into hydrogen with the assumption that any unconverted methane could be recovered or utilized by other processes. Hydrogen atoms introduced as steam are not included in calculations of hydrogen yield or selectivity.



$$Selectivity = \frac{\text{moles of } H_2 \text{ produced}}{2(\text{moles of } CH_4 \text{ converted})} * 100 \quad (\%) \quad (7)$$

Equation (8) describes the efficiency of the system as the amount of energy in the hydrogen in the reformat divided by the total system energy input from both the plasma and the feed fuel [3]. The lower heating value (LHV) is the heat of combustion measured in MJ kg<sup>-1</sup>, with the resulting water products in the vapor phase. The LHV is multiplied by the mass flow rate of the given species in order to find the power associated with the gas flow. The efficiency definition assumes that any CO present in the reformat can be converted to H<sub>2</sub> by the exothermic water gas shift reaction (Equation (9) [3]). The water gas shift reaction normally occurs in two stages, one at 350 °C and a second at 190 to 210 °C [23], and has been assumed by other groups to have 0 energy cost [24], which while unrealistic [25], allows for a direct comparison to the literature review by Petitpas [3].

$$Efficiency \ \eta = \frac{LHV_{H_2 \text{ gas}} * (\dot{m}_{H_2} + \dot{m}_{CO})_{reformat}}{Plasma \ Power + LHV_{CH_4 \text{ input}} * \dot{m}_{CH_4 \text{ input}}} * 100 \quad (\%) \quad (8)$$



The specific energy requirements (SER) is defined as the amount of plasma energy used to produce one mole of hydrogen as seen in Equation (10) [3]. The input power is measured in kW, and  $\dot{n}$  is the molar flow rate. In general, as the conversion of fuel to syngas increases, the specific energy requirement (kJ of electrical energy mole<sup>-1</sup> of H<sub>2</sub> produced) decreases [17]. Again the assumption is made that carbon monoxide can later be shifted to produce hydrogen.

$$SER = \frac{Input \ Power}{(\dot{n}_{CO} + \dot{n}_{H_2})_{produced}} \quad (kJ \ mol^{-1} \ H_2 \ produced) \quad (10)$$

Lastly methane conversion is the amount of methane converted divided by the total methane input to the system as seen in equation (11).

$$Methane \ Conversion = \frac{\dot{n}_{CH_4 \text{ in fuel}} - \dot{n}_{CH_4 \text{ in reformat}}}{\dot{n}_{CH_4 \text{ in fuel}}} * 100 \quad (\%) \quad (11)$$

### 2.2.2.1.3 Results and Discussion

This section presents results and discussion for plasma reforming of methane.

#### *Parametric Tests*

##### Gap Distance Parametric Tests

Increasing the gap distance between the electrodes increases the reaction volume and in turn increases the residence time of the gas within the plasma [21]. This allows for the production of more excited species allowing for more complete and uniform reactions. Accordingly keeping the power constant and increasing the gap distance forces the temperature of the gas to decrease while the electron temperature remains high [5]. The increased discrepancy between the electron temperature and gas temperature, in tandem with the increased convective cooling of the arc leads to a more non-thermal plasma [17] where more of the reactions stem from direct electron impact ionization as opposed to stepwise ionization [5].

The gap distance tests ran at two power levels, 160 and 200 W, because with a gap distance of 10 mm the gas mixture did not provide enough resistance to pull 200 W of power from our power supply. The benefits of the increased gap distance can clearly be seen in Figure 2.2.6. The hydrogen yield, selectivity, methane conversion and efficiency all linearly increase in performance. The specific energy requirements decreased dramatically over the first few steps but experienced diminishing returns with the later steps. At 160 W the power supply could no longer sustain the arc at 30 mm and at 200 W failed at 40 mm.

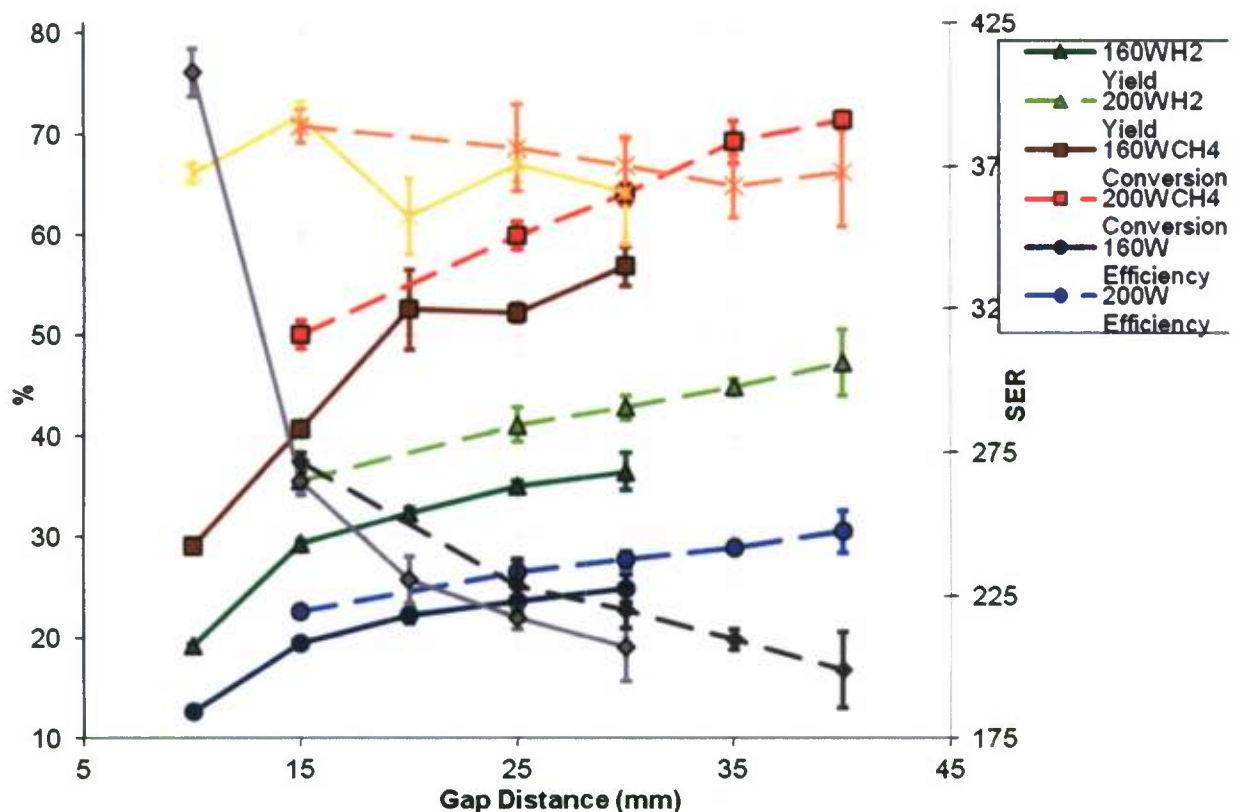


Figure 2.2.6 Summary of gas distance effects on system performance

### Steam Input Parametric Tests

Steam prevented the formation of coke in our reformer; however, increasing steam resulted in poorer performance (Figure 2.2.7). All metrics suffered linearly except for selectivity which stayed relatively constant within its error bars. As the input steam levels increase, so too does the amount of hydrogen that could be theoretically yielded by our system [26]. This is not realized however, because of the increased energy requirements [26] stemming from the steam absorption of electron energy to increase its vibrational energy state [27]. Therefore, ideally the system would run with the absolute minimum steam required to prevent coke formation leaving the bulk of the energy input for methane reforming.



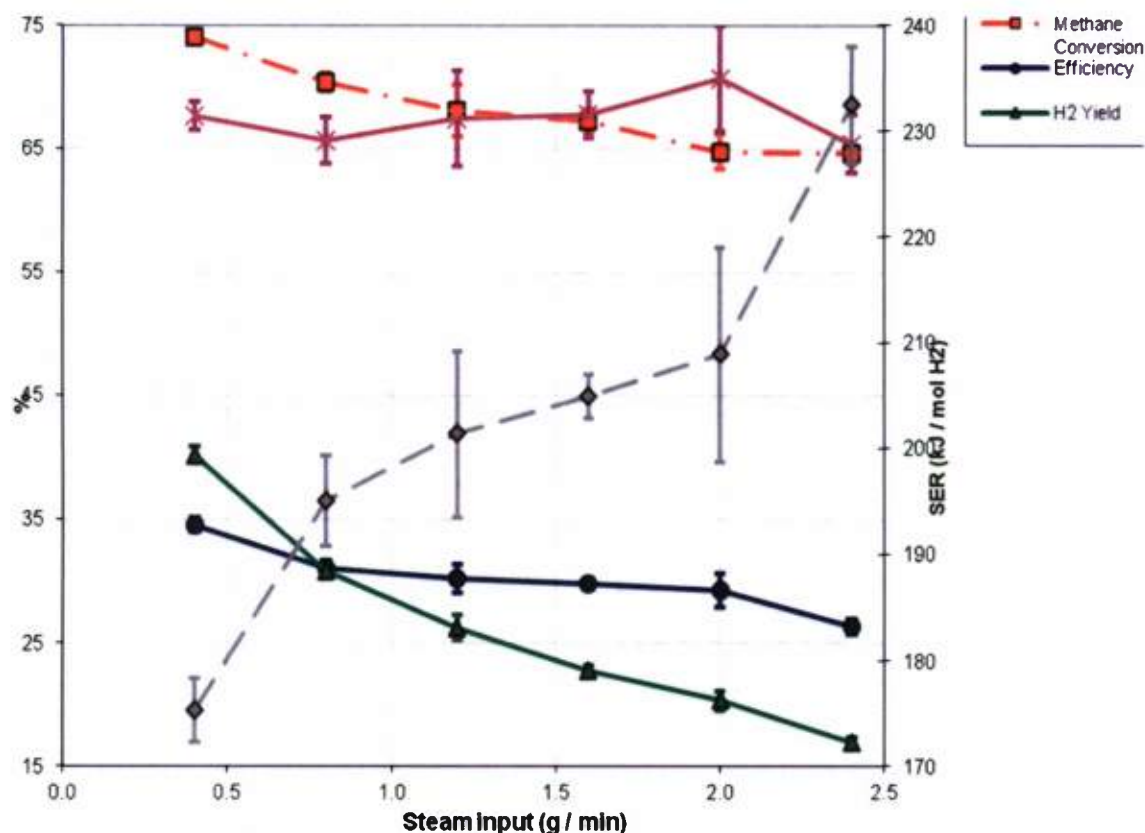


Figure 2.2.7 Summary of the effect of steam input on reactor performance

### Methane Input Parametric Tests

Increasing methane input while holding all other parameters constant lead to a more fuel rich mixture and lower equivalence ratio. Figure 2.2.8 shows that as the methane input increased, the percentage of the methane converted decreased; however, the moles of methane being converted were still increasing. Selectivity, efficiency and hydrogen yield all increased while methane input increased up to 0.8 LPM or an equivalence ratio of 0.71. After this point selectivity, efficiency and hydrogen appeared to have no definite performance changes. Specific energy requirements were the only metric that saw continued increased performance over the entire series of tests.

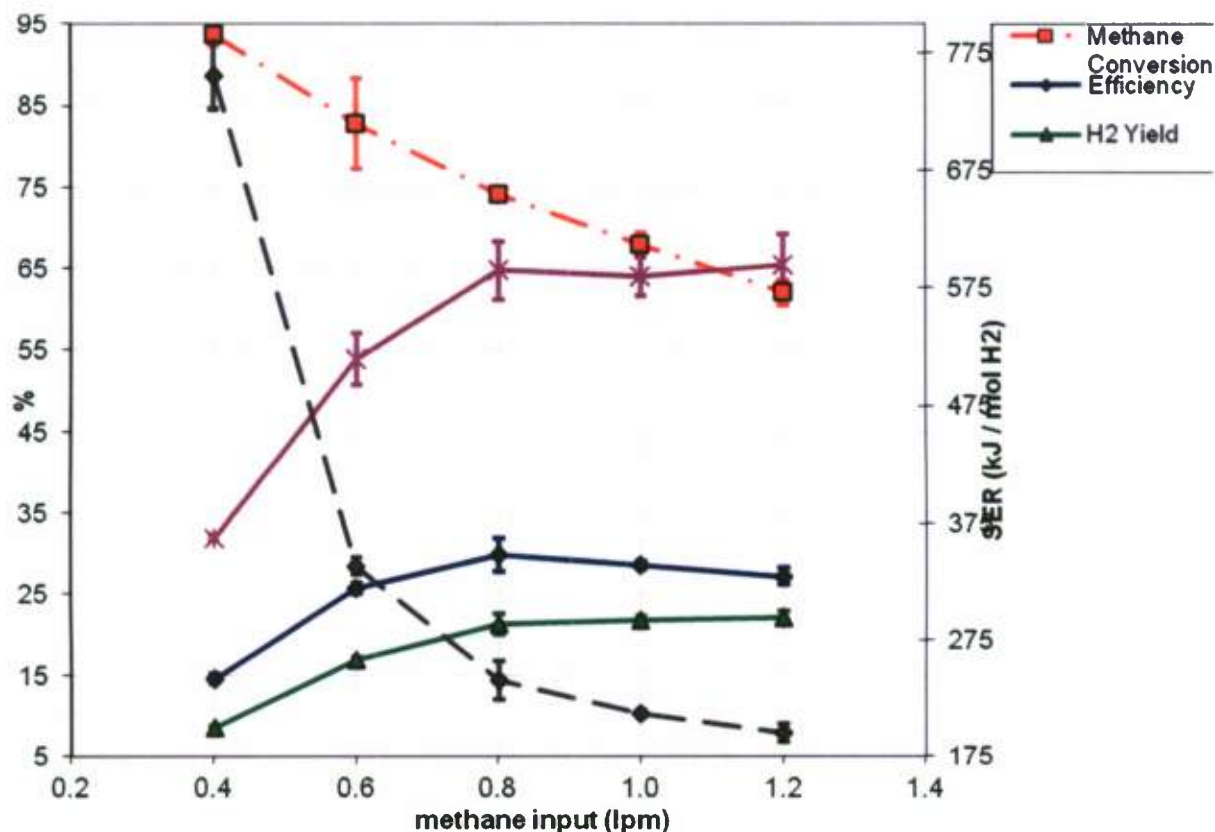
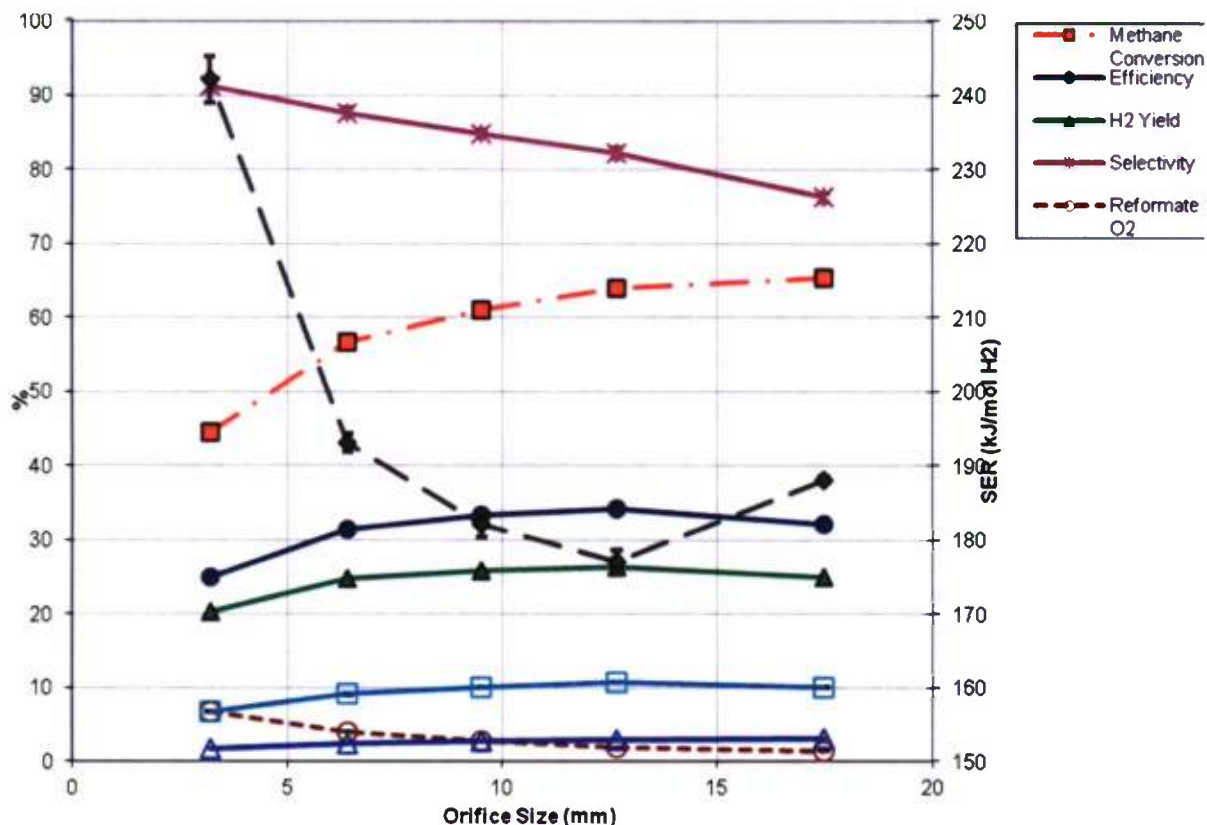


Figure 2.2.8 Summary of effects of methane input on reactor performance

### Orifice Size Parametric Tests

No previously published results have shown the effects of the axial exit orifice size for the reverse vortex flow reformer. Five different orifice sizes ranging from 3.2 to 17.4 mm, with an orifice diameter to reaction chamber diameter ratio of 7.62 to 41.42%, were used for the parametric tests. Figure 2.2.9 shows that the orifice size had significant effects on methane conversion, efficiency, hydrogen yield, selectivity and specific energy requirements. The smallest orifice size had the poorest performance for all metrics except selectivity and methane conversion was the most sensitive metric to orifice size. As the orifice size increased the methane conversion continually increased albeit with diminishing returns. At 12.65 mm efficiency, hydrogen yield, and specific energy requirements all have their best performance.



**Figure 2.2.9 Summary of orifice size effects on reactor performance**

The selectivity dropped fairly linearly over the range of the tests, because the increases in methane conversion realized with increasing orifice diameter did not produce proportional increases in hydrogen yield. As seen in Figure 2.2.9 as the methane conversion increased the reformate oxygen percentage decreased and the carbon monoxide increased. This trend would suggest that the hydrogen from the increased methane conversion was bonding with the oxygen to form additional water vapor. At the same time the injected steam did not react with the carbon monoxide to form  $\text{CO}_2$  and  $\text{H}_2$ .

#### Orifice Size Effects on Arc Attachment Location

It was reported that in the reverse vortex reformer, the arc would ignite between the stationary ring electrode and the axial exit electrode and rotate indefinitely on the inner edge of the axial exit [17]. Experiments have shown, however, that as the axial exit diameter decreased the arc would glide along the upper surface of the electrode rather than the inner edge. This phenomenon increased in frequency as the axial diameter decreased. The gas medium also affected the attachment location. Figure 2.2.10 shows photographs of a 200 W arc during operation with the various orifices in a mixture of 2 lpm nitrogen flow, 0.56 lpm oxygen flow, and 1 lpm methane. As the power level decreased, the arc connection point moved towards the interior of the washer, but not significantly. The frequency of the arc strikes on the inner edge of



the electrode increased significantly when only air was processed; however, not all strikes were on the inner edge as seen in Figure 2.2.11.

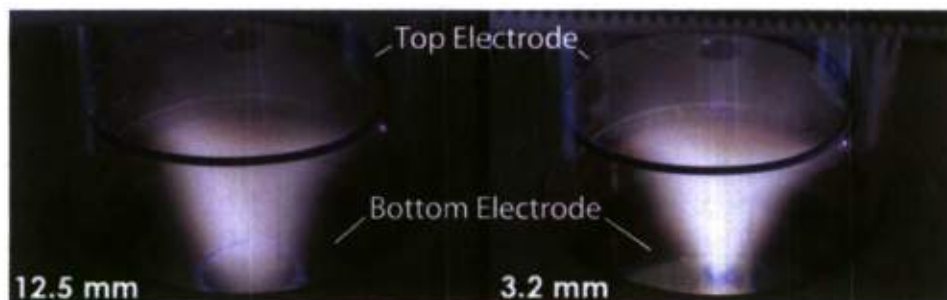


**Figure 2.2.10 Photos of plasma arcs with different orifice sizes**

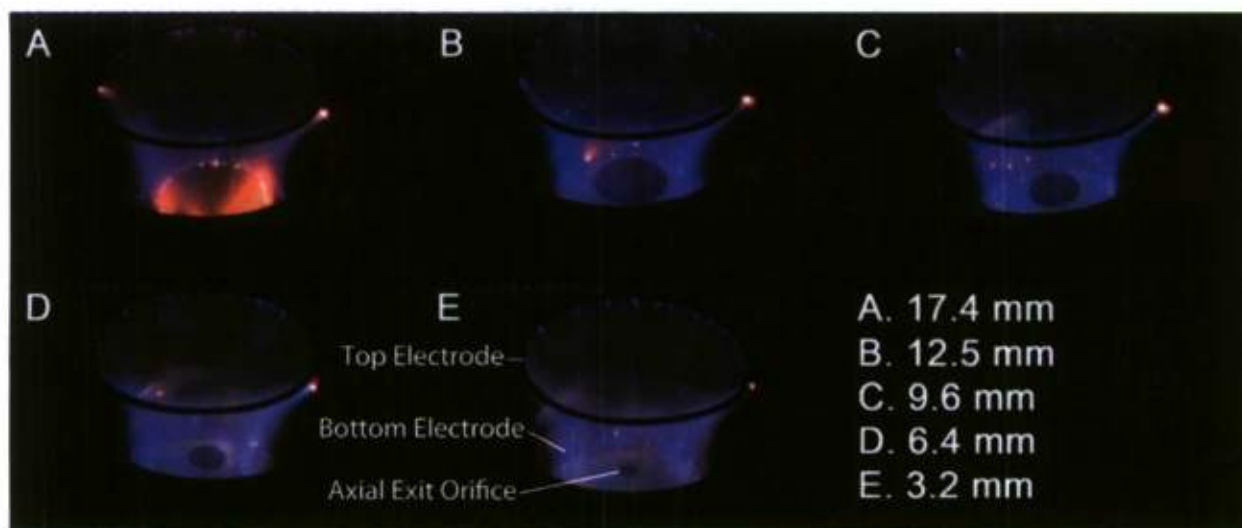


**Figure 2.2.11 Effects of orifice size on arc attachment point at the lower electrode**

The disconnected and inconsistent path of the plasma could have allowed some of the gas to pass without treatment possibly attributing to the poor performance of the smaller orifices. Also the increased axial exit velocity could have led to poor performance with the smaller diameter exit holes, as the gas was in the plasma for a shorter duration. It was originally hypothesized that the plasma would attach to the inner edge of the axial exit at small orifice diameters and would contact a larger fraction of the axial exit flow. The disconnected path completely eliminated this possibility.

#### Power Input Parametric Tests

Power input to the system was dependent on both the maximum power output of the power supply as well as the composition of the gas in the reformer. For example, at standard operating conditions for the parametric tests, with the variable autotransformer providing maximum power, and only nitrogen flowing, the system would draw 200 W of power. When the oxygen, steam,

and methane were added, the increased dielectric strength of the gas allowed for the system to draw 250 W of power.

Figure 2.2.12 shows that increasing the power input to the system increased the values for all of the metrics. Efficiency, hydrogen yield, methane conversion, and selectivity all increased favorably while the performance of the specific energy requirements decreased. The 46% power increase did not produce the same percent increases in the other metrics with hydrogen yield increasing 35% while selectivity only increased 8%. Due to the increases in production the specific energy only increased 9%. By increasing the power to the system the power dissipated per unit length of the arc increases and in turn raises the gas temperature along the arc [5]. This pushes the arc towards a thermal plasma regime and increases the stepwise ionization. Providing more electrons increases the number of radicals and ions available for the reforming of the methane and in turn the system experiences better reforming results at the cost of specific energy requirements.

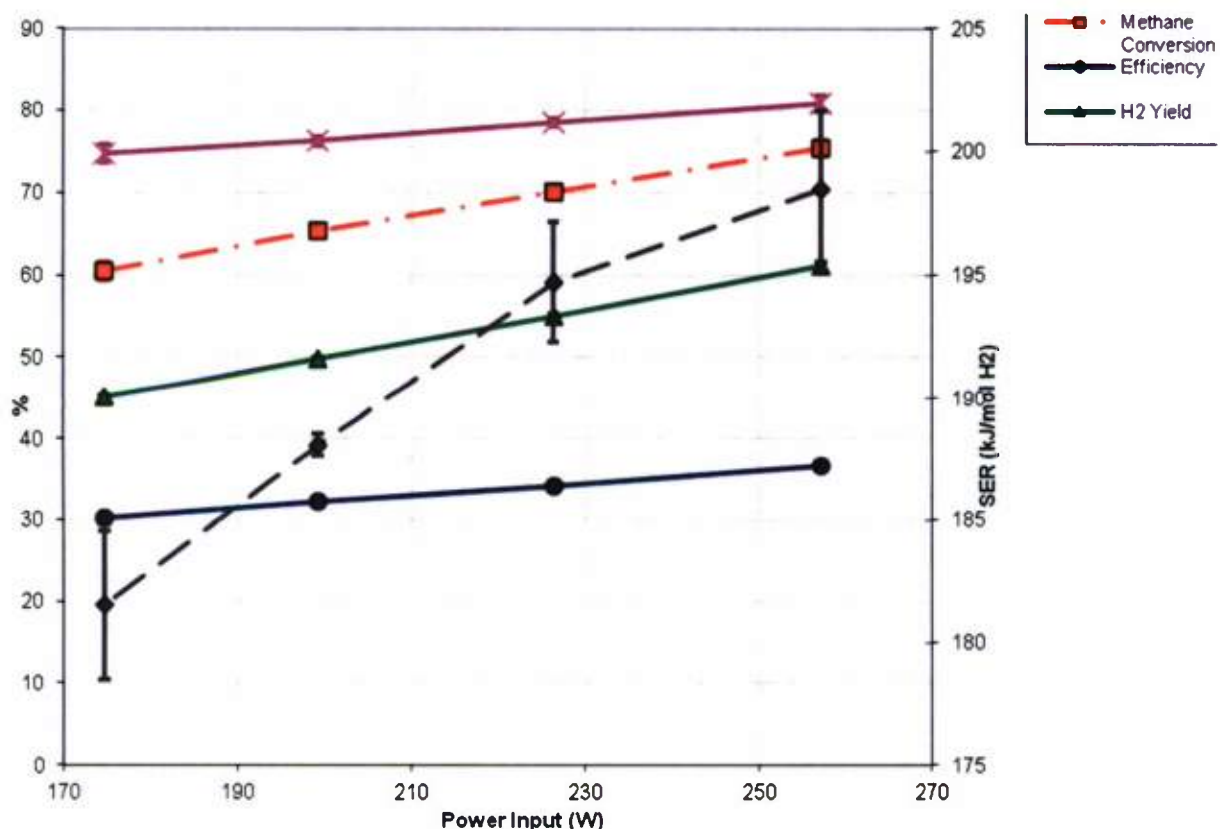


Figure 2.2.12 Summary of the effect of power input on reactor performance

#### Volumetric Flow Rate Parametric Tests

Figure 2.2.13 shows the results of the parametric test investigating the effect of volumetric flow through the reformer. As the volumetric flow rate increased, the gas residence time within the plasma decreased and convective cooling of the arc increased. This was compensated by an

increase in the electric field strength [10,17], which correspondingly increased the electron temperature. Paired with the lower gas temperature within the arc, a more non-thermal plasma developed where direct impact ionization played a larger role in the reforming. Table 2.2.3 shows the design of the parametric test, with a dry inlet flow (total of CH<sub>4</sub>, O<sub>2</sub>, and N<sub>2</sub>) increasing from 1.9 to 5.73 slpm and a total inlet flow (total of CH<sub>4</sub>, O<sub>2</sub>, N<sub>2</sub>, and H<sub>2</sub>O vapor at 25 °C and 1 atm pressure) increasing from 2.24 to 6.74 slpm. Corresponding outlet flow rates of 2.63 to 6.37 slpm (dry) were measured with temperature increasing in tandem linearly from 140 °C to 314 °C.

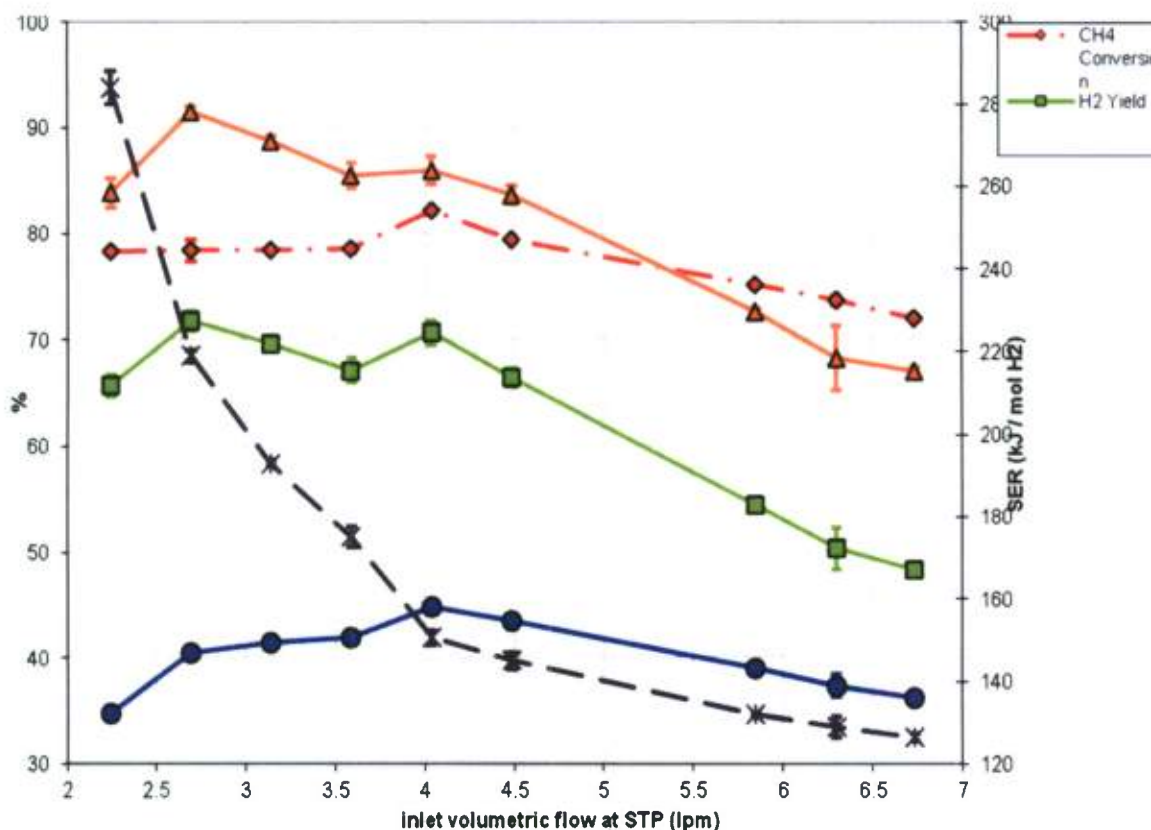


Figure 2.2.13 Summary of reactant flow rate through the reactor on reactor performance



**Table 2.2.3 Input values and reformat flow rates for volumetric flow parametric tests at 260 W and 34.5 mm gap distance**

Inputs						Output
CH4 (lpm)	N2 (lpm)	O2 (lpm)	H2O (g/min)	Dry Gas Flow (slpm)	Saturated Gas Flow (slpm)	Reformat Flow (dry lpm)
0.63	1.00	0.28	0.25	1.91	2.24	2.63
0.75	1.20	0.34	0.30	2.29	2.69	3.04
0.88	1.40	0.39	0.35	2.67	3.14	3.47
1.00	1.60	0.45	0.40	3.05	3.59	3.89
1.13	1.80	0.51	0.45	3.43	4.04	4.38
1.25	2.00	0.56	0.50	3.81	4.48	4.78
1.63	2.62	0.73	0.65	4.97	5.85	5.70
1.75	2.82	0.78	0.70	5.35	6.30	6.11
1.88	3.01	0.84	0.75	5.73	6.74	6.37

The volumetric flow had varying effects on the different performance metrics. Methane conversion and hydrogen selectivity remained relatively unchanged until an input flow of 4.48 slpm, after which they decreased linearly. Efficiency had a maximum at the 4.48 slpm flow rate while the specific energy requirements benefited the most from the increase in flow rate. As the flow increased, the SER logarithmically decayed to a minimum of 126 kJ mol<sup>-1</sup>. This is due to the increase in hydrogen and carbon monoxide production while keeping the arc power consumption constant.

#### *First Full Factorial Test*

All of the operating conditions within the first factorial experimental design produced valid data, i.e. none of the conditions produced inordinate amounts of soot or caused unstable conditions for the plasma arc. Each point for the factorial test was ran four times to ensure reproducibility. This allowed for the complete analysis of the factor space around the center point. As seen in Table 2.2.4, which presents the main and interaction effects, the variables changed the metrics at varying rates. Methane input affected methane conversion, SER and selectivity the most while the gap distance had the strongest affect on hydrogen yield and efficiency was most susceptible to steam input. Interestingly increasing the power input had no discernable effect on hydrogen yield, efficiency and selectivity. Methane conversion experienced an interaction between power input and gap distance which was 50% higher than the error estimated by the fourth order effect for methane conversion. Accordingly the affect of increasing the gap distance and power input in tandem out perform the effects power input and gap distance have on the system independent of each other. No other metrics had significant second or third order effects and can be said to independently affect the system performance.

**Table 2.2.4 Summary of results of the first factorial design showing main and higher order effects**

	Methane Conversion %	Hydrogen Yield %	SER kJ / mol	Efficiency %	Selectivity %
A (power)	2.41	1.90	16.52	0.26	0.40
B (methane)	-8.63	-1.28	-41.53	1.47	6.04
C (steam)	-3.27	-4.40	21.21	-3.17	-2.24
D (gap)	3.20	4.67	-18.40	2.65	2.94
AB	-0.20	-1.31	4.01	-0.29	-1.47
AC	-0.01	-1.83	6.75	-0.62	-2.56
AD	1.04	1.62	-8.75	0.95	1.20
BC	-0.02	-1.26	5.15	-0.73	-1.27
BD	0.30	1.82	-4.79	0.74	2.04
CD	0.33	1.45	-7.30	0.49	1.73
ABC	0.02	-0.58	2.60	-0.01	-1.48
ABD	0.03	1.61	-6.29	0.70	2.16
ACD	0.29	1.32	-5.32	0.41	1.49
BCD	0.59	0.66	-2.92	0.06	0.98
ABCD	0.68	2.25	-8.48	0.94	2.45
indicates significant effect					

### *Second Full Factorial Test*

A path of steepest ascent from the first factorial test led to a center point for the second test condition, which bordered the physical limits of system operation. This point was characterized by steam input of 0.4 g min<sup>-1</sup>, CH<sub>4</sub> input of 1.36 lpm, a gap of 36.6 mm, and power input of 250 W. Because the system operated near the physical limits of the system several combinations of the independent variables revealed failure methods due to soot formation or arc extinction as seen in Table 2.2.5. Both of these failure modes are discussed in depth in sections 3.10.1 and 3.10.2 respectively. Test points 6 and 7 resulted in the highest values of the performance indicators. Because several sets of operating conditions could not consistently run for four tests, a complete analysis of the factor space and interaction effects could not be performed. The main effects and interaction effects that could be calculated are reported in Table 2.2.6.

**Table 2.2.5 Design for second factorial tests and results for performance metrics**

Run	A (W)	B (CH <sub>4</sub> )	C H <sub>2</sub> O	D Gap	Methane Conversion	H <sub>2</sub> Yield %	Efficiency %	SER kJ/ Mol H <sub>2</sub>	Selectivity %
1	-1	-1	-1	-1	77.01	61.37	41.70	141.36	79.68
2	1	-1	-1	-1	74.65	59.49	39.98	155.89	79.69
3	-1	1	-1	-1	62.58	47.51	33.89	154.56	75.92
4	1	1	-1	-1	64.18	49.11	34.46	161.61	76.52
5	-1	-1	1	-1	76.70	62.32	42.11	140.54	81.25
6	1	-1	1	-1	79.77	66.45	43.52	144.11	83.31
7	-1	1	1	-1	69.18	56.07	38.70	136.43	81.05
8	1	1	1	-1	73.11	59.94	40.53	137.92	81.99
9	-1	-1	-1	1	76.22	60.44	41.03	143.78	79.30
10	1	-1	-1	1	76.33	63.02	41.67	149.75	82.56
11	-1	1	-1	1	75.72	38.34	34.67	0.00	50.63
12	1	1	-1	1	69.91	54.95	38.01	146.51	78.60
13	-1	-1	1	1	76.38	62.84	42.31	139.43	82.27
14	1	-1	1	1	79.87	65.85	43.31	144.52	82.44
15	-1	1	1	1	DNR	DNR	DNR	DNR	DNR
16	1	1	1	1	72.21	59.85	40.51	138.28	82.89

Soot Production Fail
Arc Extinction Fail

Best Performance for Metric
DNR : Did Not Run

**Table 2.2.6 Summary of results of the second factorial design showing main and higher order effects**

effect (% data incomplete)	Methane Conversion	Hydrogen Yield	SER	Efficiency	Selectivity
A (power) (37.5)	1.65	2.34	6.13	0.63	1.29
B (methane) (62.5)	-7.28	-6.25	-5.52	-3.06	-0.36
C (steam) (50)	2.13	3.28	-5.54	1.71	2.01
D (gap) (37.5)	-0.04	0.49	-0.81	0.20	0.71
AB (75)	1.43	0.95	-2.90	0.75	-0.22
AC (50)	2.31	1.66	-3.44	0.98	-0.29
AD (75)	0.13	0.38	-0.50	0.16	0.36
BC (100)	NA	NA	NA	NA	NA
BD (75)	-0.29	0.19	-0.54	0.20	0.60
CD (50)	-0.28	-0.67	0.75	-0.26	-0.58
ABC (100)	NA	NA	NA	NA	NA
ABD (100)	NA	NA	NA	NA	NA
ACD (50)	0.23	-1.25	2.55	-0.66	-1.92
BCD (100)	NA	NA	NA	NA	NA
ABCD* (100)	-0.05	0.48	-3.00	0.28	0.66

In order to calculate effects, the differences between the high and low levels at a given condition must be known. If an effect was defined by 4 high and low sets, yet one low point failed, the remaining three points were utilized and the data said to be 25% incomplete, which is noted in the first column of Table 2.2.6. In this way most second order effects could be calculated, yet



most of the third order effects could not be calculated due to missing data. The fourth order effects are not averaged sets of data. Instead the differences between high and low values comprise them and the missing conditions were simply omitted, which leads to a limited certainty of the value of the fourth order effects shown\*.

As can be seen in Table 2.2.6, selectivity's main effects for the four independent variables were less than the previous factorial test suggesting that an optimum was being approached. Only power input and steam input may still have effects on the selectivity of the system. Because of power supply limitations it was not possible to further pursue the effects of increasing power input. Further decreasing steam input was also not possible beyond this point because soot would be produced as explained in section 3.10.2. Thus as it stands, the best selectivity that can be achieved with our current system is  $83.3 \pm 0.85\%$  at flow rates of 2 slpm  $N_2$ , 0.56 slpm  $O_2$ , 1.25 slpm  $CH_4$ , 0.6 g steam  $min^{-1}$ , a gap distance of 34.5 mm and a power input of 260 W with an equivalence ratio of 0.224. At this point a hydrogen to carbon monoxide ratio of 2.14 was produced with a total dry reformat flow rate of 4.68 slpm comprised of 35.53%  $H_2$ , 16.58%  $CO$ , 0.23%  $O_2$ , 1.42%  $CO_2$ , 5.69%  $CH_4$ , and 40.56%  $N_2$ .

### *Operational Limits of System Reforming*

The second factorial experiment identified operational limits where the system could not operate successfully. Two different failure modes were encountered. The first occurred when the arc would extinguish and could not reignite. The second failure mode resulted from excessive soot production.

As shown in Table 2.2.5 the reformer operated initially for points 11, 12, and 15, however, after times ranging from 3 to 20 minutes the arc extinguished and failed to reestablish. The arc could be reignited by flushing the system with nitrogen. The extinguishment of the arc was likely due to the combination of the large gap distance and high dielectric strength of the gas mixture caused by the higher methane percentages in the feed gas. Harvey and Lemmon propose a method for calculating the dielectric constant for dry natural gas mixtures. Their method was employed to determine the dielectric constant for the gas mixture within the reaction chamber [28]. The densities of the gases were obtained from Cengel's Fluid Mechanics: Fundamentals and Applications [29]. It was found that increasing the methane percentage within the gas mixture in turn increased the mixture's dielectric strength. Both gap distance and methane flow rate were at their +1 value for operating points 11, 12, and 15. .

Point 16 from Table 2.2.5 successfully operated for 50 minutes without arc failure whereas the arc extinguished for point 12. The differences in operating conditions are the steam flows, (0.2 and 0.6 g  $min^{-1}$  for points 12 and 16, respectively) and the concomitant flow rates. Increased steam flow would be expected to increase the dielectric constant of the gas and the increased gas flow rate would lead to increased convective cooling of the arc and therefore increase non-thermal characteristics. Whether the combined effects of these two phenomena are sufficient to explain the difference in arc behavior observed at the two test conditions warrants further investigation.

### *Soot Formation*

Due to the low temperature nature of the non-thermal plasma reaction [8] and the fast rotation of the gliding arc [9], the soot production is minimized, and almost completely abated by

introducing steam. Points 3 and 4 in Table 2.2.5 of the final factorial test both failed due to excessive soot production. Both conditions were characterized by high methane input with an equivalence ratio of 0.193, and low steam input. Points 11 and 12 also shared these operating conditions however they failed due to arc extinction. Soot deposits could be seen on the reactor walls during operation of points 3 and 4. After enough soot had stuck to the reactor walls the plasma arc would attach to the carbon deposits instead of breaking down the gas medium. Steady operating conditions were realized at a slightly higher equivalence ratio of 0.224.

#### **2.2.2.1.4. Conclusions**

This experimental investigation included the design, fabrication, and testing of a reverse vortex flow non-thermal plasma reactor to study how system parameters affect methane reforming. Electrode gap distance, equivalence ratio, steam input, power input and the axial exit orifice diameter all determined the system performance. The parametric test determined decreasing the axial exit diameter degraded system performance, and an orifice diameter to reformer diameter ratio of 41% proved optimal. In regards to methane conversion an interaction between power input and the electrode gap distance exists. Steam, while preventing soot formation, absorbed energy from the plasma and became vibrationally excited, thus decreasing steam input increased methane conversion and hydrogen production.

The factorial tests showed that with an electrode gap of 38.5 mm and an equivalence ratio of 0.193, the 250 W power supply could not sustain a plasma arc. A smaller electrode gap or a higher equivalence ratio produced conditions where an arc was established and the system operated. Without sufficient steam, soot began to form at a H<sub>2</sub>O to carbon ratio less than 0.4 and equivalence ratios less than 0.193, which is very low due to the non-thermal characteristics of the plasma and low operating temperature of the reformer. Assuming that all non-converted methane could later be reprocessed or utilized in some way, at inputs of 2 slpm N<sub>2</sub>, 0.56 slpm O<sub>2</sub>, 1.25 slpm CH<sub>4</sub>, 0.6 g steam min<sup>-1</sup>, a gap distance of 34.5 mm and a power input of 260 W, the best system response was achieved using selectivity as the performance indicator. At this point the reformat was comprised of 35.53% hydrogen, 0.23% oxygen, 16.58% carbon monoxide, 1.42% carbon dioxide and 5.69% methane. The system operated at a steady temperature of 271 °C with a reactor outlet diameter of 12.5 mm. At this point selectivity was found to be 83.3% while other performance indicators were as follows: methane conversion – 79.8%, hydrogen yield – 66.5%, efficiency – 43.5%, and a specific energy requirement of 144 kJ mol<sup>-1</sup> of hydrogen produced.

#### **2.2.2.2 Liquid Fuel Introduction**

Introducing liquid fuels into the reformer presents challenges. First, the plasma must uniformly treat the fuel in order to have a uniform product. If liquid fuel bypasses the plasma it remains unreformed and has to be retreated or processed as waste. Initial research focused on methods to introduce liquid fuel to the system. Options included vaporization of the fuel and utilization of a nozzle to introduce liquid fuel to the system. Vaporization processes were initially rejected as most of them involved partial oxidation of the fuel within the vaporizer. This consumes additional energy and partially replaces the functions of the plasma.

Traditional nozzles develop their spray pattern via both high pressure and liquid velocity. The low volumetric flow rates we utilize in our system do not allow for the high velocity needed to



develop small particles. Needing to electrically isolate the fuel stream from the fuel delivery system prohibited us from pressurizing our fuel and disallowed a constant fuel feed. Thus the droplets produced by a traditional nozzle were too large to be entrained in the gas flow pattern, and treated during their short time in contact with the plasma. An effervescent nozzle, where carrier gas assists the liquid through the nozzle tip, decreased the droplet size. However large conglomerates of fuel passed through the nozzle without dispersion. These conglomerates were too large for the plasma to reform (Figure 2.2.14).

### Dodecane introduction to non-thermal plasma in reverse vortex flow plasma reformer via effervescent nozzle.

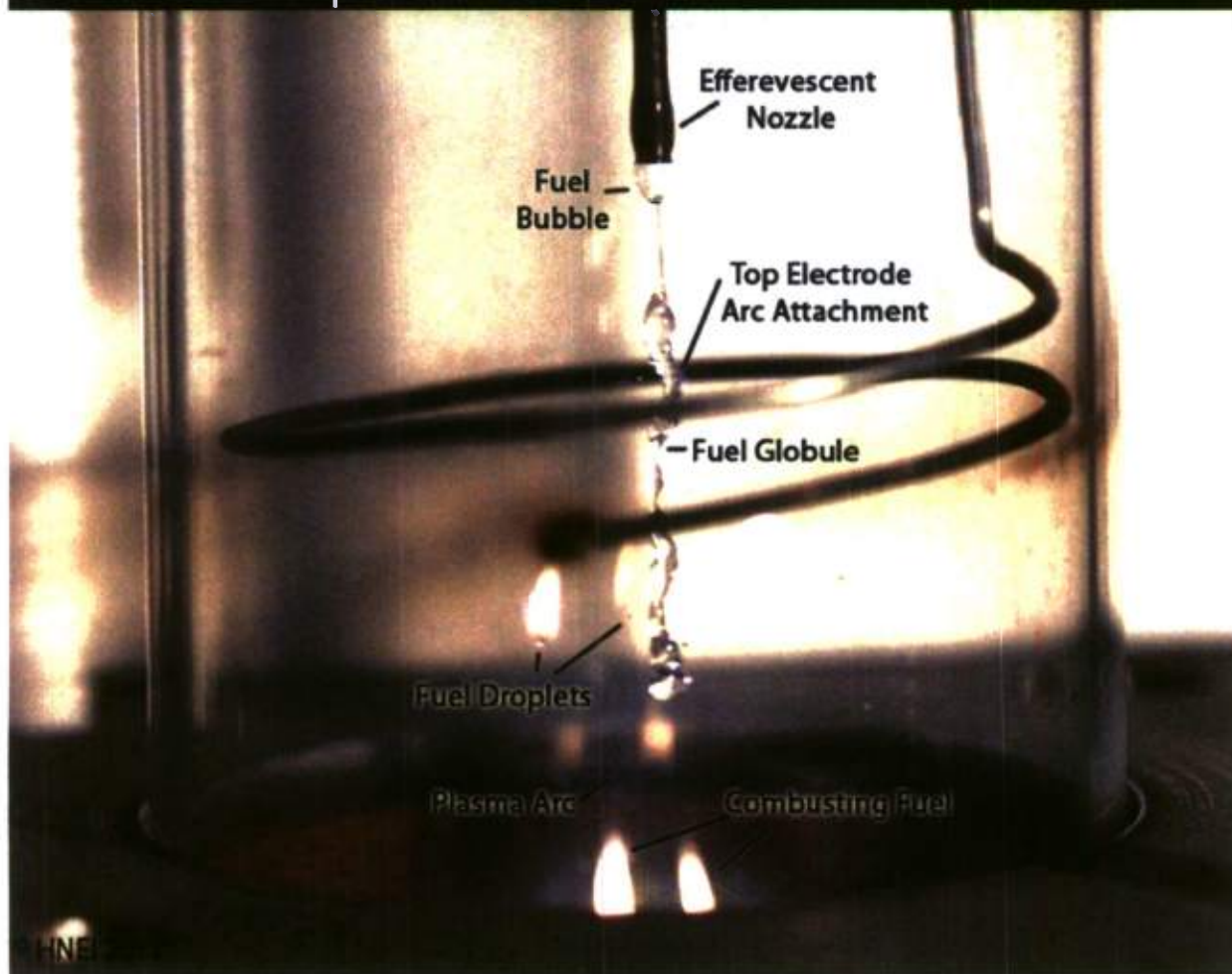


**Figure 2.2.14 Fuel globule during effervescent nozzle operation**

Ultimately we arrived at a Sonozap HTNS40K50 high operating temperature ultrasonic nozzle for the atomization of the fuel. The ultrasonic nozzle can produce droplets typically ranging from 1 to 56  $\mu\text{m}$  in diameter with a median drop size of 7  $\mu\text{m}$  at flow rates up to 50  $\text{ml min}^{-1}$ . This allowed us to attempt to entrain the droplets in a carrier gas and to directly inject the fuel



into the reformer, the latter method being adopted by our system. High-speed imaging of fuel injection allowed us to find a power level for the ultrasonic generator which developed a steady flow of particles (Figure 2.2.15) and a narrow particle spray pattern within the reverse vortex flow which does not excessively coat the reactor tube walls (Figure 2.2.16).

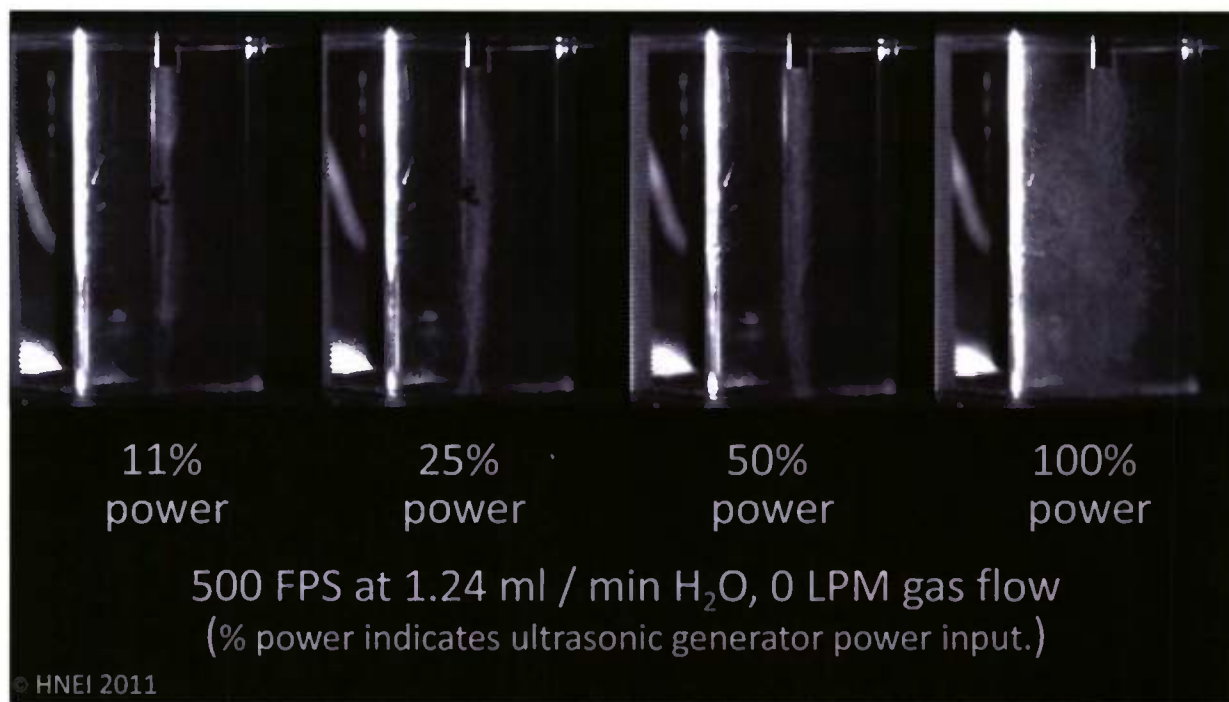


**Figure 2.2.15 Ultrasonic Injection to reformer chamber, no gas flow**

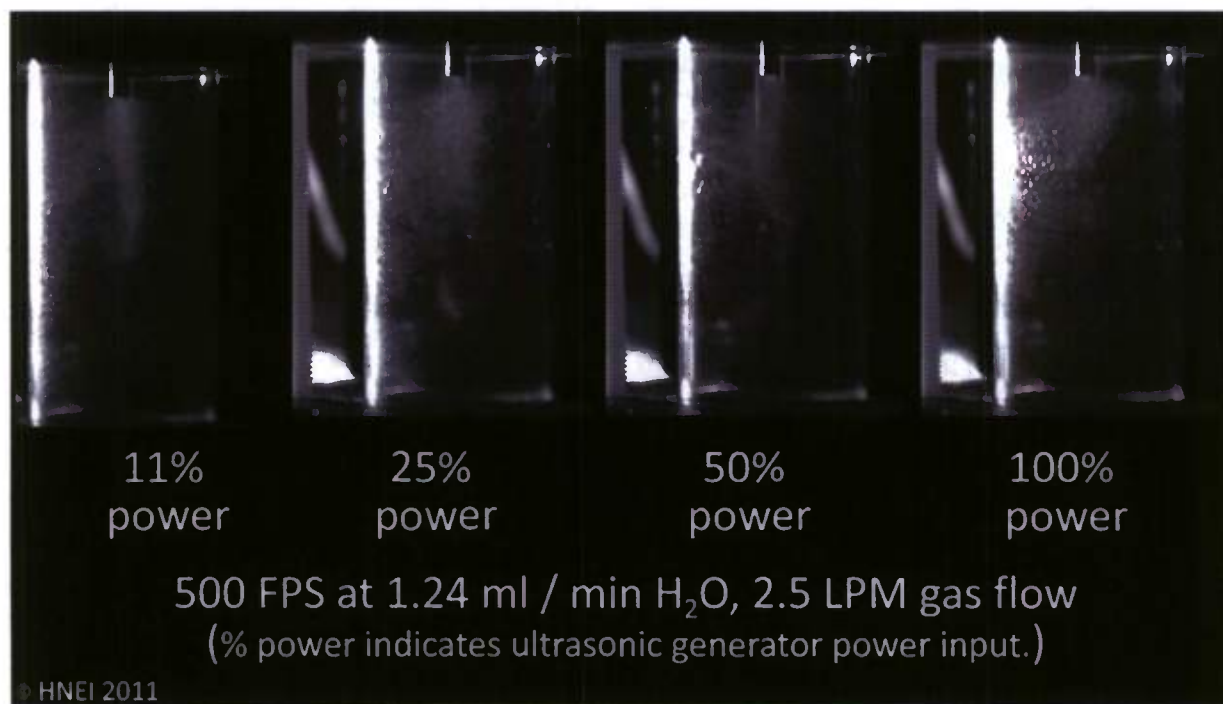


**Figure 2.2.16 Ultrasonic Injection to reformer chamber, 2.5 LPM gas flow in reverse vortex**

Injecting the fuel along the axis of the top reaction chamber allows the fuel droplets direct contact with the plasma. This is paramount to the experiment and required a redesign of the reactor chamber to insure the electrical isolation of the nozzle from the electrodes. The methane reformer had the top electrode suspended into the reaction chamber through the top plate. The proximity of the electrode in this position to the nozzle would cause a short through the nozzle's electric system, either destroying the nozzle, the power supply, arcing through the fuel lines or some unfortunate combination of failure methods.

### *System Design*

The redesign included suspending the top electrode within the reaction chamber through a mount that sits between two quartz tubes forming the top reaction chamber. To avoid arcing from the middle plate to the top electrode's lead outside of the reaction chamber, we had the middle plate reconstructed from zirconia. This allows for electrical isolation of the electrodes while still providing adequate tensile strength and thermal shock resistance for the middle plate. The redesigned reactor is seen in Figure .

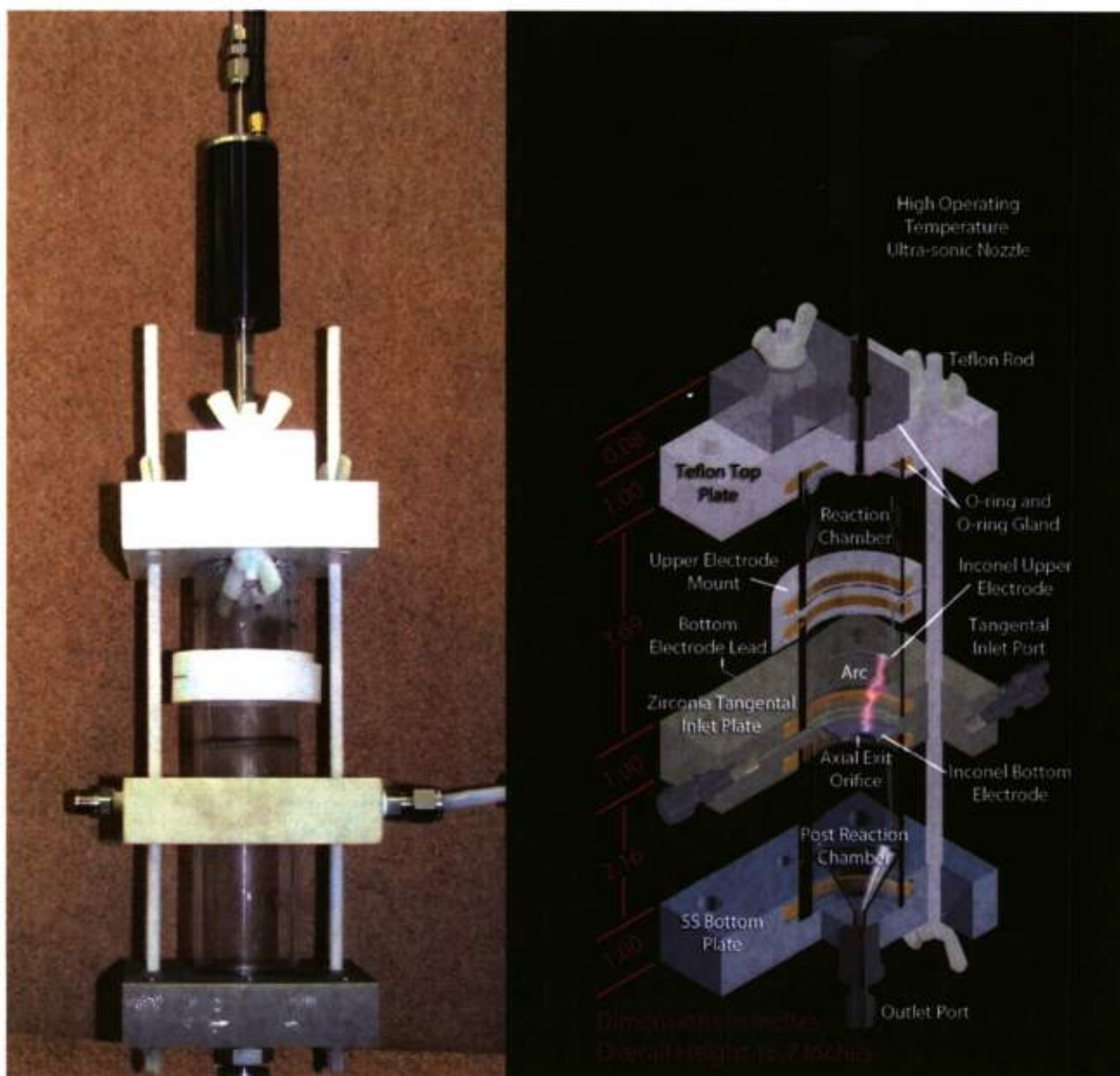


**Figure 2.2.17 Liquid fuel reformer image and diagram**

The byproduct of this system can range from simple hydrogen gas to unreformed dodecane in liquid form. We redesigned the back end of our system to capture the liquid reformat and to condition and analyze the gas in real time. The liquid reformat will be analyzed after tests have run.

We performed thermal and leak testing of the system and found no problems. Currently we are making final modifications to the back end of the system with only volumetric flow control and reintegration of the analyzers remaining. Figure 2.2.18 shows the entire test bed. With the addition of the liquid fuel delivery system, we cannibalized the front end of the system from the methane reforming test bed. The reformer was completely redesigned and fabricated, and the back end of the system modified to handle liquid reformat. After final modifications parametric and factorial tests will be designed to characterize the performance of the reformer.



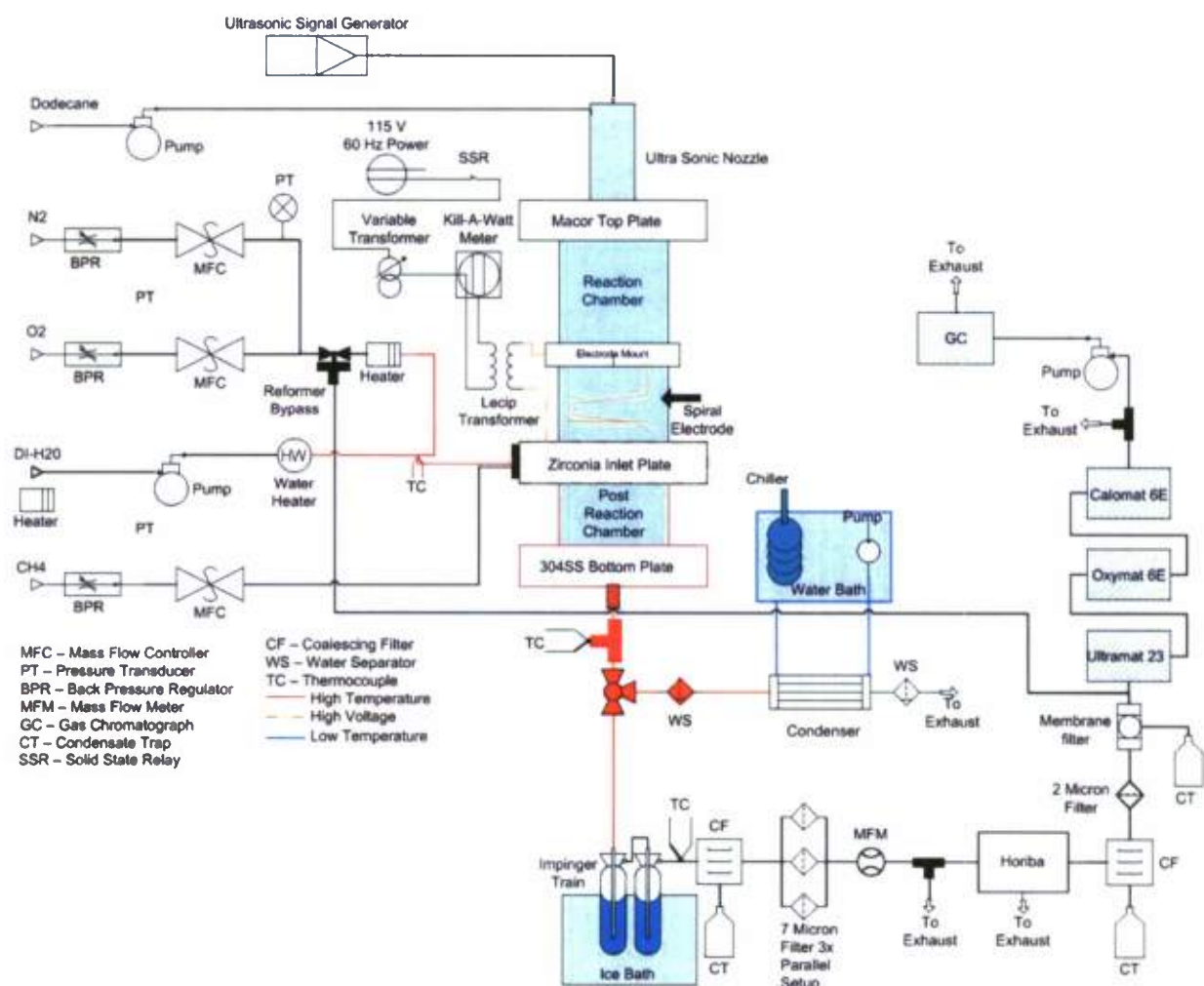


Figure 2.2.18 Reverse vortex flow non-thermal plasma liquid reforming test bed

### 2.2.2.3 Numerical modeling

The numerical modeling effort for the plasma arc project has been initiated under FY08 funding. A postdoctoral fellow, Dr. Gautier Picot, has been hired under the supervision of Dr. Marcelo Kobayashi from the University of Hawaii Department of Mechanical Engineering.

### 2.2.3 References

- [1] Mueller-Langer, F., Tzimas, E., Kaltschmitt, M., Peteves, S., 2007. Techno-economic assessment of hydrogen production processes for the hydrogen economy for the short and medium term. *Int J Hydrogen Energy* 32, 3797-3810.
- [2] Yang, C., Ogden, J., 2007. Determining the lowest-cost hydrogen delivery mode. *Int J Hydrogen Energy* 32, 268-286.

- [3] Petitpas, G., Rollier, J.D., Darmon, A., Gonzalez-Aguilar, J., Metkemeijer, R., Fulcheri, L., 2007. A comparative study of non-thermal plasma assisted reforming technologies. *Int J Hydrogen Energy* 32, 2848-2867.
- [4] Chun, Y.N., Song, H.W., Kim, S.C., Lim, M.S., 2008. Hydrogen-Rich Gas Production from Biogas Reforming Using Plasmatron. *Energy Fuels* 22, 123-127.
- [5] Fridman, A., 2008. *Plasma Chemistry*, first ed. Cambridge University Press, New York, NY.
- [6] Muta-Yardimci, O., Saveliev, A.V., Fridman, A.A., Kennedy, L.A., 2000. Thermal and nonthermal regimes of gliding arc discharge in air flow. *J Appl Phys* 87, 1632-1641.
- [7] Indarto, A., Choi, J.-W., Lee, H., Song, H.K., 2006. Effect of additive gases on methane conversion by using gliding arc discharge. *Energy* 31, 2986-2995.
- [8] Fridman, A., Nester, S., Kennedy, L.A., Saveliev, A., Muta-Yardimci, O., 1999. Gliding arc gas discharge. *Prog Energ Combust* 25, 211-231.
- [9] Kalra, C.S., Gutsol, A.F., Fridman, A.A., 2005. Gliding arc discharges as a source of intermediate plasma for methane partial oxidation. *IEEE T Plasma Sci* 33, 32-41.
- [10] Kalra, C.S., Kossitsyn, M., Iskenderova, K., Chirokov, A., Cho, Y.I., A.Gutsol, Fridman, A., 2003, Electrical discharges in the Reverse Vortex Flow – Tornado Discharges, Accessed: 8/6/2008, <http://plasma.mem.drexel.edu/publications/documents/ISPC-16-565-Tornado.pdf>
- [11] Bromberg, L., Cohn, D.R., Rabinovich, A., Alexeev, N., 1999. Plasma catalytic reforming of methane. *Int J Hydrogen Energy* 24, 1131-1137.
- [12] Sobacchi, M.G., Saveliev, A.V., Fridman, A.A., Kennedy, L.A., Ahmed, S., Krause, T., 2002. Experimental assessment of a combined plasma/catalytic system for hydrogen production via partial oxidation of hydrocarbon fuels. *Int J Hydrogen Energy* 27, 635-642.
- [13] Paulmier, T., Fulcheri, L., 2005. Use of non-thermal plasma for hydrocarbon reforming. *Chem Eng J* 106, 59-71.
- [14] Burlica, R., Kirkpatrick, M.J., Locke, B.R., 2006. Formation of reactive species in gliding arc discharges with liquid water. *J. of Electrostat* 64, 35-43.
- [15] Lee, D.H., Kim, K.-T., Cha, M.S., Song, Y.-H., 2007. Optimization scheme of a rotating gliding arc reactor for partial oxidation of methane. *Optimization scheme of a rotating gliding arc reactor for partial oxidation of methane* 31, 3343-3351.
- [16] Richard, F., Cormier, J.M., Pellerin, S., Chapelle, J., 1996. Physical study of a gliding arc discharge. *Physical study of a gliding arc discharge* 79, 2245-2250.
- [17] Kalra, C.S., Cho, Y.I., Gutsol, A., Fridman, A., Rufael, T.S., 2005. Gliding arc in tornado using a reverse vortex flow. *Rev Sci Instrum* 76, 0251101 - 0251107.
- [18] Rusu, I., Cormier, J.-M., 2003. On a possible mechanism of the methane steam reforming in a gliding arc reactor. *Chem Eng J* 91, 23-31.
- [19] Douette, A.M.D., Turn, S.Q., Wang, W., Keffer, V.I., 2007. Experimental Investigation of Hydrogen Production from Glycerin Reforming. *Experimental Investigation of Hydrogen Production from Glycerin Reforming* 21, 3499-3504.
- [20] Czernichowski, A., 2001. GlidArc assisted preparation of the synthesis gas from natural and waste hydrocarbons gases. *Oil Gas Sci Technol* 56, 181-198.

- [21] Sreethawong, T., Thakonpatthanakun, P., Chavadej, S., 2007. Partial oxidation of methane with air for synthesis gas production in a multistage gliding arc discharge system. *Int J Hydrogen Energy* 32, 1067-1079.
- [22] Narvaez, I., Orio, A., Aznar, M.P., Corella, J., 1996. Biomass Gasification with Air in an Atmospheric Bubbling Fluidized Bed. Effect of Six Operational Variables on the Quality of the Produced Raw Gas. *Ind. Eng. Chem. Res.* 35, 2110-2120.
- [23] Bhat, S.A., Sadhukhan, J., 2008. Process intensification aspects for steam methane reforming: an overview. *Process intensification aspects for steam methane reforming: an overview* 55, 408-422.
- [24] Rollier, J.-D., Gonzalez-Aguilar, J.x., Petitpas, G., Darmon, A., Fulcheri, L., Metkemeijer, R., 2008. Experimental Study on Gasoline Reforming Assisted by Nonthermal Arc Discharge. *Experimental Study on Gasoline Reforming Assisted by Nonthermal Arc Discharge* 22, 556-560.
- [25] Galvita, V., Messerle, V.E., Ustimenko, A.B., 2007. Hydrogen production by coal plasma gasification for fuel cell technology. *Hydrogen production by coal plasma gasification for fuel cell technology* 32, 3899-3906.
- [26] Biniwale, R.B., Mizuno, A., Ichikawa, M., 2004. Hydrogen production by reforming of iso-octane using spray-pulsed injection and effect of non-thermal plasma. *Hydrogen production by reforming of iso-octane using spray-pulsed injection and effect of non-thermal plasma* 276, 169-177.
- [27] Hammer, T., Kappes, T., Baldauf, M., 2004. Plasma catalytic hybrid processes: gas discharge initiation and plasma activation of catalytic processes. *Catalysis Today: Plasma Technology and Catalysis* 89, 5-14.
- [28] Harvey, A.H., Lemmon, E.W., 2005. Method for Estimating the Dielectric Constant of Natural Gas Mixtures. *Int J Thermophys* 26, 31-46.
- [29] Cengel, Y.A., Cimbala, J.M., 2010. *Fluid mechanics: fundamentals and applications*. McGraw-Hill Higher Education, Boston, MA.

#### **2.2.4 Papers and Presentations Resulting from Efforts**

A manuscript entitled, "An experimental investigation of reverse vortex flow plasma reforming of methane," has been submitted to the *International Journal of Hydrogen Research*. Initial reviews have been received and revisions are underway prior to resubmission.

### **2.3 Thermocatalytic Conversion of Synthesis Gas into Liquid Fuels**

Fischer-Tropsch (FT) synthesis is an important reaction of industrial interest for the development of new energy technologies as well as the production of liquid fuels from natural resources such as biomass, coal, or natural gas. These natural resources are converted to synthesis gas (a mixture of  $H_2$  and CO) by gasification and reforming technologies. The synthesis gas is then utilized to produce liquid fuels by FT and hydrocracking technologies. Biomass has recently received increased attention as a potential source of renewable energy. Among all biomass conversion technologies, the biomass-to-liquid (BTL) process is one of the most promising for the production of sulfur-free transportation fuels. From this viewpoint, the



FT reaction can be applied to produce a clean fuel from biomass through the use of a suitable catalyst.

About 50 percent of primary energy consumption in the United States is derived from imported oil that contains precursors to the criteria pollutants  $\text{SO}_x$ ,  $\text{NO}_x$  and particulate matter. Energy policy in the United States has encouraged the development of alternative fuels to reduce dependency on foreign fuel imports and reduce  $\text{CO}_2$  emissions responsible for global warming. FT fuels produced from biomass, can contribute to solutions for global energy and environmental problems. As a result, catalyst development is strongly desired to produce FT fuels from renewable resources. The overall process includes three main steps including reforming or gasification, FT reaction, and product upgrading. An illustration of this plan is shown in Figure 2.3.1.

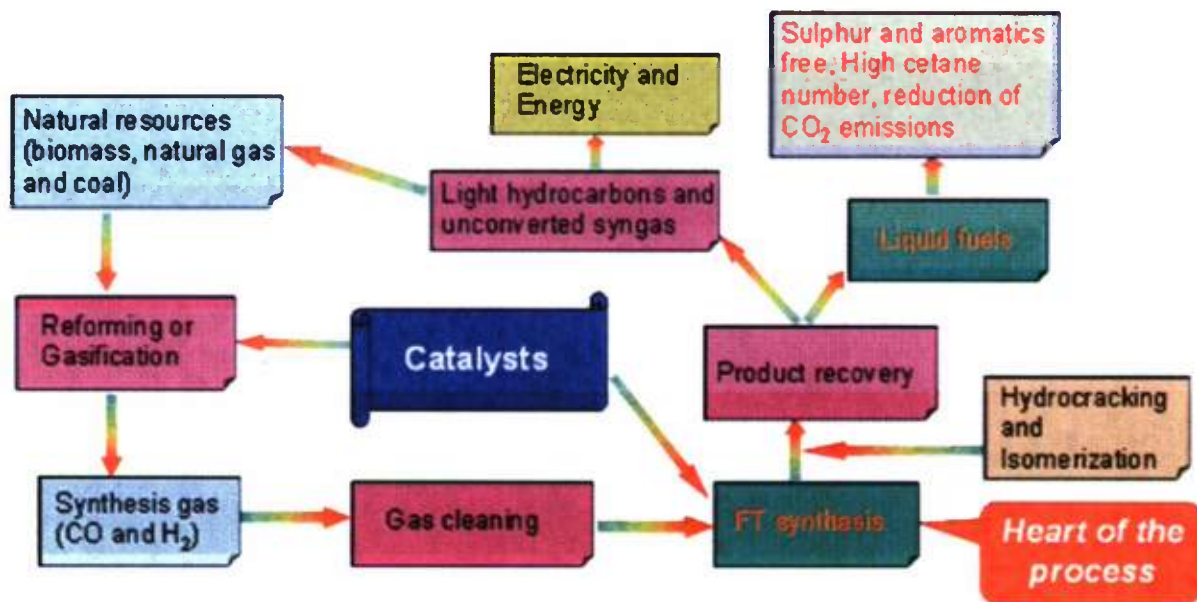


Figure 2.3.1 Outline of steps necessary in FT liquid fuel production

In the first step, synthesis gas is produced from natural resources in the process of gasification or reforming. In the second step, this synthesis gas can be utilized for FT synthesis. This step is the heart of the process to produce liquid fuels. In the third step, product upgrading is conducted to maintain carbon chain growth and increase the probability of producing liquid hydrocarbons. FT fuel can reduce the net emission of  $\text{CO}_2$  as well as oxides of nitrogen and sulfur, the latter two being EPA-criteria atmospheric pollutants. This fuel is practically free of sulfur, nitrogen and aromatics.

FT synthesis is exothermic [ $\text{CO} + 2\text{H}_2 \rightarrow -(\text{CH}_2)_n + n\text{H}_2\text{O}$ ] and hotspots can be formed on the catalyst surface during reaction. As a result, the structural integrity of the catalyst can be damaged, resulting in decreased activity and selectivity. This is a common problem in FT synthesis and a slurry-phase reactor can be an effective method of enhancing mixing and heat transfer from the catalyst, thereby lowering reaction temperatures and inhibiting hot spot formation. It is well known that Ru, Co, and Fe can be utilized for FT synthesis. Problems

associated with Co and Fe catalysts include catalyst deactivation, lower activity, and selectivity. A Ru-based catalyst shows promise for FT synthesis in a BTL process due to its higher catalytic activity, selectivity, and stability when using suitable catalyst supports and additives. Ru metal, however, suffers from issues of cost and limited availability. Therefore, there is a continued need for development of catalysts with high and stable activity to produce FT fuels from biomass-derived synthesis gas.

### 2.3.1 Scope of Work and Approach

This project focuses on developing catalysts and exploring their utility for the production of clean FT fuels from biomass-derived synthesis gas. The objective is to design, fabricate, and conduct initial evaluation of a laboratory-scale FT system capable of evaluating the effects of independent variables, reactor temperature and pressure, syngas quality, catalyst type, contaminants, etc. on biofuel synthesis production. Details of the system are described in the Technical Accomplishments section below.

### 2.3.2 Technical Accomplishments

To enable research on FT fuels from biomass-derived synthesis gas, an FT reactor system was designed as shown in the schematic diagram on Figure 2.3.2.

The system consists of three major subsystems: a pre-reactor subsystem to meter reactants to the reactors, the reactor subsystem (FT [K1] and catalyst preparation [K2]), and a post-reactor subsystem to condition the outlet stream from the reactor and analyze products to permit evaluation of system performance.

The pre-reactor system includes compressed gas cylinders of system reactants, mass flow controllers, and associated valves and fitting. Three cylinders are plumbed to the system containing N<sub>2</sub>, H<sub>2</sub>, and syngas.

The reactor system includes an Autoclave Engineers *1000 ml EZE-Seal Pressure Vessel Closure* reactor (reactor K1) rated for 3300 psi at 450 °C. The reactor is equipped with a magnetic-drive stirring system, heater system, and systems for controlling reactor temperature and reactant flow rates, and monitoring reactor pressure and product flow rates. The catalyst preparation reactor is an Autoclave Engineers *EZE-Seal 300 ml Vessel* rated for 3300 psi at 450 °C. The reactor is equipped with a temperature-controlled heater system. Both reactors are plumbed to be serviced with the same pre-reactor system.

The post-reactor system includes condensers and filters to remove particulate and any condensable species prior to being ported to one of two online gas chromatographs (GC). The first GC is a Model Arnel 4019, an engineered chromatography system that is installed in a Perkin Elmer, Clarus 580 GC. The Model Arnel 4019 provides a guaranteed analysis of H<sub>2</sub>, Ar, O<sub>2</sub>, N<sub>2</sub>, CH<sub>4</sub>, CO, CO<sub>2</sub>, the C<sub>2</sub>'s and H<sub>2</sub>S using two thermal conductivity detectors. Detection limits for each of these analytes are 100 ppm. The second GC is a Model Arnel 4035PPC, an engineered chromatography system that is installed in a Perkin Elmer, Clarus 680 GC. This analyzer features a gas sampling valve (GSV) in an external-valve oven, Al<sub>2</sub>O<sub>3</sub> PLOT column and a flame ionization detector. Locating the GSV in a heated oven assures that there is no sample condensation in the sample loop. Also, the column oven can be raised to PLOT column reconditioning temperatures without damaging the GSV. This GC is capable of analyzing

hydrocarbon species in the range from  $C_1$  to  $C_{10}$  (i.e., methane through decane). Liquid products that are retained in the reactor will be analyzed after a test run is complete, with an existing, off-line GC.

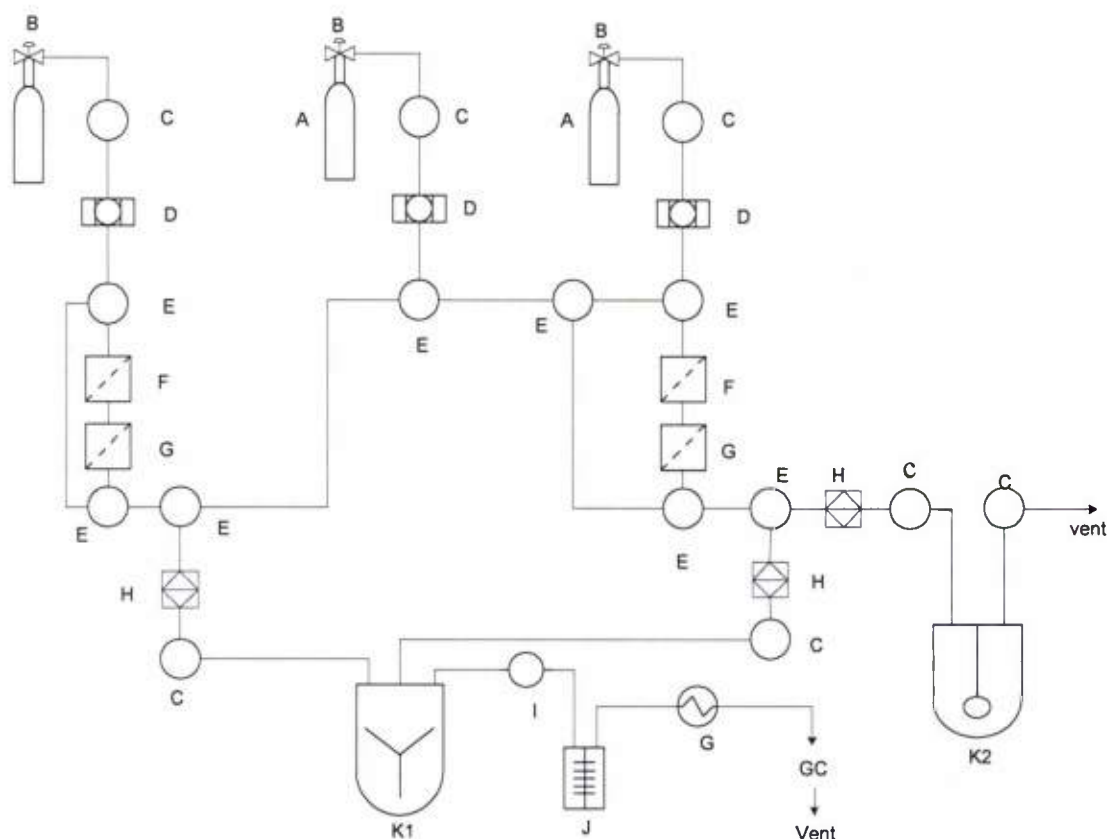


**Figure 2.3.2 Schematic diagram of FT plan to produce high quality clean fuels from biomass-derived synthesis gas. Component identification: A. gas cylinder, B. gas regulator, C. two-way valve, D. filter, E. three-way valve, F. mass flow controller, G. mass flow meter, H. check valve, I. back-pressure regulator, J. condenser, K1. FT synthesis reactor, K2. catalyst preparation reactor.**

The FT reactor system is housed under an area fume hood to vent heat and off gases from the system. Gas monitors are placed in the vicinity of the reactor and are connected to the control system to shut down reactant flows should leaks be detected.



## 2.4 Novel Solvent-Based Extraction of Bio-oils and Protein from Biomass

The overall objective of this project is to optimize methods and compositions of ionic liquid (IL) based co-solvent mixtures for the one-step extraction of bio-oils and protein from biomass, and to further develop the outlines of unit operations that fractionate and purify both products. Outcomes from this research will be used to develop the chemistry underlying the extraction and fractionation steps, as well as to evaluate, modify, and optimize the process integration of unit operations. Biomass sources to be investigated will include phototrophic and heterotrophic microalgae, heterotrophic yeast, and oil-seeds. To execute the overall objective, the following specific activities will be pursued:

1. Investigation of a wide range of polar molecules (PCMs) for their ability to catalyze the extraction of bio-oil from microalgae biomass when dissolved in ionic liquids;
2. Optimization of the direct production of fatty acid methyl esters from microalgal biomass (i.e., direct transesterification) dissolved in the ionic liquid 1-ethyl-3-methylimidazolium methyl sulfate (EMIM methyl sulfate) as a function of the methanol to biomass (w/w %) ratio; and
3. Characterization of the extent of biomass protein partitioned into the co-solvent system, and the extent to which the extracted protein precipitates or dissolves in the co-solvent, as a function of the molar ratio of the PCM-IL ratio.

### 2.4.1 Scope of Work and Approach

The solvent system to be investigated will comprise a co-solvent mixture of an ionic liquid (e.g., 1-ethyl-3-methylimidazolium methyl sulfate) and polar covalent molecules that have been previously shown to execute one-step extractions of both bio-oils and proteins at low pressure and moderate temperature. This extraction system is currently the subject of UH patent application 0088523-003PR2 [1]. If successful, this extraction system could play an important element for development of a biorefinery process that can extract bio-oils for fuel, protein for aquaculture, and carbohydrate for charcoal.

### 2.4.2 Technical Accomplishments

Our work has characterized the ability of a co-solvent system, comprised of a hydrophilic ionic liquid (IL) and polar covalent molecule (PCM), to extract and auto partition lipids from various biomass sources. The ionic liquid 1-ethyl-3-methylimidazolium methyl sulfate (EMIM-MS) was selected based upon its relatively low viscosity, immiscibility with the lipids and solubility with selected PCMs. The polar covalent molecules are defined as solvents that contain a polar functional group covalently bonded to a hydrocarbon chain. This co-solvent system is in contrast to traditional co-solvent systems, comprised of a volatile organic solvent and a PCM, which both dissolve and extract the bio-oil into a single phase, or the sole use of ILs as an extracting solvent. Figure 2.4.1 shows a plot of extraction efficiency for our co-solvent system as a function of PCM to IL ratio. It can be seen that optimum extraction efficiency occurs at co-solvent ratios between 40 and 60%, with lower extraction efficiencies occurring for pure IL (EMIM-MS) and pure PCM (methanol).

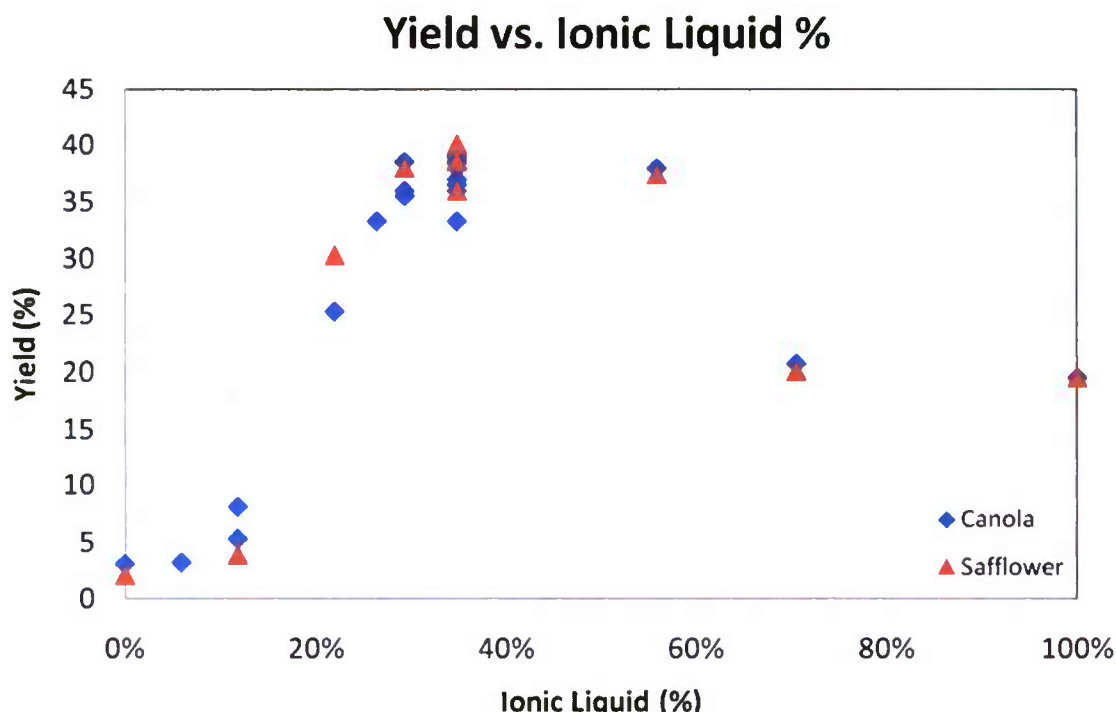


**Figure 2.4.1** Extraction efficiency (as Yield % on a mass basis) for bio-oil extraction from canola and safflower oil-seeds using the EMIN-MS and methanol co-solvent system

As previous work has demonstrated the use of strong solvents with high polarity to aid in the extraction of oils and fat soluble pigments, we have proposed that the action of the PCM is largely to disrupt the cell wall and to improve the efficiency at which the lipid is contacted with the solvent. The action of the strongly self-associating IL, the insolubility of the lipids in the co-solvent and the density difference between co-solvent and extracted lipids is proposed to promote the rapid transfer of the lipids to the surface interface where they auto partition into a self associating and separate phase. Both processes are needed to achieve maximum extraction efficiency.

With respect to task 1 several PCMs (Table 2.4.1) were paired with EMIM to evaluate their potential extraction value on *Duniella* microalgal biomass. *Duniella* is a biomass source that possesses a cell wall that is relatively difficult to penetrate and thus represents a good test case. Methanol (in this work considered our baseline PCM) and isopropyl alcohol produced similar results. DMSO and acetic acid resulted in lower lipid yields. Acetone and chloroform resulted in a larger gravimetric yield than the alcohols. The recovered product was also found to contain a solid precipitate that was not present in the other samples. Subsequent investigation revealed that acetone and chloroform had a slight solubility in the lipid phase that permitted some carryover of non-lipid extract. When the lipid phase was vacuum dried for measurement of gravimetric yield, the carryover material precipitated into a visible solid. Consequently, acetone and chloroform were determined to “over extract” and give unrealistically high yields. This work has been published [2].

**Table 2.4.1 The effect of PCM on extraction yield**

PCM	Yield (wt %)*	Comments
Dimethyl sulfoxide	6.0	Low yield, highly viscous product
Acetic Acid	5.6	Low yield, highly viscous product
Methanol	7.9	Baseline PCM
Acetone	9.2	High yield, with a solid precipitate
Chloroform	8.4	High yield, with a solid precipitate
Isopropyl Alcohol	8.5	Product very similar to methanol

\*The biomass used in this study, *Dunaliella* microalgae, had a lipid content of approximately 8-11% (wt %).

With respect to task 2, direct transesterification of internal lipids was executed on Canola oil seeds in the presence of the EMIM-methanol co-solvent mixture. In this system the methanol served as both the solvent and the reactant. Figure 2.4.2a shows the layer of fatty-acid methyl esters (FAMES) that auto-partitioned to the top of the mixture. The color of the co-solvent mixture, shown in Figure 2.4.2a, is generally much darker than the color of the extraction co-solvent when used only to extract lipids in the absence of added acid catalyst. As the discoloration would vary among biomass sources (data not reported), the darkening is believed to be derived from residual pigments in the biomass source that are released into the solvent due to interactions of the acid catalyst with the biomass. NMR analysis consistently showed a very clean spectra with very little contamination, and comparisons between solvents of canola-seed DT with that executed in purified store-bought canola oil showed no difference (data not shown). The solution was centrifuged (20 minutes, 3500 rpm, 15 °C) to clarify the interface between the FAMES and the co-solvent. The recovered FAMES product is also shown in Figure 2.4.2b. The NMR spectra of the recovered product revealed that the transesterification reaction was carried out to 100% conversion of triglycerides to FAMES (Figure 2.4.3B).

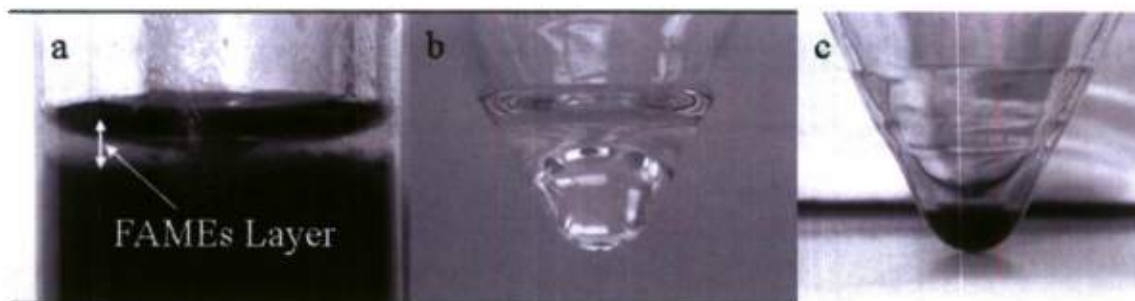


**Figure 2.4.2 (a) Canola oil seeds suspended in co-solvent system. (b) Lipid layer on the top of co-solvent extraction of canola oil seeds. (c) Recovered lipid from canola oil seed extraction.**



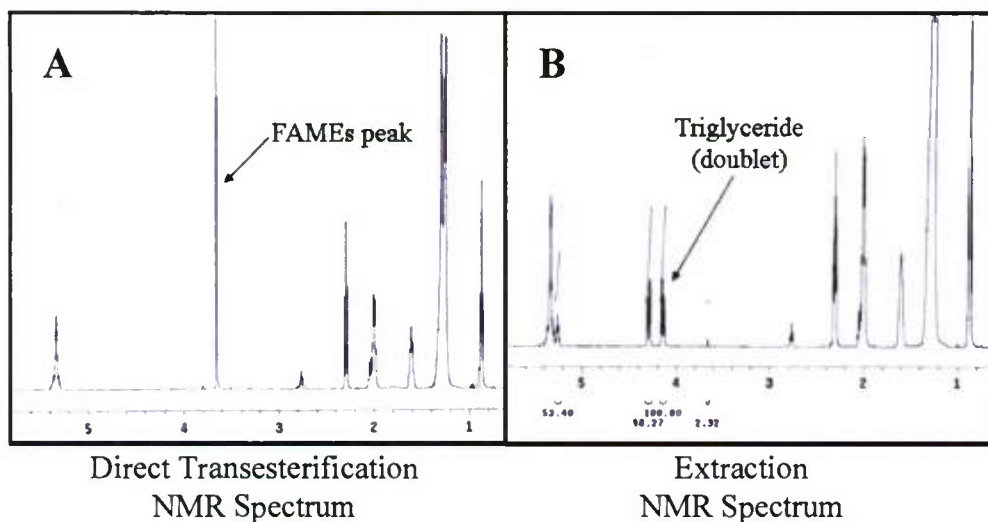


**Figure 2.4.3** NMR spectra of extracted canola oil (a), and NMR spectra of direct transesterification of Canola seeds (b).

The direct transesterification reaction was applied to several other biomass sources in the same EMIM-methanol co-solvent system. The results are summarized in Table 2.4.2. With the exception of the *Chlorella* microalgae, the conversion from triglycerides to FAMES was complete (100%) for all the biomass sources. The gravimetric yields of direct transesterification were found to be very similar to extraction yields in the absence of the acid catalyst indicating that co-solvent is equally efficient at direct transesterification for all biomass sources (*Duniella*, *Chlorella*, Canola and Jatropha). The oil seeds and heterotrophically grown *Chlorella* and yeast yield FAMES products that were light yellow and of low viscosity. By contrast, the FAMES product from the pond grown *Duniella* produces a dark brown highly viscous product. The added viscosity of the *Duniella* extract is a result of the presence of the fat soluble pigments that concomitantly extracted and partitioned with the lipid phase.

With the exception of the *Chlorella* microalgae, the conversion from triglycerides to FAMES was nearly complete (100%) for all biomass sources investigated, and the gravimetric yields of FAME product were found to be similar to those in the absence of acid catalyst [3].

**Table 2.4.2** Direct transesterification yield from various biomass sources

Biomass Type	Sample preparation	Conversion	Gravimetric yield
<i>R. toruloides</i> -yeast	Freeze dried	100%	28.8%
<i>Duniella</i> -microalgae	Freeze dried	100%	8.0%
<i>Chlorella</i> -microalgae	Freeze dried	85%	36.0%
Canola-oil seed	Oven dried	100%	34.5%

With respect to task 3, major work is underway using jatropha oil-seeds as the model biomass, although we have also completed extraction work on the phototrophically-grown microalgae *Tetraselmis*, *isocrysis*, and *Nannochloropsis*, as well as the heterotrophically-grown *Chlorella protothecoides*. In general we have found that despite the amphiphilic nature of the extraction co-solvent, the protein remains largely with the biomass, and not within the co-solvent, although the protein is easily rinsed away (with water) from the extracted biomass (Tables 2.4.3 and 2.4.4). This suggests that the co-solvent system does treat the biomass tissue in such a way as to isolate the protein, but also likely initiates its precipitation in the form of large aggregates whose density is heavier than the co-solvent and thus migrate to the pellet phase during centrifugation. This work remains in progress.

**Table 2.4.3: Protein content of the *bottom biomass phase* after extraction in EMIMMS/MeOH, co-solvent.**

EMIMMS/ MeOH	Nannochloropsis		Tetraselmis		Chlorella
	Freeze dried	Oven dried	Freeze dried	Oven dried	Freeze dried
Nitrogen/ %		10	9.5		3.4
Protein/ %		<b>63</b>	<b>59</b>		<b>21</b>
Expected Protein content (%)		56	59		21

**Table 2.4.4: Kjeldahl protein analysis of *Jatropha* samples extracted using EMIMMS/MeOH**

JATROPHA	Kjeldahl / (% protein)			Kjeldahl - water wash (% protein)		
Untreated biomass	31			-	-	-
<i>Bottom biomass phase</i> EMIMMS/MEOH	69			3		
Co-solvent phase: EMIMMS/MEOH	5			-	5	-
Total protein	74			-	-	-
Protein balance (above expected value)	14			-	-	-

### 2.4.3 Papers and Presentations Resulting from Efforts

1. Cooney, M.J. and G.Y. Young, *Methods and compositions for extraction and transesterification of biomass components*, in *Patent Application Full Text and Image Database*, U.S.P.T. Office, Editor. 2009, University of Hawaii: United States.
2. Young, G., F. Nippen, S. Titterbrandt, and M.J. Cooney, Extraction of Biomass Using an Ionic Liquid co-Solvent System. *Separation and Purification Technology*, 72, 118 - 121 (2009).
3. Young, G., F. Nippen, S. Titterbrandt, and M.J. Cooney, Direct Transesterification of Biomass Using in Ionic Liquid co-Solvent System. *Biofuels, Bioproducts, & Biorefining*, In Press (2011).



## 2.5 Biochemical Conversion of Synthesis Gas into Liquid Fuels

*Summary: A new technology was investigated and demonstrated to convert syngas into bio-oil via microbial biosynthesis and thermal methanolysis. The research developed a bacterial strain of high CO tolerance and efficient CO<sub>2</sub> reduction with H<sub>2</sub>. The primary metabolic products were identified with chemical analysis and 16S RNA sequencing. Energy-rich polyester accounting for more than 50 wt% of cell mass was formed and converted with other cellular components into liquid compounds in supercritical methanol. The bio-oil was analyzed and calibrated with bio-diesel standards. Thermal methanolysis of cell mass gives a high conversion (>90%) and high bio-oil yield (60%) in comparison with cellulosic biomass.*

### 2.5.1 Scope of Work and Approach

The research was conducted with two objectives: (1) to understand the biochemical conversion of two major energy-containing gases (H<sub>2</sub> and CO) in syngas, and (2) to convert the major organic products formed from syngas into liquid fuels. The primary achievements are reported according to the three milestones described in the next section.

### 2.5.2 Technical Accomplishments

The following sections describe the technical accomplishments for this task.

#### 2.5.2.1 Progress on biochemical conversion of artificial syngas, mechanisms, kinetics, key enzymes, and role of individual gases

A strain of hydrogen bacterium was developed that could grow in a mineral solution on artificial syngas of broad composition as shown in Table 2.5.1. A cell mass (CH<sub>1.87</sub>O<sub>0.66</sub>N<sub>0.17</sub>) was formed from reduction of CO and/or CO<sub>2</sub> with H<sub>2</sub>. The yield of cell mass on total carbon of CO and CO<sub>2</sub> varies from 0.07 to 0.54 (g/g), depending on gas composition. Cultivation of the strain on individual CO and CO<sub>2</sub>, respectively, confirms that CO<sub>2</sub> is the primary carbon source of microbial conversion.

The research reveals that CO has little toxicity to the cells, but reduces the amount of carbon available in a syngas for biological conversion. As shown in Figure 2.5.1, there is a negative linear relationship between the cell mass gain and CO content ranging from 0 to 22 mole%. This fact indicates that CO, like an inert nitrogen gas, has a volumetric dilution effect on syngas composition, but little biological toxicity to the cells. The biological conversion can be conducted under a high CO content. This is amazing since CO can inhibit many metallic enzymes at a very low concentration. This important discovery points out two possible applications of this research in syngas conversion. First, it can be directly used to remove CO<sub>2</sub> from a syngas to purify CO for high efficiency Fischer-Tropsch (F-T) synthesis or to remove CO<sub>2</sub> after F-T synthesis. Second, it can be combined with a water gas shift reaction (CO + H<sub>2</sub>O → CO<sub>2</sub> + H<sub>2</sub>) to convert CO and CO<sub>2</sub> completely. The later application is in further investigation.

The primary metabolic product from syngas bioconversion is the bacterial cell mass consisting of two major components: about 50 wt% of polyhydroxybutyrate (PHB) and the rest of residual cell mass (proteins, cell membrane/walls, etc). PHB is an energy reserve of microbial species and has a similar energy content of oil-based polyester (24 MJ/kg). Figure 2.5.2 shows the time courses of cell growth and PHB accumulation in a bioreactor fed continuously with an artificial syngas. The time development consists of an initial growth of cells reflected by the quick

increase of residual cell mass, followed by PHB synthesis and accumulation. The maximum cell growth rate was 0.084 g/g.hr, indicating that cell mass can be doubled in about 8 hours under optimal conditions. The corresponding conversion rate of CO<sub>2</sub> was 0.57 g CO<sub>2</sub>/g cell hr.

The soluble small chemicals in the aqueous medium of syngas fermentation were analyzed by using a High-Performance Liquid Chromatography (HPLC) device equipped with UV and reflective index detectors. Only one primary metabolic compound was detected, which was released from the cells during growth. Since its retention time (4.7 min) is close to that of glyceraldehyde (CH<sub>2</sub>OH-CHOH-CHO), it implies that CO<sub>2</sub> could be reduced via the Calvin cycle in which three CO<sub>2</sub> units are fixed and reduced to form one glyceraldehyde. A 16S RNA analysis of the bacterial strain was conducted and the result indicates that the strain has 100% alignment with *Ralstonia eutropha* H16, a hydrogen bacterium that is well known to reduce CO<sub>2</sub> via the Calvin cycle. Although up to 13 enzymes participate in the Calvin cycle, the key enzymes involved in the initial reactions are hydrogenase and Rubisco, the former responsible for hydrogen split ( $H_2 \rightarrow 2H^+ + 2e^-$ ) and the latter for carbon dioxide fixation. The presence of hydrogenase and Rubisco in living cells is confirmed with proteomic analysis.

#### **2.5.2.2 Effects of minor gases on biocatalysis**

A small amount of oxygen is needed as the final electron acceptor of biological conversion. Water is the product formed from the combination of oxygen and hydrogen. As shown in Figure 2.5.3, an optimal ratio of oxygen to CO<sub>2</sub> is 0.5 (mol/mol) to give a high cell yield per gram of CO<sub>2</sub> with little residual oxygen. NO and N<sub>2</sub>O can also be used by the cells as the electron acceptor and released as N<sub>2</sub> gas. They are, however, less efficient than O<sub>2</sub> in formation of energy carriers such as adenosine-5'-triphosphate (ATP), and hence generate a smaller amount of cell mass and biopolyester based on the same amount of hydrogen.

NH<sub>3</sub> is used by the bacterial cells as a nitrogen nutrient, exhibiting a positive effect on biological conversion of syngas. No positive or negative effect of CH<sub>4</sub> and H<sub>2</sub>S was observed on cell growth and biochemical conversion.

#### **2.5.2.3 Report progress of producing liquid fuels from polyesters by methanolysis and thermal degradation**

The research demonstrated thermal conversion of cell mass into liquid chemicals in calibration with biodiesel standards. The harvested cell mass was dried and cracked into liquid products at 240 °C in methanol under near supercritical conditions (MeOH T<sub>c</sub> 239 °C). By using gas chromatography, the liquid compounds were vaporized at 220 °C and separated in a biodiesel column over a temperature gradient from 40 °C to 250 °C. The mass percentage was determined with a flame ionization detector. Fatty acid methyl esters (FAMES) of C5 to C24 were used to calibrate the retention time and mass % of liquid products. In order to understand the contribution of liquid products from the major cell components, the cell mass was separated into polyester (PHB), residual cell mass, and lipids, and cracked under the same conditions. Figure 2.5.4 compares the mass distributions of liquid products from the cell mass and its components after thermal methanolysis. The products are primarily distributed in the retention time range of

C5 to C24 FAMES. This crude bio-oil may be further distilled according to corresponding boiling points.

The research investigated the effect of thermal methanolysis conditions (temperature, time and methanol/solids) on cell mass conversion and bio-oil yield defined as follows.

$$\text{Conversion\%} = \frac{W_o - W_r}{W_o} \times 100\%$$

$$\text{Yield \%} = \frac{W_L}{W_o} \times 100\%$$

Where  $W_o$ ,  $W_r$  and  $W_L$  are the weights of initial cell mass, residual solids, and liquid bio-oil, respectively. Figure 2.5.5 elucidates the effect of methanol/cell mass ratio on the conversion and yield. A high solvent/solids ratio increases the conversion of cell mass, but generates less amount of bio-oil because of vaporization loss. Carbonation of cell mass and polyester is the predominant reaction in the absence of methanol.

The research also compared this technology with direct thermal cracking of cane bagasse, a typical cellulosic biomass. As shown in Figure 2.5.6, more than 90% of the cell mass was converted, generating about 60 wt% of bio-oil. A substantial amount of small molecule products were lost during methanol evaporation and sample drying. In contrast, less than 27% of the bagasse was converted and only about 14% of the cellulosic biomass was liquid products.



**Table 2.5.1 Cell mass generated from reduction of CO and/or CO<sub>2</sub> with H<sub>2</sub>**

H <sub>2</sub> (%v/v)	CO (% v/v)	CO <sub>2</sub> (% v/v)	Total carbon ( g)	Cell mass (g)	Yield (g cell/g C)
70.0	0.0	20.0	0.67	0.37	0.54
66.5	5.0	19.0	0.81	0.30	0.37
62.9	10.1	18.0	0.94	0.22	0.24
59.4	15.1	17.0	1.08	0.26	0.24
56.0	20.0	16.0	1.21	0.15	0.12
52.5	25.0	15.0	1.34	0.20	0.15
49.0	30.1	14.0	1.48	0.21	0.14
27.0	26.5	14.7	1.38	0.24	0.18
25.4	30.7	13.9	1.50	0.16	0.11
23.7	35.3	12.9	1.62	0.12	0.07

**Note: A liquid mineral solution (100 mL) in 1 L bottles was refilled daily with syngas for 7 days. The cell mass was recovered with centrifugation and freeze-dried.**

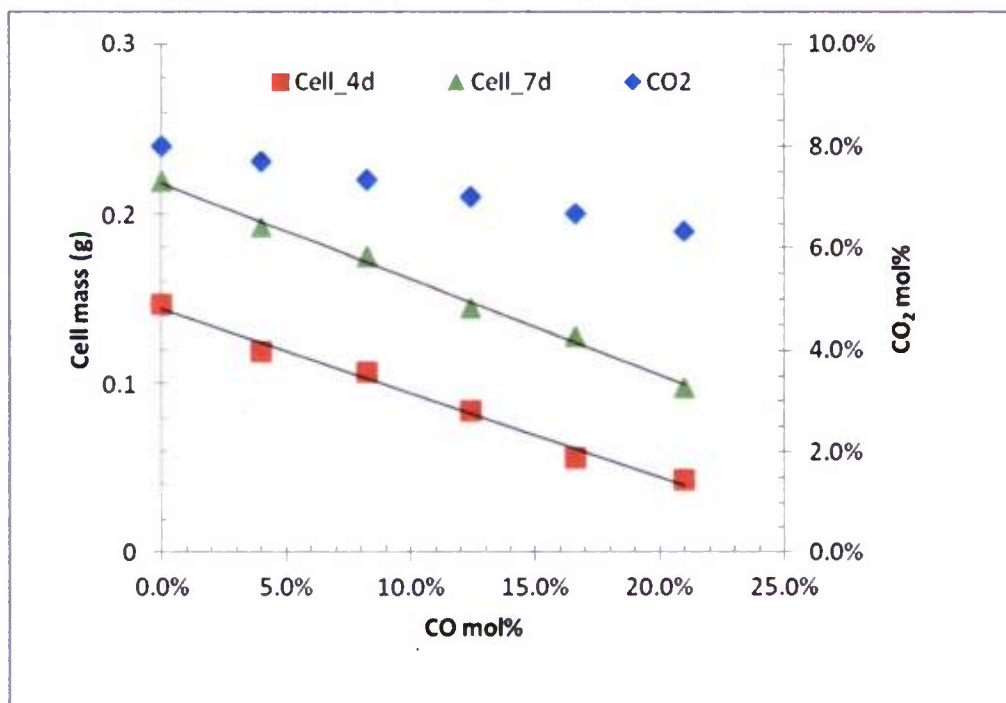


**Figure 2.5.1 A negative linear relationship ( $R^2 = 0.98-0.99$ ) exists between the cell mass gain and CO content of the syngas in microbial conversion for 4 and 7 days, respectively. CO<sub>2</sub> mol% declines with increase of CO mol% in a syngas.**

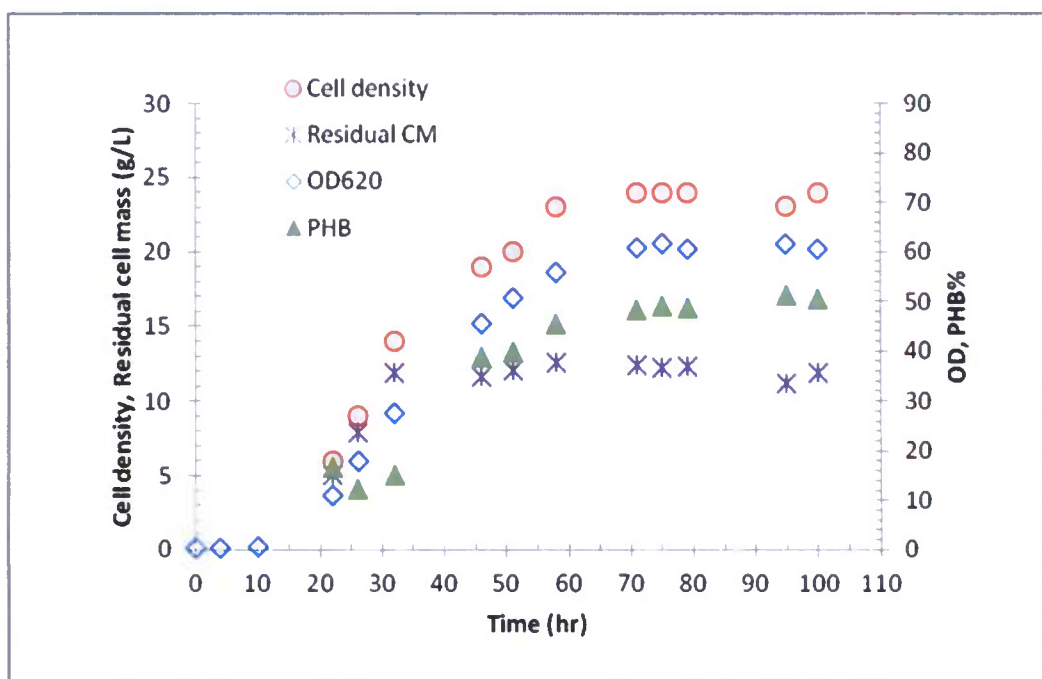


Figure 2.5.2 Time development of cell density, residual cell mass (CM), optical density at 620 nm (OD620), and biopolyester content (PHB) in a bioreactor (3 L) with continuous feeding of syngas. The residual cell mass is the difference between the cell mass and biopolyester mass.

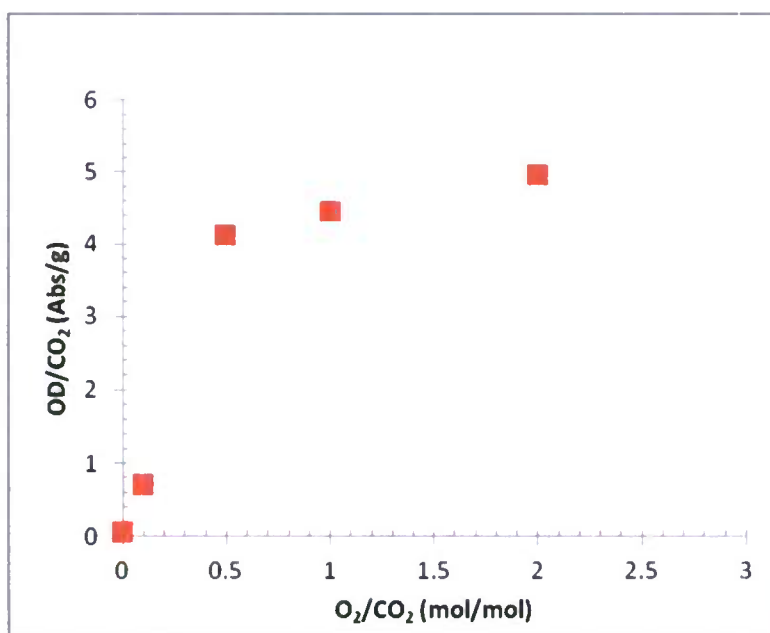
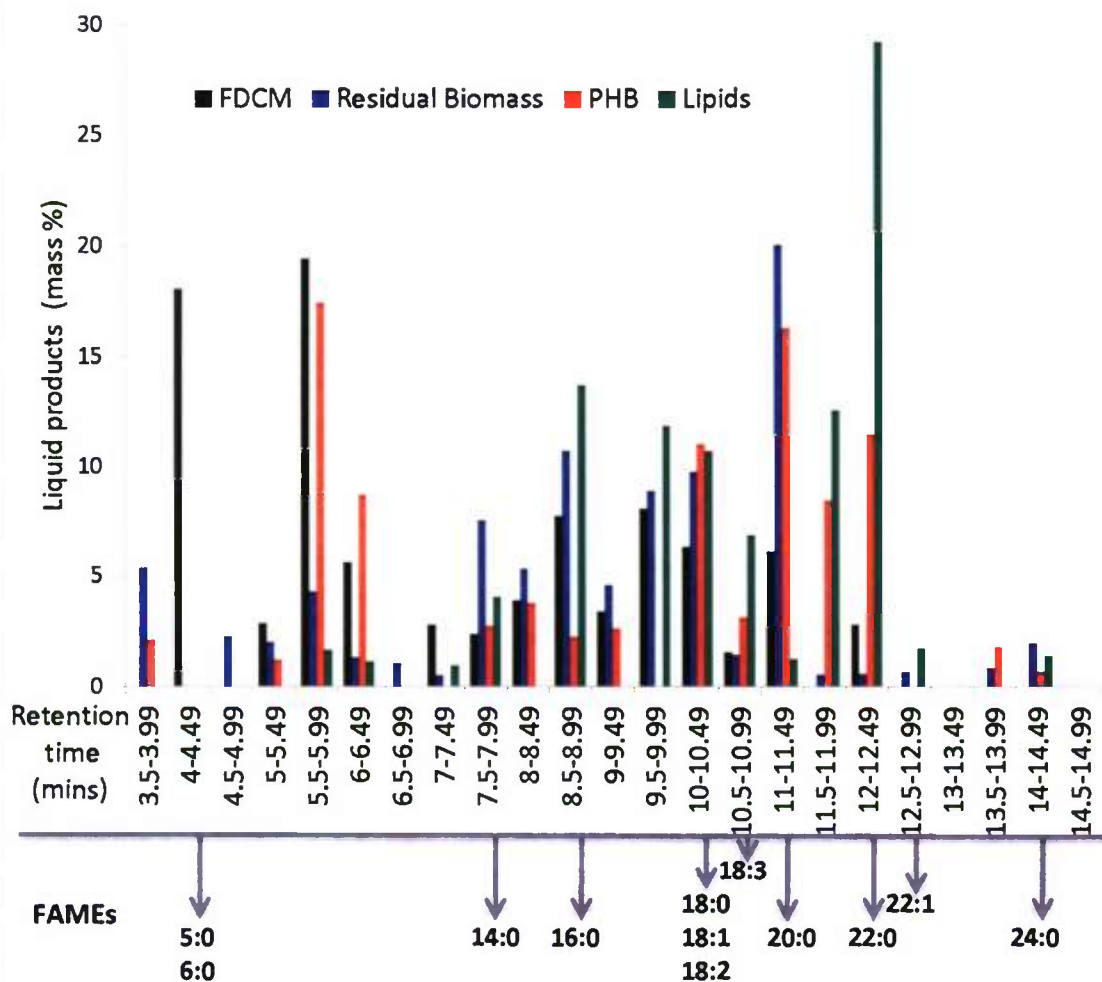


Figure 2.5.3 Oxygen demand in biochemical conversion of CO<sub>2</sub> and H<sub>2</sub> into cell mass



**Figure 2.5.4** The mass percentage and retention time of bio-oil components generated from thermal methanolysis of cell mass (FDCM), residual cell mass (residual biomass), polyester (PHB), and cellular lipids in supercritical methanol at 240 °C for 2 hours. The results are calibrated against fatty acid methyl esters (FAMES) standards (carbon number: unsaturated bonds).



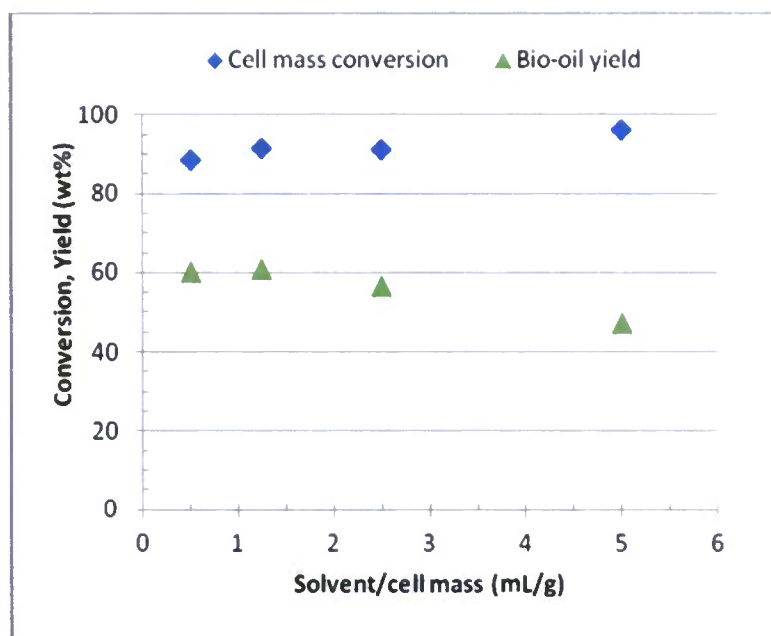


Figure 2.5.5 The effect of methanol/cell mass ratio on cell mass conversion and bio-oil yield

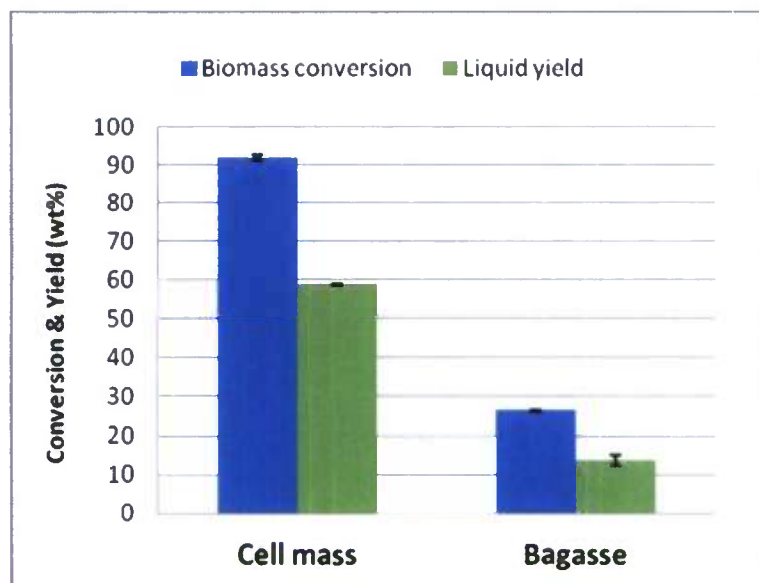


Figure 2.5.6 Comparison of thermal conversion and liquid products yield from cell mass and cellulosic biomass (cane bagasse)

## 2.6 Biocontamination of Fuels

### 2.6.1 Scope of Work and Approach

Biodiesel is a renewable fuel that is derived from the lipids of plants or animals. The lipids are chemically and physically treated by a transesterification process to produce the fuel. The first step in this process is the conversion of a triglyceride into monoglycerides. The glycerin backbone of the molecule is then separated from the fatty acids. The methyl group from methanol replaces the three ester bonds in the fatty acid chain to produce fatty acid methyl esters (FAMEs). The product of this reaction is structurally very similar to petroleum diesel (alkanes) and therefore has similar physical and chemical properties. It is important to understand the chemical and physical treatments used to produce biodiesel fuels, as they promote hygroscopicity.

Evidence shows that all diesel fuels are susceptible to biocontaminations resulting in Microbially Induced Corrosion (MIC) of fuel system components and fuel degradation, including low sulfur contents. This is especially prominent when water-contaminated bio-diesel fuels are used. MIC is commonly associated with bio-films that include Sulfate Reducing Bacteria (SRB) and other mixed bacterial and fungal populations 1,3,8. These bio-films have been found to result in the rapid corrosion of steels and even marine-use corrosion-resistant alloys. The purpose of this study is to investigate the associated biological communities with an emphasis on contaminant isolation. Isolates will give insight into metabolic functions that influence fuel biodegradation, bio-fouling, and biologically mediated corrosion. This information will be important for development of rapid contaminant detection methods and potential metabolic pathways for the maintenance of fuel quality.

There is still conflicting empirical evidence on low-sulfur and ultra-low-sulfur propensity for contamination. Low-sulfur formulations are increasing in use world-wide in efforts to reduce pollution. It is believed that the generation of hydrogen sulfide in fuels that contain sulfate account for a large amount of the biologically corrosive properties associated with biodiesel. Work has been performed that investigates different metabolic pathways for sulfate reduction that are dependent upon available sulfate (low conc. 0.1 mM / high conc. 1.0 mM), using the novel isolate *Arthrobacter* sp. P1-1. The potential utility of this novel isolate for the biological removal of sulfur compounds from diesel fuels is being studied. Further investigation of sulfate metabolisms will be performed for the development of specific inhibitors. Work has also been performed that investigates the subsequent utilization of the biodiesel contaminant glycerin, with a different *Arthrobacter* isolate, JS37.

#### *Microbiological characterization of different fuels*

During the ongoing investigation, DNA has been extracted from samples obtained through efforts with the Naval Research Laboratory, the City and County of Honolulu, and Pacific Biodiesel, and by purchasing from commercial vendors. From these samples, bacterial cell cultivations were attempted from fuel and, if available, associated water fractions. No heterotrophic aerobic or anaerobic bacteria were obtained from fuel fractions. The sample collected from the City and County storage tank was the only sample with a significant amount of water. While DNA samples and biological cultivations were not obtained from fuel fractions, heterotrophic bacteria (~1e6 CFU/ml) and DNA were grown and extracted from the water.

Initial molecular characterization suggests low diversity and sulfate-reducing bacteria were not detected through molecular analysis or through isolation techniques.

Experimentation suggests that biological contamination is strongly associated with the presence of water. Using enrichment media inoculated with fuel fraction subsamples did not result in any bacterial growth. Development of a DNA-based rapid molecular detection method will be further investigated, with this in consideration.

The purpose of this initial study is: 1) to investigate biocontamination in biodiesel, and 2) to examine the role of sulfate-reducing bacteria. Five samples (see Figure 2.6.1) were obtained from various sources: (1) a B100 sample obtained from the pump at a commercial fuel vendor; (2) another B100 obtained directly from the major commercial biodiesel producer on O‘ahu; (3) a B100 sample derived from soy feedstock provided by NASA; (4) a petroleum-based ultra-low-sulfur diesel sample (ULSD); and (5) a 20% biodiesel sample (B20), obtained from the City and County (C&C) of Honolulu storage fuel tanks. The latter showed water and microbial contamination.

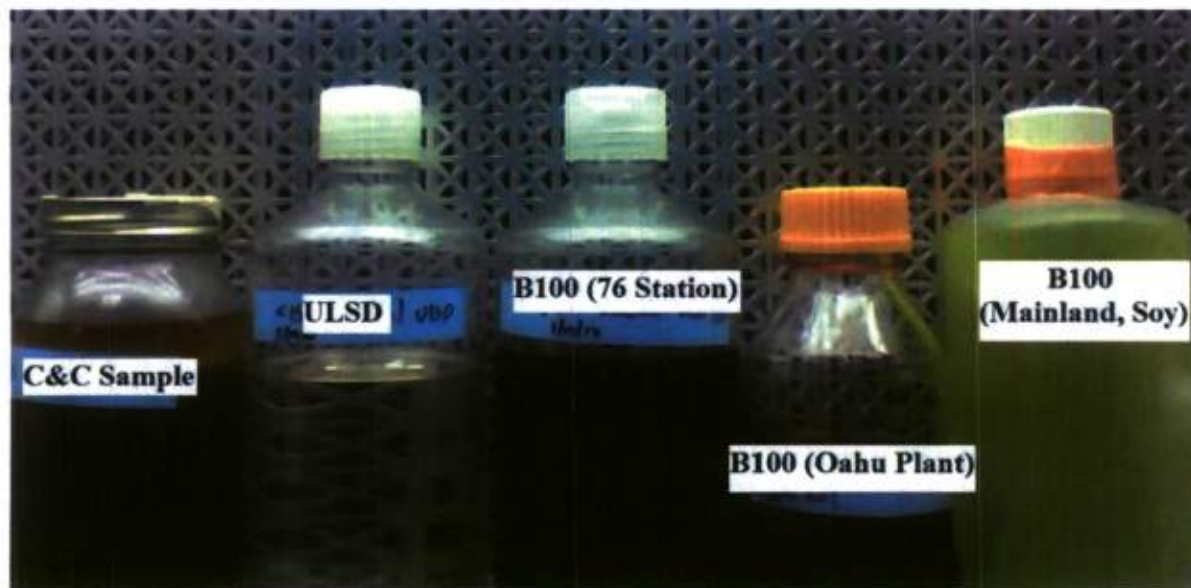


Figure 2.6.1 Collection of the different diesel samples used for experimentation

## 2.6.2 Technical Accomplishments

The following sections describe the technical accomplishments of this task.

### *Enumeration*

Several methods were used for the enumeration of microbiological contaminants and are summarized in Table 2.6.1. Fuel samples from Figure 2.6.1 were used to directly inoculate enriched media agar plates [Luria Broth (LB) and Yeast-Mold (YM) media], incubated at 30 °C for a week. All fuel inoculations resulted negative for any growth. Fuel samples were also added to 20 ml of enriched liquid media in Erlenmeyer flasks and incubated at 30 °C and 200 RPM for a month. A few samples showed signs of growth. With the assumption that the results



were not due to contamination, a most probable number (MPN) calculation was estimated at around 0.02 cells/ml for several samples.

The highly contaminated C&C sample was the obvious exception to the aforementioned results. While the fuel layer of this sample contained no microorganisms, the aqueous layer contained a high cell titer of  $\sim 1e7$  CFU/ml on both LB and YM agar plates, which was determined by serial dilution and plating. Replicates were performed in anaerobic conditions as well, using a Gas-Pak system, with the same results.

**Table 2.6.1 Summary of microbiological contaminants in different fuel samples**

Sample	.02 ml onto agar plates	20 ml with enriched broth	Serial Dilution	Final Cell Concentration
B100 (76 Pump)	negative	One positive	~	0.02 cells/ml (MPN)
B100 (Oahu Plant)	negative	negative	~	0
B100 (mainland, soy)	negative	negative	~	0
ULSD	negative	One positive	~	0.02 cells/ml (MPN)
C&C (fuel layer)	negative	negative	~	0
C&C (water layer)	~	~	$1e7$ CFU/ml	$1e7$ CFU/ml

#### *Description of Contaminated C&C Sample*

The C&C sample had three distinct phases: the fuel, water (aqueous layer) and a distinct water-fuel interface (see Figure 2.6.2). The fuel layer contained no microorganisms, but both the water and the interface contained considerable concentrations of microorganisms. The interface contains what can be described as a “slime-like” substance, a presumptive liquid-liquid biofilm (skinnogen), and direct inoculation of this substance onto an agar plate resulted in a high concentration of mold and yeast, with relatively fewer lactobacillus colonies. The water layer was brown and murky, possibly indicating metal corrosion from the storage tank. In contrast, the water layer contained a high concentration of lactobacillus.

#### *Isolation and Identification*

Microorganisms were identified by rDNA cloning and direct polymerase chain reaction (PCR) sequencing for isolates. DNA was extracted directly from the aqueous layer using a



**Figure 2.6.2** Contaminated biodiesel sample from the City & County of Honolulu. The sample shows the different separations including the interface film.

commercially available kit from MoBio and subsequently used for PCR analysis. Three primer pairs were used targeting different microorganisms: 16s primers (1492R-27F) were used for the general identification of bacteria, 26s primers (NL1-NL4) for the identification of molds and yeasts, and (DSR1F-DSR4R) for the identification of SRB. PCR amplification products did not result in the observation of rDNA specific for yeast and molds or SRB. Bacterial 16s products were, however, observed and visualized by electrophoresis. The products were cloned using Promega T-Easy vectors and transformed into JS31 competent *E. coli* cells. A plasmid miniprep was performed, and sent for sequencing. DNA was also extracted directly from the skinnogen and the same procedure repeated. PCR products were observed using the 26s primers and only faintly for 16s primers, nothing was observed specifically for SRB.

Microorganisms were isolated by direct plating using LB and YM agar plates. Random colonies were picked for isolation and grown in liquid media. DNA was extracted from the media and 16s primers were used to PCR and sequence these colonies directly. From the interface a large amount of colonies were observed. Colonies were re-isolated and sequenced using 16s and 26s primers.

In total, three microorganisms were identified from the contaminated C&C sample (see Table 2.6.2). All microorganisms that were identified were isolated.

**Table 2.6.2** Description of the different species of isolated microbial contaminants from a water contaminated fuel sample

Genus	Source	Colony Description	Type of micro-organism	Blast Homology
<i>Lactobacillus</i>	Water Layer	Wet, translucent	Bacteria	99.00%
<i>Moniliella</i>	Interface	Dry, irregular	Yeast	98.00%
<i>Byssochlamys</i>	Interface	Mold-like	Mold	100.00%

Based on published results in other studies, the low diversity in fuel contamination is atypical. This brings into question how many different microorganisms are truly required for an active contamination, or for an active biofilm. The results of this study suggest that very low diversity can still result in an active contamination.

### *Physiological Characterizations of Isolates*

Physiological characters of isolated microorganisms were examined, including pH and temperature tolerances and optima. The ability to survive in biodiesel (i.e., the fuel layer) and fuel degrading metabolisms were also examined.

To test whether the isolates could survive in biodiesel, 0.02 ml of each isolate were inoculated into 1 ml of B100 in test tubes. These test tubes were then incubated at 30 °C and agitated at 200 RPM. Viable cells were extracted by mixing the sample with enriched media and then culturing it on LB agar plates. This was repeated for several different lengths of time to obtain a curve of cell count over time.

This experiment was also performed with *E. coli* and a non-axenic culture of SRB recently isolated from soil. This experiment showed that the *Lactobacillus* will not survive in B100 even over a relatively short time, and that water is essential for its survival. *E. coli* and the SRB isolate also did not survive; however, the yeast isolates exhibited fair survival rates but did not grow after a period of several days.

These findings (see Figure 2.6.3) suggest that many ubiquitous bacteria do not survive in biodiesel for any extended period. However, the ability of yeast and mold species to persist may be due to sporulation or other mechanisms employed to survive in harsh environments.

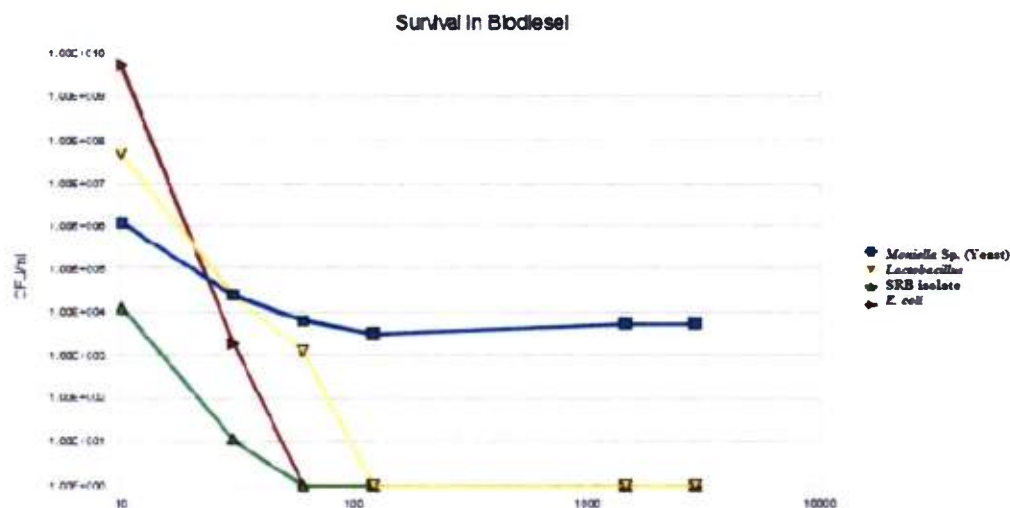


**Figure 2.6.3 Survival of the different isolates and *E. coli* in a B100 biodiesel sample. All of the organisms tested were unable to grow in the fuel. Only the yeast isolate was able to survive.**



### Temperature and pH Characteristics

Temperature and pH ranges for the isolates were determined. To test for the ability to grow at various pH, the isolates were inoculated into test tubes containing 5 ml of enriched media at different pH. The pH of the enriched media was adjusted using concentrated 5M NaOH or 5M HCL and sterilized by filtration. Growth was measured daily by serial dilution and plate count.

The ability to grow at various temperatures was tested by first culturing the bacteria in favorable conditions and then spreading an amount on to agar plates, which were subsequently incubated at various temperatures (4 °C, 20 °C, 30 °C, 37 °C and 60 °C). The results (Figure 2.6.4) were not particularly surprising: all isolates had a growth maximum around nominal range (i.e., pH 7 and 30 °C). The *Moniella* Sp. isolate was not capable of growing at temperatures of 37 °C, while the other two isolates were. None of the isolates were capable of growing at 60 °C.

### Measurement of Degradation Kinetics

The isolates were tested for their ability to degrade petroleum diesel and bio-diesel, as well as use as the sole carbon source for growth. Isolates were grown in test tubes of 1 ml of minimal salt media with either 2% diesel or 2% biodiesel. Fuel was re-extracted from the test tubes using hexane. Fuel degradation was determined by the changes in initial concentrations using a gas chromatograph equipped with a flame ionization detector (GC-FID) (Figure 2.6.5). Simultaneously, cell density was determined by serial dilution and plate count.

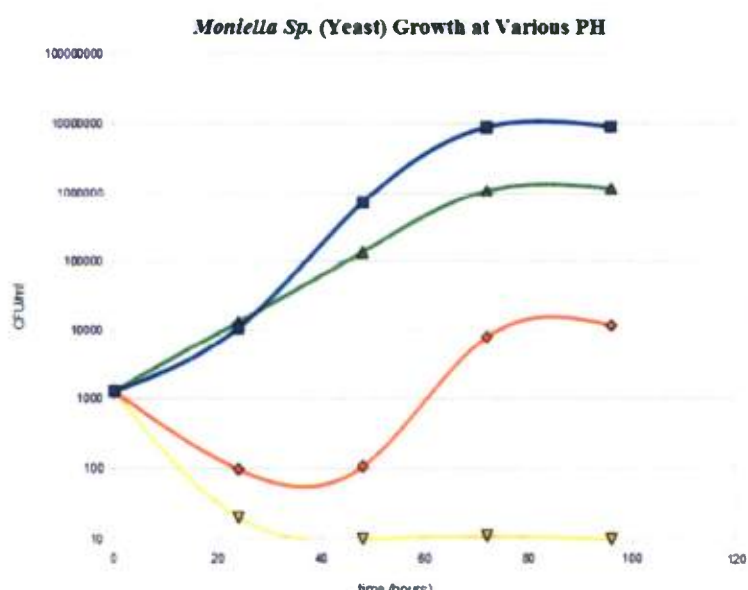


Figure 2.6.4 *Moniella* sp. growth curves at various pH. Optimum growth was achieved at neutral pH.

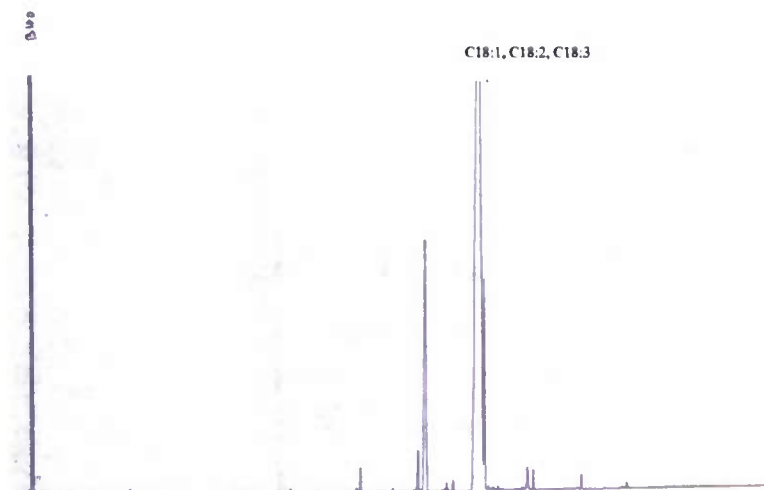


Figure 2.6.5 Gas chromatogram profile of a B100 diesel sample

Petroleum diesel was also utilized by the yeast isolate, but at a slightly slower rate. The mold isolate grew comparatively slower and did not degrade biodiesel or diesel as fast as the yeast isolate. *Lactobacillus* did not degrade either biodiesel or diesel, and growth was also not observed (cell counts fell logarithmically). When the *Lactobacillus* was inoculated along with the yeast strain in minimal media containing 2% biodiesel, *Lactobacillus* growth recovered (whereas alone, it did not grow). These results suggest that the fuel is not directly providing an adequate carbon source for heterotrophic growth and the possibility for symbiosis between the two species. Figure 2.6.6 shows that after two days the biodiesel was significantly degraded and used as a carbon source for growth.

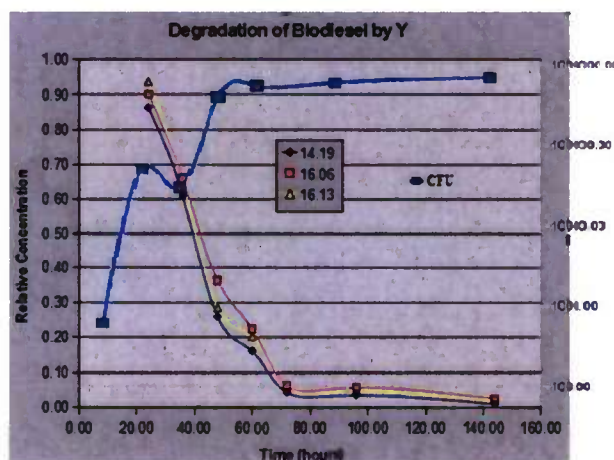


Figure 2.6.6 Measurement of degradation kinetics of biodiesel by yeast strain. Relative concentration of peaks on the left Y-axis, CFU/ml on the right Y-axis.

Future work will investigate the potential symbiosis between the eukaryotic and prokaryotic organisms found in the contaminating water layer. Our investigations strongly suggest that

minimal biological contamination will occur without the introduction of water and accessible carbon for prokaryotic growth.

#### Biodiesel Contaminant Mediation and Detection - Sulfate

From a petroleum-contaminated sample, two isolates have been used to study biodegradation of sulfur containing compounds. *Arthrobacter* sp. P1-1 has been utilized to study the degradation of dibenzothiophene, a compound inherently present in all diesel fuels. Results indicate that the biodegradation of dibenzothiophene is regulated by sulfate. Dibenzothiophene is a typical model chemical for biodegradation studies of sulfur-containing chemicals. These studies are expected to offer knowledge and information about bacterial sulfur metabolism and regulation, a step toward the development of sulfate metabolism inhibitors.

Through proteomic studies more than 600 proteins have been found and a desulfurization enzyme, DszA, has been identified. DszA is a potential marker for monitoring biodiesel corrosion. The proposed biodesulfurization pathway is shown in Figure 2.6.7. A proposed cellular function including identified cell membrane proteins from *Arthrobacter* sp. P1-1 is shown in Figure 2.6.8.

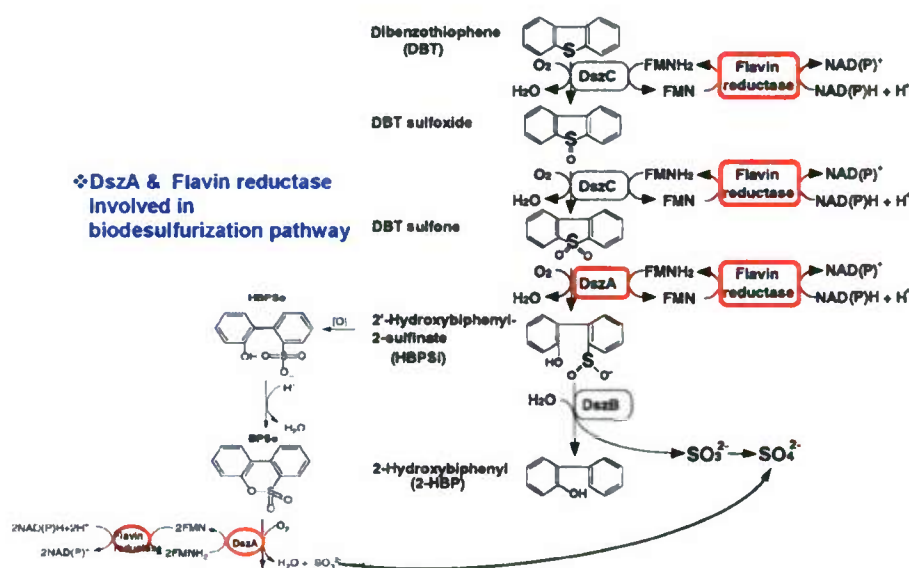
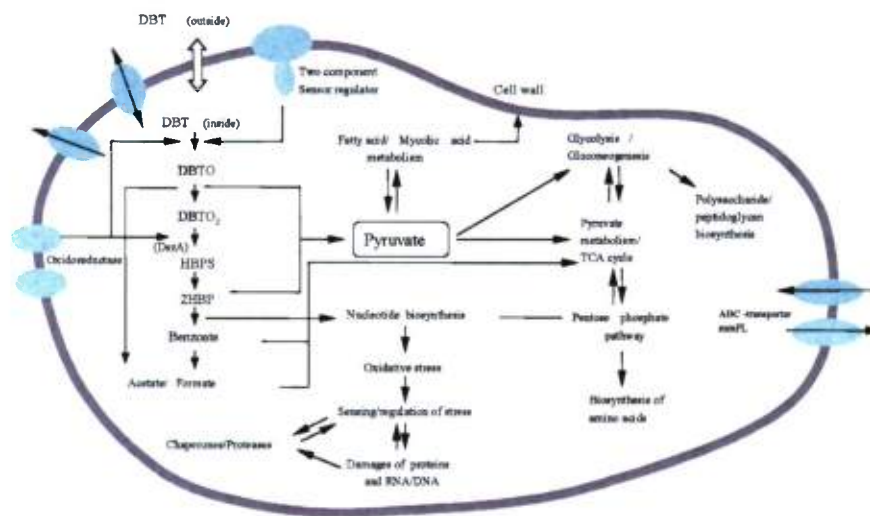


Figure 2.6.7 Proposed sulfoxide-sulfone-sulfinate-sulfate (4S) pathway





**Figure 2.6.8 Overview of cellular functional systems of *Arthrobacter* sp. P1-1 fed by DBT. The expression of proteins correlate with biodesulfurization, TCA cycle, pentose phosphate pathway, fatty acid metabolism, nucleotide and amino acids biosynthesis, and polysaccharide biosynthesis, etc.**

Mass spectrometry-based studies using a matrix-assisted laser desorption ionization time of flight mass spectrometer ((MALDI TOF MS) to develop a novel method for microbial community fingerprinting at low cell concentrations is still being investigated.

### *Biodiesel Contaminant Mediation and Detection – Glycerin*

Although biofuels such as biodiesel are thought to represent a secure, renewable, and environmentally safe alternative to fossil fuels, their economic viability is a major concern. As biodiesel production by transesterification of vegetable oil with methanol yields glycerol as the main by-product (10% by weight), crude glycerol (including methanol (8-12%) and methyl esters (15-18%) as well as 12-16% alkalis, and 2-3% water) may be treated as a waste product with a disposal cost attributed to it (Kocsisová and Cvengoš, 2006).

Due to the ample occurrence of glycerol in nature, many known microorganisms can naturally utilize glycerol as a sole carbon and energy source. These microorganisms have attracted attention to the potential use in bioconversion of abundant glycerol produced from biodiesel (Solomon *et al.*, 1995; Barbirato and Bories, 1997; Menzel *et al.*, 1997). To our knowledge, examples of possible biotechnological production processes based on glycerol demonstrate that this simple chemical is a promising abundant new carbon source for industrial microbiology. Glycerol may substitute traditional carbohydrates, such as sucrose, glucose and starch, in some industrial fermentation processes. In addition, glycerol-rich streams generated in large amounts by the biodiesel industry present an opportunity to establish biorefineries. Existing bulk product fermentations such as fermentative amino acid production may be suitable for adaptation to such biorefinery approaches. That glycerol bioconversion into valuable chemicals, such as 1,3-propanediol, dihydroxyacetone, ethanol, succinate, etc. adds significant value to the productivity of the biodiesel industry.

*Arthrobacter* sp. JS37 is a gram-positive soil bacterium isolated from a polycyclic aromatic hydrocarbon (PAH)-contaminated site (this was an oil gasification company's site from 1918 to 1965) in Hilo, HI, USA. The species can utilize a variety of carbon sources, particularly glycerin (Figure 2.6.9), for growth. It has been found to grow over a wide pH range (6.8-9.1, optimum at pH 7.1). Investigations have also shown that *Arthrobacter* sp. JS 37 can grow in the presence of 15% glycerin combined with 5% (v/v) methanol at pH 9.1. Glycerol utilization by *Arthrobacter* species up until this point has not been thoroughly investigated.

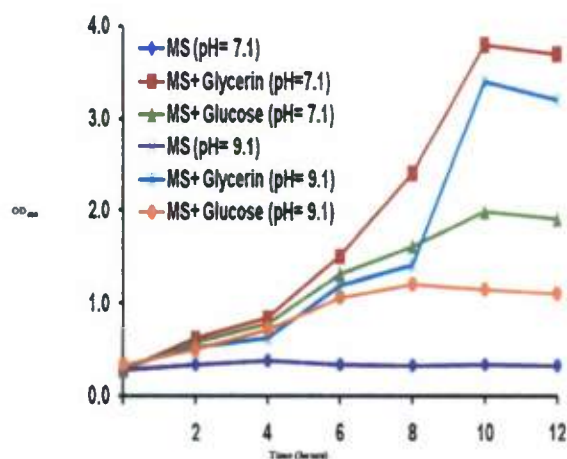


**Figure 2.6.9** *Arthrobacter* sp. JS37 can utilize a variety of carbon sources, particularly glycerin, for growth. *Arthrobacter* sp. JS37 can grow over wide pH range (6.8-9.1) optimum at 7.1

In *E. coli*, glycerol transport is facilitated by aquaglyceroporin (GlpF), and under aerobic conditions glycerol is then phosphorylated by glycerol kinase (GlpK) to yield glycerol 3-phosphate, which is oxidized by glycerol 3-phosphate dehydrogenase (GlpD) to yield the glycolytic intermediate dihydroxyacetone 3-phosphate.

Our preliminary studies have shown that strain JS37 produces both extra and intracellular lipases. Triglyceride cleavage was achieved using lipase secreted into the growth media and was estimated with a titration method. Initial protein profile analysis has also resulted in the identification of a Phospholipase C1 precursor (EC 3.1.4.3), and cell surface lipoproteins.

Protein profiling and isolation have been performed. Protein determinations have resulted in the identification of enzymes relevant to glycerin utilization (Figure 2.6.10). A hypothesized metabolic pathway is also presented in Figure 2.6.11. Through these studies, it is expected that a potential remediation method may be developed.





### 2.6.3 References

- Alleman T.L., Fouts L., McCormick R. L. 2010. Analysis of Biodiesel Blend Samples Collected in the United States in 2008. *National Renewable Energy Laboratory*
- Dzierzewicz Z., Cwalina B., Chodurek E., Wilczok T. 1997. The relationship between microbial metabolic activity and biocorrosion of carbon steel. *Res Microbiol.* 148(9): 785-93.
- Rajasekar A., Anandkumar B., Maruthanuthu S., Ting Y-P, Rahman P.K.S.M. 2009. Characterization of corrosive bacterial consortia isolated from petroleum-product-transporting pipelines. *Appl. Microbiol. Biotech.* 85 (4): 1175-1188
- Satoh H., Odagiri M., Ito T., Okabe S. "Microbial community structures and in situ sulfate-reducing and sulfur-oxidizing activities in biofilms developed on mortar specimens in a corroded sewer system." *Water Res.* 2009 Oct;43(18):4729-39
- Kocsisov'a T., Cvengo's J. 2006. G-phase from methyl ester production-splitting and refining," *Petroleum and Coal*, 48; 1-5
- Solomon B.O., Zeng A.P., Biebl H., Schlieker H., Posten C., Deckwer W.D. 1995. Comparison of the energetic efficiencies of hydrogen and oxychemicals formation in *Klebsiella pneumoniae* and *Clostridium butyricum* during anaerobic growth on glycerol. *J. Biotechnol.* 39: 107-17.
- Barbirato F., Bories A. 1997. Relationship between the physiology of Enterobacter agglomerans CNCM 1210 grown anaerobically on glycerol and the culture conditions. *Res. Microbiol.* 148:475-84.
- Menzel K., Zeng A.P., Deckwer W.D. 1997. High concentration and productivity of 1,3-propanediol from continuous fermentation of glycerol by *Klebsiella pneumoniae*. *Enzyme Microb. Technol.* 20: 82-6.
- Dharmadi Y, Murarka A, Gonzalez R. 2006. Anaerobic fermentation of glycerol by *Escherichia coli*: a new platform for metabolic engineering. *Biotechnol. Bioeng.* 94:821-9.
- Zhu X.Y., Lubeck J., Kilbane III J.J. 2003 Characterization of Microbial Communities in Gas Industry Pipelines. *App. and Environ. Microbiol.* 69(9): 5354-63

### 2.6.4 Publications and Presentations

The following publications and presentations mention the support from award number: N00014-06-1-1055.

1. Qi, S; and Li, Q. X. 2010. *Proteomics in Pesticide Toxicology*. In: "Hayes' Handbook of Pesticide Toxicology" (R. Krieger, ed.). 3<sup>rd</sup> ed. Academic Press, New York, pp 603-626
2. Keum, Y. S.; Kim, J.-H.; Li, Q. X. 2010. *Metabolomics in Pesticide Toxicology*. In: "Hayes' Handbook of Pesticide Toxicology" (R. Krieger, ed.), 3<sup>rd</sup> ed. Academic Press, New York, pp 627-643
3. Liu, M.; Cui, Y.; Duan, Y.; Zhong, J.; Sun, W.; Wang, M.; Liu, S-Z.; Li, Q.X. 2010. Synthesis of metabolites of polycyclic aromatic hydrocarbons. *Mini-Reviews in Organic Chemistry* 7(2): 134-144.
4. Keum, Y.-S.; Kim, J.-H.; Li, Q.X. 2012. *Evidence of stress: Biomarkers and metabolomics*. In: "Encyclopedia of Sustainability Science and Technology: Environmental Toxicology" (Editor-in-chief: Robert A. Meyers; Section Editor: Edward A. Laws). Springer, New York, DOI: 10.1007/978-1-4419-0851-3
5. Tittabutr, P.; Cho, I.K.; Li, Q.X. 2011. *Phn and Nag-like dioxygenases metabolize*

- polycyclic aromatic hydrocarbons in Burkholderia sp. C3. Biodegradation, DOI: 10.1007/s10532-011-9468-y*
6. Li, Q.X. *Bacterial Degradation of Polycyclic Aromatic Hydrocarbons and Heterocyclic Aromatics. International Society Biotechnology 2008 Conference at Gangtok, India, 28-30 December 2008.*
  7. Li, Q.X. *Environmental Biotechnology. Invited keynote. International Society Biotechnology Conference at Gangtok, India, 28-30 December 2008.*
  8. Tittabutr, P.; Cho, I.K.; and Li, Q.X. *Cloning, expression and proteomic studies of two different dioxygenase systems responsible for initial degradation of phenanthrene in Burkholderia sp. C3. Int'l Conf. on the Environment, Wuhan, China. June 27-30, 2009.*
  9. Jia, R.; Chen, W.F.; Cho, I.K.; Chen, W.X.; Li, Q.X. *Identification and classification of rhizobia by whole-cell protein MALDI TOF MS and BioTyper™. The 21st Northern American Nitrogen Fixation Conference. Columbia, Missouri. June 13-18, 2010.*
  10. Wang, J.; Chen, W.F.; Li, Q.X. *Classification and identification of different bacterial species by using whole-cell proteins fingerprints barcodes from MALDI TOF/TOF mass spectrometry and MALDI Biotyper™ software. The 21st Northern American Nitrogen Fixation Conference. Columbia, Missouri. June 13-18, 2010.*
  11. Su, W.; Li, Q.X. *Proteome of a desulfurization bacterium Arthrobacter sp. BIT's 1st annual world congress of petromicrobiology-2010. July 25-27, 2010. Dalian, China.*
  12. Li, Q.X.; Tittabutr, P.; Keum, Y.S.; Seo, J.S.; Cho, I.K.; Kim, J.H. *Genomic, Metabolomic and Proteomic Studies of Burkholderia sp. C3 in Response to Chemical Stresses. The International Conference on Environment OMICS, Guangzhou City, China. November 8-12, 2011.*

## **2.7 Biofuel Corrosion Research**

Renewable energy has become one of today's leading topics worldwide. From the fluctuating prices of oil to reducing the greenhouse footprint, renewable energy has gained considerable attention.

Biodiesels has begun to emerge as an alternative fuel source for passenger and commercial vehicles. Unfortunately, sparse research has been conducted on biodiesel corrosion of storage tanks, fuel tanks and pipelines. Because of the organic nature of biodiesels, microbiologically influenced corrosion (MIC) is a potential concern for pipelines and tanks used in the transportation and storage of biodiesel fuels.

This project will investigate MIC of plain carbon steel in biodiesel fuel mixtures.

### **2.7.1 Scope of Work and Approach**

This project is a comprehensive study to elucidate the effects of biodiesel on MIC of plain carbon steel that is typically used for pipelines, storage tanks, and fuel tanks. Corrosion testing will encompass both biodiesel-freshwater and biodiesel-seawater systems. At this time, only studies on the biodiesel-freshwater system have commenced. In a preliminary test, corrosion specimens were exposed for six weeks under aerobic conditions. Longer-term six-month and one-year exposures in aerobic or anaerobic environments have commenced.

Plain carbon 1018 steel was chosen based on similar chemical compositions to that of API Spec 5L X60 pipeline steel and ASTM A36 steel (often used in fuel tank storage). Biodiesel and diesel samples consisted of 100% biodiesel (B100), 20% biodiesel (B20), and ultra-low-sulfur diesel (ULSD). Biodiesel and diesel samples were split into two categories: filtered and unfiltered. Filtered fuel samples were filtered via 0.22 um filter membrane to eliminate bacteria already present in the fuel; whereas, unfiltered fuel samples were used in the "as is" condition from a diesel fuel pump of a local Oahu gas station.

Molecular biological techniques will be the primary method employed to identify bacterial species. As a supplement, biochemical techniques will also be used in characterizing bacteria species. Common techniques employed in biochemical characterization include Gram staining, enzyme production, and carbohydrate fermentation tests. Molecular identification of bacteria will be performed via 16S rRNA sequencing. DNA sequences will be analyzed via the National Center for Biotechnology Information (NCBI) GenBank and BLAST search. Corrosion of steel samples will be analyzed by weight loss; optical, scanning electron, and atomic force microscopies; Raman and Fourier Transform Infrared (FTIR) Spectroscopies; and x-ray diffraction.

The preliminary six-week exposure tests showed variations in the regions of corrosion (i.e., fuel phase or water phase) based on the fuel type, in addition to variations in the types of rust products formed.

### **2.7.2 Technical Accomplishments**

This section summarizes the technical accomplishments of the task.



### 2.7.2.1 Literature Review

Microbiologically influenced corrosion (MIC) is an electrochemical process where microorganisms initiate, facilitate, or accelerate a corrosion reaction on a metal surface (Rajasekar et al., 2009). There are three types of microorganisms. These include bacteria, fungi, and algae. Bacterial effects will be the focus in this project. Bacteria are ubiquitous single-celled prokaryotic organisms, and vary in size and shape, each having its own characteristics. Some bacteria are pathogenic, but the majority is beneficial to life and the environment.

In MIC, sulfur-reducing bacteria (SRB) are the most notable and have been shown to accelerate corrosion (Beech and Sunner, 2004). These types of bacteria are anaerobic and produce hydrogen sulfide which acidifies the environment. They are also responsible for catalyzing the penetration of hydrogen into steels, a phenomenon known as sulfide-induced stress cracking. SRBs are just one type of bacteria which have been shown to accelerate corrosion. Others include sulfur-oxidizing bacteria, iron-oxidizing/reducing bacteria, manganese-oxidizing bacteria, and bacteria secreting organic acids and slime (Beech and Sunner, 2004).

The organic nature of biodiesels makes it a prime target for microbial contamination mainly in the form of bacteria. Bacteria are able to survive in these fuels whenever there is the presence of water. Microorganisms start to grow in the water phase, but they feed on fuel at the phase boundary (Klofutar and Golob, 2007). Contamination of fuel by microorganisms causes biofouling. Whenever biofouling occurs, an extracellular polymeric substance, commonly known as a biofilm, forms on the substrate. The term biofilm refers to the development of microbial communities on submerged surfaces in aqueous environments (Characklis and Marshall, 1990). Thus, a bacterial consortium is formed and corrosion is accelerated due to the variety of bacteria present.

#### 2.7.2.1.1 Case Studies

There are three notable case studies regarding biodiesel corrosion of pipeline steel. In one of the studies, 11 different bacterial species were isolated from a diesel and naphtha-transporting pipeline in India. SRBs are usually the culprits in corrosion of petroleum production systems; however, this study revealed that no SRBs were found in the corrosion products collected from both pipelines (Rajasekar et al., 2009). Instead, ferric compounds, manganese complex, and  $\text{Fe}_2\text{O}_3$  were observed in the corrosion product in the diesel pipeline; whereas, manganese oxides, and silicon dioxides were found in the corrosion product samples collected from the naphtha pipeline (Rajasekar et al., 2009). The presence of acid-forming bacteria *K. oxytoca* ACP, *B. cereus* AN4, *P. stutzeri* AP2, and *S. marcescens* ACE2 was detected, suggesting that they may play a key role in corrosion (Rajasekar et al., 2009). Thus, this study demonstrates other types of bacteria, besides SRBs, may increase corrosion of diesel and naphtha-transporting pipelines.

Rajasekar et al., 2009 also isolated the bacterial species *Serratia marcescens* ACE2 for a study of diesel degradation and its influence on corrosion. From gas chromatography–mass spectrometry, the bacterium was shown to significantly degrade the hydrocarbons present in the diesel samples. The calculated corrosion rates, based on the weight-loss method, with and without the bacterium present in the samples, were found to be 0.0687 and 0.0026 mm/year, respectively (Rajasekar et al., 2007).

A similar experiment was conducted, but instead using the bacterial species *Bacillus cereus* ACE4 to determine its effects on corrosion of pipeline steel. This particular species was a manganese oxidizer, and corrosion rates with the bacterium present was 0.2003 mm/year or about twice as high when the bacterium was absent (0.1059 mm/year) (Rajasekar et al., 2007).

Thus, these new studies indicate that there are other bacteria besides the SRBs that have been shown to cause significant corrosion in petroleum production and transporting systems. These other types of bacteria cannot be ignored, as SRBs are not always found and hence are not the only source of MIC.

#### **2.7.2.2 Laboratory Setup for MIC**

Sterility is a major concern regarding the biofuel experiments to be conducted. A NUAIRE class II, type A2 biosafety cabinet was purchased to ensure a sterile environment when preparing the experiments. This cabinet also ensures a precautionary safety measure in the event of exposure to biohazardous substances.

A tabletop Tuttnauer autoclave was purchased to sterilize glassware and equipment. Because of the ubiquitous nature of microorganisms, an autoclave is necessary to sterilize and destroy any microorganisms. An autoclave raises the temperature to 121 °C and raises the pressure to 1 bar. For maximum sterility, the autoclave is capable of raising the temperature to 134 °C at a pressure of 2 bar.

A Shel Lab BacBasic anaerobic incubator was purchased in order to culture anaerobic bacteria. Much literature has shown that it is these types of bacteria that are responsible for corrosion in biofuels. This anaerobic chamber will also be used to simulate anaerobic environments where experimental 1018 steel coupons immersed in fuel-water mixtures can be exposed.

A Fisher Scientific laboratory incubator was also purchased in order to grow and sustain bacteria in a laboratory setting.

Identification of these bacterial species was carried out with the use of an Eppendorf thermocycler polymerase chain reaction (PCR) machine. This machine allows for the amplification of gene fragments where they can then be identified and matched to specific bacterial species.

#### **2.7.2.3 Preliminary Biofuels Corrosion Experiment in Potable Water-biofuel Mixtures**

The following explains a preliminary experiment that was conducted to assess biofuel corrosion of 1018 plain carbon steel for a six-week exposure period. The experiment also helped to develop a comprehensive methodology for the long-term 6-month and 12-month exposures.

##### **2.7.2.3.1 Methodology**

Plain carbon 1018 steel was chosen as the material to be investigated based on its similar chemical compositions to that of ASTM A36 steel and API Spec 5L X60, which are often used for fuel tank storage and pipelines, respectively. Table 2.7.1 tabulates the chemical compositions of these specifications and 1018 grade steel.

The types of fuel that were chosen for this experiment were B100, B20, and ULSD. The 1018 steel coupons were machined to the following dimensions: 2.25 in. x 1 in. x 0.125 in. The

coupons were then acetone washed to remove any oil residue and weighed to obtain an initial mass. To prevent oxidation of the steel, the coupons were kept in a dry box (< 1% relative humidity) prior to the corrosion experiment.

**Table 2.7.1 Chemical composition of selected specifications and 1018 steel**

Material Specifications	Chemical Composition			
	C, max. %	Mn, max. %	P, max. %	S, max. %
ASTM A36	0.25	-	0.04	0.05
API Spec 5L X60	0.28	1.40	0.03	0.03

Material	Chemical Composition			
	C, %	Mn, %	P, max. %	S, max. %
1018 Steel	0.15 - 0.20	0.60 - 0.90	0.035	0.04

Potable water was added to facilitate contamination within the fuels. The fuel-water mixture (40 mL fuel, 40 mL water) were stored in 100 mL glass Pyrex media bottles. The 1018 steel coupon samples were placed in these fuel-water mixtures at an approximate angle of 45° with respect to the horizon. Figure 2.7.1 depicts this setup.



**Figure 2.7.1 Experimental setup of fuel-water mixture with 1018 steel coupons immersed**

Triplicates of each fuel-water mixture and 1018 steel coupon were exposed outdoors aerobically for six weeks. Another triplicate of the same fuel-water mixtures and 1018 steel coupons were exposed outdoors aerobically for six weeks as a control. The media bottles of the controls were capped with a 0.22  $\mu\text{m}$  membrane filter to eliminate bacteria contamination from the environment. Therefore, a total of 9 uncapped samples and 9 capped samples were exposed outdoors. The sample labeling convention of each coupon is tabulated in Table 2.7.2 below.



To determine the presence of bacteria in the fuel-water mixtures, 1 mL of the water from each fuel-water sample were plated aerobically on blood agar plates (BAP) (tryptic soy agar with 5% sheep blood) and incubated for three days at 35 °C. This was done once every week for the duration of the experiment. As a control, the potable water that was used in the experiment was also tested for bacteria using the same method outlined above.

**Table 2.7.2 Summary of 1018 steel coupon labeling convention**

Fuel Type	Experiment	Control
B100	B1E1	B1EC1
	B1E2	B1EC2
	B1E3	B1EC3
B20	B2E1	B2EC1
	B2E2	B2EC2
	B2E3	B2EC3
ULSD	U2E1	U2EC1
	U2E2	U2EC2
	U2E3	U2EC3

After six weeks, the steel coupon samples were removed from their fuel-water mixtures and rinsed in an acetone bath to remove excess oil residual. The corrosion products on the steel samples were then analyzed using a Hitachi VP-SEM S-3400N scanning electron microscope (SEM) equipped with an Oxford INCA EDX350 energy dispersive X-ray (EDX) and Rigaku MiniFlex II Benchtop X-ray diffraction (XRD) system.

The penetration rate (mm/year) was calculated for each sample based on the total mass loss. To obtain the total mass loss, the samples were cleaned with an acid wash to remove the corrosion products. The acid wash procedure followed ISO 8407 – “Removal of corrosion products from corrosion test specimens.”

#### **2.7.2.3.2 Results**

Figure 2.7.2 depicts the 1018 steel coupons after the six-week exposure period. B100 samples exhibited the least amount of corrosion with corrosion occurring in the water phase. In the B20 samples, corrosion primarily occurred in the fuel phase; whereas, the ULSD samples exhibited corrosion everywhere.



**Figure 2.7.2** Photos of 1018 steel coupons after six-week exposure duration. Top row, left to right: B1E1, B2E1, U2E1; bottom row, left to right: B1EC1, B2EC21 and U2EC1 (control specimens).

The energy dispersive X-ray analysis (EDXA) revealed the elemental composition of the corrosion products on the 1018 steel coupons. Figure 2.7.3 below depicts the analysis for the 1018 steel coupon immersed in the B100 fuel mixture. The corrosion product identified was possibly iron(III) oxide.

Element	Weight%	Atomic%
Fe K	69.94	40.00
O	30.06	60.00
Totals	100.00	

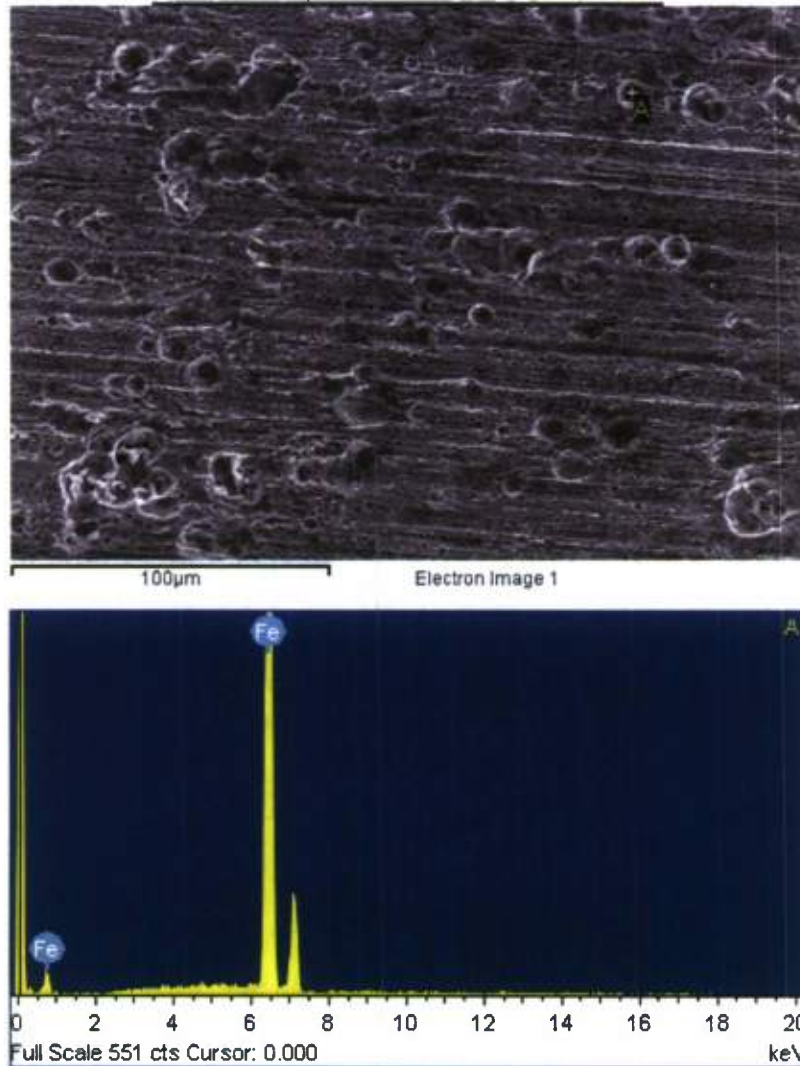


**Figure 2.7.3 EDXA for 1018 steel coupon immersed in B100 fuel mixture**

Figure 2.7.4 below depicts the analysis for the 1018 steel coupon immersed in the B20 fuel mixture. Notice the relatively high carbon content.



Element	Weight %	Atomic %
C K	24.01	31.36
Fe K	8.42	2.37
O	67.57	66.27
Totals	100.00	



**Figure 2.7.4 EDXA for 1018 steel coupon immersed in B20 fuel mixture**

Figure 2.7.5 below depicts the analysis for the 1018 steel coupon immersed in the ULSD fuel mixture. Also notice the relatively high carbon content.

Element	Weight %	Atomic %
C K	20.55	28.89
Na K	0.74	0.55
Fe K	16.57	5.01
O	62.13	65.56
Totals	100.00	

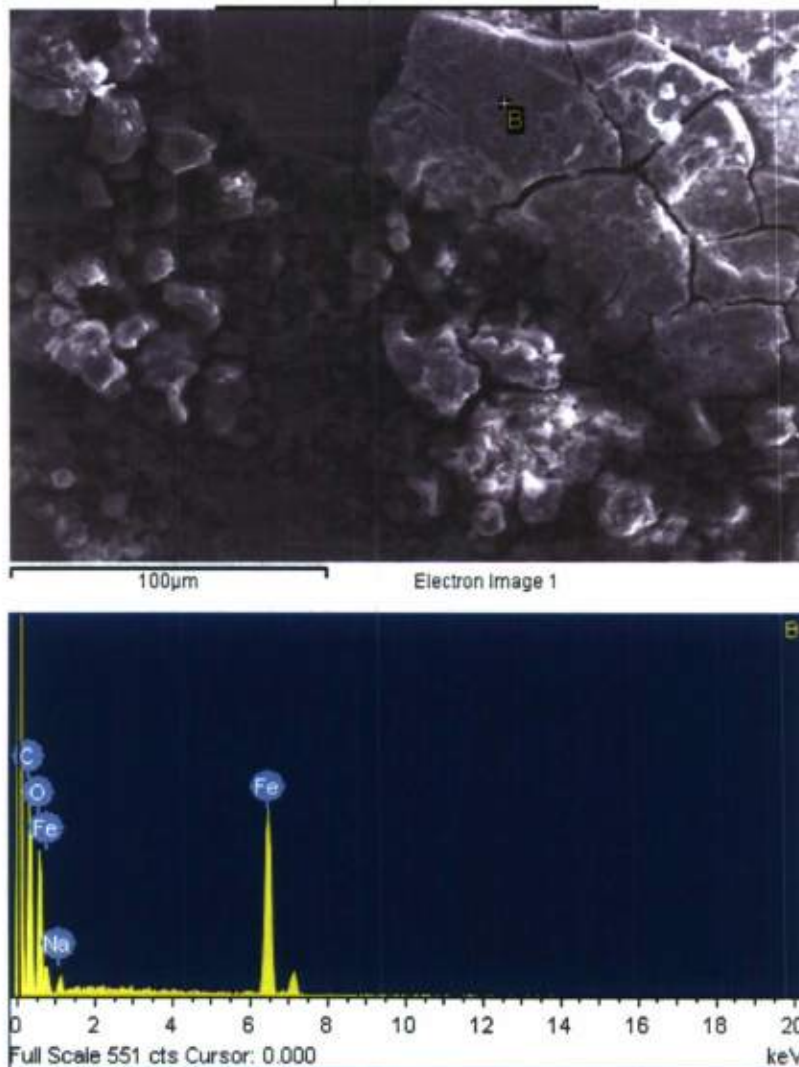
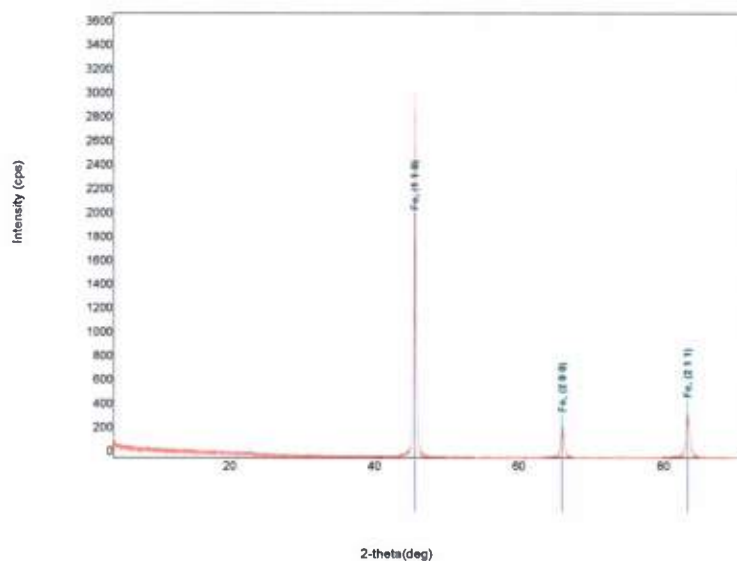


Figure 2.7.5 EDXA for 1018 steel coupon immersed in ULSD fuel mixture

XRD analysis was also performed on the 1018 steel coupons to determine the corrosion products. Figure 2.7.6 below depicts the results obtained for a virgin 1018 steel sample. This was used as a comparison to all other steel coupon samples. The three peaks correspond to the element iron.



**Figure 2.7.6 XRD for virgin 1018 steel coupon**

The remaining samples except for the B20 revealed results similar to the virgin 1018 steel coupon. Only the three iron peaks were seen with no signs of corrosion product. Figure 2.7.7 below depicts the XRD results for the B100 sample.

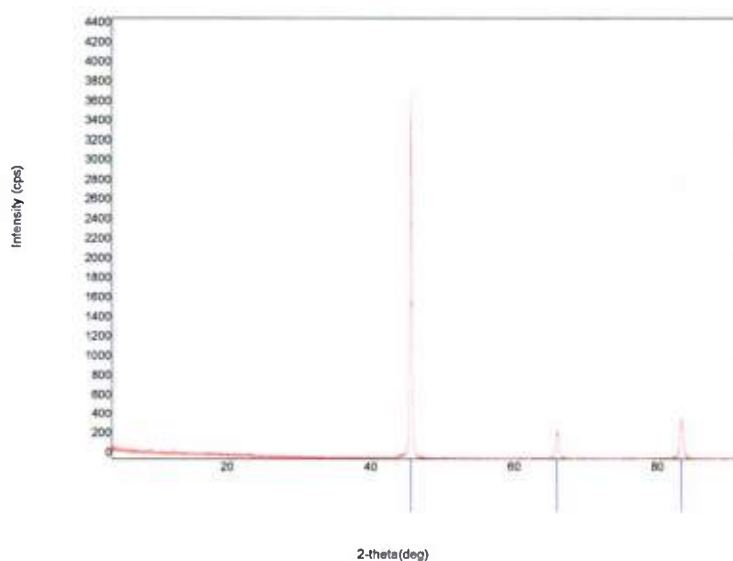


**Figure 2.7.7 XRD for 1018 steel coupon immersed in B100 fuel mixture**

Figure 2.7.8 below depicts the XRD results for the ULSD sample.



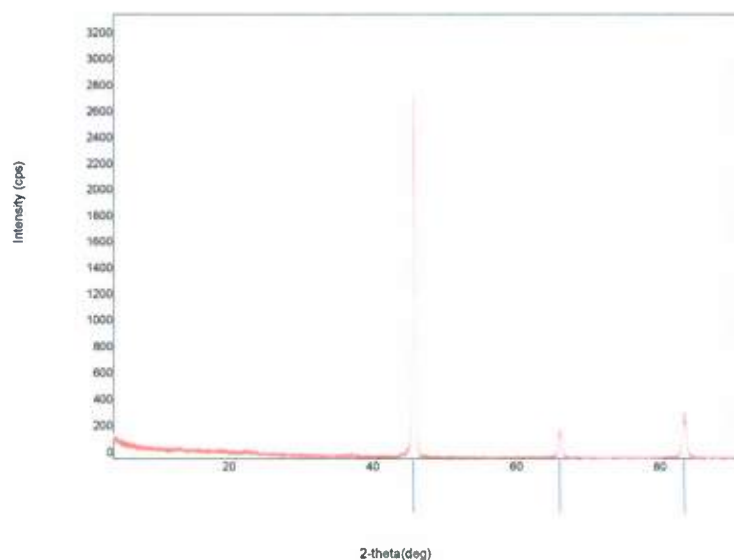


**Figure 2.7.8 XRD for 1018 steel coupon immersed in ULSD fuel mixture**

In the case of the B20 sample, Figure 2.7.9 below reveals the three iron peaks along with other peaks that corresponded to an unknown corrosion product. Figure 2.7.10 below shows the peaks for iron formate hydrate with chemical formula  $C_2H_2FeO_4 \cdot 2H_2O$ .

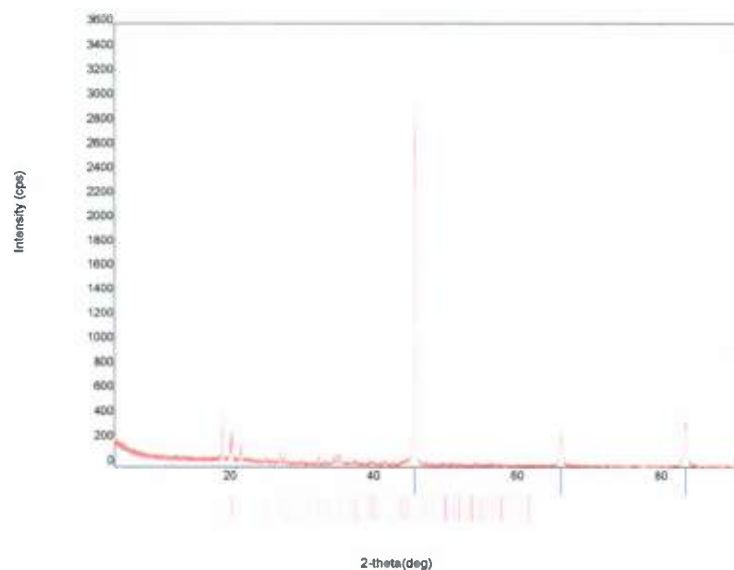


**Figure 2.7.9 XRD for 1018 steel coupon immersed in B20 fuel mixture**

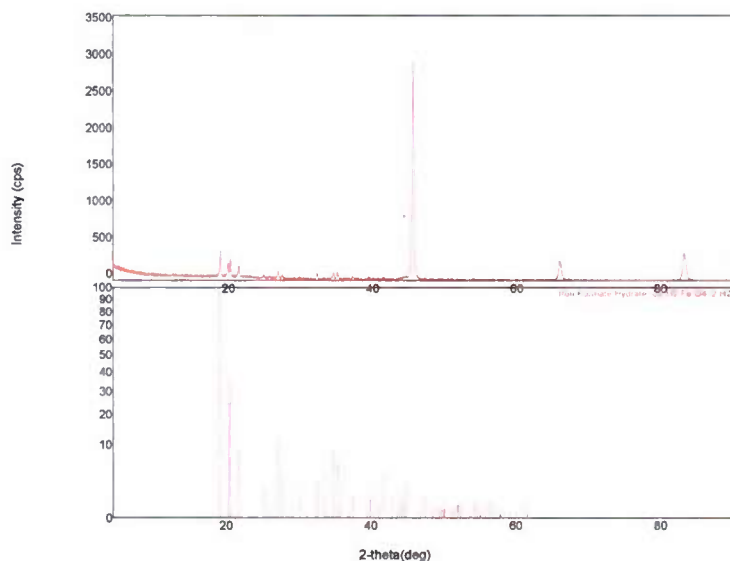


**Figure 2.7.10 XRD for 1018 steel coupon immersed in B20 fuel mixture with lines for iron formate hydrate with chemical formula  $C_2H_2FeO_4 \cdot 2H_2O$**

Utilizing a software XRD library, the most probable compound identified was an iron formate hydrate with chemical formula  $C_2H_2FeO_4 \cdot 2H_2O$ . However, more analysis needs to be performed to confirm this result.

The penetration rate for each sample was calculated, averaged and tabulated in Table 2.7.3 below.

**Table 2.7.3 Calculated averaged penetration rate values**

Sample	PR (mm/year)
B100	0.0099
B100C	0.0810
B20	-0.0730
B20C	0.1232
ULSD	0.1012
ULSDC	0.0247

The negative penetration rate of the B20 sample is a result of that sample gaining mass instead of losing mass. The specimens were cleaned twice using the ISO 8407 method.

Microbial activity after one week of exposure for each sample is shown in Figure 2.7.11 below.

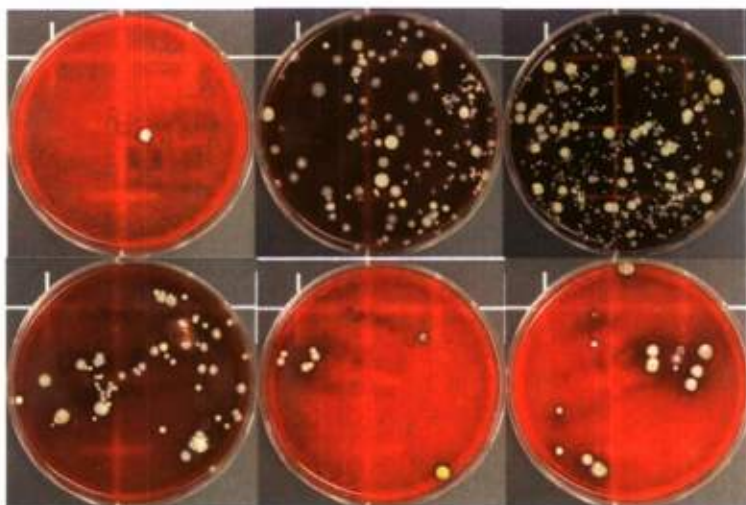


**Figure 2.7.11 1mL of water taken from B100, B20 and ULSD fuel mixtures plated on BAP**

Figure 2.7.12 below depicts the 1mL of potable water plated on BAP for comparison.



**Figure 2.7.12 1mL potable water plated on BAP**

The observed bacteria colonies from Figure 2.7.11 closely match the colony morphology of the bacteria from Figure 2.7.12. Therefore, the bacteria within the water from the fuel mixture are likely a result from potable water bacteria contamination. In the subsequent weeks, bacteria ceased to be found when cultured on BAP. It is likely that the bacteria in the water phase could not survive due to the anaerobic conditions that develop in the water phase due to the layer of fuel on top which may have impeded oxygen diffusion. Recently, PCR was performed to attain the type of bacterial species present on the agar plate of Figures 2.7.11 and 2.7.12, most notably the white bacterial colonies since these colonies were present throughout the entire duration of exposure. Thus, the white bacterial colonies are capable of living in the experimental conditions. PCR results revealed the white colonies to be of the species *Bacillus flexus* (99% certainty) and *Staphylococcus hominis* (98% certainty).



### **2.7.2.3.3 Discussion**

Penetration rates of the B100 and B20 biodiesel fuel controls were significantly higher than their respective experimental counterparts. The penetration rate of the ULSD was found to be higher than its respective control. The B100 biodiesel exhibited the slowest penetration rate of all samples tested.

SEM results indicated the presence of iron oxide as a corrosion product. XRD results revealed an organic-Fe corrosion product on B20 samples, which may have not been completely removed by the ISO 8407 cleaning method that was used to determine the weight loss for corrosion rate determination. The B20 specimens showed an increase in mass.

The microorganisms present after one week of exposure are likely due to the initial potable water contamination. These microorganisms were likely not able to survive in anaerobic conditions that developed in the water phase beneath the thick layer of fuel. It is unknown whether anaerobic microorganisms were present in the samples.

### **2.7.2.3.4 Conclusions**

Overall, the 100% biodiesel fuel B100 yielded the lowest corrosion rates. The 20% biodiesel B20 and the ULSD yielded similar corrosion rates.

The presence of bacteria found within the samples was likely from potable water contamination. There were no further signs of aerobic bacteria after the first week of exposure. Therefore, efforts will be made to investigate the presence of anaerobic bacteria with the help of an anaerobic chamber. Also, specific bacteria strains found will be identified via molecular techniques such as sequencing of 16S rRNA genes. Corrosion rates can then be correlated to specific bacterial strains.

Since B20 samples gained mass, there is likely some type of unknown corrosion product remaining on these samples. Efforts will be made to identify these corrosion products via XRD, SEM, and Raman spectroscopy.

### **2.7.2.4 Characterization of Bacteria Found**

Several bacterial species were successfully isolated from biodiesel fuel samples. Figures 2.7.13 to 2.7.16 portray the various bacteria species isolated, along with the results obtained from the 16S rRNA sequencing.

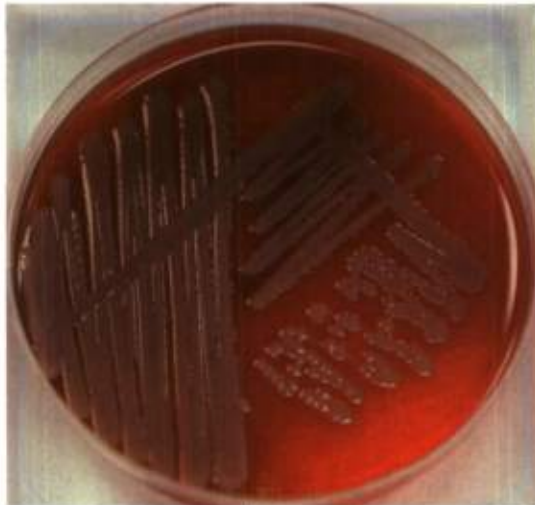


**Figure 2.7.13** Sample A, 16S rRNA sequencing yields a 65% match to the bacterial species *Bacillus licheniformis*



**Figure 2.7.14** Sample B, 16S rRNA sequencing yields a 98% match to the bacterial species *Aeromicrobium tamlense*



**Figure 2.7.15** Sample F, 16S rRNA sequencing yields a 98% match to the bacterial species *Bacillus horikoshi*



**Figure 2.7.16** Sample G, 16S rRNA sequencing yields a 93% match to the bacterial species *Bacillus novalis*

#### **2.7.2.5 Work in Progress**

The preliminary experiments revealed bacteria contamination from potable water. For the six-month and 12-month long experiments, ultrapure water will be used instead of the potable water. The biodiesel and diesel will be either filtered or unfiltered, and exposed in an aerobic or anaerobic environment. This experiment will allow for the correlation of corrosion rates in different types of fuels when a consortium of bacteria is present. To address the corrosion activities of specific bacterial species, specific bacterial strain will be inoculated into sterile fuel

samples so that the corrosion rates of that particular bacteria species can be determined. The following table summarizes the current experiments in progress.

The experiments will be run in triplicate with a total number of 108 samples. Table 2.7.4 tabulates the sample naming and experimental setup.

**Table 2.7.4 Specimen Identification Scheme**

<b>B100 (Unfiltered), 6 Months</b>				<b>B100 (Filtered), 6 Months</b>			
1UC61	1UC62	1UC63	(Anaerobic)	1FC61	1FC62	1FC63	(Anaerobic)
1UO61	1UO62	1UO63	(Aerobic)	1FO61	1FO62	1FO63	(Aerobic)
1UM61	1UM62	1UM63	(Sterile Aerobic)	1FM61	1FM62	1FM63	(Sterile Aerobic)
<b>B100 (Unfiltered), 1 Year</b>				<b>B100 (Filtered), 1 Year</b>			
1UC11	1UC12	1UC13	(Anaerobic)	1FC11	1FC12	1FC13	(Anaerobic)
1UO11	1UO12	1UO13	(Aerobic)	1FO11	1FO12	1FO13	(Aerobic)
1UM11	1UM12	1UM13	(Sterile Aerobic)	1FM11	1FM12	1FM13	(Sterile Aerobic)
<b>B20 (Unfiltered), 6 Months</b>				<b>B20 (Filtered), 6 Months</b>			
2UC61	2UC62	2UC63	(Anaerobic)	2FC61	2FC62	2FC63	(Anaerobic)
2UO61	2UO62	2UO63	(Aerobic)	2FO61	2FO62	2FO63	(Aerobic)
2UM61	2UM62	2UM63	(Sterile Aerobic)	2FM61	2FM62	2FM63	(Sterile Aerobic)
<b>B20 (Unfiltered), 1 Year</b>				<b>B20 (Filtered), 1 Year</b>			
2UC11	2UC12	2UC13	(Anaerobic)	2FC11	2FC12	2FC13	(Anaerobic)
2UO11	2UO12	2UO13	(Aerobic)	2FO11	2FO12	2FO13	(Aerobic)
2UM11	2UM12	2UM13	(Sterile Aerobic)	2FM11	2FM12	2FM13	(Sterile Aerobic)
<b>ULSD (Unfiltered), 6 Months</b>				<b>ULSD (Filtered), 6 Months</b>			
3UC61	3UC62	3UC63	(Anaerobic)	3FC61	3FC62	3FC63	(Anaerobic)
3UO61	3UO62	3UO63	(Aerobic)	3FO61	3FO62	3FO63	(Aerobic)
3UM61	3UM62	3UM63	(Sterile Aerobic)	3FM61	3FM62	3FM63	(Sterile Aerobic)
<b>ULSD (Unfiltered), 1 Year</b>				<b>ULSD (Filtered), 1 Year</b>			
3UC11	3UC12	3UC13	(Anaerobic)	3FC11	3FC12	3FC13	(Anaerobic)
3UO11	3UO12	3UO13	(Aerobic)	3FO11	3FO12	3FO13	(Aerobic)
3UM11	3UM12	3UM13	(Sterile Aerobic)	3FM11	3FM12	3FM13	(Sterile Aerobic)



Figure 2.7.17 depicts the new experimental setup to be employed.

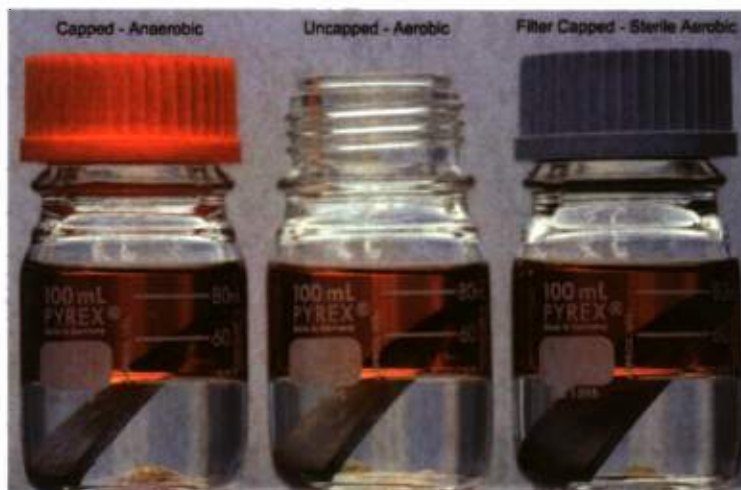


**Figure 2.7.17 The three environmental conditions of the new experiment**

The media bottles containing the 1018 steel samples along with fuel-water mixtures will be subjected to three environmental conditions. Bottles with an orange cap are air-tight sealed and simulate an anaerobic environment. Uncapped bottles simulate an aerobic environment, while bottles with a gray cap simulate a “sterile” aerobic environment. The gray cap is fitted with a 0.22um filter at the top to allow only air to be exchanged into and out of the bottle. Bacteria from the outside environment will not be able to enter the bottle.

The experimental setup of the media bottles are depicted in Figure 2.7.18. A total of 12 boxes containing nine samples are currently being exposed outdoors.



**Figure 2.7.18 Experimental setup containing nine samples**

Figures 2.7.19 and 2.7.10 depict the entire experimental setup consisting of a total of 12 boxes and 108 experimental samples to be exposed outdoors for 6 months and 1 year.



**Figure 2.7.19 Experimental setup showing individual boxes containing samples**



**Figure 2.7.20 Samples loaded on pallet to be exposed outdoors**

### **2.7.3 References**

- Beech, I. B. and J. Sunner (2004). "Biocorrosion: towards understanding interactions between biofilms and metals." *Current Opinion in Biotechnology* 15(3): 181-186.
- Characklis, W.G., Marshall, K.C., 1990. *Biofilms*. Wiley, New York.
- Klofutar, B. and J. Golob (2007). "Microorganisms in Diesel and in Biodiesel Fuels." *Acta Chimica Slovenica* 54(4): 744-748.
- Rajasekar, A., B. Anandkumar, et al. (2009). "Characterization of corrosive bacterial consortia isolated from petroleum-product-transporting pipelines." *Applied Microbiology and Biotechnology* 85(4): 1175-1188.
- Rajasekar, A., T. G. Babu, et al. (2007). "Role of *Serratia marcescens* ACE2 on diesel degradation and its influence on corrosion." *Journal of Industrial Microbiology & Biotechnology* 34(9): 589-598.
- Rajasekar, A., T. Ganeshbabu, et al. (2007). "Biodegradation and corrosion behavior of manganese oxidizer *Bacillus cereus* ACE4 in diesel transporting pipeline." *Corrosion Science* 49(6): 2694-2710.



## 2.8 Waste Management Using the Flash Carbonization™ Process

The demonstration-scale Flash-Carbonization™ Reactor (Demo FCR) that we have on campus is capable of a large throughput: consequently its testing requires a large quantity of feedstock (e.g., 1000 lb for a single run), a costly, large, rented air compressor, a costly, rented power generator, and an afterburner (for emissions remediation) so large that its size alone would exceed the space we have available. Each test requires months of preparation, and the cost of modifying commercial-scale equipment is high.

To speed our progress we designed and fabricated a 1/10<sup>th</sup> scale canister that fits within the existing pressure vessel and mimics the behavior of a full-size canister (see photo below). The 1/10<sup>th</sup> scale canister is 12 in. in diameter and 9 ft. tall and will accommodate about 100 lb of corn cobs. This canister behaves like a “core” of a full-size 3-ft. diameter canister. An air compressor and a power generator that are already available on our site will be sufficient to execute test runs using this canister. Because both the air compressor and power generator are nearly 10 years old and have been exposed to the elements continuously during their life with us, we may purchase backup equipment to assure our progress. In any case, now there will be no need to rent costly air compressors and power generators for our ongoing research.

It should be pointed out that in addition to the Demo FCR we have a laboratory-scale Flash-Carbonization™ Reactor (Lab FCR) for small-scale testing. The Lab FCR has its own Catalytic Afterburner (CAB), designated as the Lab CAB.

### 2.8.1 Scope of Work and Approach

On 1 June 2010 an experienced and talented Post-Doctoral Fellow (Dr. Javier Abrego) from the U. Zaragoza (Spain) joined us for one year. Dr. Abrego was assigned four tasks:



1. To further develop and fine tune a spreadsheet that tracks all mass and elemental balances through the Demo FCR and CAB based on measured species yields. The CAB is needed to remediate emissions (e.g., smoke and CO) in order to satisfy EPA and state regulations.
2. Measure gas flows and species concentrations entering and leaving the Lab CAB associated with the Lab FCR.
3. Use this laboratory data to calculate combustion kinetics over the monolithic catalyst in the Lab CAB. The kinetics will be employed for the design of the Demo CAB.
4. Prepare a preliminary design of the Demo CAB for the Demo FCR.

Also, during June, 2010 a MSE candidate in ME (Roland Considine) at UH began his thesis research with us. His focus during the past year was to assist Dr. Abrego with tasks 2, 3, and 4 above. During the summer, Roland worked on a complimentary NSF sponsored project with the

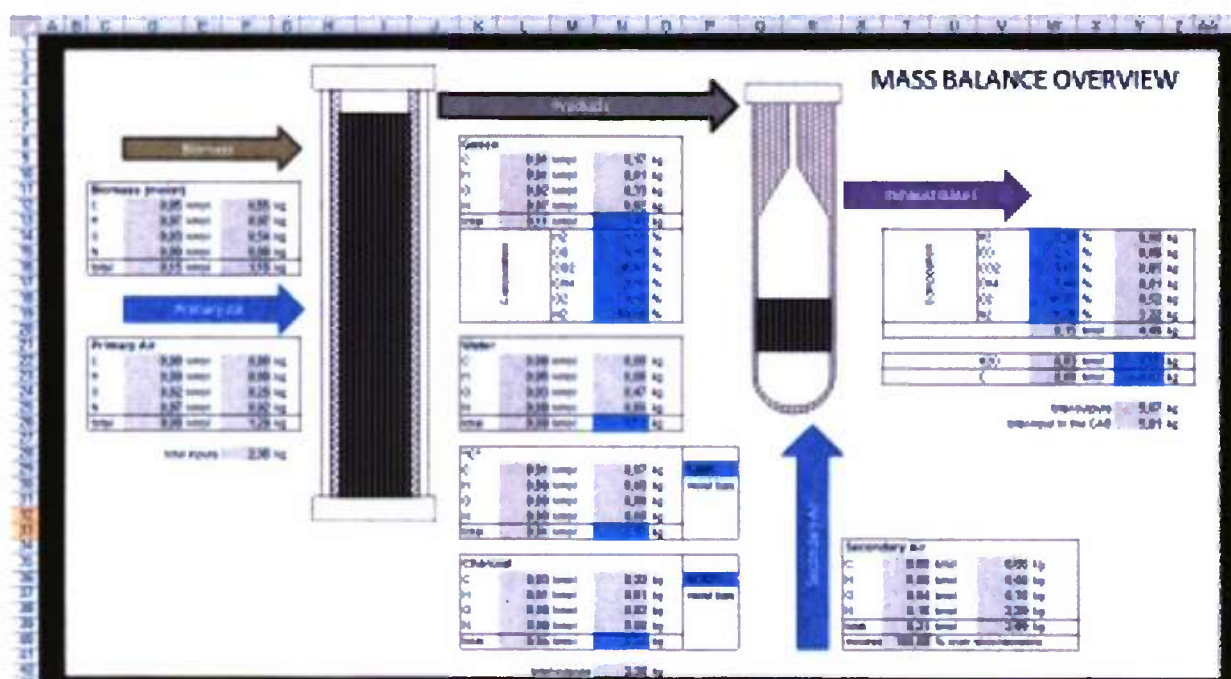


Dow Corning Corp. and the Norwegian Technological University (NTNU). Dow Corning uses wood charcoal as a reductant in its production of silicon (primarily in Brazil) for photovoltaic cells and other applications. At NTNU in Trondheim, Roland collaborated with Norwegian researchers to identify what carbonization conditions offer the highest yields of charcoal from Dow Corning woods. Since his recent return he has been heavily involved in improving the preliminary design of the Demo CAB and drawings for its fabrication.

## 2.8.2 Technical Accomplishments

Concerning Task 1: Dr. Abrego further developed a sophisticated Excel spreadsheet that simulates the performance of the Demo FC Reactor and CAB. This spreadsheet includes both mass and energy balances. Prior to the completion of the spreadsheet, we were concerned that moist feedstocks would not sustain high outlet temperatures in the CAB. The spreadsheet predicts that feedstocks with moisture contents approaching 50% will nevertheless generate high temperatures in the CAB sufficient for the oxidation of CO. At present the spreadsheet is being used to properly size the needed fans and catalyst monoliths. An extract from the spreadsheet is displayed below.

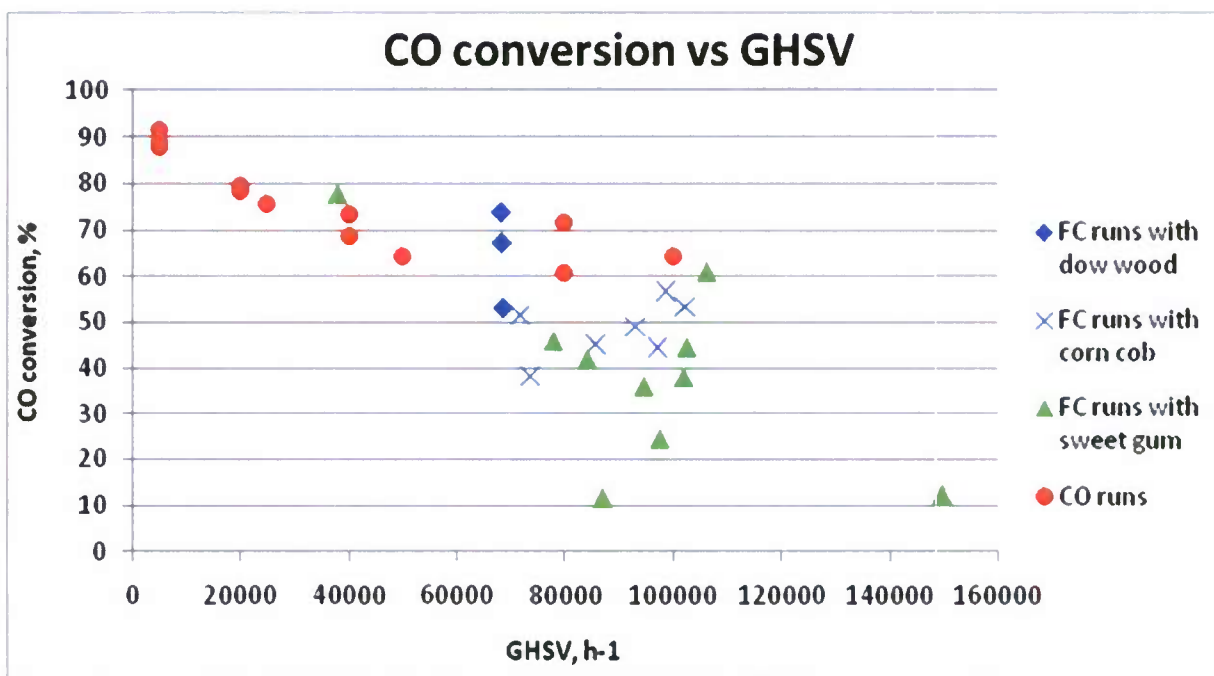
## 5 Mass balance overview for FC & CAB

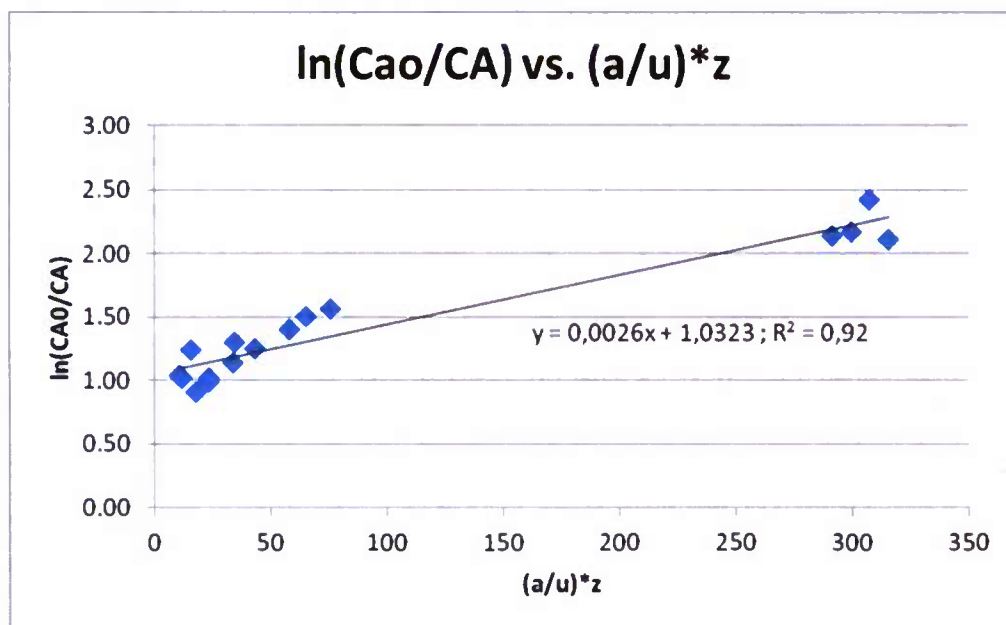


A summary of the main results of the mass balances through the FC and the Cab is presented in this sheet.

Concerning Task 2: Dr. Abrego and Roland completed an extensive study of the ability of the catalytic monoliths in the Lab CAB to oxidize CO. This ability is influenced by the inlet temperature, the inlet oxygen and carbon monoxide concentrations, the gas flow rate, the amount of catalyst present, and its condition. The graph on the top of the following page is one of several that summarize their results. Our findings indicate that we can achieve >90% conversion of CO with an affordable number of monoliths. Many of these tests used Hawaii Kai sewage sludge as the feedstock for the Lab FCR. The Hawaii Kai sewage sludge has peculiar properties, perhaps due to additives employed by the Hawaii Kai treatment facility. We are continuing to focus our work on this feedstock and its carbonization behavior.

Concerning Task 3: Dr. Abrego and Roland employed the CO measurements – together with the customary assumption that the kinetics of CO oxidation are mass transfer limited over the monolith at high temperatures – to estimate the effective mass transfer coefficient. The graph on the bottom of the following page displays a fit of the mass transfer limited model to the experimental data. Our findings indicate that the combustion of CO (and other combustibles entering the Lab CAB) generate sufficient heat to cause the CAB's temperature to steadily increase despite the delivery of copious needed secondary air to the CAB and heat losses from the CAB.





Concerning Task 4: we have completed the drawings of the Demo CAB mixer module (like a carburetor) and catalytic monolith modules and are seeking quotes from fabricators. We are ordering the needed flanges and other materials. We hope to initiate fabrication of the CAB by the end of October 2011.

All this work was summarized in a presentation that Dr. Abrego gave at the AIChE Annual Meeting in Salt Lake City (November, 2010).



### **3. Methane Hydrates**

#### **3.1 Objectives**

Methane hydrates in ocean sediments constitute an enormous energy reservoir that is estimated to exceed the energy content of all known coal, oil, and conventional natural gas resources. Located on continental margins throughout the world, methane hydrates offer unique opportunities as an onsite source of fuel for various marine applications and are believed to play a major role in seafloor stability and global climate.

National R&D programs on methane hydrates were initiated in Japan and India in the mid-1990's with the goal of commercial gas production within a 20 year time horizon. The U.S. established its own program in May 2000. The Methane Hydrate Research and Development Act of 2000 (Public Law 106-193) included seven technical areas of focus: (1) identification, exploration, assessment, and development of methane hydrate as a source of energy; (2) technology development for efficient and environmentally sound recovery of methane from hydrates; (3) transport and storage of methane produced from methane hydrates; (4) education and training related to methane hydrate resource R&D; (5) assessment and mitigation of environmental impacts of natural and purposeful hydrate degassing; (6) development of technologies to reduce the risks of drilling through methane hydrates; and (7) support of exploratory drilling projects. The objectives of the Methane Hydrates Task of the Hawaii Energy & Environmental Technology (HEET) initiative, which was initiated in 2001, reflect most of the priorities of P.L. 106-193, but emphasize those areas of particular relevance to the Office of Naval Research (ONR) and which are consistent to the overall goals of HEET. Specifically, the development of hydrates and related sources of seafloor methane as logistical fuels for Naval applications and related marine environmental issues, have been the principal areas of interest; exploratory drilling projects and seafloor stability/safety have received limited attention. Work also has been initiated to explore engineering applications of hydrates such as desalination and hydrogen storage. Task objectives were devised to leverage fully hydrate R&D expertise and infrastructure that had been developed at HNEI during previous research programs on CO<sub>2</sub> ocean sequestration and deep oil spills.

During the present reporting period (06/09-09/11), the goals of the HEET Methane Hydrates Task were:

- Pursue development of methods to recover methane gas from hydrates.
- Investigate the microbial processes in sediment that generate and modulate methane levels.
- Investigate engineering applications of hydrate.
- In cooperation with NRL and ONR Global (previously ONR-IFO), promote international collaborative research on methane hydrates.

Specific technical initiatives that were pursued to attain the above goals included:

- Conduct laboratory experiments using the Raman calorimeter on hydrate destabilization using chemical inhibitors.
- Initiate experiments to investigate hydrate formation and destabilization in porous media (i.e., sand) representative of natural hydrate deposits in the seafloor.

- Characterize the microbial assemblage that modulates methane leakage into the water column, in samples of deep ocean sediment overlying hydrates.
- Participate in collaborative field studies of offshore hydrate biogeochemistry with NRL.
- Initiate exploratory laboratory experiments of engineering applications of hydrates such as gas storage and transport.
- Organize workshops to promote international collaboration on methane hydrate R&D.

### **3.2 Score of Work and Approach**

Pursuant to the goals and technical objectives identified in the preceding section, work on the Methane Hydrates Task during the present reporting period focused on four primary areas which are described below.

#### **Hydrate Energy**

The major priority of this subtask was to elucidate the fundamental mechanism of methane hydrate destabilization for the purpose of producing fuel gas (and, to a lesser extent, to clear hydrate blockages that can form in natural gas conduits or deep ocean oil wells such as occurred during the 2010 Deepwater Horizon incident in the Gulf of Mexico). Toward that end, we continued our experimental studies of hydrate destabilization by chemical reagent injection to test the hypothesis we developed previously to explain the mode of action of these reagents. Since seafloor hydrates exist primarily in pore spaces in sand and sediment matrices, experiments were initiated to investigate hydrate formation and destabilization in porous media. Finally, we completed our experimental investigation of the specific heat of high pressure water.

#### **Environmental Impacts of Methane Release from Seafloor Hydrates**

This subtask is a continuation of activities pursued in previous years to: (1) assess the consequences of inadvertent or purposeful releases of methane from seafloor hydrates via the development of a model of methane transport through the ocean water column to the atmosphere; and (2) elucidate the mechanisms by which sediment microbes control free methane gas levels in, and methane leakage from, the seafloor sediment and arctic permafrost.

During the present phase, porewater and sediment samples collected during a research cruise with NRL in the Beaufort Sea off the North Slope of Alaska in September 2009 were cultured and tested to investigate methane consumption by resident methanotrophs. Exploratory studies of microbial metabolism employing a new micro-DSC (differential scanning calorimeter) were also initiated.

#### **Hydrate Engineering Applications**

The major priority of this subtask was to conduct exploratory studies of the use of gas hydrates for various engineering applications relevant to DOD interests, particularly fuel gas storage and transport. During the present phase of the HEET Initiative, emphasis was placed on assessing the feasibility of different hydrates to store H<sub>2</sub>.

#### **International Collaborative Research and Development**

To promote international R&D cooperation on methane hydrates in order to accelerate development of this energy resource, HNEI has sponsored and helped to organize a series of workshops on methane hydrates that was started under the HEET initiative in 2001. During the

current phase, the objective of this subtask was to provide logistical and organizational support for the 7<sup>th</sup> Workshop held in Wellington, New Zealand.

### 3.3 Technical Accomplishments

The principal technical accomplishments of the HEET Methane Hydrates Task for each of the components identified above are described in the following sections.

#### Hydrate Energy

During the present reporting period, the primary accomplishments of this subtask were: (1) initiated a new line of inquiry to investigate hydrate formation and dissociation in sand matrices to simulate conditions in natural seafloor hydrate deposits; and (2) continued the experimental study of chemical reagent destabilization of hydrates. The investigation of hydrate kinetics and equilibrium in sand is being performed as part of the Ph.D. dissertation research of a graduate student in the Department of Ocean and Resources Engineering at UH.

#### *Methane Hydrates in Porous Media*

Previously, our experimental and modeling activities have been limited to studies of simple gas-water-hydrate systems. Natural hydrate deposits, however, occur in permafrost and seafloor sediments. Commercial fuel gas production from marine methane hydrate reservoirs initially will target sites where the hydrate forms in the pore spaces of coarse sandy sediments. These “low-hanging fruit” are amenable to relatively simple production techniques based on depressurization (i.e., removal of gas from below the hydrate stability zone which results in a reduction of pressure in the overlying deposit that destabilizes the hydrate phase). Transport properties of the sand matrix determine the production characteristics of this type of extraction.

The Japanese national hydrates R&D program has standardized the sand employed in laboratory studies in order better to compare results from different laboratories. The U.S. national program has recently attempted to establish its own standard. We obtained samples of both the Japanese and U.S. standard sands known, respectively, as “Toyoura” and “Ottawa,” in late 2010 and have initiated experiments to investigate hydrate formation and dissociation in porous matrices prepared using these sands and also commercial silica. A principal near-term goal is to determine the impact of different void ratios on hydrate formation and dissociation. The primary accomplishments during the present reporting period include characterizing the sand samples and conducting exploratory experiments with the Raman calorimeter.

#### Sand Properties

Several kilograms of Toyoura and Ottawa sands were obtained from Yamaguchi University in Japan and the U.S. Department of Energy, respectively. Tests were conducted to determine physical properties of our sand samples including water content, grain size distribution and specific gravity. To investigate the effect of sand void ratio, samples of the Ottawa sand was prepared with modified particle size distribution. The Ottawa sand was sieved to remove fine particles. This sample will hereinafter be referred to as “Ottawa\*.”

Table 3.1 provides a comparison of the moisture content and density of the different sands. Particle size data are presented in Table 3.2 and Figure 3.1.



**Table 3.1 Moisture content and specific gravity of the sands**

	Moisture content (%)	Density (g/cm <sup>3</sup> )
Toyoura	0.3267	2.656
Ottawa	0.3010	2.671
Ottawa*	0.2277	2.672
Silica	-	≈ 2.700

**Table 3.2 Grain sizes of Toyoura, Ottawa, Ottawa\* sands**

			99.85% by weight of the sand is in the range of 140-425 µm 0.01% by weight of the sand is in the range of silt (< 75 µm)					
Sample	Toyoura							
	Sieve No.	Size (µm)	Mass of sieve (g)	Mass of sand (g)		Cumulative mass of sand (g)		
Sand	20	850	420.19	0.00	0.00	0.00	100.00	
	40	425	366.32	0.02	0.01	0.02	99.99	
	60	250	367.38	45.15	14.92	45.17	85.08	
	100	150	311.86	248.24	82.01	293.41	3.06	99.85
	140	140	345.12	8.83	2.92	302.24	0.15	
	200	75	292.10	0.42	0.14	302.66	0.01	
Silt	270	53	495.41	0.02	0.01	302.68	0.00	
	Tray	0	377.40	0.00	0.00	302.68	0.00	0.01
			81.81 % by weight of the sand is in the range of 140-425 µm 3.54 % by weight of the sand is in the range of silt (< 75 µm)					
Sample	Ottawa							
	Sieve No.	Size (µm)	Mass of sieve (g)	Mass of sand (g)		Cumulative mass of sand (g)		
Sand	20	850	420.08	0.00	0.00	0.00	100.00	
	40	425	366.50	0.28	0.09	0.28	99.91	
	60	250	367.34	6.09	1.91	6.37	98.00	
	100	150	312.00	127.29	39.87	133.66	58.14	81.81
	140	140	345.19	127.83	40.04	261.49	18.10	
	200	75	292.17	46.49	14.56	307.98	3.54	
Silt	270	53	495.51	10.31	3.23	318.29	0.31	
	Tray	0	377.44	1.00	0.31	319.29	0.00	3.54
			84.81 % by weight of the sand is in the range of 140-425 µm 0 % by weight of the sand is in the range of silt (< 75 µm)					
Sample	Ottawa*							
	Sieve No.	Size (µm)	Mass of sieve (g)	Mass of sand (g)		Cumulative mass of sand (g)		
Sand	20	850	420.08	0.00	0.00	0.00	100.00	
	40	425	366.50	0.28	0.09	0.28	99.91	
	60	250	367.34	6.09	1.98	6.37	97.93	
	100	150	312.00	127.29	41.33	133.66	56.60	84.81
	140	140	345.19	127.83	41.51	261.49	15.10	
	200	75	292.17	46.49	15.10	307.98	0.00	
Silt	270	53	495.51	0.00	0.00	-	-	
	Tray	0	377.44	0.00	0.00	-	-	0.00



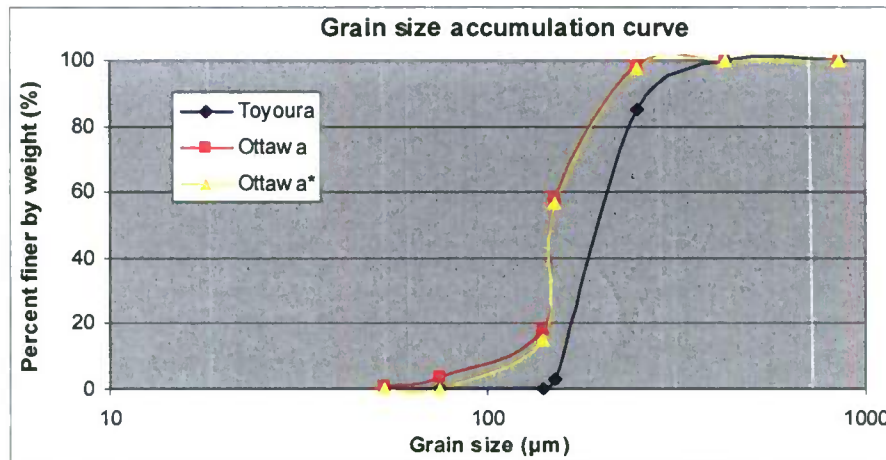


**Figure 3.1 Particle grain size distribution (%mass) for Toyoura, Ottawa, and Ottawa\* sands**

The measured densities of the various sands are reasonable since they are primarily silicates which typically have densities of about  $2.70 \text{ gm/cm}^3$ . As shown in Table 3.2 and Figure 3.1, Ottawa sand contains more fine particles than Toyoura sand. The fine particles fill voids between the larger particles which results in a higher density. Although the silt component (i.e., particles  $< 75 \text{ } \mu\text{m}$ ) of the Ottawa sand was removed to produce the Ottawa\* sample, the density and moisture content are not significantly different.

Sand samples currently are being analyzed to determine porosity and composition.

#### Formation and Dissociation of Hydrates in Sand

Exploratory experiments were conducted with the Raman calorimeter to: 1) assess the performance of that instrument when employed with sand-water-methane samples and 2) examine the effect of void fraction and other factors on hydrate formation.

Representative calorimeter thermograms of methane hydrate formation and dissociation in Ottawa sand are shown in Figures 3.2 and 3.3, respectively. Heat flow (blue line), sample temperature (red line) and furnace temperature (violet line) are plotted versus time. The sample comprises approximately 11 g sand and 2 g of de-ionized water. Methane gas pressure was held at 7.00 MPa (1,000 psig).

Methane hydrate formation in the sand matrix is indicated by the strong exothermic peak in the heat flow curve in Figure 3.2 that occurs when the sample temperature falls to about  $2 \text{ } ^\circ\text{C}$ . As the sample is subsequently heated, the hydrate phase begins to dissociate at slightly under  $10 \text{ } ^\circ\text{C}$ , as seen in Figure 3.3.

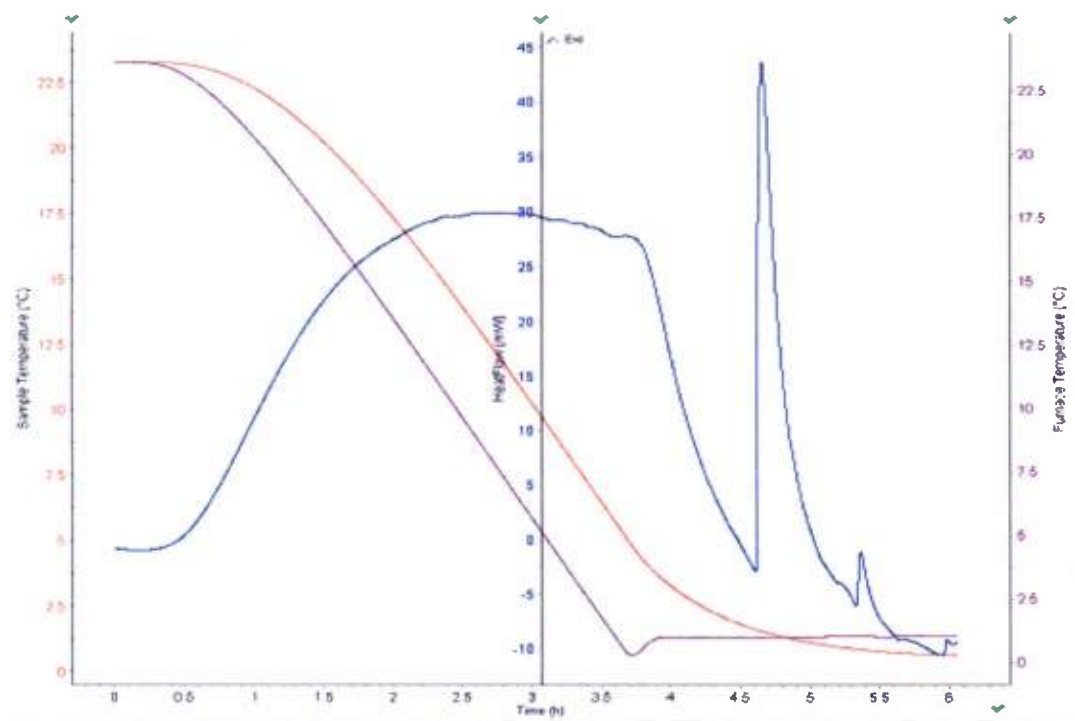


**Figure 3.2** Thermogram showing hydrate formation in Ottawa sand. Methane gas pressure = 7.00 MPa. Blue line: heat flow (mW); red line: (sample temperature); violet line: calorimeter furnace temperature. The small peak occurring at ~5.5 hours following the strong exothermic peak corresponding to hydrate formation is due to laser energy incident on the sample during a Raman spectra measurement.

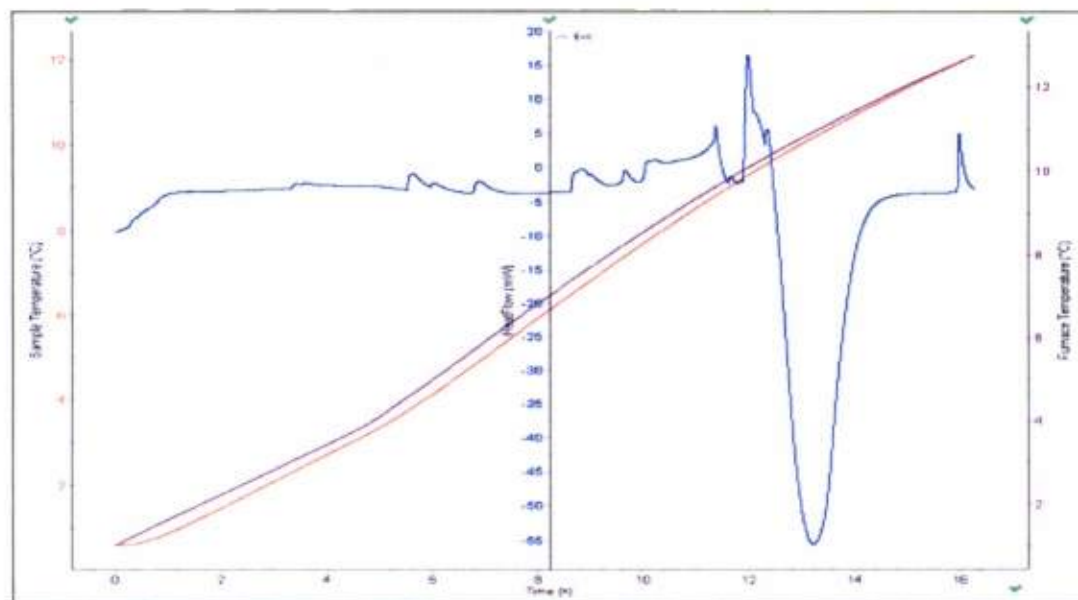


**Figure 3.3** Thermogram showing hydrate dissociation in Ottawa sand. Methane gas pressure = 7.00 MPa. Blue line: heat flow (mW); red line: (sample temperature); violet line: calorimeter furnace temperature.

The existence of methane hydrate in the sand was confirmed by *in situ* Raman spectroscopy measurements. Figure 3.4 presents a typical Raman data set. The strong line corresponds to methane gas; the smaller line adjacent to the methane gas line is characteristic of methane hydrate.

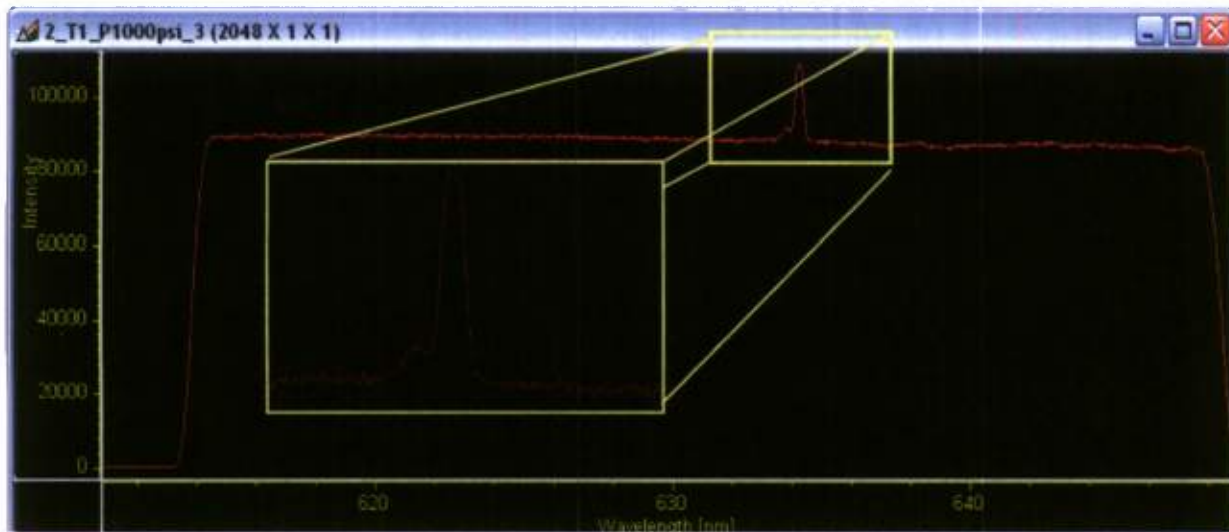


**Figure 3.4 Raman spectra of hydrate in Ottawa sand sample at 7.00 MPa and 1 °C. Methane hydrate line at  $633.90\text{ cm}^{-1}$  and methane gas line at  $634.31\text{ cm}^{-1}$ . The figure includes a magnified view of the region between about  $631$  and  $635\text{ cm}^{-1}$ .**

When the fiberoptic probe employed with the Raman calorimeter was located above the sand sample in the test cell, the s/n of the collected spectra was fair. Better data were obtained when the probe tip was inserted several millimeters into the sand sample. This necessitated the fabrication of a protective sheath equipped with a 3.43 mm diameter, 1.32 mm thick, THK sapphire window to protect the fiber ends from damage.

The exploratory experiments conducted to date have confirmed that the Raman calorimeter can be successfully employed to conduct measurements of methane hydrate formation and dissociation in sand. In addition, some preliminary data have been collected on the effect of sand void fraction and the “memory effect” phenomenon (i.e., hysteresis) that has been noted in previous investigations of hydrate formation kinetics (e.g., Makogon, 1974; Takeya *et al.*, 2000).

Table 3.3 provides a comparison of hydrate formation in Ottawa and Ottawa\* sands. As noted previously, the Ottawa\* sample is produced by sieving the Ottawa sand to remove silt particles smaller than approximately  $75\text{ }\mu\text{m}$ . In these experiments, a measured mass of sand is loaded into the sample cell. Distilled and deionized water is then added and the cell top closure assembly is installed and tightened. The sample cell is then inserted into the calorimeter well before being purged with dry  $\text{N}_2$  gas and vacuum evacuated. The cell is charged with methane gas (99.99% purity) to the desired pressure. The sample is then slowly cooled to below the hydrate formation temperature (but above the freezing point of water; typically  $1\text{ }^\circ\text{C}$ ), held at that temperature for



several hours, and then slowly warmed to a value higher than the pure hydrate dissociation temperature (10 °C). The thermal cycle (i.e., cool to 1 °C; hold; heat to 10 °C) is repeated (designated as Cycle 2 in the Table) to check for “memory effects.”

**Table 3.3 Calorimetry experiments of hydrate formation in Ottawa and Ottawa\* sands**

	Ottawa		Ottawa*	
	Cycle 1	Cycle 2	Cycle 1	Cycle 2
Sand Mass [g]	10.91		10.90	
Mass % of silt (particles $\leq 75\mu\text{m}$ )	3.54		0.00	
Mass of water added to sample [g]	2.19	2.19	2.17	2.17
Moles of water added to sample [mol]	0.121	0.121	0.120	0.120
Sample pressure [MPa]	7.00	7.00	7.00	7.00
HYDRATE FORMATION				
Observed temp. when formation begins [°C]	4.7	5.5	1.9	7.2
HYDRATE DISSOCIATION				
Observed temp. when dissociation begins [°C]	8.5	9.4	9.7	9.7
Measured energy to dissociate hydrate [J]	360	677	186	335
% added water converted to hydrate	31	59	16	30

The area under the large peaks in the heat flow curves in the thermograms, which are prominent features in Figures 3.2 and 3.3, can be integrated to estimate the energy released or absorbed by the sample during hydrate formation and dissociation. Measured dissociation energies are given in Table 3.3. Assuming that the hydrates have sI structure, the heat of fusion of the methane hydrate is 54.19 kJ/mol (Handa, 1986). Since one mole of hydrate typically contains 5.75 moles of water, dissociation requires 9.424 kJ per mole of water converted. Comparing this value to the measured dissociation energies provides an estimate of the amount of water added to the sand that forms hydrate.

The data in Table 3.3 indicate that, under the same experimental conditions, approximately twice as much hydrate forms in the Ottawa sand than in the Ottawa\* sand which is devoid of fine silt particles. Furthermore, a clear “memory effect” was detected: significantly more hydrate forms during the second cycle and this formation begins at higher temperature.

Additional evidence of memory effects is provided in Table 3.4. After the second thermal cycle described above, the Ottawa\* sand sample was heated to 23 °C and held at that temperature for 24 hours. The methane gas pressure remained at about 7 MPa during this period. The sample was then slowly cooled to 1 °C, held at that temperature for several hours as in the case of Cycle 1 and Cycle 2, and then heated to 10 °C. A second experiment was then performed using a smaller quantity of Ottawa\* sand (due, in part, to the amount of prepared sand available at that time), and the thermal process (i.e., Cycles 1 through 3) was repeated, with the exception that the methane gas was vented after the sample temperature was raised to 23 °C at the end of Cycle 2. Methane gas was added to raise the sample pressure back to 7 MPa before starting the cool-down step in Cycle 3. This experiment is denoted as “De-gassed” in Table 3.4.

**Table 3.4 Memory effects in calorimetry experiments of hydrate formation in Ottawa\* sand**

	No de-gassing			De-gassed		
	Cycle 1	Cycle 2	Cycle 3	Cycle 1	Cycle 2	Cycle 3
Sample pressure [MPa]	7.00					
Sand Mass [g]	10.90			5.84		
Mass of water added to sample [g]	2.17	2.17	2.17	1.17	1.17	1.17
Moles of water added to sample [mol]	0.120	0.120	0.120	0.065	0.065	0.065
Observed temp. when formation begins [°C]	1.9	7.2	1.9	0.6	8.7	1.0
Observed temp. when dissociation begins [°C]	9.7	9.7	9.5	9.1	8.7	8.2
Measured energy to dissociate hydrate [J]	185.7	335.1	782.5	175.0	313.2	203.0
% added water converted to hydrate	16.4	29.5	69.0	28.6	51.2	33.2

The data presented in Table 3.4 provide additional evidence that repeated formation and dissociation of hydrates may affect the amount of hydrate that forms and the conditions at which that formation occurs in porous media. In the case where no de-gassing of methane occurs, the percentage of water converted to hydrate (i.e., amount of hydrate) increases steadily and significantly between Cycle 1 and Cycle 3, from about 16% to 69%. Holding the sample at room temperature for a day does not affect this trend, although the temperature at which hydrate formation is observed to begin returns to the original value of about 2 °C after increasing to over 7 °C in Cycle 2. De-gassing the sample between Cycles 2 and 3, however, appears to “re-set” the process: in this experiment, the %water converted to hydrate increases from 28.6% to 51.2% between Cycles 1 and 2, but returns to 33.2% in Cycle 3. Similar behavior is observed in the hydrate formation temperature. It is also interesting to note that significantly more hydrate forms during Cycles 1 and 2 in the de-gassing test which uses a smaller quantity of sand. A number of possible explanations for the observed behavior include the persistence of organized water structures (“labile clusters;” see, e.g., Sloan, 1998) following dissociation that promote subsequent hydrate formation; methane adsorption by the sand; pore pressure anomalies; etc. In summary, we have confirmed that the Raman calorimeter can be applied effectively to study hydrate formation in sand-water matrices. Initial exploratory experiments have yielded preliminary evidence of the significant impact of sand properties and memory effect on hydrate formation and dissociation that will be pursued in subsequent phases of this project.

### *Reagent Destabilization of Methane Hydrates*

Three methods have been proposed to destabilize and extract fuel gas from hydrates: heating, depressurization, and chemical reagents. Chemical reagents, notably alcohols and other antifreeze compounds, also have been employed for decades to avoid hydrate blockages in natural gas pipelines and, as a result, are often referred to as thermodynamic inhibitors. While there is a substantial amount of information in the literature regarding hydrate decomposition using thermodynamic inhibitors, most studies have been limited to determining the pressure-temperature stability curve of hydrates in the presence of these inhibitors. The mechanism by which they decompose hydrates remains elusive. Knowledge about the fundamental mechanism could help identify more environmentally-benign and cost-effective alternatives (for, say, methane recovery from hydrates in seafloor sediment or permafrost where the injection of large quantities of methanol or ethylene glycol is not acceptable). Toward this end, we have been pursuing complementary experimental and modeling studies of reagent destabilization of hydrates. These studies and their results have been described in previous HEET reports. The primary result is that data obtained to date employing ethanol, methanol, 2-propanol, and ethylene glycol to dissociate methane hydrate indicate that, as the number of hydroxyl groups in a reagent increases, it becomes more effective in decomposing hydrates. It was also observed that as the size of the alkyl group in these reagents increased, it became less effective at disassociating hydrates.

We have proposed a hypothesis that an inhibitor decomposes hydrates by binding up the released water molecules in the quasi-liquid layer and preventing it from re-crystallizing. The number of hydroxyl groups and the size of the alkyl group are the primary factors that influence an inhibitor's ability to bind to the free water molecules at the hydrate surface. The hydroxyl group allows the inhibitor to bind to water molecules. Through steric effects, the alkyl group influences the hydrogen bonding capability of the inhibitor, as well as the strength of the hydrogen bonds formed between the inhibitor and water molecules.

During the present reporting period, we initiated experiments further to test our hypothesis. The reagent of interest will be glycerol ( $C_3H_8O_3$ ), a triol having three hydroxyl groups. Glycerol appears to be an attractive alternative to alcohols or ethylene glycol, since it is inexpensive and relatively benign from a toxicity/environmental health perspective. The facility we developed previously to conduct Raman calorimeter measurements of inhibitor injection onto solid hydrates, shown schematically in Figure 3.5, is being modified to conduct quantitative measurements of methane released during hydrate dissociation to correlate with the heat of dissociation data.

The primary practical hurdle in the conduct of the experiments and possible use of glycerol to dissociate hydrates in the field is its high melting point ( $\sim 17.8^\circ\text{C}$  at atmospheric pressure). Fortunately, glycerol is readily soluble in water and these solutions will be tested to determine their effectiveness as a hydrate inhibitor.



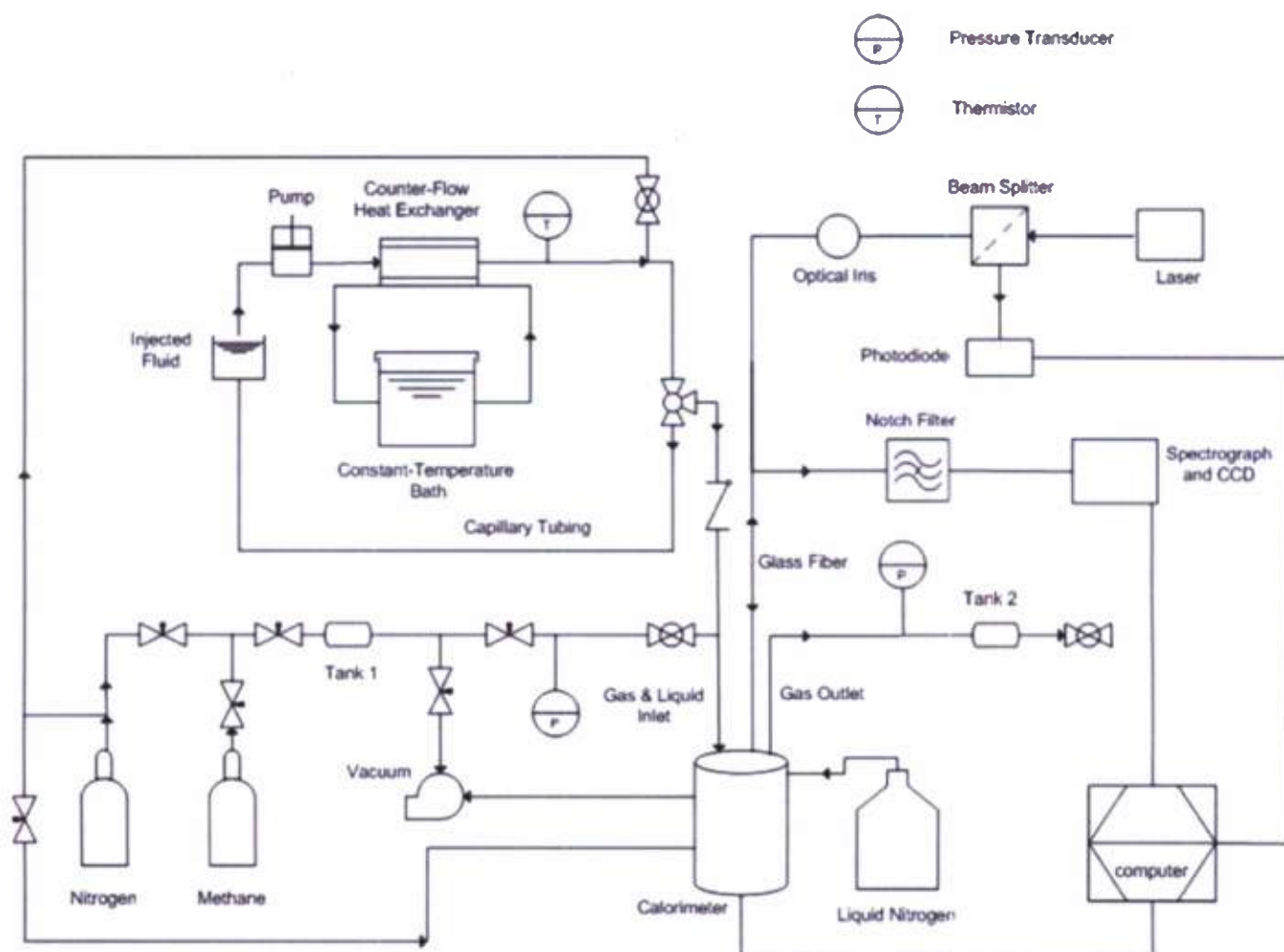


**Figure 3.5 Schematic diagram of facility to investigate hydrate destabilization by injection of chemical inhibitor**

### *Subsea Power Generation: Heat Capacity of Water at Elevated Pressure*

The deep ocean is a region of great tactical, commercial, and scientific significance. A principal hurdle to deep subsea operations is the availability of energy. For example, there are thousands of instruments deployed on the ocean floor for monitoring, surveillance, and navigation that are powered by battery packs with finite lifetimes and capacities. After these batteries are exhausted, typically in less than a year, the device must either be recovered or abandoned. Deep submersibles also run on batteries or are tethered to the surface by a power umbilical. Autonomous Underwater Vehicles (AUVs) that are driven by fuel cells using onboard stores of hydrogen and oxygen are under development, but they have limited range and will need to surface periodically for refueling. Seafloor power cables have also been employed to bring electricity from shore to the ocean depths, but they cannot be deployed at all locales to all depths and, like umbilicals, are vulnerable to natural and human hazards.

The widespread abundance of accessible methane on the seafloor, in the form of free gas seeps or hydrate deposits, offers the possibility for development as an *in situ* energy resource. Toward this end, HNEI received a grant from DARPA (Grant No. HR0011-05-1-0039) in 2005 to conduct a one year study to evaluate the technical feasibility of generating electrical power in the deep ocean from seafloor methane and to initiate the design of a first prototype system for field deployment. That investigation concluded that it would be possible to produce net power of the order of 100 W employing existing technologies. The lifetime of such a system was unclear; however, values of 1 – 5 years appear to be reasonable, and probably could be extended through additional R&D, careful design, and component redundancy.

The recommended configuration would thermochemically reform methane fuel gas from seeps or hydrates to  $H_2$ , which would be converted to electricity in a fuel cell. Although the long-reaching goal is for self-sufficient systems, i.e., devices that run entirely on ambient fuel and oxidizer resources, it was concluded that some stored oxidizer brought from the surface will be required, since the current level of technology to extract dissolved  $O_2$  from sea water is not adequate to provide the concentrations needed to reform methane. On the other hand, dissolved oxygen (DO) extraction does appear to be a viable option to supply the fuel cell cathode.

The DARPA study concluded that the necessary next step was to test and characterize major components (i.e., reformer; fuel cell; membrane contactor), first on the benchtop, then in pressure chambers at simulated underwater conditions, and finally offshore. During the assessment of candidate devices prior to initiating this testing, questions arose regarding the thermal properties of water and aqueous solutions at the elevated pressures which prevail in the deep ocean. The ability accurately to predict these properties is important to determine the performance of aqueous alkaline fuel cells and other devices that will likely be employed in the subsea power system.

In 1995, the International Association for the Properties of Water and Steam (IAPWS) adopted a new formulation called “The IAPWS Formulation 1995 for the Thermodynamic Properties of Ordinary Water Substance for General and Scientific Use.” In that work, nearly all the data for the isobaric heat capacity ( $C_p$ ) for water are based on measurements of Sirota’s group in the former Soviet Union conducted during the period from 1956 to 1970 (Wagner & Pruss, 2002; Sirota and Maltsev, 1959). Since then, only two further  $C_p$  data sets have been published that were used for fitting the IAPWS-95 formulation. These are the measurements of Angell *et al.*

(1982), who investigated subcooled liquid water at ambient pressure, and the high-pressure  $C_p$  data measured by Czarnota (1984). Recently, Archer and Carter (2000) published  $C_p$  measurements for subcooled liquid water, which cover almost the same region as the data of Angell and coworkers (1982).

When we attempted to confirm experimentally the predictions of the IAPWS 1995 model for conditions relevant to our subsea power generation application, we observed significant discrepancies. During the current reporting period, we completed our study of the heat capacity of pure water at elevated pressure and the results have recently been published (Manya *et al.*, 2011). The calorimetric results at 4.0 MPa exhibited significant deviation from the IAPWS 1995 formulation, especially at high temperatures (up to 465K) where differences are greater than 20%. This discrepancy warrants further investigation.

### **Environmental Impacts of Methane Release from Seafloor Hydrates**

The long-term goal of this subtask is to develop a robust three-dimensional numerical model of methane in the ocean. Methane is a potent greenhouse gas with a significantly higher Global Warming Potential than  $\text{CO}_2$ , but much lower levels of emissions into the atmosphere. Whereas the oceans currently are a net sink for atmospheric  $\text{CO}_2$ , they represent a net source of  $\text{CH}_4$ . Moreover, the historical record contains evidence of massive methane outgassing from marine and permafrost hydrate reservoirs that may have greatly exacerbated earlier episodes of global warming. Methane models have also become a subject of intense R&D interest in the wake of the 2010 Macondo Prospect oil spill in the Gulf of Mexico which released an estimated  $2.5 \times 10^8$  standard  $\text{m}^3$  of natural gas from the broken wellhead at a depth of about 1,500 m.

The target model will need to consider the production, oxidation, and transport of  $\text{CH}_4$  and will require an understanding of processes that affect the exchange of methane between the atmosphere, ocean, and seafloor sediment. During the present reporting period, work focused on field and laboratory experimental investigations of the role of microbes in methane production and consumption.

#### *Hydrate Microbiology*

Studies have been ongoing as part of this Task to investigate methane cycling in both sediments and the water column. To date, the sediment work has focused on understanding biological formation and the anaerobic oxidation of methane. Anaerobic oxidation of methane (AOM) occurs through an undefined process and is potentially the largest sink for methane in sediments. Biological AOM is thought to be mediated by a consortium of micro-organisms composed of sulfate reducing bacteria and methanogenic *Archaea*. Geochemical data suggests that the majority of methane produced in sediments is oxidized anaerobically within a narrow depth range called the sulfate methane interface (SMI). The sediment depth of the SMI is influenced by the rates of methane flux. Stronger methane flux results in shallower SMIs, and the possibility of methane releases into the water column.

In terrestrial environments, biological methane oxidation typically occurs as an obligate aerobic process mediated by methanotrophic bacteria. This suggests that a methane sink could also exist at the sediment-water interface in the ocean where there is dissolved oxygen. Recent community investigations utilizing molecular 16S rRNA and *pmoA* phylogenies suggest that significant populations of methanotrophs occur in methane rich environments (Inagaki *et al.*, 2004,



Niemann *et al.*, 2006, Tavormina *et al.*, 2008, Yan *et al.*, 2006); however, studies of the rates of aerobic methane oxidation in hydrate bearing sediments are limited.

In mid-September 2009, we participated in a 12 day oceanographic research cruise on the U.S. Coast Guard Cutter Polar Sea in the Beaufort Sea off the North Slope of Alaska. This cruise was organized by the Naval Research Laboratory. There were 34 international participants, including scientists from university and government research agencies from the U.S., Netherlands, Belgium, Germany and Canada.

The Arctic Ocean expedition provided a unique opportunity to study the microbial communities and aerobic C1 metabolisms in shallow and cold water environments in methane-rich areas. Comparative analysis of collected samples utilizing data that includes concentrations of C1 metabolizing prokaryotes and sediment and water chemistries could yield important information about the methane sink at the sediment-water interface.

#### Preliminary Analysis of Beaufort Sea Samples

Sediment cores were collected based on reviews of seismic profiles and topography data to try to identify methane hydrate accumulations. The cores primarily comprised fine clay sediments. Anaerobic conditions in these sediments are likely achieved within a few centimeters below the sediment water interface. Due to interface disturbances that occurred during piston coring operations, we only utilized sediments collected using a shallow depth, multi-coring system shown in Figure 3.6 that was equipped with four core tubes, each having an approximate inner diameter of 12.5 cm (5 in.). Figure 3.7 provides a map showing the multi-core sampling locations.



**Figure 3.6 Multi-core system used to collect seafloor sediment samples during the 2009 Beaufort Sea expedition**

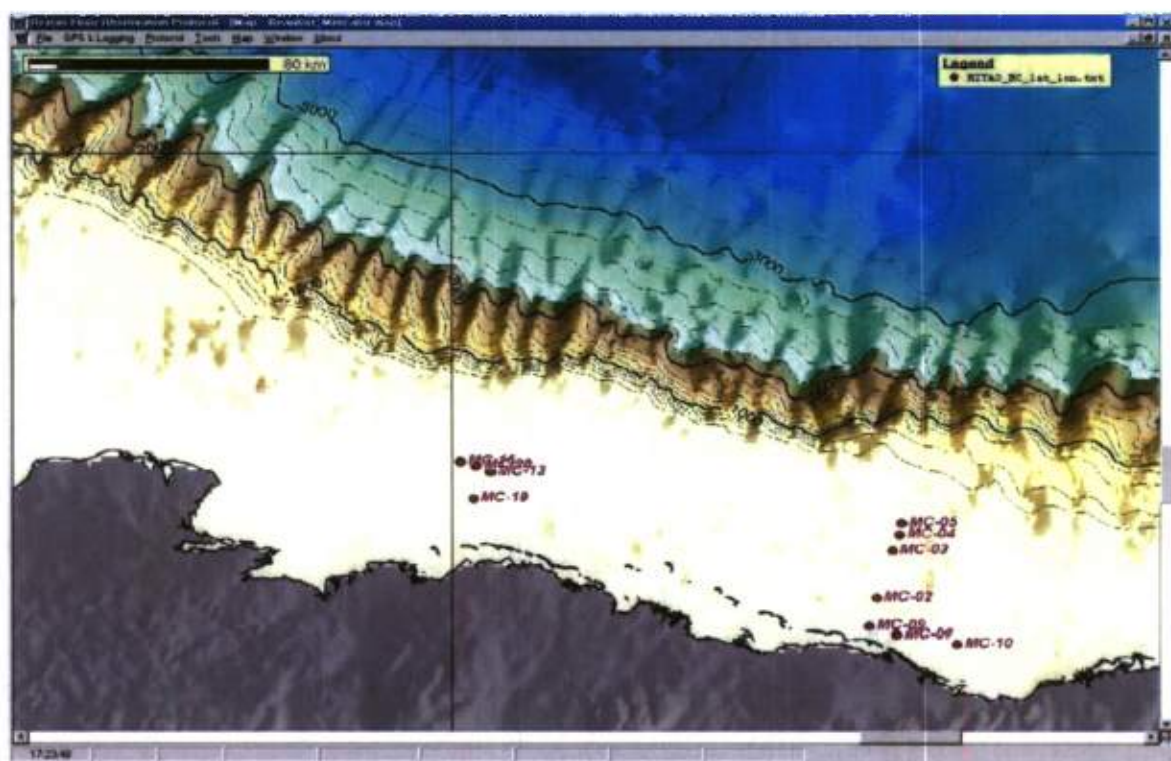


Figure 3.7 Map of core sampling locations during the 2009 Beaufort Sea expedition

Six samples were selected for long-term enrichment incubations and for DNA extraction. Although physical and chemical analyses of the multi-core sediments have not been performed, their geochemistry can be estimated by comparison with adjacent piston core sample data.

Enrichment samples were prepared by gravimetric addition of sediment into a gas tight Hungate tube containing 5 ml of sterile seawater-based media and silica gel. The silica gel was included to facilitate gas diffusion throughout the sample by artificially increasing the porosity. A mixed gas containing a 20% CH<sub>4</sub>, 25% O<sub>2</sub> and 3% CO<sub>2</sub> and 52% N<sub>2</sub> was used to provide a methane-rich atmosphere (i.e., headspace) conducive to methanotrophic bacteria cultivation. Methane and CO<sub>2</sub> concentrations in gas extracted from the headspace were measured using a gas chromatograph with an FID detector (Kiene and Capone, 1985). The samples were incubated at 4 °C for >6 months.

#### *Methanotrophic bacteria populations*

DNA extractions from both enriched and untreated samples were performed using a commercially available kit from MoBio (<http://www.mobio.com/>). PCR amplification of the extracts was conducted employing primer sets targeting specific organisms associated with methane cycling.

Figure 3.8 presents a PCR amplification profile from multi-core sample MC-03. This profile suggests a diverse community of microorganisms associated with methane cycling including

Type I methanotrophic bacteria (Wise *et al.*, 1999), sulfate reducing microbes (Wagner *et al.*, 1998), and methanogens (Marchesi *et al.*, 2001). The methanotroph *pmoA* gene sequences (Bourne *et al.*, 2001) indicated in the figure have been shown to produce phylogenies that are congruent with the 16S rRNA of the same organisms (Holmes *et al.*, 1999; Kolb *et al.*, 2003). For methanotrophic organisms, the largest data set of partial sequences available in GenBank are for the functional enzyme methane monooxygenase, for the *pmoA* gene sequence. The PCR extracts are currently being cloned to assess community diversity within this sample.

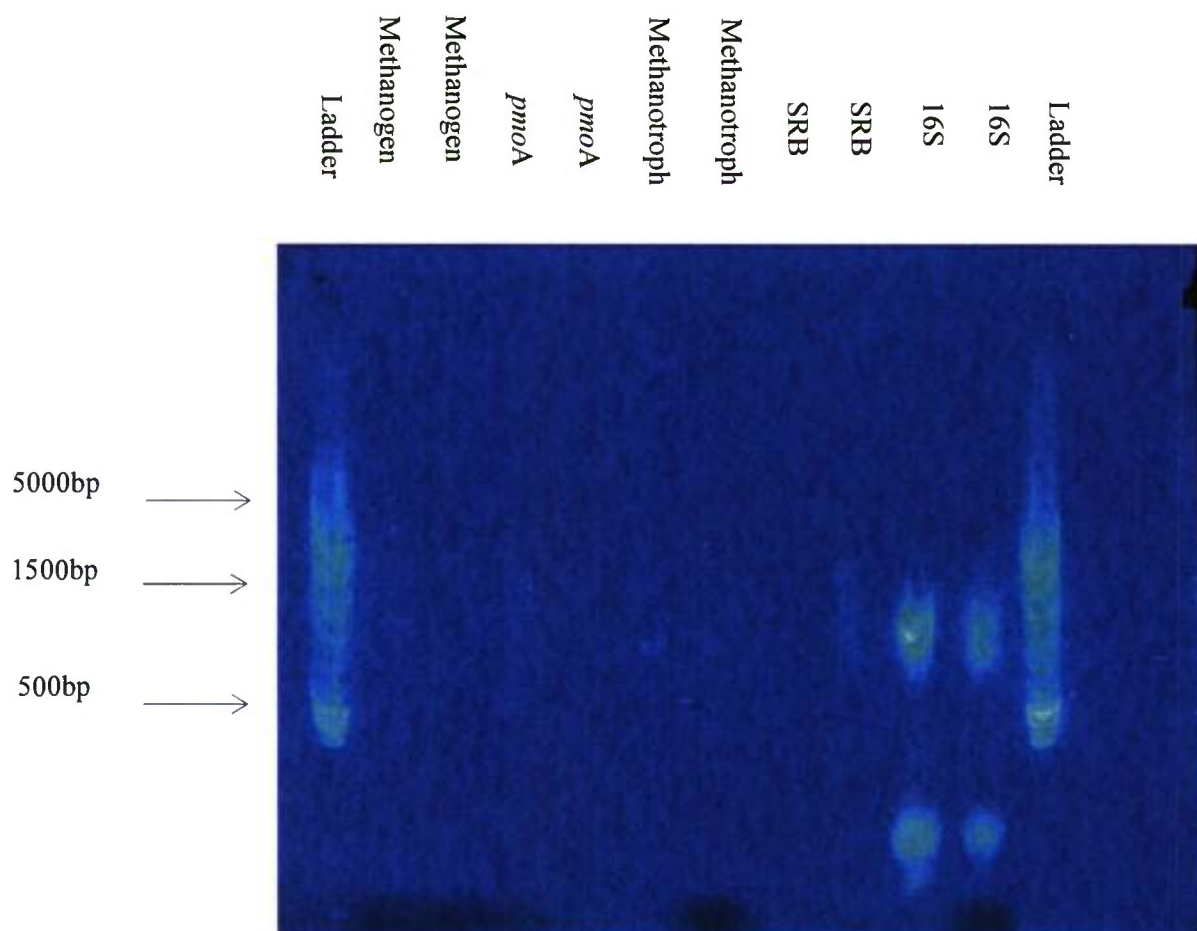


**Figure 3.8** PCR amplification of DNA extracted from multi core sample MC-03. Bands 1 and 12 (band numbers are in sequence from left to right): mid-range DNA ladders; Bands 2 and 3: + and - amplification for methanogenic bacteria (1200bp) corresponding, respectively, to sediment (S) and enrichment (E) samples; Bands 4 and 5: + (S) and - (E) amplification for *pmoA* (500bp); Bands 6 and 7: + amplification of both samples for methanotrophic bacteria (1000bp); Bands 8 and 9: - (S) and + (E) amplification for sulfate reducing bacteria; Bands 10 and 11: + amplification of both samples for general 16S (1500bp).



### *Methanotroph metabolism*

Methanotrophic bacteria are difficult to grow on solid media, making pure culture isolation challenging (Bowman, 2000). Our previous attempts have not been successful. Rather than continuing to pursue this approach, we elected instead to explore micro-calorimetry as a means to observe quantifiable rates of microbial oxidation and reduction of methane. Of the six samples collected, only MC-03 yielded PCR data that suggested a bacterial community that was sufficiently robust to permit observation of different methane metabolisms. Although the literature suggests that aerobic oxidation rates may be high in methane-rich environments (Nauhaus *et al.*, 2005; Ruo *et al.*, 2008), it was unclear whether the thermal signal associated with the microbial oxidation would be large enough to be detected by the calorimeter.

In our investigation, a TA Instruments Multi-Cell Differential Scanning Calorimeter (MC-DSC) was employed for the biocalorimetry tests, since it has a slightly lower detection limit ( $0.2 \mu\text{W}$ ) than the Raman Calorimeter and smaller thermal mass ampoules (test cells). Moreover, up to three different samples can be tested simultaneously with the MC-DSC. A schematic diagram and a photograph of the system are provided in Figures 3.9 and 3.10, respectively.

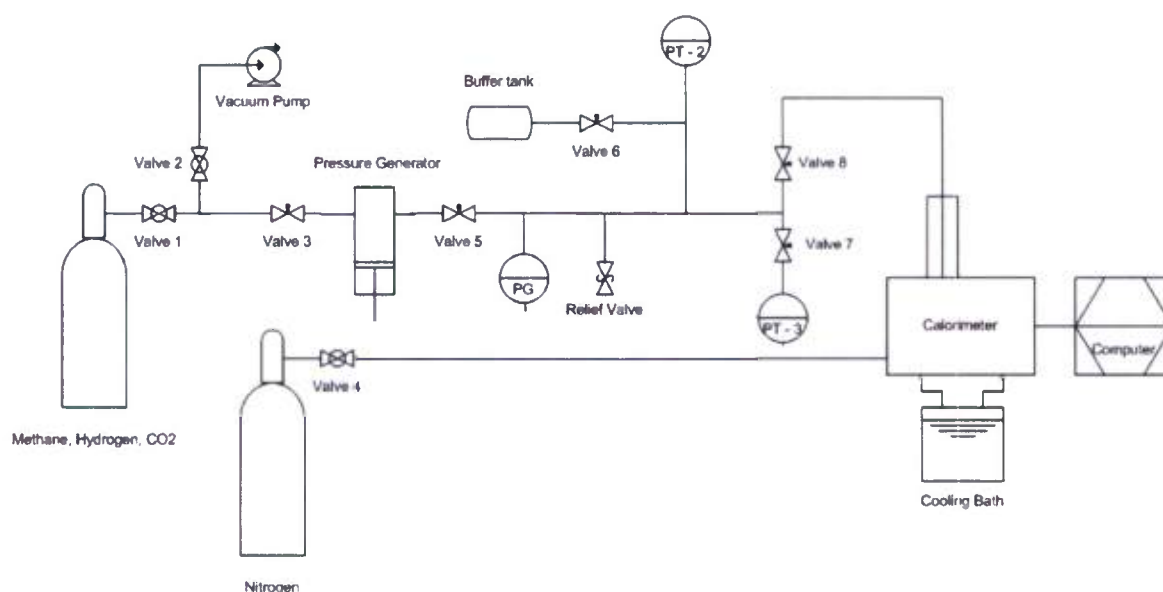


**Figure 3.9** Schematic diagram of the Multi-Cell Differential Scanning Calorimeter system employed for biocalorimetry experiments

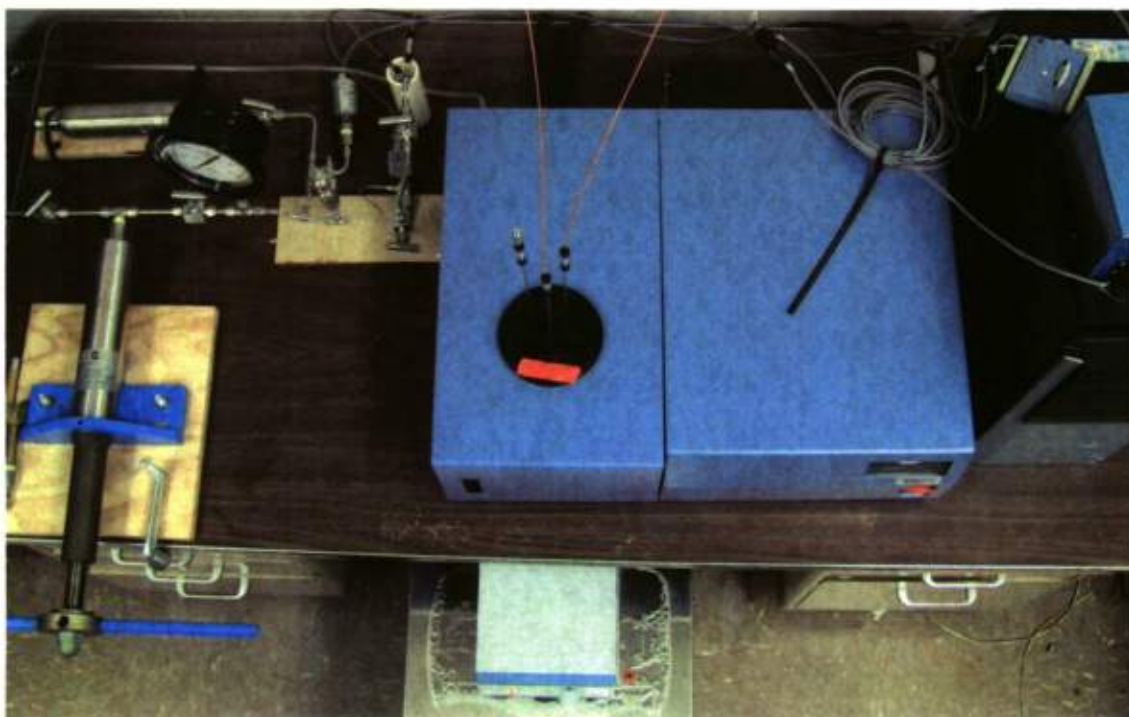


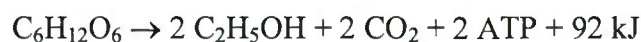
**Figure 3.10** Photograph of the MC-DSC system

The MS-DSC employs a thermoelectric heater-cooler in conjunction with a constant temperature bath to control the temperature of the samples. Its operating temperature range is -40 °C to 150 °C. Sample pressures up to 40 MPa are possible with the high pressure ampoules.

The ~0.5 ml volume Hastelloy C ampoules are partially filled with samples, closed, and inserted into the thermal wells before being purged and then charged with a selected gas to fill the headspace, via a tube integrated into the top closures. A programmable temperature regimen then is implemented.

To test the performance of the MS-DSC, experiments were conducted to observe the metabolic fermentation of glucose by *Saccharomyces cerevisiae*, a well documented and appropriate model system for biocalorimetry (Yonsel *et al.*, 2007).

Anaerobic fermentation of glucose yields the following products (AOAC International, 1995):



Kockova-Kratochvílová (1990) conducted a calorimetric determination of the enthalpy of anaerobic reduction of glucose by yeast and obtained a value of 511 kJ/kg of glucose.

A stationary phase culture was prepared, employing  $4 \times 10^5$  cells per ampoule, in a modified yeast mold media containing no additional carbon. To determine the threshold detection limits of the calorimeter, different concentrations of glucose were tested. A pure argon gas headspace was used to induce anaerobic conditions and sample temperature was held at a constant 28 °C. Figure 3.11 shows a representative thermogram for two of the three ampoules (the third was not used) obtained during one of the tests. There is a slight zero offset in the curves (~70 μW) that is a characteristic of the instrument and which can be ignored. Positive heat flow corresponds to

exothermic reactions. Cell two was loaded with approximately  $1.1 \times 10^{-4}$  moles of glucose and cell three contained twice that amount. These results suggest that the MC-DSC is easily able to detect the enthalpy of glucose reduction at these levels (similar results were obtained when the glucose levels were reduced by an order of magnitude). Integration of the thermograms yields a total heat flow of about 11 J for cell two (about 550 kJ/kg glucose) and 23 J for cell three which has double the amount of glucose. These data are in reasonable agreement with the results of Kockova-Kratochvílová (1990).

Following the instrument verification tests, preliminary biocalorimetry experiments of methanotroph metabolism were initiated with the MS-DSC. Various headspace gas mixtures were employed. All added carbon (besides what existed in the sediment) came from the gas headspace. Sample temperatures were held constant at 28 °C.

250 mg of untreated sediment or enrichment samples from location MC-03 were placed in the ampoules. The sediment sample contained approximately  $4.8 \times 10^8$  cells and the enrichment culture contained  $1.6 \times 10^7$  cells, as determined using a hemocytometer. After purging, the headspace was filled with mixtures of laboratory grade dry air, methane gas, or CO<sub>2</sub> to a pressure of 0.2 MPa (gauge) which corresponds to about  $3.0 \times 10^{-5}$  moles of gas. During the experiments, one of the three sample cells was left empty as a blank.

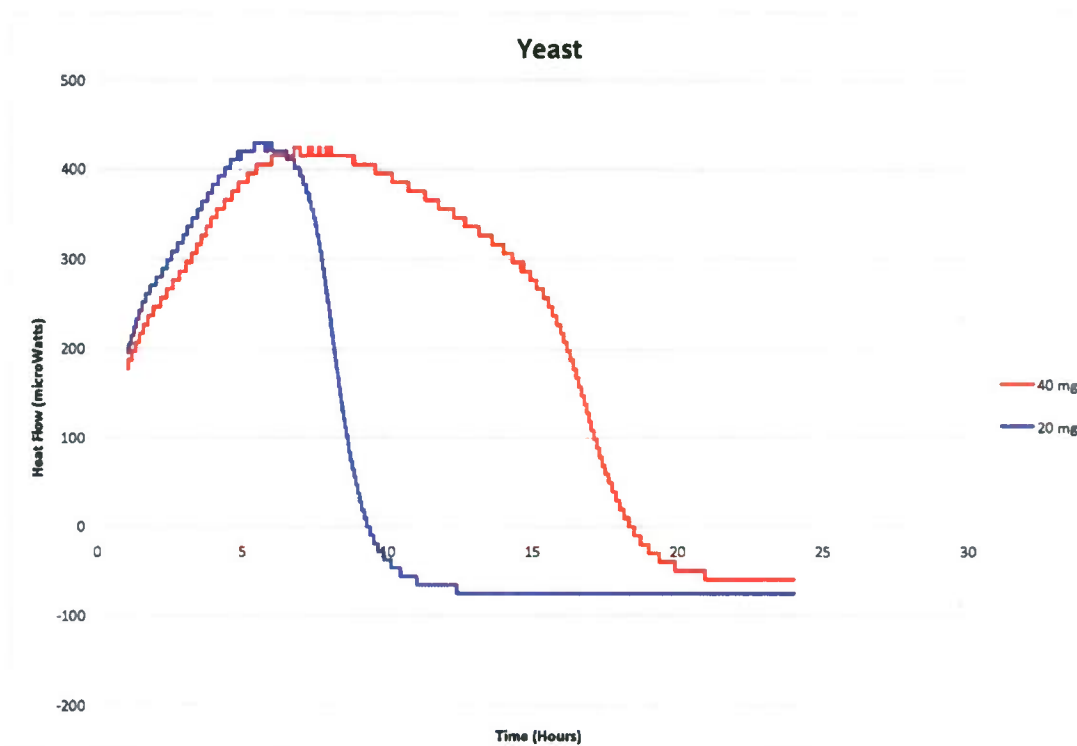


**Figure 3.11** Thermograms of the anaerobic fermentation of glucose by *Saccharomyces cerevisia* at 28 °C. Cell two (blue) contained  $1.1 \times 10^{-4}$  moles of glucose and cell three (red)  $2.2 \times 10^{-4}$  moles of glucose. Total heat flow obtained by integration of the curves is approximately 11 J for cell 2 and 23 J for cell 3.



Aerobic methanotrophic metabolism was investigated using a mixture of dry air and methane gas (50% by volume) in the headspace. The samples were observed for 72 hours. The corresponding thermogram is shown in Figure 3.12. Ignoring the constant zero offsets of the curves, the measured heat flow is negligible, indicating very low or no methanotrophic activity. Utilizing headspace gases comprising pure methane (i.e., anaerobic methanotrophy) or CO<sub>2</sub> (i.e., methanogenesis) produced similar disappointing results, as seen in Figures 3.13 and 3.14, respectively.

The addition of luria broth, a common heterotrophic media, to both of the sediment and enrichment samples resulted in the growth of heterotrophic bacterial that was detected by the MC-DSC. Thermograms are provided in Figure 3.15. Data indicate an incubation period of about 20 hours before a signal is observed and cell counts for both samples increased to  $\sim 10^9$ . The greater heat release from the sediment sample reflects its larger initial cell density compared to the enrichment sample. The onset of the peak in its thermogram occurred slightly earlier and ended sooner, after exhausting the available nutrients. These experiments suggest that the MC-DSC can be employed to investigate methanotroph metabolism but that significantly greater cell densities probably are needed to generate a detectable signal.

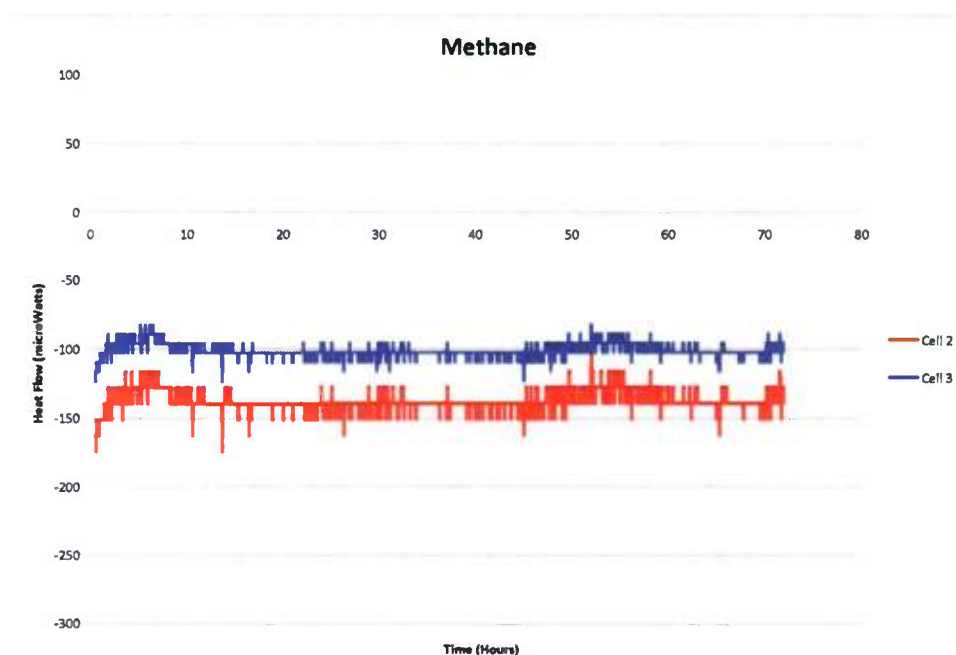


**Figure 3.12** Thermograms of Beaufort Sea samples from location MC-03. Cell two (red) contains 250  $\mu$ l of the enrichment sample and cell three contains 250 mg of the unmodified sediment. Headspace comprises 50% methane in dry air. Pressure = 0.2 MPa (gauge); temperature = 28 °C. No changes detected over 72 hours.

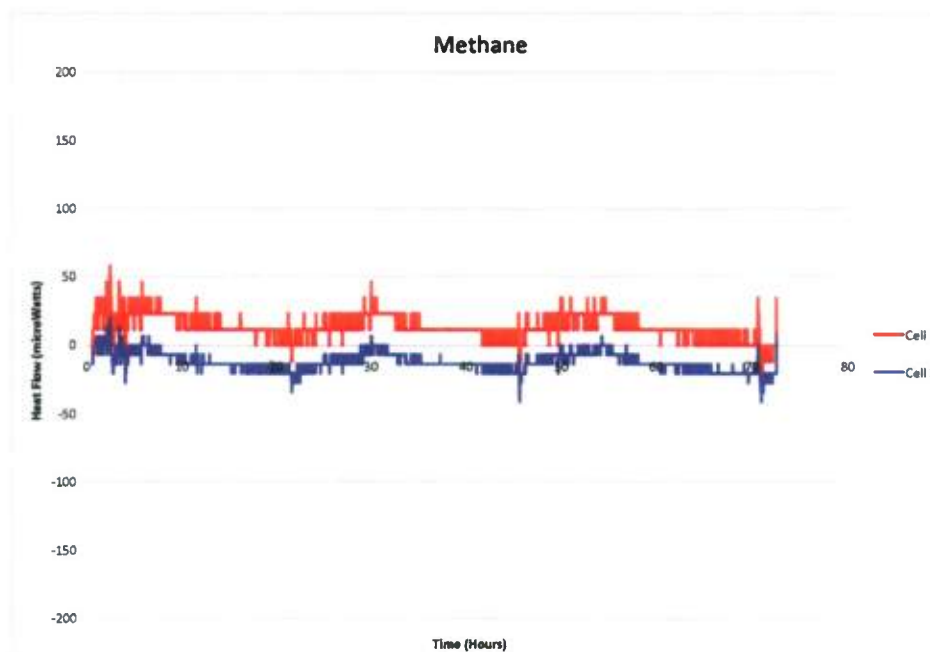


**Figure 3.13** Thermograms of Beaufort Sea samples from location MC-03. Cell two (red) contains 250  $\mu$ l of the enrichment sample and cell three contains 250 mg of the unmodified sediment. Headspace comprises pure methane. Pressure = 0.2 MPa (gauge); temperature = 28  $^{\circ}$ C. No changes detected over 72 hours.

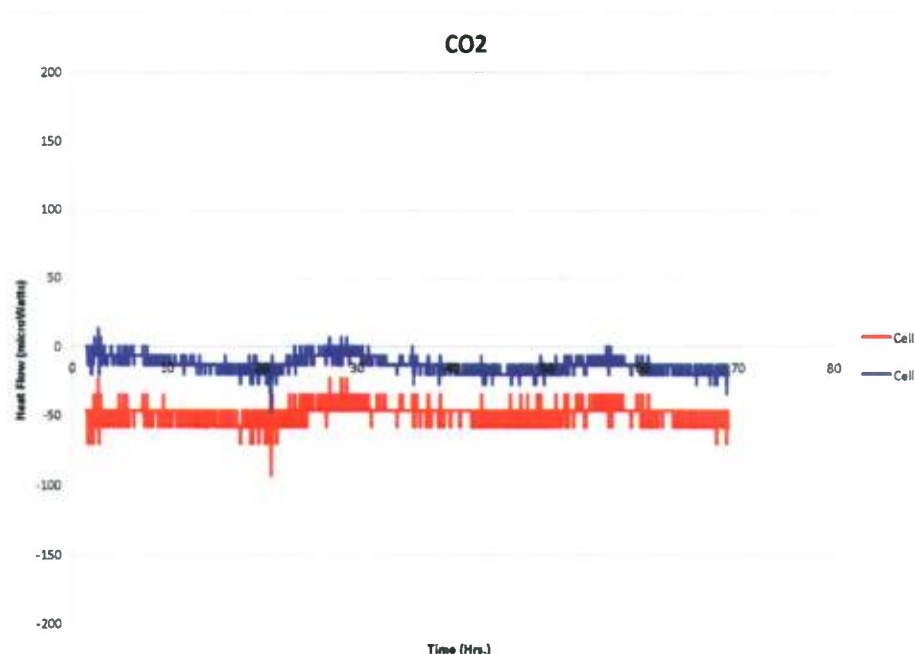


**Figure 3.14** Thermograms of Beaufort Sea samples from location MC-03. Cell two (red) contains 250  $\mu$ l of the enrichment sample and cell three contains 250 mg of the unmodified sediment. Headspace comprises pure CO<sub>2</sub>. Pressure = 0.2 MPa (gauge); temperature = 28  $^{\circ}$ C. No changes detected over 72 hours.

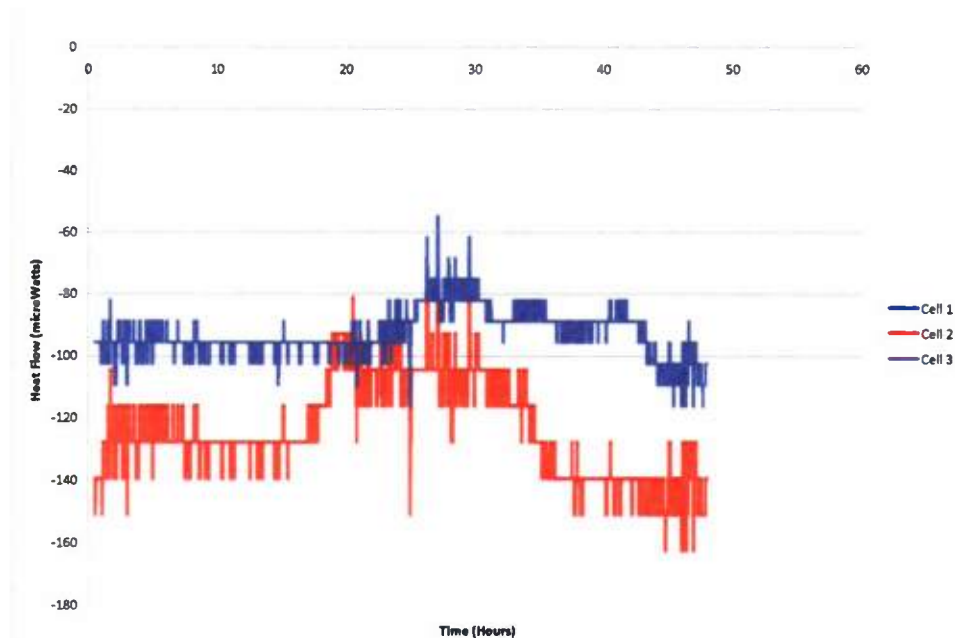


**Figure 3.15** Thermograms of Beaufort Sea samples from location MC-03. Cell two (red) contains 250  $\mu$ l of the enrichment sample and cell three contains 250 mg of the unmodified sediment. 250  $\mu$ l of Luria Broth added to both cells. Headspace comprises air. Pressure = 0.2 MPa (gauge); temperature = 28  $^{\circ}$ C.

### Hydrate Engineering Applications

Commercial development of hydrate as a means to transport and supply methane has been under development in Japan for several years and a trial distribution program of hydrate pellets currently is underway. At a larger scale, Mitsubishi Heavy Industries has conducted design studies of tanker ships to transport hydrate instead of Liquefied Natural Gas (LNG). Although LNG has a higher methane density than methane hydrate, it requires storage at much lower temperatures.

Given the progress made in Japan on this topic, it did not appear worthwhile to pursue parallel development in our HEET Task. Recently, however, advances have been reported in synthesizing hydrogen ( $H_2$ ) hydrate that suggest that it may be feasible to store and transport this molecule as a hydrate guest. Since  $H_2$  is the fuel of choice for many fuel cell systems under investigation as part of the HEET Initiative, an investigation of hydrate  $H_2$  storage appeared to warrant consideration, and work on this topic was therefore initiated during the preceding phase of this program.

During the present reporting period, we continued our experimental investigation of hydrate  $H_2$  storage, focusing on the use of hydrate promoters, specifically, tetrahydrofuran (THF) and tetra-*n*-butylammonium bromide (TBAB), to reduce storage pressure.



## *THF/H<sub>2</sub> Hydrate Synthesis Experiments*

### Objectives

The extremely high pressures and low temperatures required to synthesize and maintain pure hydrogen hydrate make it impractical as a medium to store and transport fuel (Lee *et al.*, 2005). Vos *et al.* (1993) used X-ray and Raman spectroscopy to study hydrogen/water mixtures at pressures between 0.75 GPa and 3.1 GPa and temperatures between 17 °C and 177 °C. Mao *et al.* (2002) applied Raman, infrared, X-ray, and neutron techniques to identify the presence of sII hydrate at 200 MPa and 7 °C, as well as under vacuum (~10 kPa) at a temperatures of -195 °C. They reported two hydrogen molecules in the small hydrate cages and four hydrogen molecules in the large cage. Dyadin *et al.* (1999) used differential thermal analysis to look at hydrogen hydrate formation over a temperature range of approximately -10 °C to 40 °C and pressures up to 1000 MPa. Tanaka *et al.* (2004) developed pure hydrogen hydrates at 200 MPa and -23 °C.

Recently, hydrate promoters such as tetrahydrofuran (THF) have been explored as a means to facilitate H<sub>2</sub> hydrate formation. THF has been added to the water to occupy the large hydrate cages and to stabilize the crystal at more desirable pressure and temperature conditions. Using THF, Fluorusse *et al.* (2004) were able to store H<sub>2</sub> in hydrate at 5 MPa and 6.6 °C. They employed X-ray powder diffraction to verify the sII hydrate structure, Raman spectroscopy to confirm the existence of THF/H<sub>2</sub> hydrate, and Raman and NMR spectroscopy to detect H<sub>2</sub> molecules within the hydrate crystal. They noted that adding a promoter such as THF decreased the amount of H<sub>2</sub> that could be stored within the hydrate.

Pure H<sub>2</sub> hydrate contains about 5.0 wt% H<sub>2</sub>, whereas THF/H<sub>2</sub> hydrate typically contains approximately 2.0 wt% H<sub>2</sub> (Yedlapalli *et al.*, 2010). The U.S. Department of Energy has set a goal of 7.5 wt% for onboard hydrogen storage systems for transportation applications ([http://www1.eere.energy.gov/hydrogenandfuelcells/storage/current\\_technology.html](http://www1.eere.energy.gov/hydrogenandfuelcells/storage/current_technology.html)). This metric, however, is based on total system weight, which includes tanks, storage media, insulation, chillers, etc. Hence, the gravimetric capacities of the material alone must be higher than the system-level target. Although the hydrogen density of hydrates will not meet the DOE target, they may be an option for other storage applications.

In an effort to increase the amount of H<sub>2</sub> stored in THF/H<sub>2</sub> hydrate, Lee *et al.* (2005) varied the concentration of THF added to the formation water. They showed that, as expected, the wt% of H<sub>2</sub> in the hydrate decreased with increasing THF concentration.

The use of hydrate promoters to form stable hydrates that can be employed to store and transport H<sub>2</sub> fuel at reasonable temperatures and pressures appears feasible and experiments directed toward this goal were initiated. The first step was to synthesize THF/H<sub>2</sub> hydrate with our Raman Calorimeter. During the previous phase of the HEET Initiative, we were unable to confirm the formation of THF/H<sub>2</sub> hydrate in our experimental facility. During the present reporting period, we tested alternative protocols to form the hydrate.

### THF/H<sub>2</sub> Results

Rather than form the THF hydrate first and load the crystals into the calorimeter cell as we did in earlier experiments, solutions of THF in distilled and deionized water were prepared and 0.35 ml of these solutions was pipetted into the MC-DSC ampoules. The top closures of the ampoules

were installed and tightened and the ampoules were inserted into the calorimeter well. Temperature was adjusted to 25 °C and the ampoules were then vacuum evacuated and purged with Grade 4.0 (99.99% purity) N<sub>2</sub> gas. The ampoules were vacuum evacuated a second time before being pressurized with either Grade 4.0 H<sub>2</sub> or N<sub>2</sub> (for comparison) gas. The samples were then cooled to between -20 °C and -30 °C at a rate of 1 °C/min and held at that temperature for 2 hours. The temperature was then slowly ramped up to 20 °C at a rate of 0.25 °C/min.

Figures 3.16 and 3.17 present thermograms obtained during the heating process for two different initial concentrations of THF in water (5.5 mol% and 2.75 mol%, respectively). The blue curves correspond to the case where the samples were pressurized with pure H<sub>2</sub> gas to 13.89 MPa (2,000 psig); the red curves correspond to the case where the samples were pressurized with pure N<sub>2</sub> gas. The strong endothermic event (valley) that occurs at temperatures between around 0 °C and 5 °C is due to the melting of the THF hydrate. The temperature at which THF hydrate melts depends on the amount of THF in the original solution. A second endothermic event that starts at about 9 °C is evident only in the thermograms of the samples pressurized with H<sub>2</sub>. We are reasonably confident that this corresponds to the melting of H<sub>2</sub> hydrate, since Komatsu *et al.* (2010) have reported a melting temperature of 282.25 K (9.1 °C) at 13.89 MPa for THF/H<sub>2</sub> hydrate formed from 5.3 mol% THF solution.

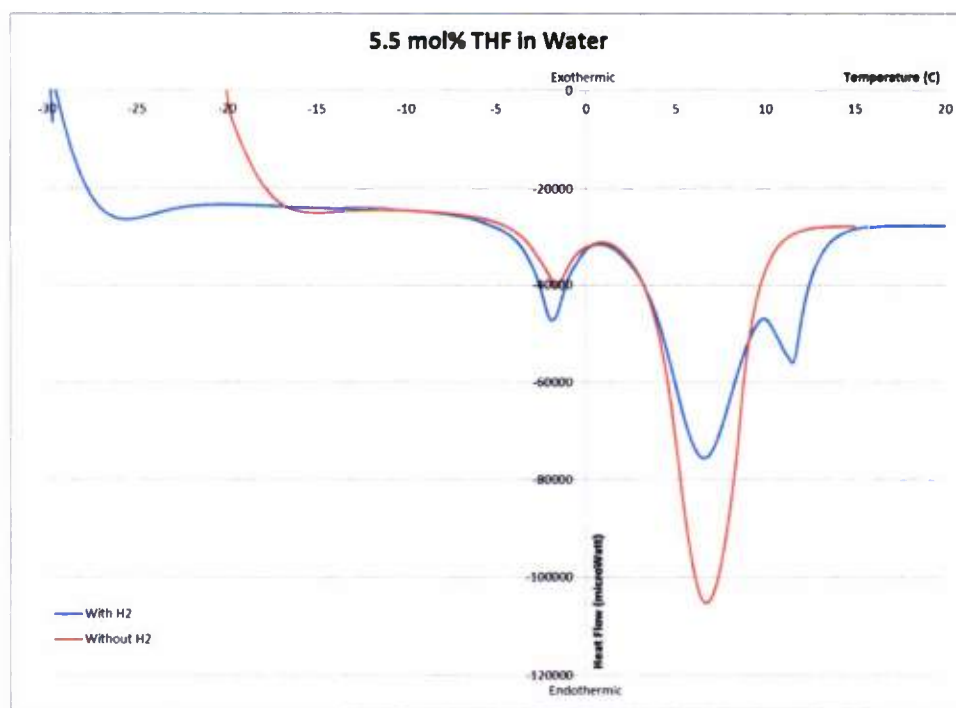


**Figure 3.16** Thermograms of hydrate dissociation for 5.5 mol% THF in water. Blue curve corresponds to pressurization with pure H<sub>2</sub> to 13.89 MPa (2,000 psig); red curve corresponds to pressurization with pure N<sub>2</sub>.

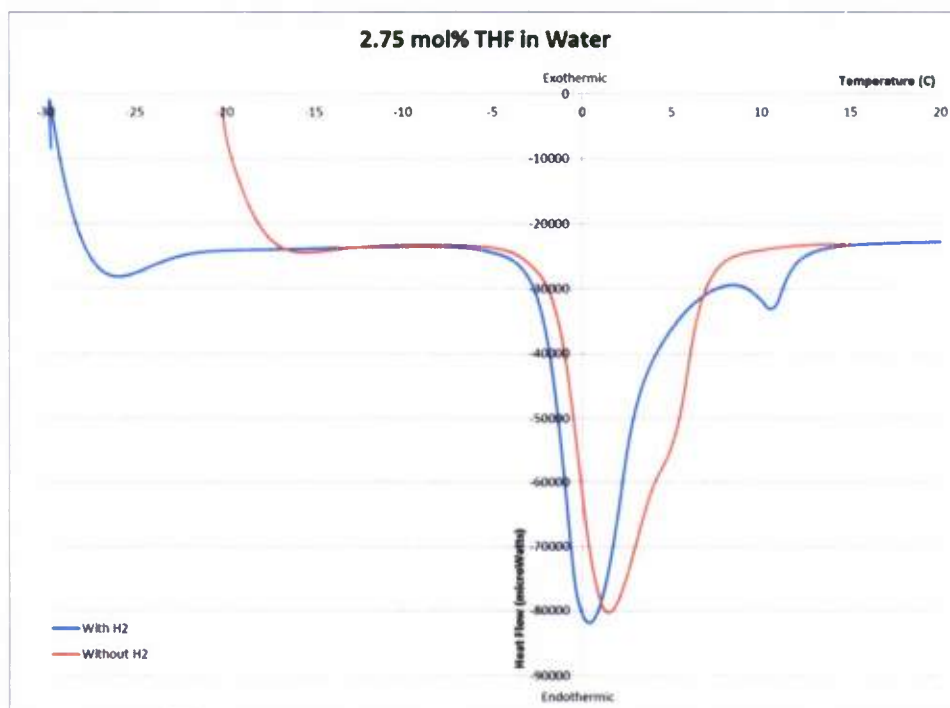


**Figure 3.17** Thermograms of hydrate dissociation for 2.75 mol% THF in water. Blue curve corresponds to pressurization with pure H<sub>2</sub> to 13.89 MPa (2,000 psig); red curve corresponds to pressurization with pure N<sub>2</sub>.

### Future Work

We have identified a protocol to synthesize THF/H<sub>2</sub> hydrate and are currently exploring ways to enhance H<sub>2</sub> storage capacity and reduce storage pressures. Toward this end, the Raman calorimeter system is being modified to try to perform quantitative measurements of H<sub>2</sub> stored in the hydrate phase through the collection and analysis of gases released during dissociation. The large-scale hydrate synthesis facility that was used in previous investigations of reagent dissociation of methane hydrates (Nihous *et al.*, 2010) is also being rebuilt to accommodate H<sub>2</sub> binary hydrate production.

### TBAB/H<sub>2</sub> Hydrate Synthesis Experiments

Although THF/H<sub>2</sub> hydrate appears to have relatively good potential as a hydrogen storage media, THF has a tendency to form highly explosive peroxides when in contact with air for prolonged periods. In consideration of this safety issue, other hydrate promoters warrant investigation. Hashimoto *et al.* (2006) and Chapoy *et al.* (2007) have published results that show that hydrogen can be stored in hydrates formed using tetra-*n*-butylammonium bromide (TBAB) at conditions similar to THF/H<sub>2</sub>. Although TBAB does not pose an explosion or flammability risk, the hydrogen storage capacity of its hydrate may be lower than that of THF/H<sub>2</sub> (Strobel *et al.*, 2007).

TBAB is an ionic salt that is used commercially as a phase transfer catalyst. Typically, the TBAB hydrate consists of two 5<sup>12</sup>6<sup>2</sup> cavities and two 5<sup>12</sup>6<sup>3</sup> cavities that are hydrogen-bonded together to form a hollow center to house the large TBA cation; the Br anion is incorporated in the hydrate lattice (Shimada & Furukawa, 1997; Shimada *et al.*, 2005). Shimada *et al.* (2005)



reported two types of TBAB hydrates: Type A (hydration number 26) and Type B (hydration number 38), and observed that the crystal structure of the hydrate varies based on the concentration of TBAB and is extremely dependent on interfacial kinetics. Addition of H<sub>2</sub> stabilizes empty small cages in the crystal (Hashimoto *et al.*, 2006).

During the present reporting period, we attempted to synthesize TBAB/H<sub>2</sub> hydrate using the Raman calorimeter. An aqueous solution of 40 wt% TBAB was prepared and loaded into the calorimeter sample cell that was vacuum evacuated twice and purged with Grade 4.0 dry N<sub>2</sub> gas. H<sub>2</sub> gas was then slowly bubbled into the solution until the cell pressure reached 7.00 MPa (1,000 psig). The sample was then slowly cooled to -2 °C and held at that temperature for three hours. The sample was then heated to 2 °C and held there for two hours to allow any ice that formed to melt. The sample was then heated at a rate of 0.01 °C/min to 22 °C, resulting in dissociation of the hydrate.

Figure 3.18 present a thermogram of the sample during the heating process. The red curve is the temperature and the blue curve corresponds to heat flow. An endothermic process begins as temperature increases above 8 °C and reaches a maximum at around 10 °C. At similar conditions, Oyama *et al.* (2005) report that TBAB/H<sub>2</sub> hydrate melts at approximately 10 °C. Further evidence of the existence of TBAB/H<sub>2</sub> hydrate can be found in Raman spectra collected during the calorimetry experiments. Figure 3.19 shows the Raman signal sampled at the start of the experiment, before any hydrate forms. The four peaks between 683 and 685 nm correspond to the H-H stretching vibrational mode in the gas phase (Hashimoto *et al.*, 2006). A second spectra taken at 7 °C during the heating phase prior to the endothermic event is presented in Figure 3.20. The single spectral peak is characteristic of TBAB/H<sub>2</sub> hydrate.

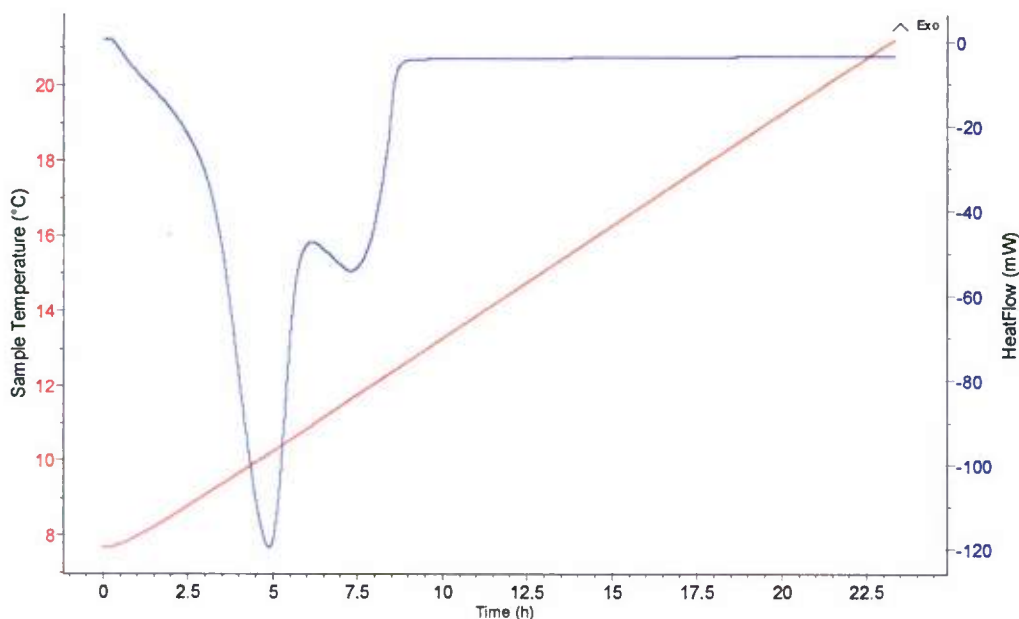


**Figure 3.18** Thermogram of hydrate dissociation for 40 wt% TBAB in water at 7.00 MPa (1,000 psig); red curve is sample temperature; blue curve is heat flow.

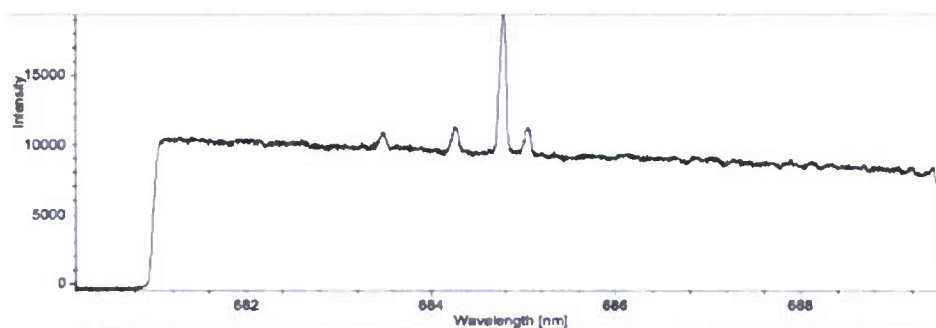


**Figure 3.19** Raman spectra collected before hydrate formation; 40 wt% TBAB in water at 7.00 MPa (1,000 psig) and room temperature.

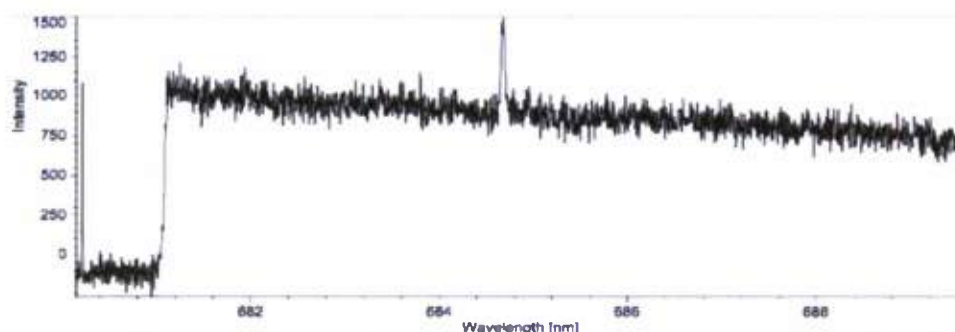


**Figure 3.20** Raman spectra collected prior to hydrate dissociation; 40 wt% TBAB in water at 7.00 MPa (1,000 psig) and 7 °C.

Experiments to investigate TBAB as an alternative hydrate promoter are being conducted in parallel with the THF/ H<sub>2</sub> hydrate development activities.

### International Collaborative Research and Development

The 7<sup>th</sup> international workshop on methane hydrate R&D was held in Wellington, New Zealand on 10-12 May 2010. This series of meetings was initiated as part of HEET and HNEI has served on the organizing committee and as a sponsor for all of the past workshops. The 7<sup>th</sup> Workshop was attended by 61 scientists, engineers, and other stakeholder from 15 countries. The workshop report is available from the GNS Science website:

<http://www.gns.cri.nz/Home/News-and-Events/Events/Fiery-Ice/The-final-conference-report>

Immediately following completion of the Wellington workshop, planning commenced for the 8<sup>th</sup> workshop that will be held in Sapporo, Japan from 28 May-1 June 2012. The Hokkaido branch of the National Institute of Advanced Industrial Science and Technology Science (AIST), an agency of the Government of Japan, is taking the lead for this workshop and HNEI will once again serve on the organizing committee and provide sponsorship. A workshop report should be available during the next phase of the HEET initiative.

### 3.4 Publications Resulting from Efforts

During the present reporting period, R&D conducted as part of the HEET Methane Hydrates Task has produced one publication:

Manya, J.J., Antal, M.J., Jr., Kinoshita, C.K. and Masutani, S.M. (2011) Specific heat capacity of pure water at 4.0 MPa between 298.15 and 465.65 K. *Ind. Eng. Chem. Res.*, **50**, 6470–6484.

### 3.5 References

Angell, C.A., Sichina, W.J.; and Oguni, M. (1982) Heat capacity of water at extremes of supercooling and superheating, *J. Phys. Chem.*, **86**, 998–1002.

AOAC International (1995) Official Methods of Analysis, 16th ed. Virginia.

Archer, D.G. and Carter, R.W. (2000) Thermodynamic properties of the NaCl + H<sub>2</sub>O System 4. heat capacities of H<sub>2</sub>O and NaCl(aq) in cold-stable and supercooled states, *J. Phys. Chem. B.*, **104**, 8563–8584.

Bourne D.G., McDonald, I.R., and Murrell, J.C. (2001) Comparison of *pmoA* PCR primer sets as tools for investigating methanotroph diversity in three Danish soils, *App. Environ. Micro.*, **67**(9), 3802-3809.

Bowman, J. (2000) The methanotrophs – the families Methylococcaceae and Methylocystaceae. in: *The Prokaryotes* (Dworkin M., ed.). <http://link.springer-ny.com/linkservice/books/10125>.

Chapoy, A., Anderson, R., and Tohidi, B. (2007) Low pressure molecular hydrogen storage in semi-clathrate hydrates of quaternary ammonium compounds, *J. Am. Chem. Soc.*, **129**, 746-747.

Czarnota, I. (1984) Heat capacity of water at high pressure, *High Temp.-High Press.*, **16**, 295-302.

Dyadin, Y.A., Larionov, E.G., Aladko, E.Y., Manakov, A.Y., Zhurko, F.V. and Mikina, T.V. (1999) Clathrate formation in water-noble gas (hydrogen) systems at high pressures, *Journal of Structural Chemistry*, **40**, 790-795.

Florusse, L.J., Peters, C.J., Schoonman, J., Hester, K.C., Koh, C.A., Dec, S.F., Marsh, K.N. and Sloan, E.D. (2004) Stable low-pressure hydrogen clusters stored in a binary clathrate hydrate, *Science*, **306**, 469-471.

Handa, Y.P. (1986). Compositions, enthalpies of dissociation, and heat capacities in the range 85 to 270 K for clathrate hydrates of methane, ethane, and propane, and enthalpy of dissociation of isobutane hydrate, as determined by a heat-flow calorimeter. *Journal of Chemical Thermodynamics*, **18**, 915-921.

Hashimoto, S., Murayama, S., Sugahara, T., Sato, H., and Ohgaki, K. (2006) Thermodynamic and Raman spectroscopic studies on H<sub>2</sub>+tetrahydrofuran+water and H<sub>2</sub>+tetra-n-butyl ammonium bromide+water mixtures containing gas hydrates, *Chem. Eng. Sci.*, **61**, 7884-7888.

Holmes A.J., Roslev P., McDonald R., Iversen N., Henriksen, K. and Murrell, J.C. (1999) Characterization of methanotrophic bacterial populations in soils showing atmospheric methane uptake, *Appl. Environ. Microbiol.*, **65**, 3312-3318.



Inagaki, F., Tsunogai, U., Suzuki, M., Kosaka, A., Machiyama, H., Takai, K., Nonoura, T., Nealson, K.H., and Horikoshi, K. (2004) Characterization of C1- metabolizing prokaryotic communities in methane seep habitats at the kuroshima knoll, Southern Ryuku Arc, by analyzing *pmoA*, *mmoX*, *mxoF*, *mcrA*, and 16S rRNA genes, *Appl. Environ. Microbiol.*, **70**(12), 7445-7455.

Kiene R.P. and Capone, R. (1985) Degassing of pore water methane during sediment incubations, *Appl. Environ. Microbiol.*, **49**: 143-147.

Kockova-Kratochvilova, A. (1990) Yeasts and yeast-like organisms, VCH, Weinheim, 305 ff.

Kolb, S., Kneif, C., Stubner, S. and Conrad, R. (2003) Quantitative detection of methanotrophs in soil by novel *pmoA* targeted real time PCR assays, *Appl. Environ. Microbiol.*, **69**, 2423-2429.

Komatsu, H., Yoshioka, H., Ota, M., Sato, Y., Watanabe, M., and Smith Jr., R.L. (2010) Phase equilibrium measurements of hydrogen-tetrahydrofuran and hydrogen-cyclopentane binary clathrate hydrate systems, *J. Chem. Eng. Data*, **55**, 2214-2218.

Lee, H., Lee, J-W., Kim, D.Y., Park, J., Seo, Y-T., Zeng, H., Moudrakovski, I.L., Ratcliffe, C.I., and Ripmeester, J.A. (2005). Tuning clathrate hydrates for hydrogen storage, *Nature*, **434**(7034), 743-746.

Makogon, Y.F. (1994). *Hydrates of Natural Gas*, Moscow, Nedra, Izdatel'stvo, PennWell Books, Tulsa, Oklahoma, p.237 in Russian (1981 in English).

Manya, J.J., Antal, M.J., Jr., Kinoshita, C.K. and Masutani, S.M. (2011) Specific heat capacity of pure water at 4.0 MPa between 298.15 and 465.65 K. *Ind. Eng. Chem. Res.*, **50**, 6470-6484.

Mao, W.L., Mao, H., Goncharov, A.F., Struzhkin, W.W., Guo, Q., Hu, J., Shu, J., Hemley, R.J., Somayazulu, M. and Zhao, Y. (2002) Hydrogen clusters in clathrate hydrate, *Science*, **297**, 2247-2249.

Marchesi, J.R., Weightman, A.J., Cragg, B.A., Parkes, R.J., and Fry, J.C. (2001) Methanogen and bacterial diversity and distribution in deep gas hydrate sediments from the Cascadia Margin as revealed by 16S rRNA molecular analysis, *FEMS Microbiol. Ecol.*, **34**(3), 221-228.

Nauhaus, K., Treude, T., Boetius, A. and Kruger, M. (2005) Environmental regulation of the anaerobic oxidation of methane: a comparison of ANME-1 and ANME II communities, *Appl. Environ. Microbiol.*, **71**, 98-106.

Niemann, H., Losekann, T., de Beer, D., Elvert, M., Nadalig, T., Knittel, K., Amann, R., Sauter, E.J., Schluter, M., Klages, M., Foucher, J.P., and Boetius, A.. (2006) Novel microbial communities of the Haakon Mosby mud volcano and their role as a methane sink, *Nature*, **443**, 854-858.

Nihous, G.C., Kuroda, K., Lobos-González, J.R., Kurasaki, R.J. and Masutani, S.M. (2010) An analysis of gas hydrate dissociation in the presence of thermodynamic inhibitors, *Chem. Eng. Sci.*, **65**(5), 1748-1761.

Oyama, H., Shimada, W., Ebinuma, T., Kamata, Y., Takeya, S., Uchida, T., Nagao, J., and Narita, H. (2005) Phase diagram, latent heat, and specific heat of TBAB semiclathrate hydrate crystals, *J. Fluid Phase Equilibria*, **234**, 131-135.

- Ruo, H., Ruan, A., Jiang, C. and Shen, D.S. (2008) Responses of oxidation rate and microbial communities to methane in simulated landfill cover soil microcosms, *Biosource. Technol.*, **99**, 7192-7199.
- Shimada, W. and Furukawa, Y. (1997) Pattern formation of ice crystals during free growth in supercooled water, *J. Phys. Chem. B*, **101**, 6171-6173.
- Shimada, W., Ebinuma, T., Oyama, H., Kamata, Y. and Narita, H. (2005) Free-growth forms and growth kinetics of tetra-n-butyl ammonium bromide semi-clathrate hydrate crystals, *J. Crystal Growth*, **274**, 246-250.
- Sirota, A.M. and Mal'tsev, B.K. (1959) Experimental investigation of the heat capacity of water at 1–500° C and to pressures of 500 kbar/cm<sup>2</sup>, *Teploenergetika*, **6**, 7.
- Sloan, E.D. (1998) Clathrate Hydrates of Natural Gases (2<sup>nd</sup> ed.), Marcel Dekker, New York, 730 pp.
- Strobel, T.A., Koh, C.A., and Sloan, E.D. (2007) Hydrogen storage properties of clathrate hydrate materials, *J. Fluid Phase Equilibria*, **261**, 382-389.
- Strobel, T.A., Sloan, E.D. and Koh, C.A. (2009) Raman spectroscopic studies of hydrogen clathrate hydrates, *J. Chemical Physics*, **130**, 014506.
- Takeya, S., Hori, A., Hondoh, T., Uchida, T. (2000) *Journal of Physics and Chemistry B*, **104**, 4164.
- Tanaka, H., Nakatsuka, T. and Koga, K. (2004) On the thermodynamic stability of clathrate hydrates IV: double occupancy of cages, *J. Chemical Physics A*, **121**(11), 5488-5493.
- Tavormina, P.L., Ussler, W., and Orphan, V.J. (2008) Planktonic and sediment associated aerobic methanotrophs in two seep systems along the North American Margin, *App. Environ. Microbiol.*, **74**(3), 3985-3995.
- Vos, W.L., Finger, L.W., Hemley, R.J., and Mao, H-K. (1993) Novel H<sub>2</sub>-H<sub>2</sub>O clathrates at high pressures, *Physical Review Letters*, **71**(19), 3150-3153.
- Wagner, M., Roger, A.J., Flax, J.L., Brusseau, G.A., and Stahl, D.A. (1998) Phylogeny of dissimilatory sulfite reductases supports an early origin of sulfate respiration, *J. Bacteriol.*, **180**(11), 2975 – 2982.
- Wagner, W. and Pruss, A. (2002) The IAPWS formulation 1995 for the thermodynamic properties of ordinary water substance for general and scientific use, *J. Phys. Chem. Ref. Data*, **31**, 387–535.
- Wise, M.G., McAuthur, J.V. and Shimkets, L.J. (1999) Methanotroph diversity in landfill soil: isolation of novel type I and type II methanotrophs whose presence was suggested by culture independent 16S ribosomal DNA analysis, *App. Environ. Microbiol.*, **65**(11), 4887-4897.
- Yedlapalli, P., Lee, S. and Lee, J.W. (2010) Stable occupancy of hydrogen molecules in H<sub>2</sub> clathrate hydrates and H<sub>2</sub>+THF clathrate hydrates determined by *ab initio* calculations, *Journal of Thermodynamics*, Article ID 651819.

Yan, T., Ye ,Q., Zhou, Z., and Zhang, C.L. (2006) Diversity of functional genes for methanotrophs in sediments associated with gas hydrates and hydrocarbon seeps in the Gulf of Mexico, *FEMS*, **57**, 251-259.

Yonsel, S., Bulbul-Caliskan, G., Koni, M., and Dagasan, L. (2007) Monitoring of yeast metabolism with calorimetry, *Chem. Biochem. Eng. Q.*, **21**(4), 395-408.



This page is intentional blank.

## **4. Alternative Energy Systems**

The Office of Naval Research is currently formulating plans for an effort intitled the Asia Pacific Technology and Education Program (APTEP). The goal of APTEP is to promote commerce and partnerships in the Asia-Pacific region through advancements in research, technology development and education. Hawaii is uniquely suited to serve as the center for APTEP activities due to geographic location, environmental similarities to other Asia-Pacific regions, cultural, educational and economic ties to many Asia-Pacific nations, and world-leading research capabilities in scientific and technology areas highly relevant to Asia-Pacific needs.

Prior to the development of this integrated research and education concept, HNEI, in collaboration with ONR, proposed Hawaii as a model for development, deployment, testing, and evaluation (DDT&E) of energy systems of interest to the Department of Defense in the Pacific Region. Under this initial phase of the DDT&E effort, HNEI initiated activities in three technology areas: testing of subscale heat exchangers to validate performance for Ocean Thermal Energy Conversion (OTEC) application, planning and site development for testing and evaluation of grid-scale battery energy storage, and evaluation of the performance and durability of photovolataic (PV) technologies.

### **4.1 OTEC Heat Exchangers**

The heat exchangers are the heart of an OTEC plant: they are the single most expensive component and the most critical relative to the overall efficiency of the plant. Small changes in heat exchanger performance will have immense economic consequences and any failure from corrosion or fouling would be catastrophic. The heat exchangers require very careful design and thorough testing and evaluation prior to incorporating them into full-scale OTEC plants. Such plants are expected to cost hundreds of millions of dollars.

Under separate funding from NavFac, Makai Ocean Engineering developed the infrastructure for a heat exchanger test facility at the Natural Energy Laboratory of Hawaii Authority (NELHA) on the Island of Hawaii. This is the only industrial park in the world that is specifically designed to provide the infrastructure to immediately and economically support such a test facility. Existing infrastructure at NELHA includes ready access to deep seawater (from 2,200' or 3,000' deep) and surface seawater flows in quantities exceeding 10,000 gpm.

The overall objectives for the heat exchanger (HX) test facility include:

- Design, develop and fully test a practical set of heat exchangers for use in the world's first commercial-size OTEC plant.
- Determine the long-term and short-term corrosion characteristics of heat exchanger designs currently being considered for use. This includes considerations of various materials, fabrication techniques, and anti-corrosion methods, and then comparing these results with previous testing.
- Determine if any difference exists between corrosion characteristics of 2,200-foot-deep water from the 40" intake pipe at NELHA and 3,000-foot-deep water from the 55" intake pipe at NELHA.
- Evaluate anti-fouling techniques and demonstrate their successful operation. Determine practical anti-fouling measures.

- Test the performance of evaporators and condensers with both seawater and ammonia flows at various seawater and ammonia flow rates. Determine optimum performance parameters.
- Evaluate heat exchangers in parallel- and series-flow arrangements on both the seawater and ammonia circuits. Determine limitations important to each type of heat exchanger construction.
- Identify and/or originate heat exchanger design software that can accurately predict the performance obtained from heat exchanger testing.
- Suggest, analyze, evaluate and put into prototype form new heat exchanger designs. Investigate heat exchanger arrangements, candidate materials, anti-corrosion processes and fabrication alternatives that require testing and evaluation.
- Determine the required attributes of a larger-sized permanent OTEC heat exchanger test facility and complete the design of same. Coordinate this design with and construct the facility at NELHA.

Under this award, HNEI contracted Makai Ocean Engineering (OE) to procure and test heat exchangers with the following goals: a) arrange test facilities and begin small-scale heat exchange testing, b) conduct modeling and design of heat exchanger systems, c) assemble the HX test facility, and d) initiate shakedown testing of the HX test facility. Makai OE also developed an on-site corrosion test facility to evaluate durability of various potential heat exchanger test materials. Results from this effort have been separately reported to ONR.

## 4.2 Storage Analysis

Under a series of awards from the US Department of Energy, HNEI contracted GE Global Research Center to develop dynamic load flow and dispatch models of the various island grid systems. The neighbor island grid system loads (excluding Oahu) range from as low as approximately 35 MW to as high as 180MW, while the Oahu grid system has a nameplate capacity approaching 1.4 GW. Each island power system is characterized by its own generation mix, load characteristics, and ramping rate limits determining its response to intermittent generation and load variations, making these systems ideal for testing of grid-scale battery storage. For example, on the smaller grid systems, models indicate that as little as one MW of fast storage has the potential to provide significant frequency regulation and other ancillary services to the grid. Other potential applications include ramp-rate control of grid-scale photovoltaic (PV) systems, and voltage and power support on distributions systems with high penetration of renewables. Under this subtask, HNEI conducted site evaluations, and developed and initiated design studies to identify opportunities for deployment, testing and evaluation of battery storage systems.

Initially, UH-HNEI developed a project plan for deployment of a high-power 1 MW, 250 kw-hr, Li-ion titanate battery energy storage system from Altairmano Inc. on the Big Island of Hawaii to evaluate performance for smoothing of wind farm output and frequency regulation. Funding for deployment was included and awarded in a subsequent proposal to ONR. However, during this award period, funding for additional battery energy storage systems became available due to ownership changes with the selected vendor. As a result, site planning was expanded to include a second site, this one on the island of O'ahu, and interconnection studies conducted in collaboration with Hawaiian Electric Light Company (HELCO, Hawaii Island) and Hawaiian



Electric Company (HECO, Oahu). The second site offers the opportunity to evaluate battery performance and impact to provide voltage and power support on a distribution feeder line with a high penetration of distributed photovoltaic systems.

Figure 4.1 illustrates the relative size and configuration of a single 1 MW / 250 kWh storage system.



**Figure 4.1 ALTI-ESS Battery System (photographs courtesy of Altairnano Technologies)**

As stated, two sites were identified as ideal candidates for the initial battery storage tests: one at the Hawi Renewable Development (HRD) wind plant located in Kapaa on the Island of Hawaii and the second interconnected to the Waiawa substation in Waipahu on the island of Oahu on a circuit with a high penetration of distributed PV systems. Figure 4.2 shows the locations of the two battery systems. Included in Figure 4.2 is a GIS map of the annual wind speed for the islands.

Each utility system site is characterized by its own generation mix, load characteristics, and ramping rate limits determining its response to intermittent generation and load variations. To better understand how a fast-response grid-size battery could mitigate the effects of a rapid down ramp event for a 10.6 MW Wind farm, modeling studies were conducted. The model used high-resolution two-second data from a worst-case down-ramp event from HELCO data for May 23<sup>rd</sup> 2007. The results of the simulation and a fast-response battery system to maintain satisfactory frequency and minimize the size of excursions from 60 Hz are illustrated in Figure 4.3.

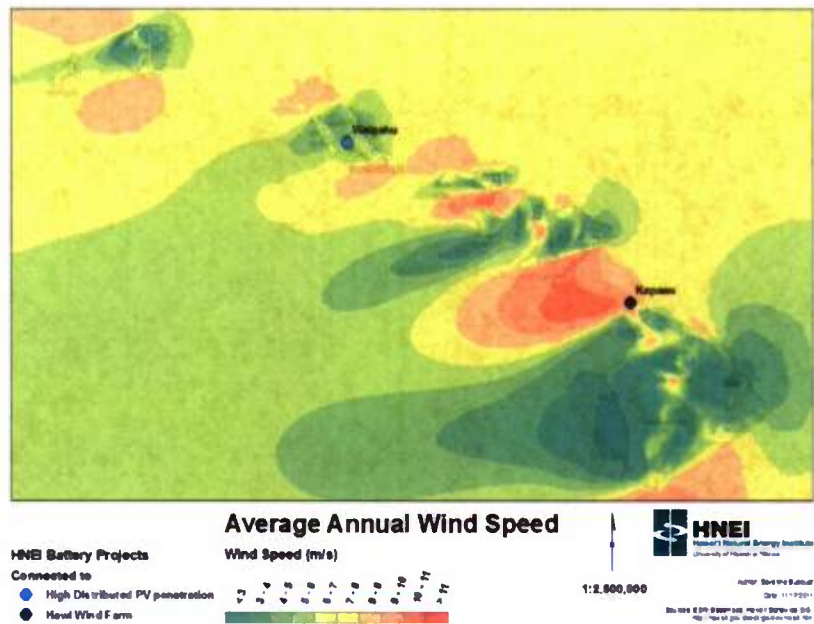


Figure 4.2 Locations of the grid-tied battery storage systems on the islands of Hawaii and Oahu plus average annual wind speed [1]

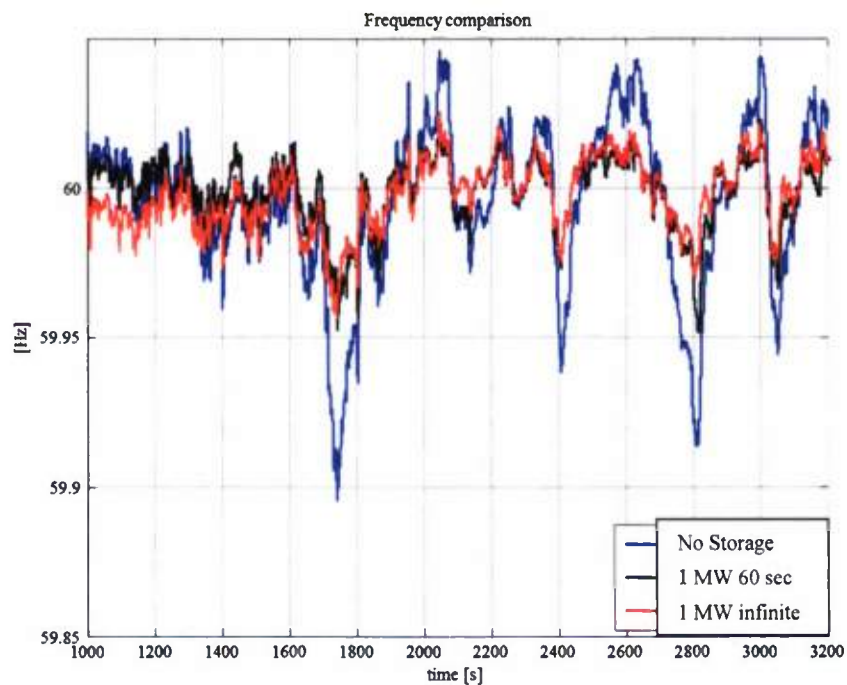


Figure 4.3 Frequency Mitigation with Increased Wind Penetration [2]

The two MW battery storage systems will be developed and fielded under a separate ONR contract to validate the simulation with real-world data.

#### References:

- [1] State GIS program web site <http://hawaii.gov/dbedt/gis/> visited on 11/17/2011.
- [2] HELCO Lisa Dangelmaier.

### 4.3 Photovoltaic (PV) Assessment

PV performance is strongly dependent on environmental variables (cloud shadowing, irradiance, wind, cell temperature, etc.) that make accurate prediction of the output at any instant in time difficult. The most severe condition in PV generation is encountered when sudden passage of a cloudbank sweeps the entire PV generator, resulting in a large power variation. The effect on the electrical grid can be one of further deterioration if covering of the PV arrays occurs at a time of sudden change in load demand. The utility must adequately respond to these variations with its own generation or imported energy. Each power system is characterized by its own generation mix and ramping rate limits, determining its ability to respond to generation and load variations. The effect of PV on the grid-system dynamic may vary in severity depending on the response characteristics of individual modules, array designs, geographic location of the arrays, and size of the arrays.

Under this subtask, HNEI executed a project plan to instrument up to 14 grid-connected photovoltaic (PV) arrays to monitor their performance, response characteristics to environmental changes, and interaction with the grid. Activities included planning, designing, implementing, and managing tasks to fully instrument an existing grid-connected PV Inverter system at Pu'u Wa'awa'a. The existing system was developed and fielded under separate award from the US Department of Energy.

The Pu'u Wa'awa'a PV test bed, commissioned July 9<sup>th</sup>, 2010, is located on the North Kona coast on the island of Hawaii (Latitude: 19.77°, Longitude: -155.84°, Altitude: 686 m). The test bed lies on the edge of the Honua'ula Forest Reserve and is less than five miles from the coast line (see Figure 4.4). The landscape is a combination of tropical dry and moist forest, and grasslands. It is an idea site to assess PV performance and intermittency of renewable generation under a variety of weather conditions in a highly corrosive salt air environment.

The system is configured for side-by-side comparisons of 7 (seven) module pairs representing 7 (seven) different manufacturers and 4 (four) different technologies (see Table 4.1).





**Figure 4.4 Pu'u Wa'awa'a Testbed**

**Table 4.1 Selected PV modules being tested at Pu'u Wa'awa'a**

Company	P/N	Peak Power W	Module Area m <sup>2</sup>	Efficiency (specs @ STC)	Type
<b>SunPower</b>	SPR-215-WHT	215	1.2441	17.3%	m-Si (mono)
<b>Kyocera</b>	KD205GX-LPU	205	1.4550	13.8%	p-Si (poly)
<b>SANYO</b>	HIP-210NKHA5	210	1.2608	16.7%	a/m-Si
<b>Suntech</b>	STP 175S-24/Ab-1	175	1.2766	14.6%	m-Si
<b>BP solar</b>	BP175B	175	1.2585	13.9%	p-Si
<b>SolarWorld</b>	SW175-P	175	1.3041	13.4%	m-Si
<b>UNI-SOLAR</b>	PVL-68 2 in series	136	2.2441	6.1%	a-Si (amorphous)

The subtask included the following activities:

- Developing or modifying existing sensor measurement units to support data collection using the high-resolution (1 Hz) data acquisition system (DAS);
- Developing or procuring required tools to support calibrating the sensors installed on the PV and inverters and weather station;
- Developing and/or procuring equipment or licenses as needed to develop the MATLAB-based visualization applications; and
- Contributing to development of a data base architecture which included HW and SW concepts necessary to support the following functions: connect and collect, local storage and backup, remote achieve and manage, processing, and visualization.

Figure 4.5 shows the positioning of the weather station and the DAS enclosure at the Pu'u Wa'awa'a site. Time-stamped data collected from the module and inverter includes temperature, voltage, and current. Time-stamped data collected from the weather station includes wind speed and direction, ambient temperature, relative humidity, barometric pressure, and insolation.

The installed data (1-sec sample rate) collection system is providing time-stamped weather data sets that will be utilized to validate high-resolution spatial monitoring and forecasting of solar resources for use in Hawai'i (under separate contract) and their applicability for future grid integration with HELCO, HECO, MECO, or KUIC.



**Figure 4.5 Weather Station/DAS Enclosure**

Figure 4.6 is representative of the type of visualization that can be done for module and solar irradiance data using an application developed in the MATLAB environment.

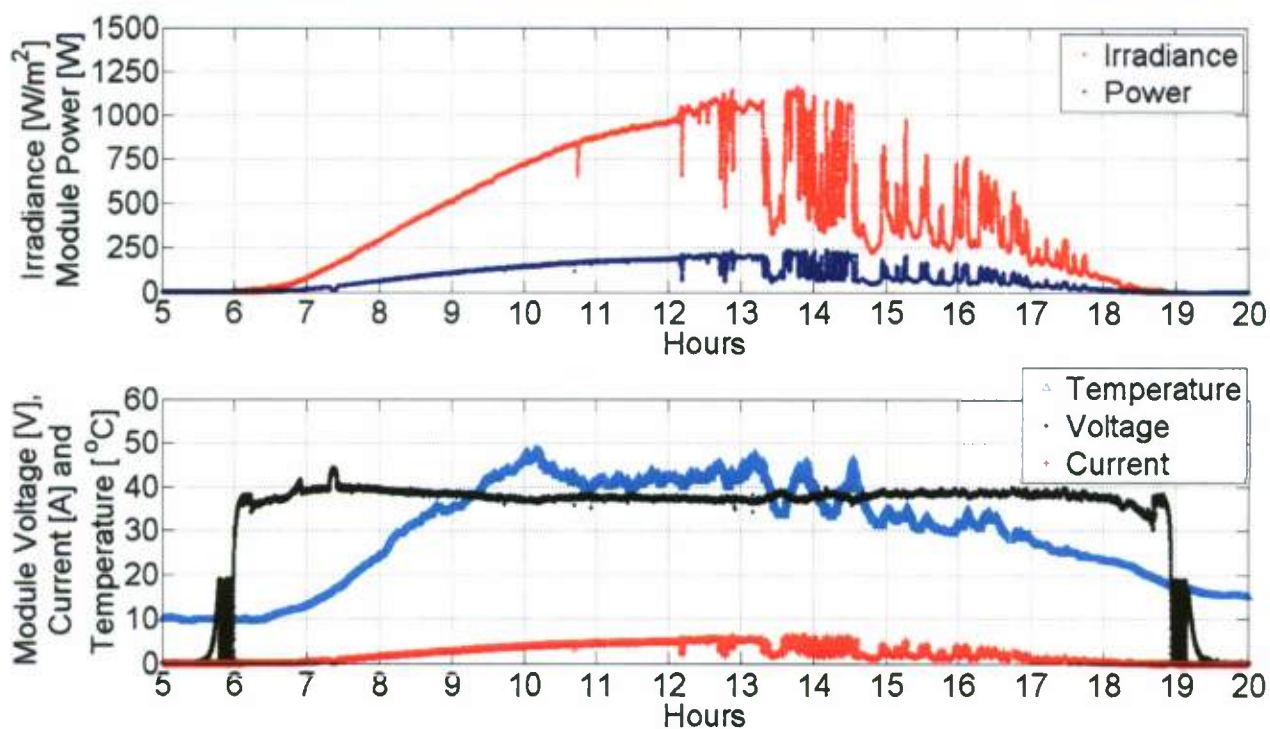


**Figure 4.6 Irradiance and module performance on August 6<sup>th</sup>, 2011**  
 Top) Irradiance and module power versus time;  
 Bottom) Module voltage, current and temperature versus time.